WEIGHTED ARRAYS FOR MODAL ISOLATION AND ACTIVE CONTROL OF COMPLEX STRUCTURES

by

Michael L. Fripp

B.S., Department of Engineering Science and Mechanics,
Virginia Polytechnic Institute, 1992
M.S., Department of Aeronautics and Astronautics,
Massachusetts Institute of Technology, 1995

SUBMITTED TO THE DEPARTMENT OF AERONAUTICS AND ASTRONAUTICS
IN PARTIAL FULFILLMENT OF THE REQUIREMENTS FOR THE DEGREE OF
DOCTORATE OF PHILOSOPHY
AT THE
MASSACHUSETTS INSTITUTE OF TECHNOLOGY

June 2000

Signature of Author _____
Department of Aeronautics and Astronautics
May 25, 2000

Certified by _____
Professor Nesbitt W. Hagood, Committee Chair
Department of Aeronautics and Astronautics

Certified by _____
Dr. Mauro J. Atalla
Department of Aeronautics and Astronautics

Certified by _____
Professor David W. Miller
Department of Aeronautics and Astronautics

Accepted by _____
Professor Nesbitt W. Hagood, Graduate Representative
Department of Aeronautics and Astronautics

WEIGHTED ARRAYS FOR MODAL ISOLATION AND ACTIVE CONTROL ON COMPLEX STRUCTURES

by

MICHAEL L. FRIPP

Submitted to the Department of Aeronautics and Astronautics
on May 19, 2000 in Partial Fulfillment of the
Requirements for the Degree of Doctorate of Philosophy
at the Massachusetts Institute of Technology

ABSTRACT

Arrays of sensors and actuators are designed to provide modal isolation and robust broadband feedback control on complex structures with high performance and limited modeling. The weighted array technique proposed here enables the design of reduced-order controllers for complex structures and offers the potential to improve closed-loop robustness and to broaden the region of good performance even as the plant changes. The weighted summation of the transducer signals senses the modes that are relevant to performance while rejecting the remaining modes; therefore reducing the required complexity of the controller. These weights are obtained from the minimization of a cost function and, under certain assumptions, it can be shown that a single optimum solution exists.

The use of weighted arrays is motivated by the need to control the vibration response of aircraft. A representative fuselage test-bed was designed to retain the essential structural-acoustic dynamics of aircraft on a reduced size structure. Sensing and actuation plies of piezoelectric transducers were bonded to the fuselage test-bed and to other representative cylinder sections. Array weights were computed and successfully applied to isolate the targeted modes. The modal isolation allowed the implementation of simple control algorithms on the complex structures. Different methods of computing the weights are implemented and compared. The deleterious effects of spatial aliasing, the performance as a function of the array size, the sensitivity to random perturbations, and the effects of transducer failure are explored.

Doctoral Committee Chairman:
Professor Nesbitt W. Hagood
Department of Aeronautics and Astronautics

This thesis is dedicated to my true teachers, Archie and Jean Fripp
and to my true advisor, Deborah Fripp

Acknowledgements

This project would not have been possible without the assistance of many people, but there are three principle characters around whom the story of my thesis has revolved. Without the assistance of Mauro Atalla, I doubt that I would have completed this degree. Steve Tistaert's assistance greatly expanded the useful work that this dissertation was able to accomplish. My advisor, Nesbitt Hagood, stood by me during the many tribulations of this thesis process.

Technical assistance came from many sources. Early direction assistance was provided by Richard Silcox of NASA Langley. Dave Miller provided pivotal directional assistance as the research progressed. Finite element modeling work was performed in conjunction with Katie Lilienkamp and Elaine Chen. I would also like to thank Mr. Don O'Sullivan, who collaborated in the conceptual design of the acoustic test-bed, and who was responsible for the final design and procurement of the test-bed structure. Tim Booher provided electronic assembly, manufacturing designs, and comic relief. Djuna Copley-Woods spearheaded the construction of the single panel impedance tube. Daniel Kwon built amplifiers and worked with Christian Garcia on manufacturing active plies. Their final hour drive to instrument the fuselage test-bed was especially appreciated. Cagri Savran proved critical in coordinating the work on the fuselage test-bed. His data helped complete the picture that my thesis sought to present.

Psychological assistance was provided by many more people. Deborah Fripp exercised great patience during this process while Nathan Fripp reminded me that a new child is more fun than an old thesis. My family offered sage advice when the thesis became rough. Kamyar Ghandi, Jennifer Rochlis, Jennifer Donaldson, John Rodgers, Margee Best, Benon Janos, Marylin Good, SharonLeah Brown, Malinda Lutz, Tim Glenn, Jeremy Yung, Chris Dunn, Kin Chan, Karen Marais, Scott Uebelhart, Patrick Trappa, Becky Masterson, and Sh'kia Fripp all offered unique avenues to decompress from the tribulations of this thesis.

Funding for this research was provided by a contract from the U.S. Army Research Office (ARO) under contract DAAH04-95-1-0104, which is monitored by Gary Anderson. Mai Nguyen is the MIT contract administrator.

Contents

List of Figures

List of Tables

CHAPTER 1

Introduction

It ain't what you know, it's what you know that ain't so that causes trouble.
- Edward Redish, 1999

Complex systems are difficult to model and, thus, are difficult to actively control. This thesis describes how weighted arrays can be used to pre-filter the sensor and actuator signals. The filtering can be designed to isolate individual modes of the resonant system, which will simplify the apparent dynamics of the complex system and enable simpler and more robust control algorithms. This chapter discusses the motivation for using modal sensors and actuators as well as discussing previous research that has been conducted on the design and implementation of modal sensors and actuators.

1.1 Motivation

This thesis is motivated by the need to perform active control on complex systems. The control of large and complex structures, such as aircraft or automobiles, is difficult because these structures exhibit complicated dynamics, high modal density, and time varying dynamics. Traditionally, the dynamics of these systems have been damped with

passive control. Wide varieties of passive control technique have been implemented ranging from foams to fiberglass to tuned-mass dampers. However, all of the passive control implementations are difficult to implement for low-frequency disturbances because lower frequencies require thicker and heavier passive dampers. Active control is needed to minimize the response from low- and mid-frequency disturbances or where design requirements impose weight restrictions or performance requirements.

The traditional approach for active control relies upon a model-based controller to estimate the dynamics of the system. These traditional model-based control techniques, such as LQG optimal feedback control or filtered-X LMS feedforward control, use a numerical model to estimate the dynamics of the system in order to achieve a stable control loop. The information that needs to be modeled is illustrated in Figure 1.1. Most of the model-based controllers use a numerical model of the modal coordinate transformations to map the sensor signals to the system's modal behavior. The numerical model needs to be of roughly the same order as the system that it describes in order to achieve robust performance. Modeling errors due to unmodeled dynamics, missed dynamics, or time-varying dynamics can mar performance and lead to instability [von Flotow, 1988]. Modeling errors are more significant in the lightly damped and modally dense systems that are the focus of this thesis.

Proper design of the sensors and actuators can reduce the model-based controller's sensitivity to error. Modal sensors and actuators reduce the sensitivity to

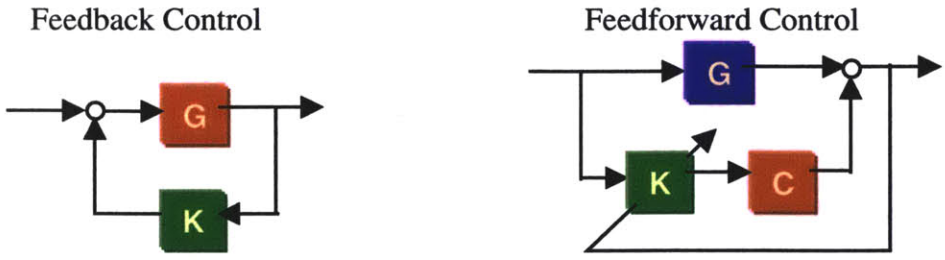

Figure 1.1: Both kinds of active control, feedback control and feedforward control, require a numerical model of the system dynamics in order to design the controller, **K**. Feedback control requires a model of the plant **G**, which is the transfer function from the actuators to the sensors. Feedforward control requires a model of the signal path, **C**, which is the transfer function from the actuators to the performance sensors.

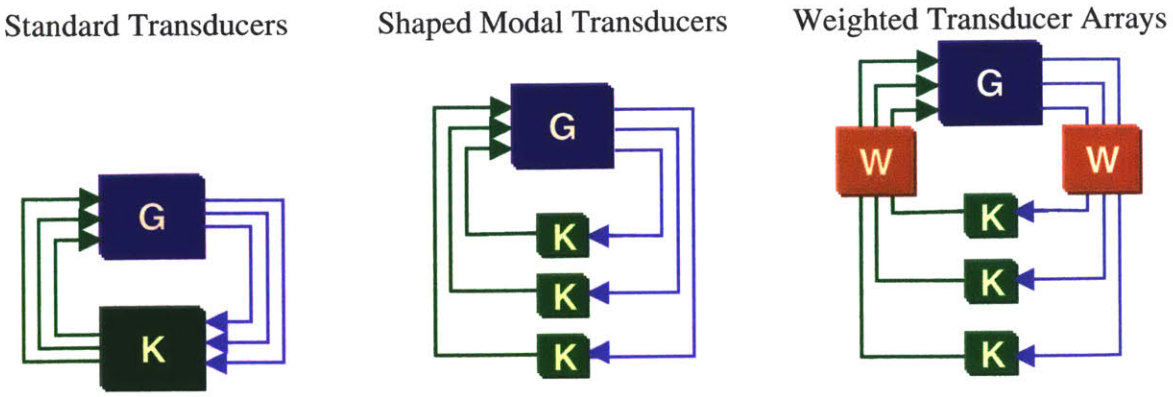

Figure 1.2: Standard control features an array of transducers feeding into a large model-based controller. Modal transducers sense individual modes of vibration, which allows the modes to be controlled independently. Shaped modal transducers sense a separate mode for each transducer. Weighted transducer arrays use a weighted summation of the transducers to approximate individual desired modes.

error in the numerical model by simplifying the modal coordinate transformation. Modal sensors and actuators are designed to directly sense the modal state of the system, and, thus, remove the need for the modal coordinate transformation. As a result, a perfect modal transducer would feature a single mode in their transfer function instead of the summation of modes measured by typical transducers.

Control with modal sensors and actuators is simpler than control where a modal transformation is required. The modal transducers reduce the complicated dynamics into a series of modal responses, which allows each of the modal responses to be controlled independently. As illuminated in Figure 1.2, the standard control approach takes an array of sensor data into a large model-based controller, **K**, and returns an array of actuator signals to the system, **G**. In the case of using standard transducers, the controller uses a numerical model to transform the transducer signals into modal coordinates. Modal sensors and actuators remove the need for a numerical model to transform the transducer signals into modal coordinates, and, thus, simpler controllers can be implemented. Modal transducers can be implemented either by shaping the transducers or by taking a weighted summation of a transducer array.

1.2 Modal Transducers

The shape and location of sensors and actuators on a structure determines which modes are sensed and actuated. For example, placing a point sensor on a modal node renders that mode unobservable to the sensor. Modal sensors and actuators are a class of transducers that are carefully designed so that only one mode is addressed by a particular sensor or actuator. The shape and position of modal transducers creates a spatial filtering so that all modes except one are orthogonal to the sensor or actuator [Clark et. al., 1998].

Modal sensors and actuators reduce the apparent complexity of complex structures because they reduce the dynamics to the response of a single mode. This single mode correspondence between the actuators and sensors diagonalizes the transfer function matrix. As a result, modal sensors and actuators serve as a pre- and post-filters to the ultimate application. Modal transducers are application independent and can be implemented for any form of actuator or sensor combination on any type of system. Modal transducers implement spatial integration, which is a smoothing operation that cannot lead to instability [Meirovitch, 1985].

Active control and shape estimation are the principle applications that have driven the development of modal sensors and actuators. These applications are greatly simplified if the modal behavior of the system is known. Modal sensor and actuators have been shown to offer a number of practical advantages in reducing the complexity of the system. If a system is known to involve only a few significant modes, then independent modal transducers can minimize the number of sensors and actuators, can reduce the dimensionality of the controller, and can minimize the control energy [Meirovitch, 1983A]. Additionally, if an adaptive feedforward control algorithm is implemented, then the convergence problem is minimized by uncoupling the modal responses because the convergence time is limited by the unequal spatial eigen-values, even for single-frequency tones [Morgan, 1990; Clark, 1995]. Controller spillover, which degrades adaptive feedforward control techniques, is minimized through the use of modal filters [Clark, 1995]. Since modal transducers couple the controller with the system's modes, global power control is more readily achieved [Clark, 1995]. Perhaps most important, the

use of modal transducers reduces the apparent complexity of the system and, thus, reduces the needed size of the controller or shape estimator.

The development of modal transducers has been a quest to design and to apply these transducers to increasingly complex structures. The early implementations of modal transducers required a very accurate knowledge of the structural dynamics, and, thus, were initially applied to flat beams. Successive refinements to the theory of modal sensing and actuation have allowed on-line adaptation and identification and have been applied to structures ranging from bridges [Shelley, 1995] to spacecraft [Shelley, 1991B] and aircraft [Fripp, 1999].

1.3 Shaped Distributed Transducers

Shaped sensors rely upon orthogonality of strain mode shapes (eigenvectors) in order to isolate individual modes. If the electrode pattern of the transducer is etched into the shape of a particular strain mode of a structure, then the sensor effectively acts as a modal filter, measuring only the modal amplitude of the targeted mode.

The concept of modal sensors was first introduced by Balas (1978) for the control of distributed parameter systems. Meirovitch (1982) first used the term "modal filter" and derived a method for calculating the weights on continuous and discrete sensor elements. Meirovitch's design assumes that the mode shapes are exactly known and that the strain mode shapes are orthogonal. If these assumptions are met, then the optimal weights are the strain mode shape of the targeted mode. In other words, the shape of the strain sensor, $\mathbf{w}(x)$, designed to detect the r^{th} mode of a flat Bernoulli-Euler beam should have the shape equal to

$$\mathbf{w}(x) = \frac{\partial \psi_x^r}{\partial x} - \frac{t}{2}\frac{\partial^2 \psi_z^r}{\partial x^2} \tag{1.1}$$

where ψ_x^r is the stretching shape of the r^{th} mode, ψ_z^r is the bending shape of the r^{th} mode, and t is the thickness of the structure. The stretching term is very important for the low modes of curved structures but can generally be ignored for flat structures. In other words, if the electrode pattern of the piezoelectric transducer is etched into the shape of a

particular strain mode of a structure, then the sensor effectively acts as a modal filter with respect to all modes and only returns the modal amplitude of that targeted mode. Shaped modal transducers offer advantages of robustness to system parameter uncertainty and errors that arise from spatial discretization [Meirovitch, 1983B; Baruh, 1985].

The early experiments with shaped sensors were conducted on beams [Burke, 1987; Chiang, 1989; Lee, 1990]. By etching the electrode of a Polyvinylidene fluoride (PVDF) film into the mode shape of the first mode, Lee (1990) was able to minimize the response of the second mode over the response of the first mode. Other investigators encountered similar levels of performance of about 15 dB for shaped sensors on smooth beams [Sumali, 1991; Zhou, 1991] or beam-like robot arms carrying a load [Collins, 1992]. Summaries of the concept of shaped sensors are available in textbooks [Fuller, 1996; Preumont, 1997; Clark, 1998]. The shaped sensors greatly ease the control effort and allow for simpler and more robust control algorithms [Chiang, 1989; Lee, 1991]. A good summary of the trade-offs for using shaped modal transducers in adaptive feedforward control is found in Clark (1995). A good summary of the manufacturing technique is found in Pines (1997B).

Although most shaped sensors are designed to detect an individual mode of vibration, they can also be shaped to detect acoustic radiation modes [Clark, 1992A, 1993; Rex, 1992; Johnson, 1993, 1995; Snyder, 1993, 1995, 1996; Charette, 1998]. Acoustic radiation modes are a combination of structural vibration modes that, when combined, approximate the far field sound radiated perpendicularly from a planar structure. Thus, using a sensor that shaped to detect acoustic radiation modes is also sensing the performance metric, which dramatically increased the performance of the control of acoustic radiation over using structural modal sensors [Clark, 1992A, 1993; Snyder, 1993, 1995, 1996]. In the general case, sensors shaped to the acoustic radiation modes are complex and, thus, require a separate sensor for the real part of the weight and for the imaginary part. Implementation of acoustic modal filters is much more complex in the case of non-planar structures because the Rayleigh integral is not valid and a formulation involving a Green's function needs to be derived [Maillard, 1997].

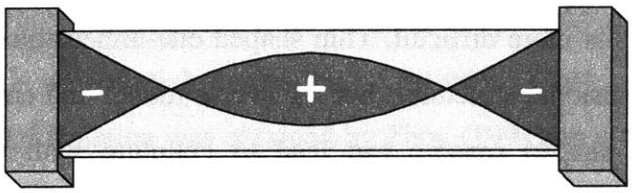

Figure 1.3: Shaped sensor pattern for a strain sensor to detect the first mode of a clamped-clamped beam. Some of the strain must be added while some must be subtracted, as denoted by the plus and minus signs.

Another approach is to shape the transducers so that *all* modes are observed and controlled [Burke, 1990A, 1990B, 1991; Sullivan, 1994, 1995, 1996, 1997]. For a simply-supported plate, two-dimensional modal sensors can be constructed, in theory, from triangular elements [Sullivan, 1994, 1996, 1997]. By using collocated actuators and sensors, rate feedback can be used for control with guaranteed stability until the region of controller roll-off. This approach of sensing all modes requires an accurate estimation of the structure's mode shapes and then an optimization routine to determine the proper placement and location of the triangular elements [Burke, 1991]. The transducers generally need to cover the entire extent of the structure. Additionally, the simplifications used to design the transducers limits the application to planar structures that exhibit limited in-plane stretching. The concept was experimentally implemented on a simply supported plate [Sullivan, 1995] but encountered problems due to acoustic coupling from room noise to the PVDF sensors [Sullivan, 1995; Burke, 1995].

Charette [1998] used experimentally measured mode shapes in the design of the shaped PVDF sensors. In a set of linear equations, the complexity of the sensor shape is directly related to the total number of modes to be addressed by the sensor. This concept was experimentally implemented on a clamped plate and the sensors set to estimate the acoustic excitation. Feedforward control was implemented and the acoustic amplitude was reduced by 10 dB to 30 dB.

1.3.1 Two-Dimensional Structures

While one-dimensional shading needed for beams can be realized with shaped transducers, the practical realization of two-dimensional shading needed for distributed

transducers on plates is more difficult. Thin shaped one-dimensional modal sensors can be used on two-dimensional structures, but transverse modes and errors in the placement of one-dimensional shaped sensors can lead to coupling with undesired modes in experimental implementations [Burke, 1995C].

There are several methods for obtaining two-dimension arrays: varying the material sensitivity or varying the material excitation/electroding. Changing the material sensitivity is difficult to physically implement with high accuracy although ideas about partial depoling of the transducers [Lee, 1990] and varying the thickness have been voiced [Sullivan, 1997]. Variable size arrays use elements of different sizes in order to effectively vary the material electroding [Burke, 1995A]. However, problems with spatial aliasing will wreck the performance as well as errors in placement, estimation, and construction. Selectively doped PVDF film has been considered for a spatially varying two-dimensional sensor [Johnson 1993; Clark, 1993; Snyder 1996; Miller, 1997], however implementation has proven difficult. Current manufacturing techniques prohibit the tight control of two-dimensional sensitivity for most actuators or sensors.

The early implementations that used shaped sensors on two-dimensional structures reduced the system so that the two-dimensional system behaves like a one-dimensional system, such as using a cantilevered plate [Lee, 1989]. It has been shown that modal sensors can only be rigorously achieved on simply-supported plates [Clark, 1996], but approximate modal sensors have been attempted with other boundary conditions.

The most successful technique for modal sensing on plates has been through the use of narrow strips of the shaped modal transducer. By making the modal transducer narrow, the sensitivity of the transducer to transverse modes is reduced. The narrow modal transducer will no longer perform spatial filtering in the transverse direction and, thus, may experience problems at higher frequencies. However, the point at which the transverse affects start to become significant is typically well beyond the low modes that are effectively addressed with shaped transducers. Narrow strips of PVDF were used to isolate individual modes on a plate [Zhou, 1991], to isolate the modes on a plate that

radiate well [Clark, 1992A, 1992B; Gu, 1994; Tanaka 1995, 1996; Charette, 1998] and to isolate the lower circumferential modes on a cylinder [Clark, 1994; Sung, 1996]. Especially good modal isolation was obtained by Zhou (1991) on a clamped plate and by Gu (1994) on a simply supported plate.

1.3.2 Spatially Convolving Sensors

Shaped sensors have proven to be very successful in changing the roll-off behavior of transfer functions [Miller, 1990; Collins, 1994; Pines, 1997A]. Instead of seeking to become a band-pass filter and isolate an individual mode, these spatially convolving wave sensors seek to become low-pass filters and minimize their sensitivity to all higher frequency modes. Unlike temporal filters, the spatially convolving sensors do not introduce extra phase lag, which is an anathema to active control.

The theory behind spatially convolving sensors involves the transformation between the spatial domain and the wave number domain [Miller, 1990; Collins, 1994; Pines, 1997A]. For example, a sensor with the spatial shape of the sinc function, $\frac{1}{\vartheta x}\sin(\vartheta x)$, is a step function in the wave number domain and has a flat response for wave numbers below the characteristic wavelength φ and no response above φ. Experimental results showed a sinc shaped sensor providing a fifth order roll off on a long beam [Miller, 1990]. Sinc-shaped spatially convolving sensors have also been used to measure waves traveling in one direction, using that information for adaptive feedforward control [Pines, 1997B]. Limited closed-loop performance was obtained due to the need to make the sensor of finite length, and to sensor noise.

Although a sinc function can be implemented on one-dimensional structures, albeit with difficulty, it is virtually impossible to implement complicated sensor geometries on two-dimensional structures [Yung, 1999]. Andersson (1995) showed that it is equally beneficial to maximize the number of derivatives that equal zero at the edges of the transducer. Thus, a circular transducer, which goes to zero at all edges, will provide better roll-off than a square transducer, which has non-zero derivatives. Spatially convolving sensors are commercially available from Midé Technology Corporation

[Midé, 1999] and have been used in an active acoustic control system for space launch vehicles [van Schoor, 1999].

1.3.3 Difficulties of Shaped Distributed Transducers

The desired shape of the modal transducer is the strain mode shape of the targeted mode expressed over the entire domain of the structure [Meirovitch, 1985]. In the experimental realization, the sensor is shaped so that it matches the strain distribution of the targeted mode shape [Lee, 1990]. However, a distributed measurement over the entire domain is required. The response at other parts of the structure can be modeled [Meirovitch, 1985], but the local dynamics at the other locations is not measured and orthogonality is difficult to obtain, even on structures with a simple geometry [Zhang, 1990].

Lee and Moon (1990) believed that their response was limited by errors in etching. High precision is required in the design of the shaped sensor in order to achieve a modal sensor [Zhang, 1989]. The mode shapes of the system also need to be known to high precision and some believed that inaccuracies in estimating the mode shapes were the limit on performance [Zhou, 1991] although some have achieved excellent performance with experimentally identified mode shapes [Charette, 1998]. Others believed the principle error limiting their modal isolation was inaccuracy in the placement of the sensor [Gu, 1994; Burke 1995; Clark, 1996; Charette, 1998]. It has been shown that small angular misalignment can render the shaped sensor to be ineffective [Mains, 1995]. Each of these sources of error can dramatically limit the ability of the spatial transducers to isolate an individual mode.

A through investigation of the sensitivity of shaped modal sensors by Clark and Burke (1996) illustrates the high sensitivity of modal performance to sensor placement errors. A transducer placement error of 0.26% of the beam length renders the transducer non-orthogonal to unwanted modes. Through examinations of a simply-supported beam and a simply-supported plate, they demonstrated that the errors that they encountered were best described by a 0.26%, or 1 mm, placement error.

Shaped sensors are designed to detect one mode per sensing element because the sensor is physically shaped to sense that one mode. The alternatives to using a single sensor per mode require a meticulous examination of the intersections between the modal transducer for different modes and are very cumbersome [Lee, 1990].

1.3.3.1 Orthogonality Condition

Many of the designs for shaped actuators and sensors are predicted upon using the orthogonality of the strain modes. However, the orthogonality principle is not always applicable. In particular, for the orthogonality principle to hold, the transducer must cover the entire surface of the structure and the structure must have idealized boundary conditions. These requirements generally are not met.

The deflection mode shapes of any self-adjoint system are, by definition, orthogonal. Modal analysis is predicated upon the mode shapes of structures, ψ, being orthogonal.

$$\psi^T \psi = \mathbf{I} \tag{1.2}$$

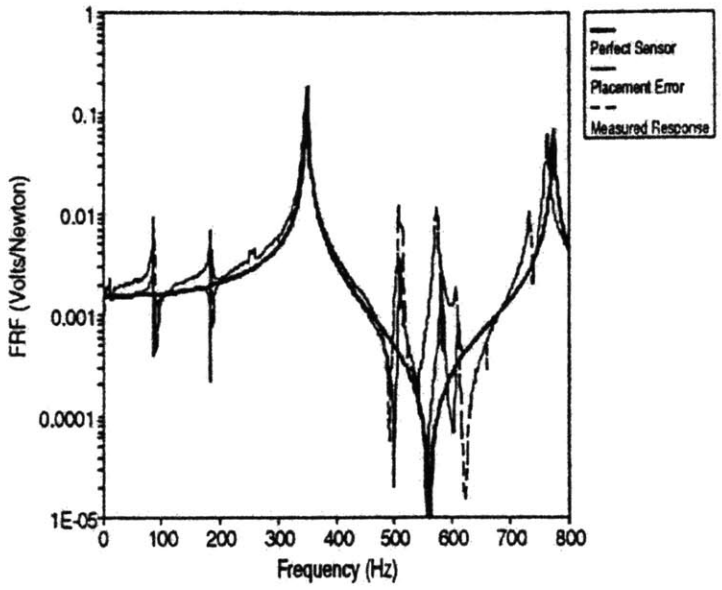

Figure 1.4: Figure from Clark (1996) illustrating the performance of a shaped modal sensor on a simply-supported plate. The sensor is designed to sense the (3,*) modes of the plate but also senses other plate modes. The amount of sensing of other modes is best described by a 0.26% error in placement.

However, the strain mode shapes are not necessarily orthogonal [Prakash, 1980; Rao 1990]. Consider the simply-supported beam with torsional spring boundary. The mode shape for the beam is

$$\begin{aligned}\psi(x) = &\left(\frac{2\frac{EI\lambda}{k}\sin(\lambda L) - \cos(\lambda L) + \cosh(\lambda L)}{\sin(\lambda L) - \sinh(\lambda L)}\right)\sinh(\lambda x) + \cosh(\lambda x) \\ &+\left(\frac{\cos(\lambda L) - \cosh(\lambda L) - 2\frac{EI\lambda}{k}\sinh(\lambda L)}{\sin(\lambda L) - \sinh(\lambda L)}\right)\sin(\lambda x) - \cos(\lambda x)\end{aligned} \tag{1.3}$$

where EI is the beam stiffness, k is the torsional spring constant, L is the beam length, and λ determines which mode is featured and is calculated from the root of

$$\begin{aligned}1 = &\,2\frac{EI\lambda}{k}\sinh(\lambda L)\cos(\lambda L) - 2\left(\frac{EI\lambda}{k}\right)^2\sinh(\lambda L)\sin(\lambda L) \\ &- 2\frac{EI\lambda}{k}\cosh(\lambda L)\sin(\lambda L) + \cosh(\lambda L)\cos(\lambda L)\end{aligned} \tag{1.4}$$

The bending strain is the second derivative of equation (1.3) with respect to x. Note that many references give an incorrect relationship for the mode shape [Blevins, 1995]; they use an incorrect sign on their x=L boundary condition.

The orthogonality of the strain modes is illustrated in Figure 1.5. If the boundary conditions on the beam are either clamped or pinned, then the strain modes are orthogonal. If the boundary conditions are an intermediate condition, then the strain modes are not orthogonal. Although the beam system is self-adjoint, if the torsional spring absorbs some of the system energy, then only measuring the bending strain will not completely measure the state of the system. While measuring the energy in the torsional springs would allow the modes to be orthogonal simply measuring the bending strain is insufficient. In other words, shaped strain sensors will not isolate individual modes on a general structure. Although this example illustrates the problems with strain sensors, a similar problem will occur for any system that contains modal energy at locations that cannot be directly measured, such as in reinforcing frames or in acoustic modes. Additionally, the same lack of orthogonality will arise if the transducers do not cover the *entire* extent of the structure.

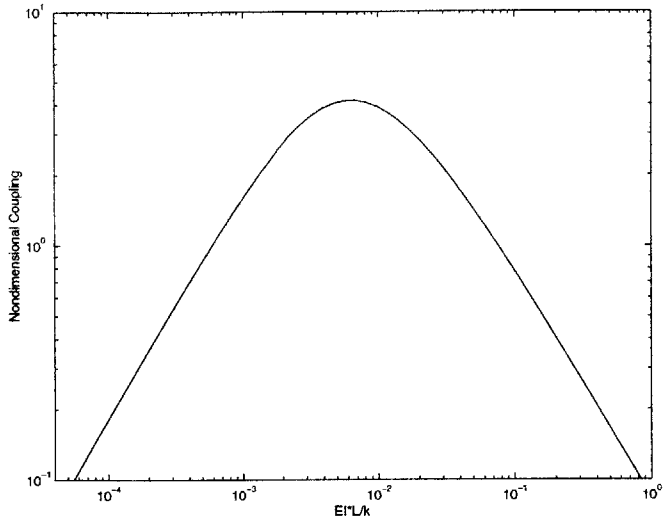

Figure 1.5: Coupling between strain shape of mode 1 and the strain shape of mode 3 on a simply-supported beam with torsional spring at each end. Cross coupling is nondimensionalized by the magnitude of the coupling between mode 1 and itself. A low value of *EIL/k* corresponds to a clamped boundary condition while a high value corresponds to a pivot boundary condition.

1.3.3.2 Mode Shape Accuracy

Proper determination of the shape for the modal transducers is predicated upon an accurate knowledge of the system mode shapes. Unfortunately, mode shapes are sensitive to small structural changes and are difficult either to accurately numerically model or to efficiently experimentally measure. While natural frequencies might be know to within narrow band, the error in the overall mode shape is generally an order of magnitude larger [Vandepitte, 1990]. Most numerical simulations and modal analysis experiments express the mode shapes in terms of displacements. Strains are obtained by numerically evaluating the derivatives of the displacement mode shapes, a highly unstable mathematical procedure. In other words, a strain sensor is roughly 25 times more sensitive to the normalized fifth mode of a straight beam than to the first mode of a straight beam. Small errors in locating or shaping the sensor can result in significant errors in the response characteristics [Clark, 1993].

Quadratic interpolation is sometimes used to interpolate and smooth the displacements between measurements at discrete points but the value of the curvature is extremely sensitive to variations of the displacements [Vandepitte, 1990]. While these

limits on the accuracy of the mode shape might be acceptable for a qualitative understanding of the motion of the system, the limits dramatically reduce the performance of shaped modal sensors, which require an accurate knowledge of the mode shape. As a result, shaped modal sensors have only been successfully applied to relatively simple structures.

1.4 Discrete Element Transducers

Shaped distributed modal transducers represent fixed-shape designs of modal transducers. All of these techniques require *a priori* knowledge of the structural mode shapes before the shaped transducer can be implemented. An alternative approach known as weighted arrays determines the optimal transducer shape after the transducers have been incorporated into the structure. Weighted arrays feature an array of discrete transducer elements whose weighted sum creates a modal transducer. The key to weighted arrays lies in the proper determination of the weights. There are several methods for determining the weights: mode shape of the targeted mode; matrix inversion; cost function optimization. Each of these weighted options are discussed in this section.

1.4.1 Weighting from Targeted Mode Shape

Modal transducers can be constructed from a weighted array of transducer elements. The first method for assigning the weights followed the principle of the shaped modal sensors and assigned the weights based upon the targeted mode shape. Meirovitch originally proposed that the weights should be the mode shape of the targeted mode evaluated at the transducer elements [Meirovitch, 1982]. Others have sought to use arrays of sensors where the weights are set to the targeted mode evaluated at the transducer elements [Sumali, 1991, 1993, 1997; Cazeau 1994]. This approach for assigning the weights is limited by the accuracy of the numerical model.

Variable-weight arrays with weightings based upon the *a priori* predicted mode shape outperformed shaped sensors. Sumali and Cudney (1991) experimentally showed that a 2-element array of accelerometers on a simply-supported beam obtained better

modal isolation performance than a shaped PVDF sensors. In experimental implementation with a 10-element PVDF sensor array on a beam, the modal isolation performance was slightly better than that which was obtained for shaped PVDF sensors [Cazeau 1994]. Arrays with more sensor elements would yield better performance.

In numerical simulation, arrays of discrete sensor elements can be used to accurately estimate the deflection of a beam by integrating the strain under the strain sensors [Sumali, 1998].

In other numerical simulations, arrays of PVDF sensors were used to estimate the acoustic radiation from a beam and a plate by combining the sensor signals to form modal signals and then combining the modal signals to estimate the volume displacement [Preumont, 1999]. A least-means-square (2-norm) minimization is used to determine the proper weights by minimizing the difference between the estimated volume displacement and the actual volume displacement. Unfortunately, experimental estimations of the volume displacement would require either a high fidelity numerical model or a scanning laser vibrometer [Preumont, 1999].

The array weights can be set as the measured target mode shape, however there are no papers in the literature using such a technique. Assigning the weights to the targeted mode would remove problems associated with assembly errors, mode shape estimation, or modeling errors. However, the measured mode shapes are typically complex quantities for structures with nonzero damping and complex weights double the required number of elements in the array because a separate transducer channel is needed for the real part of the weights and another for the imaginary part [Clark, 1993].

Weighted arrays of PVDF patches and accelerometers have been used to estimate the acoustic radiation from beams [Clark, 1992C; Maillard, 1994B], plates [Maillard, 1994A, 1995] and cylinders [Maillard, 1997]. The sensor arrays are weighted to estimate the volume velocity of the structure, and, hence, the acoustic excitation of the structure. These frequency-dependent complex weights are determined by analytically evaluating either the Rayleigh integral of planar structures or the Green's function of curved structures [Junger, 1993]. The mode shapes are not used in the calculation of the weights;

hence, the weights depend solely on the geometric shape of the structure. Errors can arise from incorrect estimations of the weights [Clark, 1992C] and from placement errors. Problems with spatial aliasing are avoided by temporally filtering the signals with a low-pass filter. The time delay inherent to the weighting algorithm effectively prohibits its application to feedback control. The weighted response from an accelerometer array was used as a performance metric for adaptive feedforward control with PZT actuators and excellent experimental acoustic noise reduction was obtained [Maillard 1994B, 1995, 1997]. In fact, better performance is obtained with the weighted array of accelerometers as performance sensors than with microphones as performance sensors [Maillard 1995]. A comparison between frequency-dependent weights and unity-gain weights showed that the frequency-dependent weights doubled the dB sound reduction over the unity-gain weights [Maillard, 1998].

1.4.2 Weighting from Matrix Inversion

1.4.2.1 From Measured Data

Several researchers have used matrix inversion from measured data to determine the optimal weighting [Shelley, 1991A, 1992; Leo, 1997]. In the work by Leo (1997), an array of 22 PVDF sensors was arrayed in a cross configuration on a clamped plate and the transfer function between the actuator and the sensors was measured. The system transfer functions, $\mathbf{G}(\omega) = [G_1(\omega), G_2(\omega), \ldots, G_n(\omega)]$, are inverted to yield the weights. For the case where there are no actuator weights, the inverse is

$$\mathbf{w}_s = \left(\mathbf{G}^T\mathbf{G}\right)^{-1}\mathbf{G}^T\mathbf{f} \tag{1.5}$$

where $\mathbf{f}$ is the desired modal transfer function.

In general, the weights calculated from the matrix inversion will be complex, which doubles the required number of elements in the array [Clark, 1993]. It is unclear whether Leo implemented complex weights or the real part of the complex weight. Nevertheless, good modal isolation was obtained on the plate. The isolated modes were

used in a LQG feedback controller and in a separate Filtered-X LMS controller. Both controllers produced up to 18 dB in vibration reduction.

There are several key features in computing the array weights from matrix inversion as described in equation (1.5). The first feature is that the weights are determined from experimental measurements after the structure is already constructed. Thus, there are no problems from assembly errors, mode shape estimation, modeling errors. Additionally, this approach allows the weights to be implement by digitally programmable analog circuits and, thus, either reduce or eliminate the number of data acquisition channels. Leo (1997) constructed such a circuit.

1.4.2.2 From Predicted Response

Meirovitch (1982) also realized that if the number of modes in the system equaled the number of elements in the array, then the optimal weights could be determined through matrix inversion. Other investigations using variable weight arrays have also been predicated upon the number of sensors being equal to or greater than the number of modes [Zhang, 1990]. There are an infinite number of modes in continuous structures; thus, these techniques are difficult to implement. In a numerical simulation, Stöbener (1998) was able to use matrix inversion to isolate and control a pinned plate with 9-element sensor and 9-element actuator arrays. The pseudo-inverse was used to isolate modes on a small numerical model of a plate [Chen, 1997]. Many of these methods [Meirovitch, 1982; Zhang, 1990; Chen, 1997] also suffer from being setup to use the inverse of numerical models to choose the weights. Leo (1997) demonstrated that a pseudo-inverse from experimental data obtains excellent modal isolation and does not require numerical modeling. Hybrid techniques that use some estimated data and some measured data have been developed [Shelley, 1992]

Morgan (1991) achieved frequency-dependent weights from a pseudo-inverse of the frequency dependent matrix that describes the modal coupling from the transducers. The weights on each element were different depending on the disturbance frequency, which defeats the purpose of building modal sensors. If the frequency-dependent

behavior of the system is known, then a Kalman estimator could be constructed for a more accurate description of the system dynamics.

1.4.3 Weighting from Cost Function

The first researcher to propose the use of a cost function for modal isolation was Shelley (1991). Shelley developed an on-line algorithm that optimized the weights so that the weighted response would match a desired modal response [Shelly, 1993A]. The weights use a least-means-square algorithm to optimize the weights of the array. The weights at time k+1, $\mathbf{w}_{k+1}$, are

$$\mathbf{w}_{k+1} = \mathbf{w}_k + 2\mu\varepsilon_k\mathbf{y}_k \tag{1.6}$$

where μ is the scalar adaptation rate, $\mathbf{y}$ are the sensor measurements, and ε is the error measure between the measure response and the desired modal response, η:

$$\varepsilon_k = \eta_k - \mathbf{w}_k^T\mathbf{y}_k \tag{1.7}$$

The desired modal response, η, can be estimated based upon its targeted frequency and estimations of the damping ratio and its mode shape. Through the updating in equation (1.6) the weights are changed so that the filtered response iterates towards the targeted modal response. The expected value of the square of the error term, $E[\varepsilon_k^2]$, is a quadratic function of the modal filter vector, $\mathbf{w}$, with a unique minimum point defining the optimum weighting [Shelley, 1993A]. The need to know the mode shape of the desired response limits the applicability of the estimator [Clark, 1998].

The on-line adaptation algorithm for modal filtering developed by Shelley has been successfully applied to complicated structures, such as vibration control on a large space truss [Shelley, 1991A, 1991B, 1993B], health monitoring on a large space truss [Shelley, 1993C], vibration control on a highway bridge [Shelley, 1995], and vibration control on a cantilevered beam [Schultze, 1997]. However, the adaptive modal filter tends to deleteriously interact with the controller and causes the control effort to fade [Shelley 1993A, 1997]. In addition, the excellent performance obtained by Shelley [1995, 1991B] is partially due to using more sensors than there are modes in the measured data [Shelley, 1997]. The on-line modal adaptation algorithm will converge with fewer

sensors, but performance will suffer. This algorithm requires the number of data acquisition channels to be equal to the number of sensors; no analog preprocessing is allowed.

The approach by Fripp (1999), which is also the subject of this thesis, trades the real-time implementation of Shelley's technique [Shelley, 1993A] for decreased signal processing and on-line implementation. Additionally, because a more general form of the cost function is used, more tailored applications can be implemented. For example, the magnitude of the loop transfer function might be reduced in the region of controller roll-off with frequency-based weights in the cost function. In such a case, the use of a cost function for the weight optimization more readily allows a direct mechanism for expressing these design options. Alternatively, the weights could be optimized to detect an acoustic radiation mode, such as advocated by Clark (1993).

1.4.4 Problems with Spatial Aliasing

One of the problems associated with discrete arrays is spatial aliasing between the targeted modes and the unwanted modes [Meirovitch, 1981; Morgan, 1991; Clark, 1991; Collins, 1994; Fripp, 1999, 2000]. Some researchers assumed that the contribution from the spatially aliased modes would be reduced by the fact that they were spatially aliasing [Meirovitch, 1982]; however, this is not true.

All of the weighted array options encounter problems with spatial aliasing. Spatial aliasing is a limiting factor in the performance of discrete element arrays. Spatial aliasing is behaviorally similar to aliasing in temporal signals in that shorter wavelength modes get mapped back to longer wavelength modes, that is higher modes cannot be distinguished from lower modes [Maillard, 1994A]. The implication of spatial aliasing is that the aliased higher frequency unwanted mode cannot be minimized while the targeted lower frequency mode is targeted. Spatial aliasing sets an upper limit to the number of modes that can be minimized in the design of modal filters.

Distributed transducer elements in the discrete array can help to minimize the effects of spatial aliasing by reducing the transducer's coupling to higher modes. Distributed sensors and actuators are spatial integrators and their coupling is proportional

to the average response across the area of the transducer [Andersson, 1995]. In other words, smaller transducers couple better to higher modes than larger transducers. By using larger transducers, which create an area averaging effect, the system response can roll-off before spatial aliasing arises. Piezoelectric transducers are the typical choice as a distributed or an area averaging transducer. A more thorough discussion of spatially convolving transducers is presented in section 1.3.

1.5 Summary of Modal Transducer Approaches

Modal sensors and actuators are designed to sense or to actuate an individual mode of a system. Modal transducers reduce the apparent complexity of a system, which is advantageous for active control or for shape estimation. The use of modal transducers does not predicate a particular solution technique nor does it preclude the use of temporal filters.

There are two general approaches for implementing modal transducers: shaped distributed modal transducers and discrete element modal transducers. The trade-offs between the approaches are listed in Table 1.1. Shaped distributed transducers are formed by shaping the sensors and actuators. The shaping is typically performed by either cutting a distributed transducer or by etching the electrodes of a piezoelectric transducer. In the case of modal transducers, the transducer is shaped to the desired mode shape. The shaped distributed modal transducers suffer from errors in approximation and implementation, and, thus, are best implemented on simple structures. In the case of spatially convolved transducers, the transducer is shaped to create a low-pass filter. Shaped spatially convolved transducers are limited in their application to two-dimensional structures.

Discrete element transducers are formed from weighted arrays of individual actuator and sensor elements. The discrete elements are weighted and summed in order to create a modal transducer. The same array of transducers can be given multiple weights, and, thus, the same array can serve as a modal transducer to multiple modes. Multiple techniques have been developed to determine the optimal weights and are summarized in

Table 1.1. Array weights based upon a cost function are the most generally applicable. Discrete element transducers suffer from spatial aliasing, which limits their high frequency performance. Discrete element transducers can be created from any type of actuator or sensor, thus the use of shaped spatially convolved transducer elements can limit the effects of spatial aliasing by rolling-off the transducer's response before the advent of spatial aliasing.

1.6 Thesis Outline

This thesis describes the techniques through which arrays of sensors and actuators can be weighted and summed in order to provide modal sensing and actuation of a structure. These weighted arrays are used to robustify and simplify the active control on complex structures. The concept is implemented on a representative aircraft fuselage.

The goal of weighted arrays is to ease the active control of complex structures. This work is motivated by the need to minimize the noise and vibration of aircraft. Chapter 2 explains the previous work that has been conducted on aircraft noise control. The design of the representative aircraft fuselage that was used in this thesis is detailed as well as the actuators and sensor integration. This chapter also describes the numerical modeling of the fuselage and the limitations of the modeling.

Chapter 3 describes the principles behind weighted arrays. One of the keys to successful implementation of weighted arrays lies in the proper determination of the weights. The different options for determining the weights are detailed. The only method for finding the weights that is causal and offers good isolation performance uses a cost function. A cost function is derived and proved to have a single and global minimum. A perturbation analysis is conducted to elucidate the sensitivity of the modal isolation performance to changes in the array weights or to changes in the mode shape. The implications of spatial aliasing are reviewed.

Implementation of weighted arrays for modal isolation is explained in Chapter 4. Arrays of piezopolymer sensors and piezoceramic actuators are used for modal identification on a cylinder section that is designed to represent a single panel of the

representative aircraft fuselage test-bed. Different weighting metrics are compared and investigations are conducted about the techniques' sensitivity to perturbations to the array weights, to variations in the number of array elements, and to transducer failure. The importance of collocation is also investigated.

Chapter 5 describes the use of weighted arrays in broadband feedback control. Vibration and acoustic emissions on a 3-panel cylinder section are controlled with a single actuator and an 8-element sensor array. Vibration control performance as a function of the number of array elements is measured. Vibration control is also performed on the fuselage test-bed. A detailed comparison is made of the implementation costs of control with weighted arrays and of control with un-weighted arrays. Numerical simulations of weighted and un-weighted control are compared.

Chapter 6 summarizes the accomplishments of this thesis and the contributions that this thesis has made towards designing modal transducers and applying the modal transducers to complex structures.

Table 1.1: COMPARISON BETWEEN DIFFERENT TECHNIQUES USED TO CREATE MODAL TRANSDUCERS.

	Shaped Distributed Transducers		Discrete Element Transducers		
	Modal Transducer	Spatially Convolved Transducers	Weight from target mode shape	Weight from matrix inversion	Weight from cost function
Isolates individual modes	Yes	No	Yes	Yes	Yes
Applicable to systems with complex boundary conditions	No[1]	Yes	No	Yes	Yes
Robust to errors in placement	No	Yes	Yes	Yes	Yes
Robust to errors in construction	No	No	Yes	Yes	Yes
Robust to errors in modal estimation	No	Yes	Yes	Yes	Yes
Robust to torsional and transverse modes	No[2]	No[2,3]	Yes	Yes	Yes
Robust to spatial aliasing	Yes	Yes	No	No	No
Implementable without modeling	No	Yes	Yes	Depends on technique	Yes
Adaptable to changes in system dynamics	No	No	Yes	Yes	Yes
Allows small transducer elements	No	No	Yes	Yes	Yes
Allows partial coverage of system	No	Yes	Yes	Yes	Yes
Can be embedded in composite structures	Yes	Yes	Yes	Yes	Yes
Allows few transducer elements	Yes	Yes	No	No	No
Requires few wiring connections	Yes	Yes	No	No	No

[1] Charette (1998) used experimentally measure mode shapes to design the shaped distributed transducer, but most implementations are not applicable to systems with complex boundary conditions.
[2] The robustness of shaped distributed transducers to torsional and transverse modes can be increased if the transducer is very thin in the orthogonal direction.
[3] Circular spatially convolved transducers are robust to torsional and transverse modes

CHAPTER 2

The Structural-Acoustic Test-Bed

Theoretical understanding, comprehension of practical and economic limitations, common sense, ability to do original and hard work – these are the requirements for a good design engineer, and they must be used in the approach to any design problem
- Max S. Peters, 1958

The design of weighted arrays is motivated by the need to minimize the vibration and interior noise of aircraft. This chapter describes previous work that has been conducted on the design of a test-bed that is representative of the structural-acoustic dynamics encountered in aircraft. The design and construction of sensing and actuation plies are explained. Modal identification is described as well as three-dimensional numerical models of the structural-acoustic dynamics.

Computer models were created to help understand the dynamics and to help refine the design of the structural-acoustic test-bed. It was expected that the numerical models would form the basis of the control algorithm. After extensive modeling, the models yielded insufficient resolution in order to design the control algorithm. Two models of the test-bed were constructed: a finite element model and a Rayleigh-Ritz model. The finite element model was used to predict the coupled dynamics of the test-bed and to design the

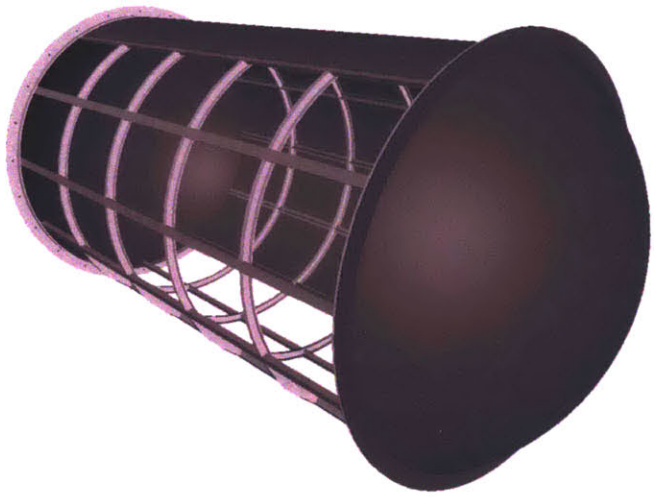

Figure 2.1: Drawing of the fuselage test-bed showing the thin skin covering the frame of ribs and stringers.

end-caps. The Rayleigh-Ritz model also was used to predict the structural-acoustic dynamics and to provide further insight into the coupled dynamics.

2.1 Representative Fuselage Test-Bed

The fuselage test-bed features a thin skin over a frame of ribs and stringers and includes modal complexity similar to that of a fuselage. The representative dynamics were maintained through a combination of geometric scaling and dynamic scaling. Geometrically scaling an aircraft fuselage to allow the resulting structure to fit in the anechoic chamber would yield a test-bed that was unnecessarily complicated and that would be very difficult to construct. As a result, hybrid scaling was used to design a test-bed that maintained the complex dynamics of aircraft while allowing the test-bed to be constructed from commercially available components.

The test-bed was designed to maintain the panel dynamics, the global dynamics, the acoustic dynamics, and the structural-acoustic coupling that are found on aircraft. These dynamics were preserved by designing the fuselage test-bed to match a series of geometric and dynamic non-dimensional scaling parameters that were measured on existing aircraft and aircraft structures. The scaling parameters are the ratio of the first panel frequency over the first acoustic frequency, the ratio of the panel mass to the mass

of a representative air volume, the panel aspect ratio, the test-bed's length over radius, the scaled mass per unit length, the scaled rib bending inertia, the scaled rib torsional inertia, the scaled stringer bending inertia, and the scaled stringer torsional inertia. The test-bed design process is described in detail elsewhere [Fripp et al., 1997; O'Sullivan, 1998] and the final design of the test-bed is featured in O'Sullivan [O'Sullivan, 1998].

The test-bed does not include the effects of pressurization, which can significantly alter the dynamics of the fuselage. Internal pressurization of the fuselage places tension on the ribs and on the cylinder skin. The pressurization elongates the fuselage and can modify the order of the structural modes and the bandwidth over which they act [Henry and Clark, 1999a, 1999b].

The end-caps of the test-bed were designed to minimize interaction with the fuselage. The geometry of the end-caps was chosen to minimize the coupling, both structurally and acoustically, and thus was designed to be very rigid. To meet these requirements, the end-caps are 30° spherical sections, which are much stiffer and more massive than the frame and skin portion of the fuselage. Optimizing the end-cap design was accomplished with a finite element model. Both the design and the model are discussed in section 2.4.2.

Figure 2.1 presents a schematic of the test-bed design. This figure shows the test-

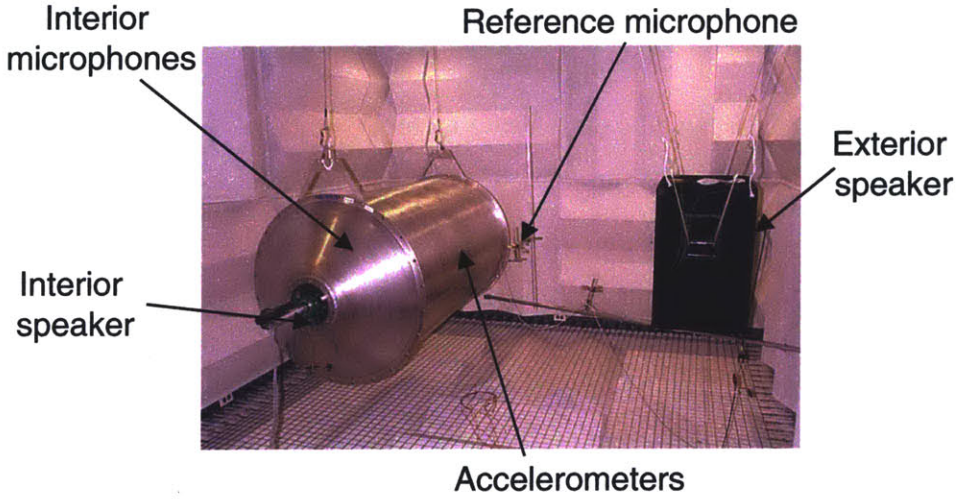

Figure 2.2: Experimental setup for modal identification of the fuselage test-bed.

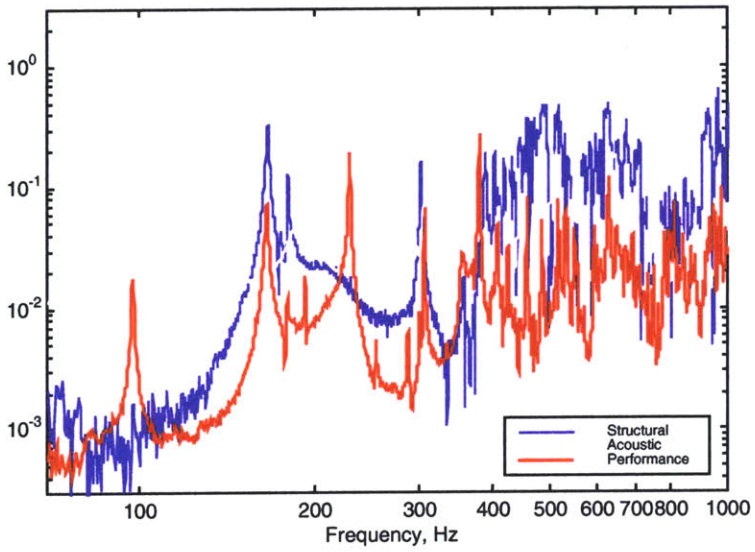

Figure 2.3: Frequency response measured on the fuselage test-bed. Structural refers to the fuselage acceleration from an exterior speaker disturbance. Acoustic refers to the interior acoustic response from an interior speaker disturbance. Performance is the interior acoustic response from an exterior speaker disturbance, and, thus, includes both structural and acoustic resonances.

bed half covered with skin so that the frame structure is visible. Figure 2.2 shows a photograph of the fuselage installed in its anechoic chamber. The basic dimensions of the test-bed are 91 cm in diameter and 198 cm in length. The test-bed is made from 60 panels: 12 stringers, and 6 ribs. The test-bed is manufactured from commercially available components, except for the end-caps, which were cold formed using a spinning process. The ribs are comprised of C-sections and the stringers are comprised of T-sections. The skin was fastened to the frame members with rivets spaced approximately every centimeter. The skin is aluminum sheet 0.762 mm in thickness and is applied in four ninety degree sections with the seems running down the length of the stringers. The skin and frame are made from 6061 aluminum alloys.

2.2 Experimental Modal Identification

The frequency response and the structural vibration modes of the fuselage test-bed were experimentally identified. For this modal identification, an exterior speaker was used to excite the structure. The interior acoustic response was measured with a 30-element

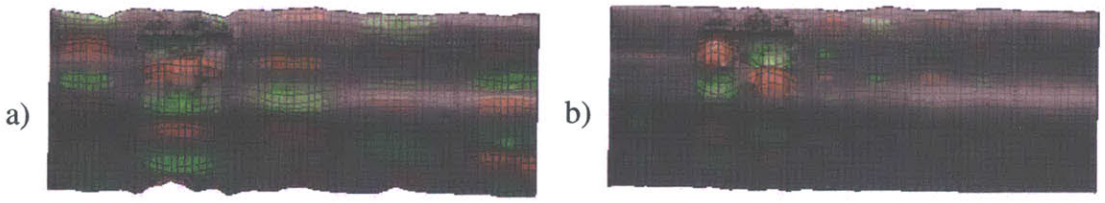

Figure 2.4: Structural mode shapes of the fuselage test-bed. Excitation is a 6.35 cm x 6.35 cm piezoceramic wafer mounted on the most active panel. Modal frequency is a) 461 Hz; b) 674 Hz.

microphone array. The structural response was measured with accelerometers and with a scanning laser vibrometer. The experimental setup is illustrated in Figure 2.2.

The frequency response of the fuselage test-bed is shown in Figure 2.3. The performance transfer function reflects the metric that needs to be minimized and is measured by the transfer function from the exterior speaker disturbance to the interior microphone array. The structural response is the transfer function from the exterior speaker disturbance to an accelerometer at the center of the central panel. The acoustic transfer function is the transfer function from an *interior* speaker to the interior microphone array. The interior speaker is mounted on the inside of the fuselage next to an end-cap. The performance transfer function features both structural resonances and acoustic resonances. Note that some structural modes do not strongly couple with some acoustic modes, and, hence, the performance transfer function does not feature all of the structural and all of the acoustic resonances. Excellent coherence is obtained above

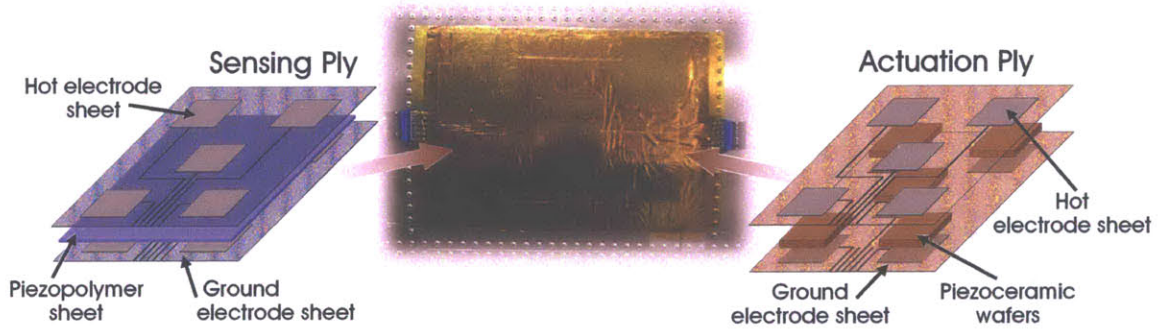

Figure 2.5: Lay-up of the active ply that is composed of collocated piezoceramics actuators and piezopolymer sensors. Electrodes for actuators and sensors are etched into copper-covered Kapton polyimide sheets. The sensing ply is placed directly on top of the actuation ply and this active layer is attached to three panels of the fuselage test-bed.

300 hertz and each peak above 300 hertz corresponds to a separate mode, which illustrates the extremely high modal density of the fuselage test-bed.

Identification of the modes of vibration was performed with a scanning laser vibrometer. A scanning laser vibrometer uses a laser to measure the out-of-plane displacements at discrete points on a structure. An array of point measurements from a known disturbance source is combined to create a picture of the modal deflection. Mode shapes from a speaker disturbance and from a surface mounted piezoceramic disturbance were calculated. Figure 2.4 shows two of the mode shapes for the piezoceramic disturbance. More mode shapes are contained in the appendix.

2.3 Actuation and Sensing Plies

Structural sensors and structural actuators are needed in order to perform structural-acoustic control of the fuselage test-bed. Piezoelectric transducers were chosen because they possess high energy densities, deliver broad bandwidth, and couple efficiently with structural vibrations. Additionally, most piezoelectrics are distributed transducers and

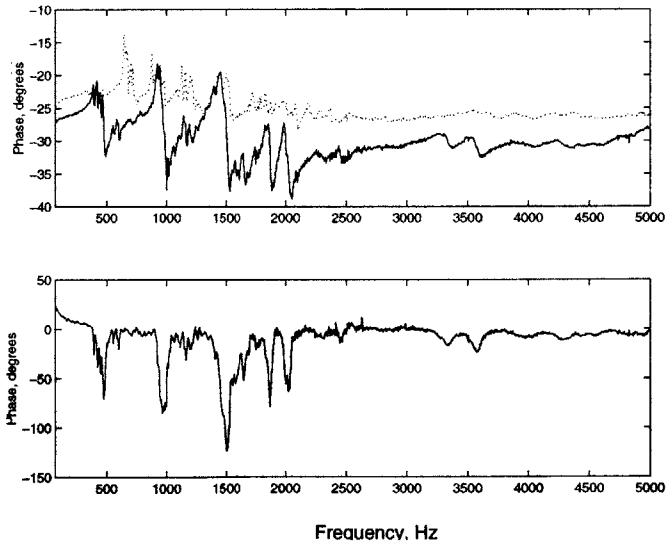

Figure 2.6: Transfer function from the central piezoceramic actuator to its collocated piezopolymer sensor. The phase is bounded, which simplifies the control algorithm. The dotted line is the response envelope or maximum singular value, which is the maximum response at each frequency among all of the transfer functions.

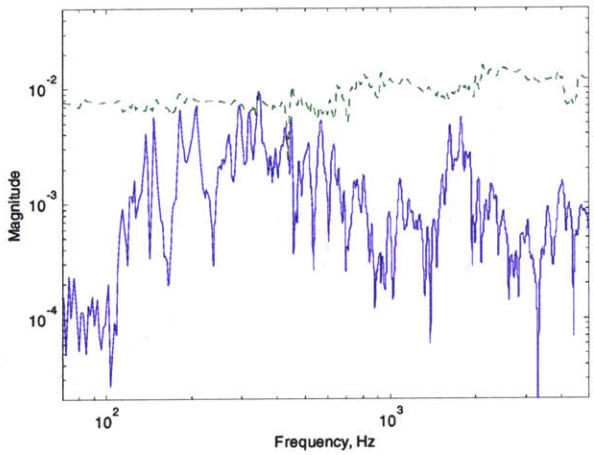

Figure 2.7: The transfer function between an PZT actuator and its collocated PVDF sensor features substantial electrical feed-through, dotted line, unless a ground-plane is inserted between the sensing ply and the actuation ply, solid line.

perform spatial filtering, which tends to minimize their coupling with high frequency modes. As a result, piezoelectrics are a natural choice for transducer material for vibration control on aircraft. Wafers of PZT-5A measuring 6.35cm x 6.35cm x 0.0254cm (2.5"x2.5"x10 mil) from Morgan Matroc Electro Ceramics were chosen as the actuator material. Sheets of unelectroded 52μm PVDF from Measurement Specialties, Inc. were chosen as the sensor material.

Piezoelectric materials, such as piezoceramic PZT or piezopolymer PVDF [Measurement Specialties, Inc., 1999], exhibit a coupling between electric field and mechanical strain [Fuller, 1996; Preumont, 1997; Clark, 1998]. Piezoelectric materials, which encompass piezoceramics and piezopolymers, require a high electric field to orient the electrical domains or pole the material. Piezoelectric materials exhibit peak electro-mechanical coupling in the direction of poling, which is typically through the thickness of the material and is known as the 33-direction. This application of piezoelectrics, like most structural applications of piezoelectrics, uses the transverse or 31-direction.

Each array of transducer material is encapsulated between two layers of flexible electrode. The flexible electrodes are composed of a copper-coated Kapton polyimide film and are used to align and connect the arrays of transducer materials. The copper-

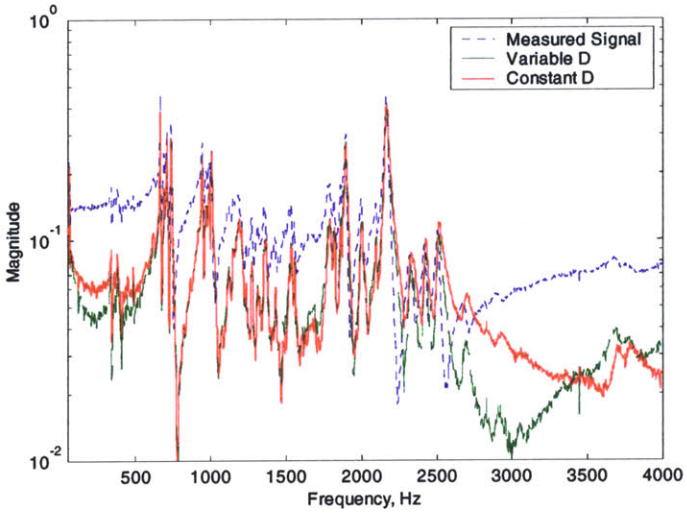

Figure 2.8: Manually removing the mechanical feed-through dramatically increases the observability of the transfer function zeros.

coated Kapton was etched to create electrode patches at the transducers and surface wire paths to the edge of the active ply. Crimp connectors allowed external wires to attach to the surface wires on the flexible electrode. The manufacturing process is sketched in Figure 2.5 and was performed with the help of Djuna Copley-Woods and Cagri Savran.

The actuators and sensors are collocated in order to simplify the control design [Mac Martin, 1995]. Collocated actuators and sensors have a transfer function that features alternating poles and zeros and, hence, a phase that remains within a 180°-phase band. As a result, a simple control algorithm can be phase stabilized in this region. A collocated transfer function from the central actuator-sensor pair on the central panel is shown in Figure 2.6.

2.3.1 Feed-Through

Many implementations of collocated transfer functions often have troubles due to either electrical feed-through or due to mechanical feed-through. For strain-based sensors and actuators, electric feed-through is a function of the capacitive coupling between the high-voltage and high-current actuation cables and the low-voltage and low-current sensing cables. The electrical feed-through can be minimized by inserting a ground-plane

between the sensors and the actuators. As shown in Figure 2.7, the transfer function from an actuator to its collocated sensor features substantial feed-through but the addition of a ground-plane dramatically reduces the feed-through. The two collocated transducer pairs are located at different positions along the structure, thus their modal resonances are not directly comparable.

The collocated strain-based transducer pairs exhibit mechanical feed-through. The mechanical feed-through occurs when the piezoceramic strain actuator induces local stretching that doesn't couple with the structural dynamics. As a result, the piezopolymer sensor mis-interprets the local strain induced by the actuator as strain associated with the structural dynamics. The feed-through seen by the sensors, $\mathbf{y}$, can be modeled as

$$\mathbf{y} = \mathbf{G}\mathbf{u} + \mathbf{D}\mathbf{u} \tag{2.1}$$

where $\mathbf{D}$ is a diagonal matrix featuring the feed-through from the actuators, $\mathbf{u}$. If $\mathbf{D}$ is known, then the feed-through can be subtracted from the transfer function, $\boldsymbol{G}$:

$$\hat{\mathbf{G}}(\omega) = \mathbf{G}(\omega) - \mathbf{D}(\omega) \tag{2.2}$$

The elements of the feed-through matrix, $D(\omega)$, can either be considered constant with frequency, or it can be accurately fit with a simple roll-off filter given by

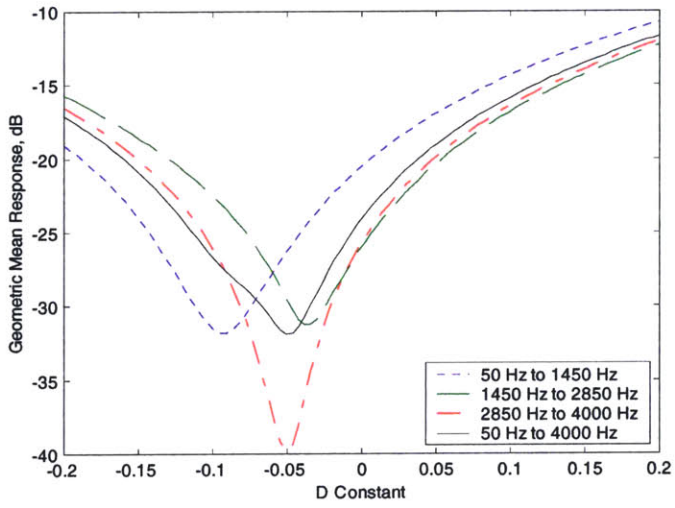

Figure 2.9: The average logarithmic response of the transfer function changes as the mechanical feed-through D constant changes. The optimal D constant is different at different frequency ranges.

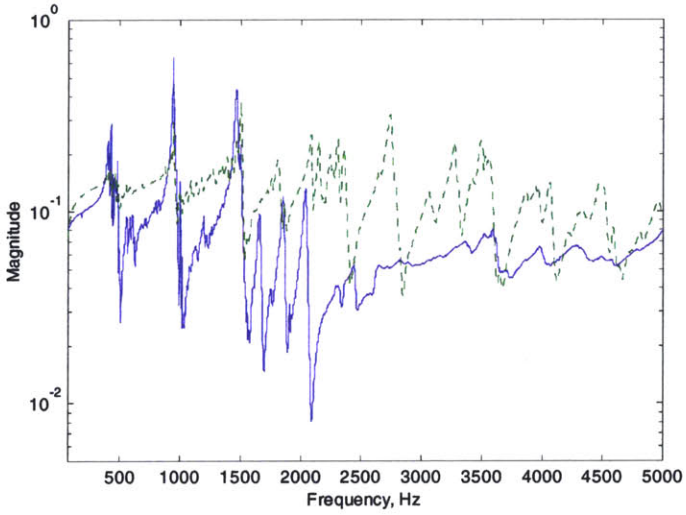

Figure 2.10: Collocated transfer functions of different size transducers bonded to the center of panels on the fuselage test-bed. Solid line is a transducer measuring 6.35cm by 6.35cm. The dotted line is a transducer measuring 3.2cm by 3.2 cm. [Data from Cagri Savran (2000)]

$$D(\omega) = \frac{D_o}{\omega + \omega_D} \tag{2.3}$$

where D_o sets the magnitude and ω_D sets the corner of the roll-off. The effect of manually removing the mechanical feed-through can be seen in Figure 2.8. This transfer function was measured from a collocated transducer pair located in the center of a central panel on the fuselage test-bed. The variable D constant is given by equation (2.3) where D_o is 50 and ω_D is 500. The constant D is 0.086, which is the average of the variable D of the operative frequency range.

The sensitivity of the transfer function to changes in the D constant is shown in Figure 2.9. The D constant serves to bring out the system zeros. Thus, the optimal D constant is that which minimizes the mean response of the transfer function. The optimal D constant is a mild function of frequency where lower frequencies need a slightly larger D constant than higher frequencies. The optimal D can be found by minimizing the geometric mean of the transfer function over the desired frequency range. Figure 2.8 and Figure 2.9 feature the same transducer pair.

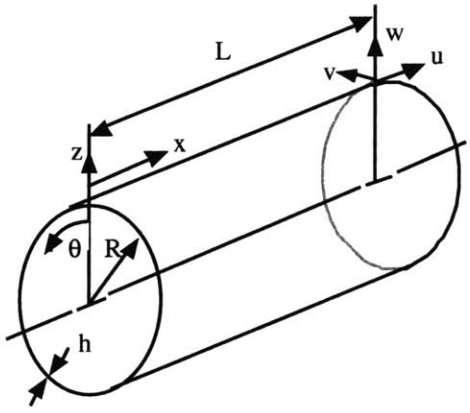

Figure 2.11: Rayleigh-Ritz cylinder geometry

2.3.2 Transducer Size

The size of the transducers was chosen to ease the control design, since the size of the transducers influences the amount of spatial filtering that will occur. Spatial filtering initiates when the transducer spans multiple structural wavelengths. Thus, larger sized transducers will tend to have reduced coupling to higher frequency modes. The size of the transducers on the fuselage test-bed was chosen so that there would be good modal observability up to 2 kHz.

Experimental iteration with different sized patches resulted in the chosen transducer size. Figure 2.10 shows the difference in the transducer roll-off as a function of transducer size. This transfer function was conducted on collocated sensor and actuator plies that were bonded to two panels of the fuselage test-bed. Each of the array elements in one of the transducer pairs measured 6.35 cm by 6.35 cm while the smaller transducer elements in the other array measured 3.2 cm by 3.2 cm. Halving the dimensions of the standard transducer means that strong modal behavior is observed throughout the bandwidth of interest. This result also indicates that the saturation observed above 2500 Hz on the larger transducers is a function of spatial integration and is not a function of electrical feed-through nor mechanical feed-through. Although square transducers were used in this study, circular transducers would improve the roll-off behavior of the loop transfer function.

2.4 Rayleigh-Ritz Model

A Rayleigh-Ritz model of the cylinder was created in order to further understand the dynamics of the test-bed. The Rayleigh-Ritz model includes the ribs and stringers on the cylinder but does not include the end-caps. Simply-supported structural end conditions and hard-wall acoustic boundary conditions were assumed. The structural dynamics were coupled with the interior acoustics to produce a coupled analysis of the test-bed.

2.4.1 Equations-of-Motion

The Rayleigh-Ritz assumed mode analysis was used to numerically solve the coupled equations of motion for the test-bed dynamics. A three-dimensional analysis was conducted in order to describe the stretching as well as the bending of the curved shell. The shape functions for the structural dynamics of the reinforced cylinder were taken from the mode shapes of a simply supported smooth cylinder:

$$\begin{aligned} U_m(x,\theta) &= \cos\left(j\pi\frac{x}{L}\right)\begin{Bmatrix}\cos(i\theta)\\ \sin(i\theta)\end{Bmatrix} \\ V_m(x,\theta) &= \sin\left(j\pi\frac{x}{L}\right)\begin{Bmatrix}\sin(i\theta)\\ \cos(i\theta)\end{Bmatrix} \\ W_m(x,\theta) &= \sin\left(j\pi\frac{x}{L}\right)\begin{Bmatrix}\cos(i\theta)\\ \sin(i\theta)\end{Bmatrix} \end{aligned} \tag{2.4}$$

In the representation of the structural shape functions, j dictates the number of longitudinal modes and ranges from 1 to 5. Modes corresponding to j=5 will have nodal lines that align with the ribs. The circumferential mode number is given by i and ranges from 1 to 13. Modes corresponding to i=6,12 will have nodal lines that align with the stringers. As a result, the first panel mode of the test-bed corresponds to j=5, i=6. This resulted in a total of 405 structural shape functions. More information about the Rayleigh-Ritz solution process can be found in numerous references [Meirovitch, 1986; Rosario, 1995]

The structural shape functions from equation (2.4) are substituted into the structural equations-of-motion in order to form an estimate of the structural resonances

and the structural mode shapes. The structural equations of motion are a re-expression of the three-dimensional displacement Flügge's thin shell equations [Leissa, 1973] so that the general equations of motion can be solved using an assumed modes analysis. The equations are

$$\begin{aligned}
&\underbrace{\frac{\partial^2 u}{\partial s^2}+\frac{1-\nu}{2}\frac{\partial^2 u}{\partial \theta^2}+\frac{1+\nu}{2}\frac{\partial^2 v}{\partial s\partial\theta}+\nu\frac{\partial w}{\partial s}}_{Extension}\underbrace{-h\left(\frac{\partial^3 w}{\partial s^3}+\frac{\partial^3 w}{\partial s\partial\theta^2}\right)}_{Frame}=\underbrace{-\frac{R^2}{D}p_x}_{Forcing}\\
&\underbrace{\frac{1+\nu}{2}\frac{\partial^2 u}{\partial s\partial\theta}+\frac{\partial^2 v}{\partial\theta^2}+\frac{1-\nu}{2}\frac{\partial^2 v}{\partial s^2}+\frac{\partial w}{\partial\theta}}_{Extension}+\underbrace{h\left(\frac{1+\nu}{2}\frac{\partial^2 u}{\partial s\partial\theta}+\frac{1-\nu}{2}\frac{\partial^2 v}{\partial s^2}+\frac{\partial^2 v}{\partial\theta^2}+\frac{\partial w}{\partial\theta}-\frac{\partial^3 w}{\partial^2 s\partial\theta}-\frac{\partial^4 w}{\partial\theta^4}\right)}_{Frame}\\
&\underbrace{+t\left(\frac{\partial^3 w}{\partial s^2\partial\theta}+\frac{\partial^3 w}{\partial\theta^3}\right)}_{Bending}=\underbrace{-\frac{R^2}{D}p_\theta}_{Forcing}\\
&\underbrace{-\nu\frac{\partial u}{\partial s}-\frac{\partial v}{\partial\theta}-w}_{Extension}+\underbrace{h\left(\frac{\partial^3 u}{\partial s\partial\theta^2}+\frac{\partial^3 u}{\partial s^3}+\frac{\partial^3 v}{\partial\theta^3}+\frac{\partial^3 v}{\partial s^2\partial\theta}+2\frac{\partial^2 w}{\partial\theta^2}+2\nu\frac{\partial^2 w}{\partial s^2}\right)}_{Frame}\\
&\underbrace{+t\left(\frac{\partial^4 w}{\partial\theta^4}+2\frac{\partial^4 w}{\partial s^2\partial\theta^2}-\frac{\partial^4 w}{\partial\theta^4}\right)}_{Bending}=\underbrace{-\frac{R^2}{D}p_r}_{Forcing}
\end{aligned}\tag{2.5}$$

where ν is Poisson's ratio, $s=x/L$, t is the thickness of the skin, and h is the frame thickness. The components in the equations due to extensional stiffness, bending stiffness, frame stiffness, and forcing are noted in the structural equations of motion. The frame stiffness models the fact that the frame is not symmetric about the neutral axis of vibration. The forcing terms include a D'Alembert inertia term. In the solution process, the strong form of the equations represented in equation (2.5) is transformed into the weak form of the equations in order to allow solution by an assumed modes analysis [Strang, 1986; Banks et al., 1995]. The process of transforming from the strong form to the weak form and the resulting non-dimensionalized equations-of-motion are presented in Appendix B.

The structural natural frequencies for the reinforced cylinder without air and without end-caps were calculated using the Rayleigh-Ritz technique. The structural modal frequencies are plotted in Figure 2.12 as a function of the number of circumferential modes. The out-of-plane deflections of the test-bed are a combination of stretching and bending. Modes with small circumferential mode numbers are dominated

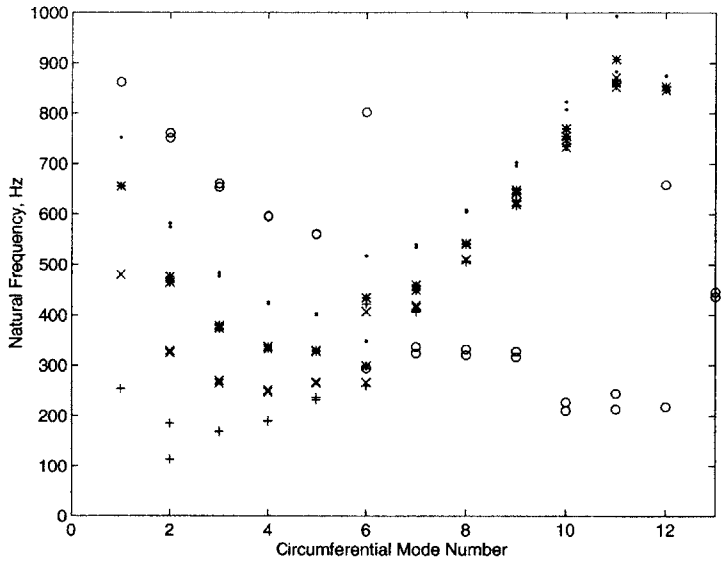

Figure 2.12: Natural frequencies of the test-bed without end-caps and without air, calculated by Rayleigh-Ritz method.
Legend: Number of longitudinal variations: + - 1, x - 2, * - 3, : - 4, o – 5

by stretching of the shell while modes with large circumferential mode numbers are dominated by bending. The minimum modal frequency occurs at the crossover between stretching and bending. As a result, the lowest natural frequency does not coincide with the mode that has the lowest number of modal diameters. For the modes that cross a rib, the lowest natural frequency occurs with three modal diameters.

At low circumferential mode numbers, the ribs and stringers add more mass than stiffness and, hence, lower the modal natural frequencies. The natural frequencies are a strong function of the number of longitudinal variations at low number of modal diameters. At higher number of modal diameters, the circumferential bending dominates and the modes with different number of longitudinal variations converge except for the fifth longitudinal mode. The fifth longitudinal mode does not produce bending the in the ribs and, hence, occurs at a much lower frequency at high number of modal diameters. Concurrently, the lowest natural frequency of the fifth longitudinal mode occurs at twelfth circumferential mode.

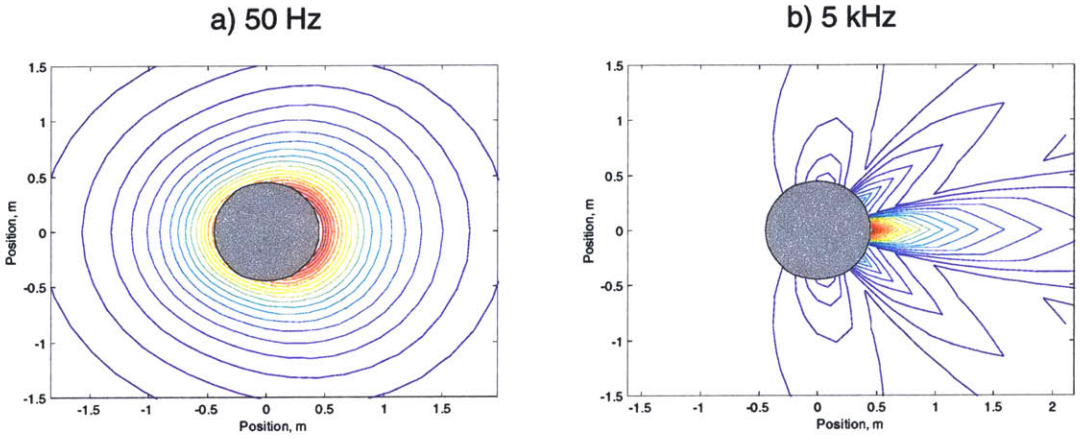

Figure 2.13: Axial slice of the radiation patterns from a small piston vibrating on the side of the fuselage test-bed, as calculated with equation (2.9). The fuselage is represented by the solid circle at the center and acoustic contour lines are plotted in the surrounding air. At low frequency, the sound diffuses around the cylinder while the radiation pattern is highly directional at high frequency.

The acoustic equations-of-motion are the standard acoustic Helmholtz wave equations for the pressure variation in a bounded acoustic medium:

$$\frac{1}{c^2}\frac{\partial^2 P}{\partial t^2} - \nabla^2 P = 0 \tag{2.6}$$

where c is the speed of sound, t is time, and P is the pressure. The equations were rephrased for solution by assumed modes analysis [Kohnke, 1992]. The process of rephrasing the equations is presented in Appendix B. The acoustic shape functions were taken from the mode shapes of a right circular hard-walled cylinder:

$$P_m(x,r,\theta) = J_j\left(\lambda_{jk}\frac{r}{R}\right)\cos(j\theta)\begin{Bmatrix}\cos\left(i\pi\dfrac{x}{L}\right)\\ \sin\left(i\pi\dfrac{x}{L}\right)\end{Bmatrix} \tag{2.7}$$

where J_i is the Bessel function of the first kind and i^{th} order, and λ is defined when the gradient of the pressure or acoustic velocity at the wall is zero. In the representation of the acoustic shape functions, i indicates the longitudinal mode number and ranges from 1 to 5, j indicates the circumferential mode number ranges from 0 to 13, and k indicates the radial mode number and ranges from 0 to 2. This resulted in 525 acoustic shape functions.

Once the structural equations-of-motion and the acoustic equations-of-motion have been cast into the weak form, then the coupled equations of motion can be assembled [Kohnke, 1992]. The coupled equations allow pressure loading on the structure as well as acoustic loading by the structure.

$$\begin{bmatrix} \mathbf{M}_s & \mathbf{0} \\ \rho\mathbf{R}^T & \mathbf{M}_f \end{bmatrix} \begin{Bmatrix} \ddot{\mathbf{U}} \\ \ddot{\mathbf{P}} \end{Bmatrix} + \begin{bmatrix} \mathbf{C}_s & \mathbf{0} \\ \mathbf{0} & \mathbf{C}_f \end{bmatrix} \begin{Bmatrix} \dot{\mathbf{U}} \\ \dot{\mathbf{P}} \end{Bmatrix} + \begin{bmatrix} \mathbf{K}_s & -\mathbf{R} \\ \mathbf{0} & \mathbf{K}_f \end{bmatrix} \begin{Bmatrix} \mathbf{U} \\ \mathbf{P} \end{Bmatrix} = \begin{Bmatrix} \mathbf{F} \\ \mathbf{0} \end{Bmatrix} \tag{2.8}$$

where $\mathbf{M}$ is the mass matrix, $\mathbf{C}$ is the damping matrix, $\mathbf{K}$ is the stiffness matrix, $\mathbf{R}$ is the structural-acoustic coupling matrix, $\mathbf{F}$ is the forcing matrix, the subscript s denotes structural matrices, and the subscript f denotes fluid matrices. The $\mathbf{M}$, $\mathbf{C}$, and $\mathbf{K}$ matrices are calculated from the weak form of equations (2.5) and (2.6). The eigen solution to equation (2.8) represents the coupled structural-acoustic behavior of the reinforced cylinder.

The forcing term in equation (2.8) represents the control actuation by a

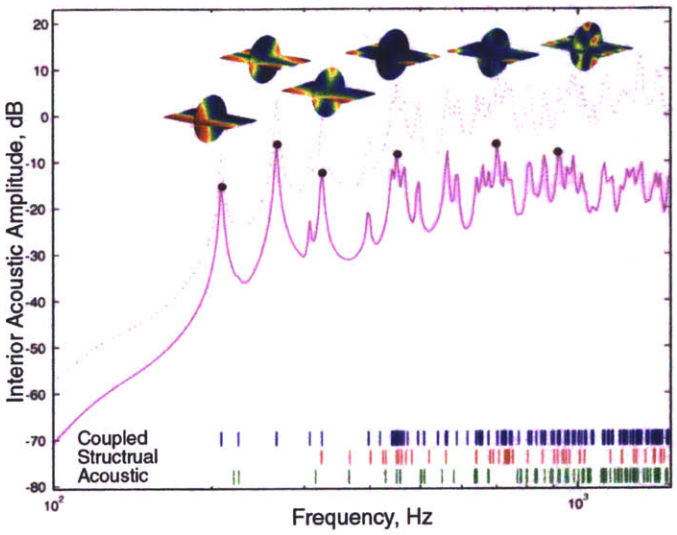

Figure 2.14: Numerical simulation of the interior acoustic sound pressure level from an exterior speaker disturbance. The interior amplitude is normalized so that 0 dB corresponds to the amplitude of the exterior speaker. The average acoustic response is shown with a solid line and the peak acoustic response is shown with a dotted line. The mode shapes of important acoustic modes are illustrated above with large positive amplitudes in red and large negative amplitudes in blue. The frequency of the acoustic modes, structural modes, and coupled structural-acoustic modes are indicated at the bottom.

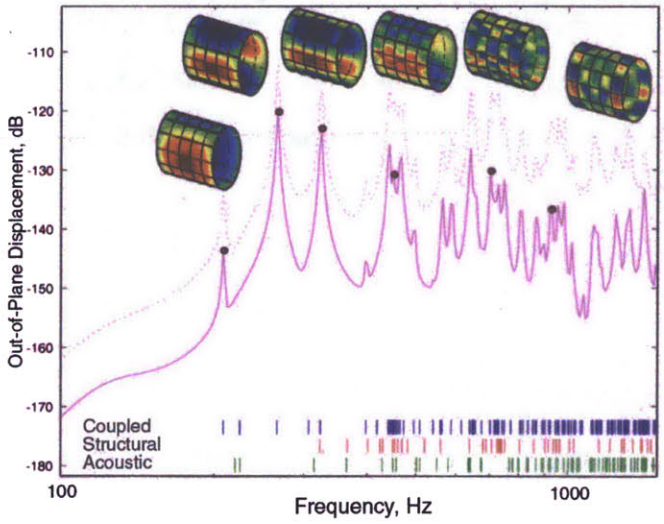

Figure 2.15: Numerical simulation of the out-of-plane displacement from an exterior speaker disturbance. The average displacement is shown with a solid line and the peak displacement is shown with a dotted line. The mode shapes of important structural modes are illustrated above with large positive amplitudes in red and large negative amplitudes in blue. The frequency of the acoustic modes, structural modes, and coupled structural-acoustic modes are indicated at the bottom.

piezoceramic actuator and the disturbance by an exterior speaker. The excitation by a piezoceramic is approximated by assuming the piezoceramic produces an off-center in-plane strain. This strain couples with the structural extension shape functions and with the structural bending shape functions of vibration. The excitation by a speaker can be determined by evaluating the Green's function over the cylinder. The Green's function for estimating the acoustic pressure caused by vibration of the fuselage is [Junger and Feit, 1993]

$$p(R,\theta,\phi) = \frac{2\rho L\alpha \ddot{W} j_0(kL\cos\theta)\, e^{ikR}}{\pi^2 kR\sin\theta} \sum_{q=0} \frac{\varepsilon_q j_0(q\alpha)(-i)^{q+1}\cos q\phi}{H_q'(ka\sin\theta)} \tag{2.9}$$

where R is the radial distance measured from the center, θ is the azimuthal angle, ϕ is the radial angle, ε is 2 except when q=0 when ε is 1, k is the wave number, a is the radius, W is the surface displacement, j_0 is the Bessel function, and H' is the derivative of the Hankel function. This method of calculating the radiation pressure from a cylinder has successfully been used by Maillard (1994A, 1994B, 1995, 1997, 1998) in active noise

radiation control experiments. In the model presented in this chapter, the acoustic reciprocity principle was used [Rayleigh, 1896] and the radiation efficiency in equation (2.9) was used as a direct measure of the structural excitation from a point speaker at location (R,θ,ϕ). The coupling as a function of mode number was calculated by convolving equation (2.9) with the structural mode shape. The acoustic radiation from a small piston on the side of the cylinder is shown in Figure 2.13.

2.4.2 Forced Response

The transfer function from an exterior speaker to the acoustics inside of the fuselage model is shown in Figure 2.14. This is the performance transfer function and both the average acoustic response and the peak acoustic response are illustrated. Acoustic mode shapes of some of the dominant peaks are plotted. The resonant frequency of the uncoupled acoustic modes, the uncoupled structural modes, and the coupled structural-acoustic modes are also plotted. The modal density greatly increases above 400 Hz when the modes of the panels arise. The lowest frequency resonances are predominantly acoustic resonances.

The structural dynamics from an exterior speaker disturbance are illustrated in

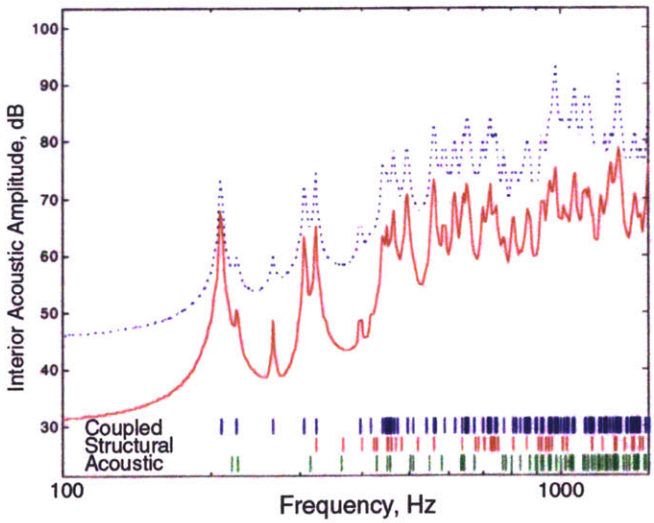

Figure 2.16: Numerical simulation of the acoustic response from a piezoceramic excitation of the fuselage. The piezoceramic actuator is one quarter the size of a panel and is located in the center of the central panel.

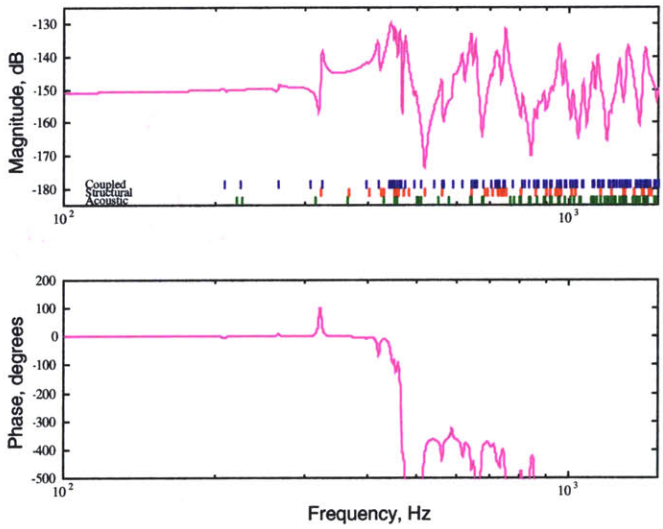

Figure 2.17: Transfer function from a piezoceramic actuator to a collocated accelerometer, both of which are located in the center of a panel.

Figure 2.15. Both the average out-of-plane displacement and the peak out-of-plane displacements are plotted. The structural mode shapes are plotted at the same frequency as the acoustic mode shapes were plotted in Figure 2.14. The first three peaks in the structural response are driven by resonances in the interior acoustic field. A resonance in the fluid excites the cylinder. This reciprocal coupling would have been missed if the enclosed air had not been treated as a heavy fluid.

The acoustic response from a piezoceramic actuator bonded to the surface of a panel is illustrated in Figure 2.16. The average interior acoustic response and the peak interior acoustic response are plotted. This plot illustrates that a structural piezoceramic actuator should have high controllability over the important performance modes. Although the single piezoceramic actuator is unable to control all of the performance modes, a different piezoceramic location would allow controllability of the modes that are uncontrollable in Figure 2.16.

The structural transfer function response from a piezoceramic actuator bonded on the surface of the center of a panel to an accelerometer located at the center of the piezoceramic actuator is noted in Figure 2.17. This transfer function predominantly only feature the structural modes of vibration. Acoustic dominated modes are not visible in

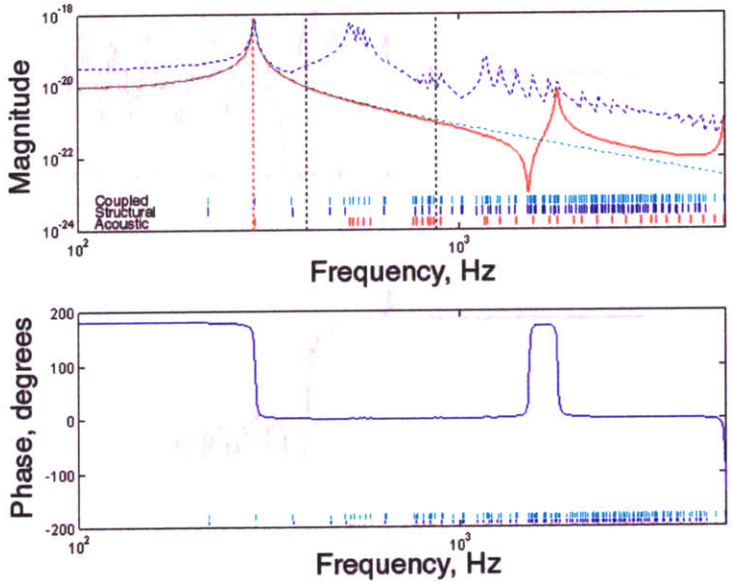

Figure 2.18: Numerical simulation of a weighted 12-element weighted array on a two-dimensional model of the fuselage test-bed. Solid line is weighted response, dashed line is the response envelope, and dotted line is a perfect modal response.

this structural transfer function. The phase of this actuator to sensor transfer function is not bounded, which would necessitate an accurate model-based control design.

2.4.3 Modal Isolation

The three-dimensional Rayleigh-Ritz model was reduced to two dimensions and was used to test the performance of weighted arrays to the first structural modes of vibration. Variation in the x-direction was discarded. Twelve piezoelectric sensors and twelve collocated piezoelectric actuators were placed in the center of the twelve circumferential panels. Each piezoelectric transducer was half of the size of the panel. A 2-norm cost function was minimized in order to obtain the optimal weights. As shown in Figure 2.18, the array was able to effectively isolate the first structural mode of vibration. Spatial aliasing near 1700 Hz limits the high frequency performance.

2.5 Finite Elements Model

A finite element model of the frame reinforced cylinder, the cylinder end-caps, and the enclosed air was constructed using ANSYS. The cylinder skin and end-caps were assembled using curved shell elements, the ribs and stringers were assembled from beam elements, and the air was assembled from symmetric and un-symmetric fluid elements. Symmetric half models and quarter models of the test-bed were analyzed. A symmetric half model of the cylinder was used to design the end-caps. A symmetric quarter model of the test-bed was used to analyze the dynamics of the test-bed. Asymmetric modes were not captured because only symmetric cases were considered in the model. The element mesh of the finite element model is shown in Figure 2.19. The coding of the finite-element mesh was conducted by Katie Lilienkamp and Elaine Chen who were undergraduate students working for the author.

A four by four element mesh was used on the panels. This grid size allowed the representation of modes up to 1500 Hz with 10% accuracy in the modal natural frequency. The first two modes are represented with 5% accuracy in the natural frequencies. The modal accuracy was determined by calculating the natural frequency of a simply supported curved panel with varying mesh sizes. As the mesh size decreased,

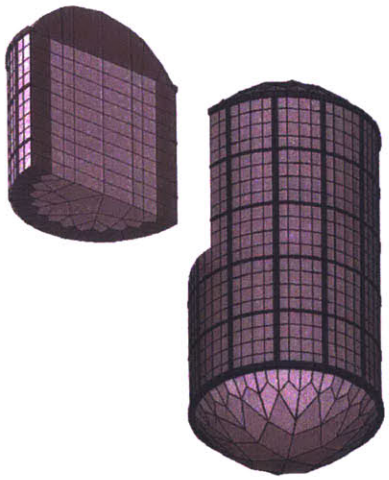

Figure 2.19: Finite elements mesh of the test-bed. A symmetric quarter model (exploded section) was analyzed.

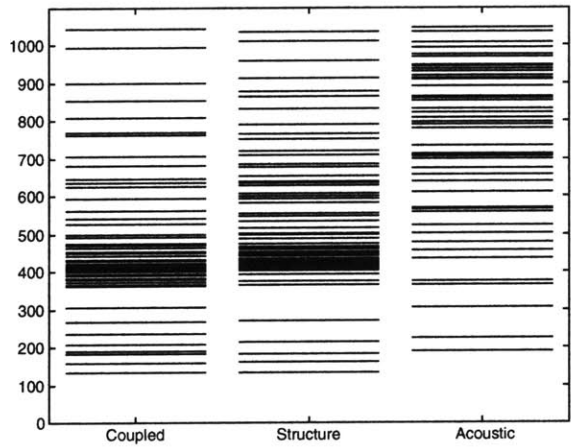

Figure 2.20: Natural frequencies of the quarter model test-bed calculated with finite element methods.

the accuracy of the natural frequencies increased. A four by four element mesh balanced the accuracy of the modal natural frequencies with the time to arrive at a solution. The chosen mesh size resulted in 240 shell elements for the skin, 132 beam elements for the frame, and 450 fluid elements for the air in the quarter model of the test-bed. This combination of elements translates to roughly 5800 active degrees of freedom.

2.5.1 FEM Structural-Acoustic Dynamics

A modal analysis of the cylinder was performed using a quarter cylinder model. The modal natural frequencies below 1 kHz were calculated for the cylinder structure, the enclosed air, and the coupled system and are presented in Figure 2.20. A quarter model of the cylinder was analyzed; hence, only the symmetric modes are captured.

The test-bed is modally dense. There are 63 structural modes, 42 acoustic modes, and 49 coupled structural-acoustic modes below 1 kHz in the quarter model. The structural modes occur in the same frequency range as the acoustic modes. The coupled modes occur at frequencies that are a combination of the structural modes and the acoustic modes. The cluster of structural and coupled modes near 400 Hz consists of modes whose nodal line aligns with the ribs but have different circumferential mode numbers. The decrease in the number of coupled modes in the 700 Hz to 1000 Hz region

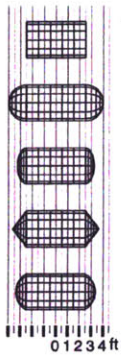

Shape	Relative Deflection
Flat	1.000
Hemisphere	0.004
Elipsoid	0.168
Cone	0.224
30 Hemisphere	0.049

Figure 2.21: Relative deflection of the different end-cap geometries due to interior acoustic pressure loading. The hemispherical end-caps feature the minimal coupling between the interior acoustic dynamics and the structural dynamics of the end-cap.

is unexpected. The modal density and modal frequency range of the test-bed are consistent with the modal density and modal frequency range experimentally identified in a DC-9 section [Simpson et al., 1991].

2.5.2 FEM End-Cap Design

The design metric used when designing the end-caps was that the structural dynamics of the end-caps of the cylinder should minimally couple with the dynamics of the test bed. The cylinder structure should not strongly couple with the end-cap nor should the interior acoustics strongly excite the end-cap structural dynamics. These criteria prevents needing to place actuators or sensors on the end-cap. The end-cap should remain reflective to the interior sound so that the acoustic energy is not damped. The other design criterion was to minimize the size of the end-cap.

Several shapes of end-cap were considered: flat, hemispherical, ellipsoidal (half-height hemisphere), conical, and a 30° spherical section. A half model of the cylinder with each of the end-caps shapes was created using finite elements. The same shell thickness was used for each of the end-caps. A constant pressure was applied inside of the cylinder and the average deflection of the end-cap was measured. The deflection serves as a rough measure of the coupling between the end-cap and the interior acoustics.

Table 2.1: COUPLED MODAL FREQUENCIES CALCULATED BY FINITE ELEMENT METHODS AND BY RAYLEIGH-RITZ TECHNIQUE

Ritz Mode Number	Ritz Frequency (Hz)	FEM Mode Number	FEM Frequency (Hz)	Percent Difference
1	95	-	-	
2	190	4	189	+ 1%
3	259	6	237	+ 9%
4	261	6	237	+ 9%
5	284	-	-	
6	316	12	381	-17%
7	318	12	381	-17%
8	356	8	306	+16%
9	371	9	362	+ 2%
10	376	11	374	+ 1%
11	379	10	367	+ 3%

The scaled magnitudes of the deflections for the five different end-cap shapes are shown in Figure 2.21. The flat, ellipsoidal, and conic end-caps strongly couples with the interior acoustics. A hemispherical end-cap has very small coupling with the interior acoustics but couples strongly with the structural dynamics of the cylinder; the radial deflections were much larger than the longitudinal deflections. The spherical section not only minimizes the coupling with the interior acoustics but also offers small radial deflections during structural excitation. The spherical section also is one of the smaller end-caps considered. As a result, the end-caps of the test-bed are in the shape of a spherical section. A similar investigation indicated that the thickness of a spherical section end-cap need be at least 100 mil in order to have minimal impact on the structural-acoustic modal frequencies.

2.6 Model Correlation

There is only qualitative correlation between the numerical models and the experimentally identified dynamics of the fuselage test-bed. Although the Finite Elements Model and the Rayleigh-Ritz model's natural frequencies agree within 17%, much higher accuracy is needed to be able to correlate with the experimentally observed dynamics. A 17% error in a natural frequency would dramatically rearrange the mode shape and, as noted in Table 2.1, significantly rearranges the modal ordering due to the high modal density of the structure.

Mode shapes are much more sensitive than modal frequencies [Fleming and Crawley, 1991]. The mode shapes could not be correlated beyond the 10^{th} mode because the mode shapes found by one technique could not be identified with the mode shapes found by another technique. Assumptions about symmetry that were needed in order to make the numerical models tractable prevented correlation of the lower modes. Distortions due to reflections and compliance from the end-caps also diluted the accuracy of the numerical models. Table 2.1 compares the natural frequencies calculated by the Rayleigh-Ritz technique with those calculated by the finite element method. Modes were correlated by matching the mode shapes generated by the two techniques. Beyond the 10^{th} mode, there was little correlation between the mode shapes and, thus, comparisons could not be continued.

The rib and stringer stiffened cylinder is a complicated structure. Small changes in the test-bed geometry have a strong effect on the natural frequencies of the system, especially since the system is being modeled over hundreds of modes. Small differences in the modeling technique cascade. Coupled structural-acoustic systems are modally dense and this density requires high modeling resolution. Close correlation between model and test-bed would be virtually impossible. For this reason, further attempts to model the structure were not attempted.

The high modal density was a goal of the test-bed design. Actual aircraft are modally dense and the test-bed maintains the modal complexity. Additionally, aircraft have the structural modes and the acoustic modes in the same frequency region, which,

again, the test-bed maintains. Finally, the modal frequencies of the test-bed are in the same region as the modal frequencies of a geometrically-scaled DC-9 [Simpson et al., 1991]. Although the test-bed does not exactly represent an aircraft, it does represent the dynamic complexity of a large class of aircraft.

2.7 Summary of Test-Bed Design and Modeling

The structural-acoustic test-bed was designed to represent the structural, acoustic, and coupled structural-acoustic dynamics of aircraft. Hybrid scaling parameters were defined from existing aircraft and aircraft models and these parameters were used to design the representative fuselage test-bed. Experimental modal identification indicates that the fuselage exhibits complex structural-acoustic behavior.

Active plies of piezopolymer sensors and piezoceramic actuators were designed and constructed in order to control the dynamics of the fuselage test-bed. The active plies are encased in an etched copper-coated plastic film, which provides electrical connections, aids alignment, eases implementation, and protects the transducers. An electrical ground plane is necessary to prevent electrical feed-through. Mechanical feed-through, where local dynamics dominate the actuator-sensor transfer function, can be addressed by subtracting a constant from the transfer function.

A detailed three-dimensional Rayleigh-Ritz model of the coupled structural-acoustic dynamics of the fuselage test-bed was constructed. A Green's function solution allowed for excitation from an exterior speaker. A three-dimensional finite element model of the coupled structural-acoustic dynamics also was constructed. Moderate correlation was observed between the modeling techniques in the natural frequencies. Neither of these numerical models held sufficient resolution to provide an accurate quantitative description of the fuselage dynamics. The models provide a qualitative description of the system dynamics. A two-dimensional model of the fuselage was used to validate the concept of modal isolation from weighted arrays.

CHAPTER 3

Theory of Weighted Arrays

He who loves practice without theory is like the sailor who boards ship without a rudder and compass and never knows where he may cast.
- Leonardo da Vinci

Weighted arrays are weighted arrays of discrete actuators or sensors. The goal of weighted arrays is to enable the design of reduced order controllers for complex structures, improving closed-loop robustness and broadening the region of good performance as the plant changes. The weighting on the array can be tuned so that individual modes are targeted. From the same set of transducer elements, multiple weights can be used so that multiple modes can be isolated from the same array elements. The weighting can be updated to track the modes as the system changes. This chapter derives the proper method for determining the weights of the array and discusses the limitations of discrete element arrays.

3.1 Goal of Weighted Arrays

Active controllers feature inputs from sensors and output to actuators. With weighted arrays, the inputs and outputs are weighted off-line from the controller. As illustrated in

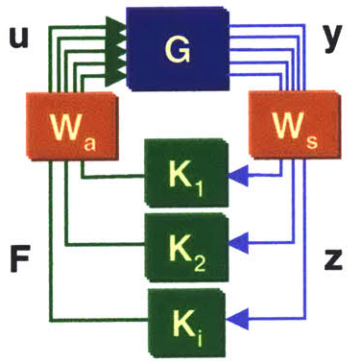

Figure 3.1: The weights on the arrays, $\mathbf{W}$, serve as a filter to the sensors, $\mathbf{y}$, and to the actuators, $\mathbf{u}$. The weighted signals, $\mathbf{F}$ and $\mathbf{z}$, can be designed to be modal signals, which allows for simpler controllers, $\mathbf{K}$.

Figure 3.1, the weightings that are applied to the sensor array serve as a pre-filter to the control algorithm and the weightings applied to the actuator array serve as a post-filter from the controller. The weighting does not seek to replace the controller; instead, the weighting seeks to allow a simpler controller to be implemented.

The key to weighted arrays lies in determining the optimal weighting for the sensor and actuator elements. For a modal transducer, the optimal weights are those that map a single mode from actuation to sensing. Consider a measured transfer function, $\mathbf{G}$, from actuators, $\mathbf{u}$, to sensors, $\mathbf{y}$,

$$\mathbf{y} = \mathbf{G}\mathbf{u} \tag{3.1}$$

The array weights on the actuators and sensors create a weighted sensor response, z, and a weighted actuator input, F. Note that the different weighting vectors are used for sensors and for actuators.

$$z = \mathbf{w}_s{}^T\mathbf{y} \quad \text{and} \quad \mathbf{u} = \mathbf{w}_a F \tag{3.2}$$

The superscript T indicates matrix transpose. Substituting equation (3.2) into equation (3.1) yields the transfer function from the weighted actuators to the weighted sensors.

$$z = \mathbf{w}_s{}^T\mathbf{G}\mathbf{w}_a F \tag{3.3}$$

The weights are determined so that the new transfer function from the weighted actuator signals to the weighted sensor signals, $\mathbf{w}_s{}^T\mathbf{G}\mathbf{w}_a$, features only the desired modes.

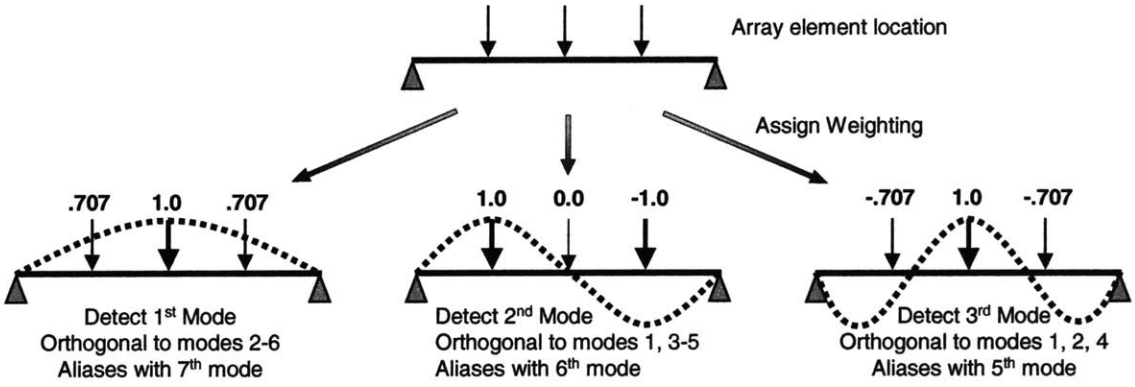

Figure 3.2: The weighting on the weighted arrays can be reconfigured so that multiple modes can be isolated from the same array of transducer elements. The optimal weights for equally spaced arrays on structures with simple boundary conditions are the mode shape evaluated at the transducer locations. A minimized cost function is needed for systems that are more general.

3.2 Weighting Options

The key to proper use of weighted arrays lies in the proper determination of the weights on the array elements. There are three principle techniques for assigning the weights: 1) weights equal to the targeted mode shape at the transducer locations; 2) weights assigned from matrix inversion; and 3) weights determined by minimization of a cost function. All of these weighting options can be implemented from measured information, which allows them to be implement-able on complex structures. The concept of implementing a weighted array to isolate individual modes is illustrated in Figure 3.2.

3.2.1 Weights from Mode Shape

The most natural choice for weighting is to use the mode shape of the targeted mode. For beam-like structures with pinned or clamped boundary conditions, the weights of an equally spaced array can simply be the mode shape of the desired mode evaluated at the element locations. Weightings based upon the targeted mode shape of realistic systems encounter problems due to the component of potential energy in the boundary, due to localization of the transducers, and due to spatial aliasing.

If the boundary conditions have intermediate torsional stiffness, then there will be potential energy stored in the boundaries. This boundary energy is immeasurable with traditional transducers, and, thus, the measured modes will not be orthogonal. Similarly, if the transducers do not cover the entire extent of the structure, then there will be unmeasured strain energy and the measured modes will not be orthogonal. For systems with non-zero damping, the weights will be complex.

3.2.2 Weights from Matrix Inversion

If the transfer function between the actuators and sensors is known, then that transfer function matrix can be inverted to find the weights. If the number of relevant modes in the system equals the number of elements in the arrays, then the optimal weights can be found through matrix inversion otherwise the weights can be found with the pseudo-inverse. The experimentally measured system transfer functions, $\mathbf{G}(\omega) = [G_1(\omega), G_2(\omega), \ldots, G_n(\omega)]$, are inverted to yield the weights. For the case where there are no actuator weights, the inverse is

$$\mathbf{w}_s = \left(\mathbf{G}^T\mathbf{G}\right)^{-1}\mathbf{G}^T\mathbf{f} \tag{3.4}$$

where $\mathbf{f}$ is the desired transfer function. For realistic systems with non-zero damping, the weights will be complex. Although some have suggested using integrators to implement the imaginary weight (Clark, 1993), the variation in magnitude due to the integration will wreck the performance.

There are two major problems with using matrix inversion to decide the weights. First, the matrix inversion is difficult to define if both an actuator array and a sensor array are implemented. If two arrays are used, then the transfer function matrix is a three-dimensional matrix (actuator elements by sensor elements by frequency points) and the inverse of a three-dimensional matrix is not defined. The inverse can be calculated for each actuator element (thus reducing the matrix to two dimensions), but this approach will not yield a symmetric weighting and, thus, will not yield collocated performance. Second, this technique is unable to tailor the shape of the desired transfer function, and, thus, cannot trade performance at one frequency for performance at another frequency.

3.2.3 Weights from Cost Function

A cost function can be used to determine the weights on the array elements. A cost function is the inverse of a performance metric and the magnitude of the cost function is minimized. In the case of design of modal transducers, the cost function is defined so that the targeted mode is maximized and the unwanted modes are minimized. The cost function can include a penalty if the phase does not remain bounded or if the transfer function does not roll-off.

The chief problem with using cost functions is that there are often multiple solutions to the cost function. Thus, the optimization process can become trapped in a local minimum and miss the global minimum of the cost function. Section 3.3 presents a cost function that is guaranteed to have a single and global minimum.

3.3 Weights from Cost Function

The chosen form of the cost function for optimizing the weights seeks to maximize the modal residue of the targeted mode, R_m, and to minimize the modal residues from the undesired modes, R_n. The modal residue represents the coupling between the transducers and an individual mode. The performance of the cost function can be expressed either in terms of a 2-norm, J_2, or an infinity-norm, J_∞. The 2-norm seeks to minimize the *average* modal response from the unwanted modes while the infinity-norm seeks to minimize the *peak* modal response of the unwanted modes:

$$J_2 = \frac{\sum_n (\alpha_n R_n^2)}{R_m^2} \; ; \quad J_\infty = \frac{\max_n (\alpha_n R_n^2)}{R_m^2} \tag{3.5}$$

where the modal weighting function, α, allows different modes to be given extra weight. It is assumed that there is no intersection between the set of targeted modes and the set of unwanted modes. The cost function is illustrated in Figure 3.3.

A 2-norm cost function possesses the desirable feature of having one and only one minimum. A short proof of there being a unique and global minimum will follow. However, the infinity-norm cost function is useful in the design of active control. The infinity-norm penalizes the peak response of the undesired modes and since active

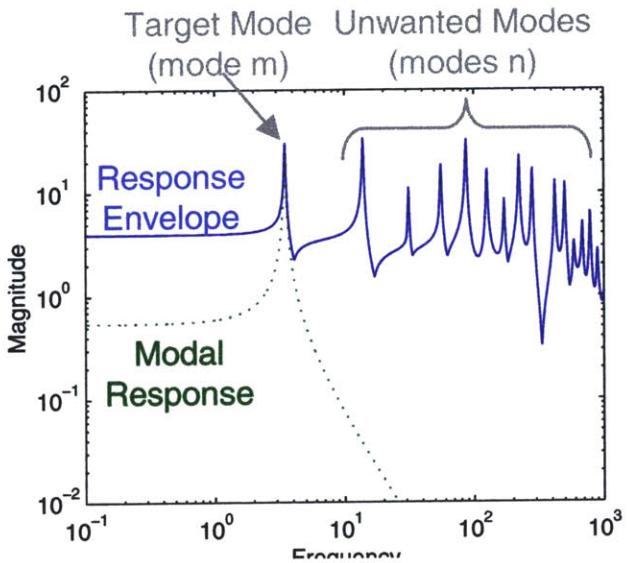

Figure 3.3: The cost function is defined so that the response from the unwanted modes, n, are in the numerator and the response from the targeted mode, m, is in the denominator. Minimizing the cost function leads to the modal response.

controllers are driven into instability by a single peak, the infinity-norm would be the preferred cost function. Unfortunately, the infinity-norm cost function features the ratio of similar terms and this fact makes it difficult to check the infinity-norm by any means other than evaluating the norm. As a result, proofs about the existence of a minimum threshold of infinity-norm performance are nearly impossible to construct. However, experimental and numerical investigations indicate that the infinity-norm cost function features a single and global minimum.

If the transfer function from actuator elements to sensor elements, **G**, is a positive real transfer function (symmetric and collocated) and if the actuator weights are the same as the sensor weights, then the transfer function from weighted actuators to weighted sensors, $\mathbf{w}_s^T\mathbf{G}\mathbf{w}_a$, is guaranteed to be positive real. However, if the transfer functions are not positive real, then the weighted transfer function may not have collocated phase. The cost function can be modified to include an extra term that penalizes phase roll-off, an issue if a closed-loop system is of interest. The phase-penalized infinity-norm cost function is

$$\bar{J}_{\infty} = \frac{\max_{n}\left(\alpha_n R_n R_n^*\right)}{R_m R_m^*} + \beta \,\mathrm{int}\left(\frac{\mathrm{abs}\left(\angle \mathbf{w}_s^T \mathbf{G} \mathbf{w}_a\right)}{\pi}\right) \tag{3.6}$$

where and int takes the integer part of the absolute value of the phase angle of the weighted transfer function, $\angle \mathbf{w}_s^T \mathbf{G} \mathbf{w}_a$. β is a scaling factor to decide the relative weight of the phase penalty. The phase penalty only affects the cost when the weighted transfer function no longer exhibits a phase bounded by $\pm\pi$ radians.

3.3.1 2-Norm Optimization: Proof of Single Solution

The 2-norm cost function, defined in equation (3.5), seeks to minimize the average modal response from the unwanted modes. The modal residue used in defining the cost function, R, reflects the addressability of an individual mode. The residue of the i^{th} mode is defined as the product of the mode shape matrix evaluated at the transducer elements, ψ_i, and the vector of weights applied to the transducer elements, $\mathbf{w_s}$ and $\mathbf{w_a}$. The effects of an individual transducer element, d, can be brought out of the matrices.

$$\begin{aligned} R_i &= \mathbf{w}_s \Psi_i \mathbf{w}_a^T \\ &= w_{s_d} \psi_{i_d} \mathbf{w}_a^T + \tilde{\mathbf{w}}_s \tilde{\Psi}_i \mathbf{w}_a^T \end{aligned} \tag{3.7}$$

The matrix of mode shapes and array weights are of the form

$$\Psi_i = \begin{bmatrix} \psi_{i_1} & \psi_{i_2} & \cdots & \psi_{i_q} \end{bmatrix}^T, \ \mathbf{w}_a = \begin{bmatrix} w_{a_1} & w_{a_2} & \cdots & w_{a_r} \end{bmatrix}, \text{ and } \mathbf{w}_s = \begin{bmatrix} w_{s_1} & w_{s_2} & \cdots & w_{s_q} \end{bmatrix} \tag{3.8}$$

where r is the number of actuator elements and q is the number of sensor elements in the array. The modified matrices, which are differentiated with a tilde, have the d^{th} element removed.

$$\tilde{\Psi}_i = \begin{bmatrix} \psi_{i_1} & \cdots & \psi_{i_{d-1}} & \psi_{i_{d+1}} & \cdots & \psi_{i_r} \end{bmatrix}^T \text{ and } \tilde{\mathbf{w}}_s = \begin{bmatrix} w_{s_1} & \cdots & w_{s_{d-1}} & w_{s_{d+1}} & \cdots & w_{s_q} \end{bmatrix} \tag{3.9}$$

The mode shape matrix, ψ_i, is a two dimensional matrix with dimensions of r by q. The mode shape vector, ψ_{id}, is a column of the i^{th} mode shape evaluated at the actuator locations and has dimension of 1 by r.

The cost function can be evaluated by placing the expression for the modal residue, equation (3.7), into the cost function, equation (3.5). Variations with respect to

transducer element number d need to be specially evaluated. The variations on element d will be brought out of the summation and the complex conjugate will be distributed.

$$J_2 = \frac{\sum_n \left(\alpha_n \left(w_{s_d} \psi_{n_d} \mathbf{w}_a^T + \tilde{\mathbf{w}}_s \tilde{\Psi}_n \mathbf{w}_a^T \right) \left(w_{s_d}{}^* \psi_{n_d}{}^* \mathbf{w}_a^{T^*} + \tilde{\mathbf{w}}_s{}^* \tilde{\Psi}_n{}^* \mathbf{w}_a^{T^*} \right) \right)}{\left(w_{s_d} \psi_{m_d} \mathbf{w}_a^T + \tilde{\mathbf{w}}_s \tilde{\Psi}_m \mathbf{w}_a^T \right) \left(w_{s_d}{}^* \psi_{m_d}{}^* \mathbf{w}_a^{T^*} + \tilde{\mathbf{w}}_s{}^* \tilde{\Psi}_m{}^* \mathbf{w}_a^{T^*} \right)} \tag{3.10}$$

The optimal weights are found where the cost function is a minimum. The derivative of equation (3.10) is taken with respect to w_{sd} in order to find the weight on sensor element d that minimizes the cost function.

$$\begin{aligned}
\frac{\partial J_2}{\partial w_{s_d}} = & \frac{\sum_n \left(\alpha_n \left(w_{s_d}{}^* \psi_{n_d}{}^* \mathbf{w}_a^{T^*} + \tilde{\mathbf{w}}_s^* \tilde{\Psi}_n{}^* \mathbf{w}_a^{T^*} \right) \psi_{n_d} \mathbf{w}_a^T \right)}{\left(w_{s_d} \psi_{m_d} \mathbf{w}_a^T + \tilde{\mathbf{w}}_s \tilde{\Psi}_m \mathbf{w}_a^T \right) \left(w_{s_d}{}^* \psi_{m_d}{}^* \mathbf{w}_a^{T^*} + \tilde{\mathbf{w}}_s^* \tilde{\Psi}_m{}^* \mathbf{w}_a^{T^*} \right)} \\
& - \frac{\psi_{m_d} \mathbf{w}_a^T \sum_n \left(\alpha_n \left(w_{s_d} \psi_{n_d} \mathbf{w}_a^T + \tilde{\mathbf{w}}_s \tilde{\Psi}_n \mathbf{w}_a^T \right) \left(w_{s_d}{}^* \psi_{n_d}{}^* \mathbf{w}_a^{T^*} + \tilde{\mathbf{w}}_s^* \tilde{\Psi}_n{}^* \mathbf{w}_a^{T^*} \right) \right)}{\left(w_{s_d} \psi_{md} \mathbf{w}_a^T + \tilde{\mathbf{w}}_s \tilde{\Psi}_m \mathbf{w}_a^T \right)^2 \left(w_{s_d}{}^* \psi_{m_d}{}^* \mathbf{w}_a^{T^*} + \tilde{\mathbf{w}}_s^* \tilde{\Psi}_m{}^* \mathbf{w}_a^{T^*} \right)} \\
& + \frac{\sum_n \left(\alpha_n \left(w_{s_d} \psi_{n_d} \mathbf{w}_a^T + \tilde{\mathbf{w}}_s \tilde{\Psi}_n \mathbf{w}_a^T \right) \psi_{n_d}{}^* \mathbf{w}_a^{T^*} \right)}{\left(w_{s_d} \psi_{m_d} \mathbf{w}_a^T + \tilde{\mathbf{w}}_s \tilde{\Psi}_m \mathbf{w}_a^T \right) \left(w_{s_d}{}^* \psi_{m_d}{}^* \mathbf{w}_a^{T^*} + \tilde{\mathbf{w}}_s^* \tilde{\Psi}_m{}^* \mathbf{w}_a^{T^*} \right)} \\
& - \frac{\psi_{m_d}{}^* \mathbf{w}_a^{T^*} \sum_n \left(\alpha_n \left(w_{s_d} \psi_{n_d} \mathbf{w}_a^T + \tilde{\mathbf{w}}_s \tilde{\Psi}_n \mathbf{w}_a^T \right) \left(w_{s_d}{}^* \psi_{n_d}{}^* \mathbf{w}_a^{T^*} + \tilde{\mathbf{w}}_s^* \tilde{\Psi}_n{}^* \mathbf{w}_a^{T^*} \right) \right)}{\left(w_{s_d} \psi_{md} \mathbf{w}_a^T + \tilde{\mathbf{w}}_s \tilde{\Psi}_m \mathbf{w}_a^T \right) \left(w_{s_d}{}^* \psi_{m_d}{}^* \mathbf{w}_a^{T^*} + \tilde{\mathbf{w}}_s^* \tilde{\Psi}_m{}^* \mathbf{w}_a^{T^*} \right)^2}
\end{aligned} \tag{3.11}$$

Evaluating the derivative of equation (3.11) indicates that there are two weightings where the first derivative will be zero. As a result, there is not a unique and global solution to the case where the mode shapes are complex. However, if the mode shapes and the array weights are real, then equation (3.11) becomes

$$\frac{\partial J_2}{\partial w_{s_d}} = \frac{\sum_n \left(2\alpha_n \psi_{n_d} \mathbf{w}_a^T \left(w_{s_d} \psi_{n_d} \mathbf{w}_a^T + \tilde{\mathbf{w}}_s \tilde{\Psi}_n \mathbf{w}_a^T \right) \right)}{\left(w_{s_d} \psi_{m_d} \mathbf{w}_a^T + \tilde{\mathbf{w}}_s \tilde{\Psi}_m \mathbf{w}_a^T \right)^2} - \frac{2\psi_{m_d} \mathbf{w}_a^T \sum_n \left(\alpha_n \left(w_{s_d} \psi_{n_d} \mathbf{w}_a^T + \tilde{\mathbf{w}}_s \tilde{\Psi}_n \mathbf{w}_a^T \right)^2 \right)}{\left(w_{s_d} \psi_{m_d} \mathbf{w}_a^T + \tilde{\mathbf{w}}_s \tilde{\Psi}_m \mathbf{w}_a^T \right)^3} \tag{3.12}$$

Setting the derivative equal to zero and solving for the desired weight, w_{sd}, will yield the weighting on the d^{th} element that minimizes the cost function. Setting the derivative to zero yields:

$$0 = \left(w_{s_d}\psi_{m_d}\mathbf{w}_a^T + \tilde{\mathbf{w}}_s\tilde{\Psi}_m\mathbf{w}_a^T\right)\cdot\sum_n\left(\alpha_n\psi_{n_d}\mathbf{w}_a^T\left(w_{s_d}\psi_{n_d}\mathbf{w}_a^T + \tilde{\mathbf{w}}_s\tilde{\Psi}_n\mathbf{w}_a^T\right)\right) - \psi_{m_d}\mathbf{w}_a^T\sum_n\left(\alpha_n\left(w_{s_d}\psi_{n_d}\mathbf{w}_a^T + \tilde{\mathbf{w}}_s\tilde{\Psi}_n\mathbf{w}_a^T\right)^2\right) \tag{3.13}$$

Breaking the summations into components and canceling terms yields a linear relationship for w_{sd},

$$w_{s_d} = \frac{\psi_{m_d}\mathbf{w}_a\sum_n\left(\left(\tilde{\mathbf{w}}_s\tilde{\Psi}_m\mathbf{w}_a^T\right)^2\right) - \tilde{\mathbf{w}}_s\tilde{\Psi}_m\mathbf{w}_a^T\cdot\sum_n\left(\alpha_n\psi_{n_d}\mathbf{w}_a^T\left(\tilde{\mathbf{w}}_s\tilde{\Psi}_n\mathbf{w}_a^T\right)\right)}{\tilde{\mathbf{w}}_s\tilde{\Psi}_m\mathbf{w}_a^T\cdot\sum_n\left(\alpha_n\left(\psi_{n_d}\mathbf{w}_a^T\right)^2\right) - \psi_{m_d}\mathbf{w}_a^T\sum_n\left(\alpha_n\psi_{n_d}\mathbf{w}_a^T\left(\tilde{\mathbf{w}}_s\tilde{\Psi}_n\mathbf{w}_a^T\right)\right)} \tag{3.14}$$

Equation (3.14) offers several very important pieces of information: 1) there is *a unique and global set of weights* that optimizes the modal isolation; 2) there is *a implicit expression for the optimal weight*; and 3) the optimal weights only depend on the mode shape measured at the transducer elements. There can be only one solution to the 2-norm cost function because there is only one solution for w_d in equation (3.14). As a result, there is only one value of w_d that solves for the derivative of the cost function equal to zero and, hence, there can be only one solution to the optimal weight. This result indicates that the solution space does not have multiple local minimums where the solution algorithm can become trapped. The optimal weights can be found using a simple gradient descent optimization.

Equation (3.14) offers an implicit expression for the optimal weight. The solution to the desired weight on element d, w_d, depends on the weights on other elements, $\tilde{\mathbf{w}}$, and on the mode shapes measured by all the elements. Determination of the optimal weights requires iterating upon equation (3.14) until the weights converged to their optimal values.

3.3.2 2-Norm Optimization: Proof of Global Minimum

The following proof shows that the second derivative of the cost function is guaranteed to be positive which means that the optimized weights reflect the minimum cost and not the maximum cost. The second derivative of equation (3.12) taken with respect to w_{sd} is

$$\frac{\partial^2 J_2}{\partial w_{s_d}{}^2} = \frac{2\sum_n \left(\alpha_n \left(\psi_{n_d} \mathbf{w}_a^T\right)^2\right)}{\left(w_{s_d}\psi_{m_d}\mathbf{w}_a^T + \tilde{\mathbf{w}}_s\tilde{\boldsymbol{\Psi}}_m\mathbf{w}_a^T\right)^2} - \frac{8\psi_{m_d}\mathbf{w}_a^T\sum_n \left(\alpha_n\psi_{n_d}\mathbf{w}_a^T\left(w_{s_d}\psi_{n_d}\mathbf{w}_a^T + \tilde{\mathbf{w}}_s\tilde{\boldsymbol{\Psi}}_n\mathbf{w}_a^T\right)\right)}{\left(w_{s_d}\psi_{m_d}\mathbf{w}_a^T + \tilde{\mathbf{w}}_s\tilde{\boldsymbol{\Psi}}_m\mathbf{w}_a^T\right)^3} + \frac{6\left(\psi_{m_d}\mathbf{w}_a^T\right)^2\sum_n \left(\alpha_n\left(w_{s_d}\psi_{n_d}\mathbf{w}_a^T + \tilde{\mathbf{w}}_s\tilde{\boldsymbol{\Psi}}_n\mathbf{w}_a^T\right)^2\right)}{\left(w_{s_d}\psi_{m_d}\mathbf{w}_a^T + \tilde{\mathbf{w}}_s\tilde{\boldsymbol{\Psi}}_m\mathbf{w}_a^T\right)^4} \tag{3.15}$$

Rearranging the second derivative so that there is a common denominator yields

$$\begin{aligned}\frac{\partial^2 J_2}{\partial w_{s_d}{}^2} = {} & \frac{\left(w_{s_d}\psi_{m_d}\mathbf{w}_a^T + \tilde{\mathbf{w}}_s\tilde{\boldsymbol{\Psi}}_m\mathbf{w}_a^T\right)^2\sum_n \left(\alpha_n\left(\psi_{n_d}\mathbf{w}_a^T\right)^2\right)}{\left(w_{s_d}\psi_{m_d}\mathbf{w}_a^T + \tilde{\mathbf{w}}_s\tilde{\boldsymbol{\Psi}}_m\mathbf{w}_a^T\right)^4} + \frac{\left(\psi_{m_d}\mathbf{w}_a^T\right)^2\sum_n \left(\alpha_n\left(w_{s_d}\psi_{n_d}\mathbf{w}_a^T + \tilde{\mathbf{w}}_s\tilde{\boldsymbol{\Psi}}_n\mathbf{w}_a^T\right)^2\right)}{\left(w_{s_d}\psi_{m_d}\mathbf{w}_a^T + \tilde{\mathbf{w}}_s\tilde{\boldsymbol{\Psi}}_m\mathbf{w}_a^T\right)^4} \\ & - \frac{2\left(w_{s_d}\psi_{m_d}\mathbf{w}_a^T + \tilde{\mathbf{w}}_s\tilde{\boldsymbol{\Psi}}_m\mathbf{w}_a^T\right)\psi_{m_d}\mathbf{w}_a^T\sum_n \left(\alpha_n\psi_{n_d}\mathbf{w}_a^T\left(w_{s_d}\psi_{n_d}\mathbf{w}_a^T + \tilde{\mathbf{w}}_s\tilde{\boldsymbol{\Psi}}_n\mathbf{w}_a^T\right)\right)}{\left(w_{s_d}\psi_{m_d}\mathbf{w}_a^T + \tilde{\mathbf{w}}_s\tilde{\boldsymbol{\Psi}}_m\mathbf{w}_a^T\right)^4} \\ & - \frac{2\left(\psi_{m_d}\mathbf{w}_a^T\right)\left(w_{s_d}\psi_{m_d}\mathbf{w}_a^T + \tilde{\mathbf{w}}_s\tilde{\boldsymbol{\Psi}}_m\mathbf{w}_a^T\right)\sum_n \left(\alpha_n\psi_{n_d}\mathbf{w}_a^T\left(w_{s_d}\psi_{n_d}\mathbf{w}_a^T + \tilde{\mathbf{w}}_s\tilde{\boldsymbol{\Psi}}_n\mathbf{w}_a^T\right)\right)}{\left(w_{s_d}\psi_{m_d}\mathbf{w}_a^T + \tilde{\mathbf{w}}_s\tilde{\boldsymbol{\Psi}}_m\mathbf{w}_a^T\right)^4} \\ & + \frac{2\left(\psi_{m_d}\mathbf{w}_a^T\right)^2\sum_n \left(\alpha_n\left(w_{s_d}\psi_{n_d}\mathbf{w}_a^T + \tilde{\mathbf{w}}_s\tilde{\boldsymbol{\Psi}}_n\mathbf{w}_a^T\right)^2\right)}{\left(w_{s_d}\psi_{m_d}\mathbf{w}_a^T + \tilde{\mathbf{w}}_s\tilde{\boldsymbol{\Psi}}_m\mathbf{w}_a^T\right)^4}\end{aligned} \tag{3.16}$$

When equation (3.16) is evaluated at the point where the first derivative is zero, equation (3.14), then the last term of equation (3.16) drops out of the equation. The terms in the second derivative can be brought inside of the summation:

$$\begin{aligned}\frac{\partial^2 J_2}{\partial w_{s_d}{}^2} = {} & \frac{\sum_n \left(\alpha_n\left(w_{s_d}\psi_{m_d}\mathbf{w}_a^T + \tilde{\mathbf{w}}\tilde{\boldsymbol{\Psi}}_m\mathbf{w}_a^T\right)^2\left(\psi_{n_d}\mathbf{w}_a^T\right)^2\right)}{\left(w_{s_d}\psi_{m_d}\mathbf{w}_a^T + \tilde{\mathbf{w}}\tilde{\boldsymbol{\Psi}}_m\mathbf{w}_a^T\right)^4} \\ & - \frac{\sum_n \left(2\alpha_n\left(w_{s_d}\psi_{m_d}\mathbf{w}_a^T + \tilde{\mathbf{w}}\tilde{\boldsymbol{\Psi}}_m\mathbf{w}_a^T\right)\psi_{m_d}\mathbf{w}_a^T\psi_{n_d}\mathbf{w}_a^T\left(w_{s_d}\psi_{n_d}\mathbf{w}_a^T + \tilde{\mathbf{w}}\tilde{\boldsymbol{\Psi}}_n\mathbf{w}_a^T\right)\right)}{\left(w_{s_d}\psi_{m_d}\mathbf{w}_a^T + \tilde{\mathbf{w}}\tilde{\boldsymbol{\Psi}}_m\mathbf{w}_a^T\right)^4} \\ & + \frac{\sum_n \left(\alpha_n\left(\psi_{m_d}\mathbf{w}_a^T\right)^2\left(w_{s_d}\psi_{n_d}\mathbf{w}_a^T + \tilde{\mathbf{w}}\tilde{\boldsymbol{\Psi}}_n\mathbf{w}_a^T\right)^2\right)}{\left(w_{s_d}\psi_{m_d}\mathbf{w}_a^T + \tilde{\mathbf{w}}\tilde{\boldsymbol{\Psi}}_m\mathbf{w}_a^T\right)^4}\end{aligned} \tag{3.17}$$

The terms inside of the summation are expansion of a square. Arranging the terms to illuminate the square yields

$$\left.\frac{\partial^2 J_2}{\partial w_{s_d}{}^2}\right|_{\frac{\partial J}{\partial w_{s_d}}=0} = \frac{\sum_n \left(2\alpha_n \left(\left(\psi_{n_d}\mathbf{w}_a^T\right)\tilde{\mathbf{w}}_s\tilde{\Psi}_m\mathbf{w}_a^T - \left(\psi_{m_d}\mathbf{w}_a^T\right)\tilde{\mathbf{w}}_s\tilde{\Psi}_n\mathbf{w}_a^T\right)^2\right)}{\left(w_{s_d}\psi_{m_d}\mathbf{w}_a^T + \tilde{\mathbf{w}}_s\tilde{\Psi}_m\mathbf{w}_a^T\right)^4} \tag{3.18}$$

Equation (3.18) is positive for any non-trivial solution of the weights as long as all of the modal weights, α, are positive and there are no traveling modes with complex valued mode shapes. Thus, the derivative calculated in equation (3.14) reflects the minimum value of the cost function. A similar analysis shows that the iteration on the implicit equation for weights is stable by noting that the minimum of the cost function evaluated on different elements occurs for the same value of the element weights.

3.3.3 2-Norm Optimization: Limits of Proofs

The proof of the existence of a single and global minimum to the 2-norm cost function has several severe limitations. The proof is available only if a single mode is targeted and if the modes are entirely real. The reasons behind these limits are discussed below.

3.3.3.1 Limit of Proof: Multiple Targeted Modes

The proof of the existence of a single and global minimum to the 2-norm cost function is only available if a single mode is being targeted. If multiple modes are featured in the denominator of the cost function, then the cost function expressed by equation (3.5) becomes

$$J_2 = \frac{\sum_n \left(\alpha_n \left(w_{s_d}\psi_{nd}\mathbf{w}_a^T + \tilde{\mathbf{w}}_s\tilde{\Psi}_n\mathbf{w}_a^T\right)^2\right)}{\sum_m \left(\beta_m \left(w_{s_d}\psi_{md}\mathbf{w}_a^T + \tilde{\mathbf{w}}_s\tilde{\Psi}_m\mathbf{w}_a^T\right)^2\right)} \tag{3.19}$$

where there are m targeted modes and β_m is the relative weights on the targeted modes. The optimal weights occur when the derivative of the cost function is zero. Taking the derivative of the multi-mode cost function in equation (3.19) and setting the derivative to zero yields:

$$\begin{aligned} 0 = &\sum_m \left(\beta_m \left(w_{s_d}\psi_{m_d}\mathbf{w}_a^T + \tilde{\mathbf{w}}_s\tilde{\Psi}_m\mathbf{w}_a^T\right)^2\right)\cdot \sum_n \left(\alpha_n\psi_{n_d}\mathbf{w}_a^T\left(w_{s_d}\psi_{n_d}\mathbf{w}_a^T + \tilde{\mathbf{w}}_s\tilde{\Psi}_n\mathbf{w}_a^T\right)\right) - \\ &\sum_m \left(\beta_m\psi_{m_d}\mathbf{w}_a^T\left(w_{s_d}\psi_{m_d}\mathbf{w}_a^T + \tilde{\mathbf{w}}_s\tilde{\Psi}_m\mathbf{w}_a^T\right)\right)\sum_n \left(\alpha_n \left(w_{s_d}\psi_{n_d}\mathbf{w}_a^T + \tilde{\mathbf{w}}_s\tilde{\Psi}_n\mathbf{w}_a^T\right)^2\right) \end{aligned} \tag{3.20}$$

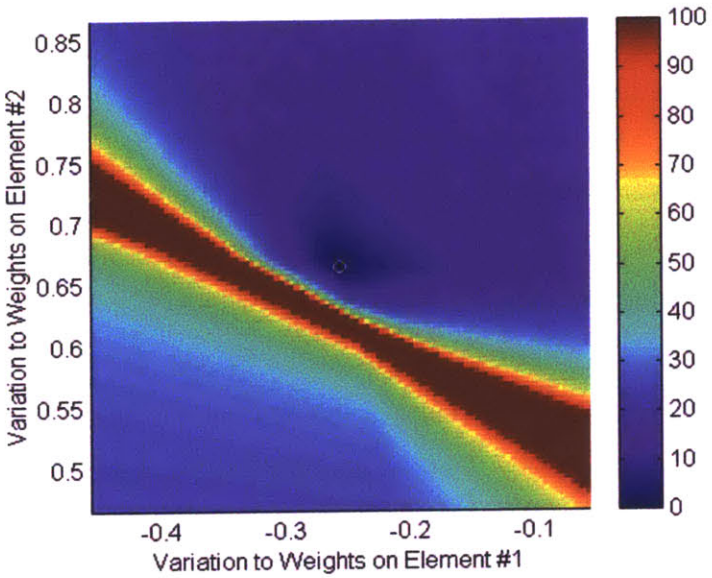

Figure 3.4: Numerical evaluation of the cost function on a clamped-clamped beam with four evenly spaced sensors at the middle quarter of the beam. The 2-norm cost function is defined to target the first two modes and minimize the other modes. The cost is plotted as the weights on two of the elements are varied. In this plot, there are only two zeros to the first derivative of the cost function; one corresponds to the minimum of the cost function and is marked with a circle, the other corresponds to a maximum of the cost function and is located along the diagonal ridge.

Expanding the squares, breaking the summations into components, and grouping terms in order of powers of $\mathbf{w}_{sd}$ yields a quadratic relationship for $\mathbf{w}_{sd}$.

$$
\begin{aligned}
0 = &\left(\sum_n\left(\alpha_n\left(\psi_{n_d}\mathbf{w}_a^T\right)^2\right)\sum_m\left(\beta_m\left(\psi_{m_d}\mathbf{w}_a^T\right)\tilde{\mathbf{w}}_s\tilde{\Psi}_m\right)-\sum_n\left(\alpha_n\left(\psi_{n_d}\mathbf{w}_a^T\right)\tilde{\mathbf{w}}_s\tilde{\Psi}_n\right)\sum_m\left(\beta_m\left(\psi_{m_d}\mathbf{w}_a^T\right)^2\right)\right)w_{s_d}^2 \\
&+\left(\sum_n\left(\alpha_n\left(\psi_{n_d}\mathbf{w}_a^T\right)^2\right)\sum_m\left(\beta_m\left(\tilde{\mathbf{w}}_s\tilde{\Psi}_m\mathbf{w}_a^T\right)^2\right)-\sum_n\left(\alpha_n\left(\tilde{\mathbf{w}}_s\tilde{\Psi}_n\mathbf{w}_a^T\right)^2\right)\sum_m\left(\beta_m\left(\psi_{m_d}\mathbf{w}_a^T\right)^2\right)\right)w_{s_d} \\
&+\sum_n\left(\alpha_n\left(\psi_{n_d}\mathbf{w}_a^T\right)\tilde{\mathbf{w}}_s\tilde{\Psi}_n\mathbf{w}_a^T\right)\sum_m\left(\beta_m\left(\tilde{\mathbf{w}}_s\tilde{\Psi}_m\mathbf{w}_a^T\right)^2\right) \\
&-\sum_n\left(\alpha_n\left(\tilde{\mathbf{w}}_s\tilde{\Psi}_n\mathbf{w}_a^T\right)^2\right)\sum_m\left(\beta_m\left(\psi_{m_d}\mathbf{w}_a^T\right)\tilde{\mathbf{w}}_s\tilde{\Psi}_m\mathbf{w}_a^T\right)
\end{aligned}
\tag{3.21}
$$

Since there are two solutions to equation (3.21), there will be two regions with a zero derivative in the cost function. One of the plateaus reflects a global minimum and the other reflects a local maximum. Although there will be only one minimum, the shape of the solution space for multiple targeted modes makes a gradient descent optimization of the weights more difficult, as illustrated in Figure 3.4.

3.3.3.2 *Limit of Proof: Complex Mode Shapes*

The proof of the existence of a single and global minimum to the 2-norm cost function is only available if the mode shapes are real. If the mode shapes are complex, then the derivative of the complex 2-norm cost function is

$$\begin{aligned}\frac{\partial J_2}{\partial w_{s_d}} = & \frac{\sum_n \left(\alpha_n \psi_{n_d} \mathbf{w}_a^T \left(w_{s_d} \psi_{n_d}^* \mathbf{w}_a^T + \tilde{\mathbf{w}}_s \tilde{\psi}_n^* \mathbf{w}_a^T\right) + \alpha_n \psi_{n_d}^* \mathbf{w}_a^T \left(w_{s_d} \psi_{n_d} \mathbf{w}_a^T + \tilde{\mathbf{w}}_s \tilde{\psi}_n \mathbf{w}_a^T\right)\right)}{\left(w_{s_d} \psi_{m_d} \mathbf{w}_a^T + \tilde{\mathbf{w}}_s \tilde{\psi}_m \mathbf{w}_a^T\right)\left(w_{s_d} \psi_{m_d}^* \mathbf{w}_a^T + \tilde{\mathbf{w}}_s \tilde{\psi}_m^* \mathbf{w}_a^T\right)} \\ & - \frac{\psi_{m_d} \mathbf{w}_a^T \sum_n \left(\alpha_n \left(w_{s_d} \psi_{n_d} \mathbf{w}_a^T + \tilde{\mathbf{w}}_s \tilde{\psi}_n \mathbf{w}_a^T\right)\left(w_{s_d} \psi_{n_d}^* \mathbf{w}_a^T + \tilde{\mathbf{w}}_s \tilde{\psi}_n^* \mathbf{w}_a^T\right)\right)}{\left(w_{s_d} \psi_{m_d} \mathbf{w}_a^T + \tilde{\mathbf{w}}_s \tilde{\psi}_m \mathbf{w}_a^T\right)^2 \left(w_{s_d} \psi_{m_d}^* \mathbf{w}_a^T + \tilde{\mathbf{w}}_s \tilde{\psi}_m^* \mathbf{w}_a^T\right)} \\ & - \frac{\psi_{m_d}^* \mathbf{w}_a^T \sum_n \left(\alpha_n \left(w_{s_d} \psi_{n_d} \mathbf{w}_a^T + \tilde{\mathbf{w}}_s \tilde{\psi}_n \mathbf{w}_a^T\right)\left(w_{s_d} \psi_{n_d}^* \mathbf{w}_a^T + \tilde{\mathbf{w}}_s \tilde{\psi}_n^* \mathbf{w}_a^T\right)\right)}{\left(w_{s_d} \psi_{m_d} \mathbf{w}_a^T + \tilde{\mathbf{w}}_s \tilde{\psi}_m \mathbf{w}_a^T\right)\left(w_{s_d} \psi_{m_d}^* \mathbf{w}_a^T + \tilde{\mathbf{w}}_s \tilde{\psi}_m^* \mathbf{w}_a^T\right)^2}\end{aligned} \tag{3.22}$$

The optimal weights occur when the derivative of the cost function equals to zero. Setting the derivative of the complex cost function to zero and multiplying by the denominator yields a quadratic expression for the weights.

$$\begin{aligned}0 = & w_{s_d}^2 \left[\begin{array}{l}\left(\psi_{n_d} \mathbf{w}_a^T\right)\left(\psi_{n_d}^* \mathbf{w}_a^T\right)\left(\psi_{m_d} \mathbf{w}_a^T\right)\left(\tilde{\mathbf{w}}_s \tilde{\psi}_m^* \mathbf{w}_a^T\right) + \left(\psi_{n_d} \mathbf{w}_a^T\right)\left(\psi_{n_d}^* \mathbf{w}_a^T\right)\left(\psi_{m_d}^* \mathbf{w}_a^T\right)\left(\tilde{\mathbf{w}}_s \tilde{\psi}_m \mathbf{w}_a^T\right) \\ -\left(\psi_{n_d} \mathbf{w}_a^T\right)\left(\psi_{m_d} \mathbf{w}_a^T\right)\left(\psi_{m_d}^* \mathbf{w}_a^T\right)\left(\tilde{\mathbf{w}}_s \tilde{\psi}_n^* \mathbf{w}_a^T\right) - \left(\psi_{n_d}^* \mathbf{w}_a^T\right)\left(\psi_{m_d} \mathbf{w}_a^T\right)\left(\psi_{m_d}^* \mathbf{w}_a^T\right)\left(\tilde{\mathbf{w}}_s \tilde{\psi}_m \mathbf{w}_a^T\right)\end{array}\right] \\ & + w_d \left(2\left(\psi_{n_d} \mathbf{w}_a^T\right)\left(\psi_{n_d}^* \mathbf{w}_a^T\right)\left(\tilde{\mathbf{w}}_s \tilde{\psi}_m \mathbf{w}_a^T\right)\left(\tilde{\mathbf{w}}_s \tilde{\psi}_m^* \mathbf{w}_a^T\right) - 2\left(\psi_{m_d} \mathbf{w}_a^T\right)\left(\psi_{m_d}^* \mathbf{w}_a^T\right)\left(\tilde{\mathbf{w}}_s \tilde{\psi}_m \mathbf{w}_a^T\right)\left(\tilde{\mathbf{w}}_s \tilde{\psi}_m^* \mathbf{w}_a^T\right)\right) \\ & + \left(\psi_{n_d} \mathbf{w}_a^T\right)\left(\tilde{\mathbf{w}}_s \tilde{\psi}_n^* \mathbf{w}_a^T\right)\left(\tilde{\mathbf{w}}_s \tilde{\psi}_m \mathbf{w}_a^T\right)\left(\tilde{\mathbf{w}}_s \tilde{\psi}_m^* \mathbf{w}_a^T\right) + \left(\psi_{n_d}^* \mathbf{w}_a^T\right)\left(\tilde{\mathbf{w}}_s \tilde{\psi}_n \mathbf{w}_a^T\right)\left(\tilde{\mathbf{w}}_s \tilde{\psi}_m \mathbf{w}_a^T\right)\left(\tilde{\mathbf{w}}_s \tilde{\psi}_m^* \mathbf{w}_a^T\right) \\ & - \left(\psi_{m_d} \mathbf{w}_a^T\right)\left(\tilde{\mathbf{w}}_s \tilde{\psi}_n \mathbf{w}_a^T\right)\left(\tilde{\mathbf{w}}_s \tilde{\psi}_n^* \mathbf{w}_a^T\right)\left(\tilde{\mathbf{w}}_s \tilde{\psi}_m^* \mathbf{w}_a^T\right) - \left(\psi_{m_d}^* \mathbf{w}_a^T\right)\left(\tilde{\mathbf{w}}_s \tilde{\psi}_n \mathbf{w}_a^T\right)\left(\tilde{\mathbf{w}}_s \tilde{\psi}_n^* \mathbf{w}_a^T\right)\left(\tilde{\mathbf{w}}_s \tilde{\psi}_m \mathbf{w}_a^T\right)\end{aligned} \tag{3.23}$$

Since there are two solutions to equation (3.23), there are two regions with a zero derivative in the complex cost function. One of the zero derivatives will correspond to the global minimum and another will correspond to a maximum. Search algorithms searching for the zero derivative cannot be guaranteed to find the desired global minimum instead of the unwanted maximum.

3.3.4 Perturbation Analysis

The 2-norm cost function that is used to optimize the array weights is a function of the mode shapes measured at the array elements and of the weights on those elements. This section examines the sensitivity of the 2-norm cost function to variations in the mode

shapes and to variations in the array weights. Through the perturbation analysis, it will be shown that the change in modal isolation performance as a function of variations in the array weights will be of the same order as variations in the mode shapes. As a result, experimental studies can note the effects of variations in the array weights and use this as an estimate of the performance change that would result from shifts in the mode shapes.

3.3.4.1 Perturbations of the Unwanted Mode Shapes

The effects of perturbation of one element on one mode will be evaluated. This perturbation analysis will assume that the mode shapes are real-valued and that all of the weights are real. In this case, the 2-norm cost function of equation (3.5) can be represented as

$$J_2 = \frac{\sum_n \left(\alpha_n \left(\mathbf{w}_s \psi_n \mathbf{w}_a^T\right)\right)^2}{\left(\mathbf{w}_s \psi_m \mathbf{w}_a^T\right)^2} \tag{3.24}$$

Consider a perturbation of order ε on the d^{th} element of the p^{th} mode shape, ψ_{pd}, in the numerator of equation (3.24). The perturbation is of the form

$$\tilde{\psi}_{p_d} = \psi_{p_d} + \varepsilon \tag{3.25}$$

where the tilda denotes the perturbed value. Equation (3.24) becomes

$$\tilde{J}_2 = \frac{\left(\alpha_p \left(\mathbf{w}_s \psi_p \mathbf{w}_a^T\right) + w_{s_d} \varepsilon w_{a_d}^T\right)^2 + \sum_{n,n\neq p} \left(\alpha_n \left(\mathbf{w}_s \psi_n \mathbf{w}_a^T\right)\right)^2}{\left(\mathbf{w}_s \psi_m \mathbf{w}_a^T\right)^2}, \tag{3.26}$$

where the p^{th} mode shape is a set of the unwanted modes and $\tilde{J}_2$ is the perturbed 2-norm cost. Note that the summation over the p^{th} mode has been brought outside of the summation. Evaluating the quadratic terms and only retaining terms that are first-order in ε, the perturbed cost function becomes

$$\tilde{J}_2 = \frac{\sum_n \left(\alpha_n \left(\mathbf{w}_s \psi_n \mathbf{w}_a^T\right)\right)^2 + 2\alpha_p \left(w_{s_d} \varepsilon w_{a_d}^T\right)\left(\mathbf{w}_s \psi_p \mathbf{w}_a^T\right)}{\left(\mathbf{w}_s \psi_m \mathbf{w}_a^T\right)^2} + HOT \tag{3.27}$$

The first-order perturbation to the 2-norm cost function is the difference between the perturbed and unperturbed solution. Simplifying the equation to elucidate the perturbation to errors in the mode shape of an unwanted mode:

$$\tilde{J}_2 = J_2 + \varepsilon \frac{2\alpha_p \left(w_{s_d} w_{a_d}^T\right)\left(\mathbf{w}_s \psi_p \mathbf{w}_a^T\right)}{\left(\mathbf{w}_s \psi_m \mathbf{w}_a^T\right)^2} \tag{3.28}$$

The variation in the cost is of the same order as the error in determining the mode shape. The influence of the error is directly tied to the magnitude of the product, $\mathbf{w}_s \psi_p \mathbf{w}_a^T$, and to the magnitude of the weights on the array element, $w_{s_d} w_{a_d}$. If the desired mode, m, is well isolated, then the cost function is less sensitive to errors in the modal estimation.

3.3.4.2 *Perturbations of the Targeted Mode Shape*

The effects of perturbation of one element on the targeted mode will be evaluated in a manner similar to perturbation analysis of unwanted mode shapes. Like the preceding analysis, this perturbation analysis will assume that all of the mode shapes are real-valued and that all of the weights are real. Consider a perturbation of order ε on the d^{th} element of the targeted mode shape, ψ_{md}, so that

$$\tilde{\psi}_{m_d} = \psi_{m_d} + \varepsilon \tag{3.29}$$

Evaluating the perturbation to the denominator of the 2-norm cost function yields

$$\tilde{J}_2 = \frac{\sum_n \left(\alpha_n \left(\mathbf{w}_s \psi_n \mathbf{w}_a^T\right)\right)^2}{\left(\mathbf{w}_s \psi_m \mathbf{w}_a^T\right)^2 + 2\left(w_{s_d} \varepsilon w_{a_d}^T\right)\left(\mathbf{w}_s \psi_m \mathbf{w}_a^T\right)} \tag{3.30}$$

Expanding the quadratic in the denominator yields, to first order:

$$\tilde{J}_2 = \frac{\sum_n \left(\alpha_n \left(\mathbf{w}_s \psi_n \mathbf{w}_a^T\right)\right)^2}{\left(\mathbf{w}_s \psi_m \mathbf{w}_a^T + w_{s_d} \varepsilon w_{a_d}^T\right)^2} \tag{3.31}$$

Performing a binomial expansion and only retaining terms that are of first-order, the perturbed 2-norm cost function becomes:

$$\tilde{J}_2 = J_2 + \varepsilon J_2 \frac{2 w_{s_d} w_{a_d}^T}{\left(\mathbf{w}_s \psi_m \mathbf{w}_a^T\right)^2} + HOT \tag{3.32}$$

The sensitivity of the modal isolation performance to variations in the mode shapes is of first-order in ε. Errors in the mode shape of the targeted mode decrease as the modal isolation improves. In other words, if the targeted mode is well isolated and the 2-

norm cost is small, then the targeted mode shape can be measured with a lower accuracy. The error increases as the element weights increase.

3.3.4.3 Perturbations in the Array Weights

The effects of perturbation of one element on the sensor weights will be evaluated in a manner similar to the previous perturbation analyses. The variation on the weights affects both the numerator and the denominator of the cost function. Like the preceding analyses, this perturbation analysis will assume that all of the mode shapes are real-valued and that all of the weights are real. Consider a perturbation of order ε on the d^{th} element of the sensor weight, w_{sd}, so that

$$\tilde{w}_{s_d} = w_{s_d} + \varepsilon \tag{3.33}$$

Evaluating the perturbation in both the numerator and the denominator of the 2-norm cost function yields

$$\hat{J}_2 = \frac{\sum_n \left(\alpha_n \left(\varepsilon \psi_{n_d} \mathbf{w}_a^T + \mathbf{w}_s \psi_n \mathbf{w}_a^T \right)^2 \right)}{\left(\varepsilon \psi_{m_d} \mathbf{w}_a^T + \mathbf{w}_s \psi_m \mathbf{w}_a^T \right)^2} \tag{3.34}$$

Expanding the quadratic yields

$$\hat{J}_2 = \frac{\sum_n \left(\alpha_n \left(\mathbf{w}_s \psi_n \mathbf{w}_a^T \right)^2 + 2\alpha_n \varepsilon \psi_{n_d} \mathbf{w}_a^T \left(\mathbf{w}_s \psi_n \mathbf{w}_a^T \right) \right)}{\left(\mathbf{w}_s \psi_m \mathbf{w}_a^T \right)^2 + 2\varepsilon \psi_{m_d} \mathbf{w}_a^T \left(\mathbf{w}_s \psi_m \mathbf{w}_a^T \right)} + HOT \tag{3.35}$$

Regrouping the perturbed cost function and dropping the higher-order-terms yields

$$\hat{J}_2 = \frac{\sum_n \left(\alpha_n \left(\mathbf{w}_s \psi_n \mathbf{w}_a^T \right)^2 \right)}{\left(\mathbf{w}_s \psi_m \mathbf{w}_a^T \right)^2 + 2\varepsilon \psi_{m_d} \mathbf{w}_a^T \left(\mathbf{w}_s \psi_m \mathbf{w}_a^T \right)} + \frac{\sum_n \left(2\alpha_n \varepsilon \psi_{n_d} \mathbf{w}_a^T \left(\mathbf{w}_s \psi_n \mathbf{w}_a^T \right) \right)}{\left(\mathbf{w}_s \psi_m \mathbf{w}_a^T \right)^2 + 2\varepsilon \psi_{m_d} \mathbf{w}_a^T \left(\mathbf{w}_s \psi_m \mathbf{w}_a^T \right)} \tag{3.36}$$

Performing a binomial expansion of the denominator and only keeping terms that are first order in ε yields

$$\hat{J}_2 = J_2 - \varepsilon \left(J_2 \frac{2\psi_{m_d} \mathbf{w}_a^T}{\left(\mathbf{w}_s \psi_m \mathbf{w}_a^T \right)} + \frac{\sum_n \left(2\alpha_n \psi_{n_d} \mathbf{w}_a^T \left(\mathbf{w}_s \psi_n \mathbf{w}_a^T \right) \right)}{\left(\mathbf{w}_s \psi_m \mathbf{w}_a^T \right)^2} \right) \tag{3.37}$$

As with perturbations to the mode shapes, the sensitivity of the modal isolation performance to variations in the weights is of first-order in ε. Errors due to variations in

Figure 3.5: If the first mode is targeted with an evenly spaced array on a simply-supported beam, then the seventh mode will also be measured. The unintentional featuring of the seventh mode is called spatial aliasing.

the sensor weights decrease as the modal isolation improves. In other words, if the targeted mode is well isolated and the 2-norm cost is small, then the targeted mode shape can be measured with a lower accuracy. The error increases as the element weights increase.

It is often difficult to experimentally vary the system mode shapes in order to experimentally ascertain the sensitivity of the performance to errors. However, it is very easy to experimentally measure the change in modal isolation performance as a function of variation in the array weights. This perturbation analysis shows that the performance change as a function of errors in the array weights will be of the same order as the performance change as a function of errors in the mode shape. As a result, experimental perturbation analysis based upon changing the array weights will also provide a good understanding of the sensitivity of the system to perturbations to the mode shapes.

3.4 Spatial Aliasing and Filtering

Spatial aliasing is a limiting factor in the performance of discrete element arrays. Spatial aliasing is behaviorally similar to aliasing in temporal signals in that shorter wavelength modes gets mapped back to longer wavelength modes; that is, higher modes cannot be distinguished from lower modes. Spatial aliasing means that the aliased mode cannot be minimized while the fundamental mode is targeted. Spatial aliasing sets an upper limit to the number of modes that can be minimized. The concept of spatial aliasing is illustrated in a simple example in Figure 3.5.

On a simply supported beam with an evenly distributed array of point transducers, there is a simple relationship for the spatial aliasing. The first spatially aliased mode

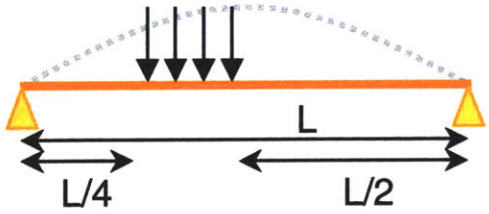

Figure 3.6: The numerical example of weighted arrays features four evenly spaced point displacement sensors between the quarter and half the length of the beam.

number, a, is related to the number of array elements, e, and the targeted mode number, m. The observed relationship is

$$a = 2(e+1) - m \qquad e > 0 \tag{3.38}$$

If the 1st mode is targeted for sensing or actuation on a beam with 3 elements, then the 7th mode will also be featured. Increasing the number of elements in the array delays the advent of spatial aliasing. Higher modes are more prone to aliasing problems than lower modes.

Distributed transducer elements in the discrete array can help to minimize the effects of spatial aliasing by reducing the transducer's coupling to higher modes. Distributed sensors and actuators are spatial integrators and their coupling is proportional to the average response across the area of the transducer [Anderson and Crawley, 1995]. In other words, smaller transducers couple better to higher modes than larger transducers. By using larger transducers, which create an area averaging effect, the system response can roll-off before spatial aliasing arises. The distributed piezoelectric transducers used in the experimental investigation were sized to take advantage of this effect. Piezoelectric transducers are the typical choice as a distributed or an area averaging transducer. The transducers' shape also influences the roll-off behavior and circular transducers will roll-off quicker than square transducers [Andersson and Crawley, 1985].

3.5 Simple Example of Weighted Arrays

This section presents a simple example in order to illustrate weighted arrays and the different methods for determining the array weights. An array of four point displacement sensors is modeled on a simply supported beam. The sensor array is evenly spaced

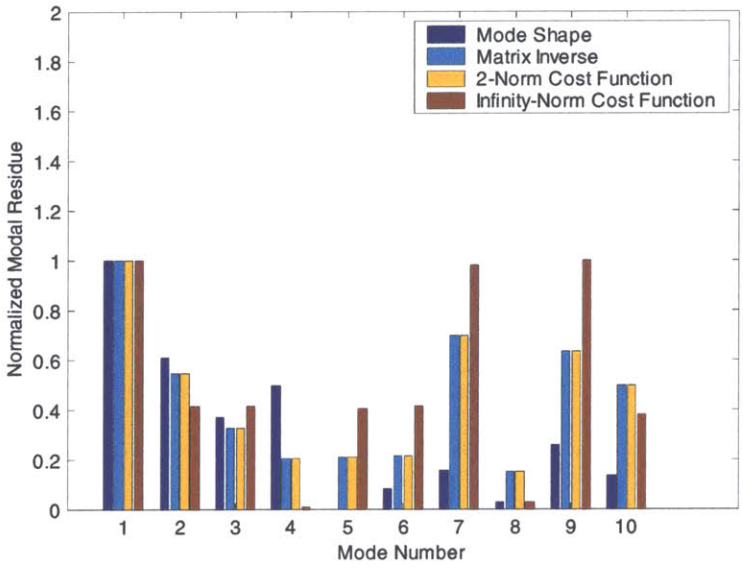

Figure 3.7: Modal residues from weighted 4-element sensor on a simply-supported beam. Residues are normalized so that the targeted mode, mode 1, has a magnitude of 1. The matrix inverse and the cost function techniques seek to minimize the residue of modes 2 through 6. Modal residue is a measure of the observability of a mode.

between 25% and 50% of the beam length. The sensor array will be weighted in order to isolate the first mode of vibration. The setup for this numerical investigation is illustrated in Figure 3.6.

Sinusoidal mode shapes of a simply supported beam are used. The sensor signals are

$$y = \sin(k\pi x), \quad x = \left[\tfrac{1}{4} \quad \tfrac{1}{3} \quad \tfrac{5}{12} \quad \tfrac{1}{2}\right] \tag{3.39}$$

where k is the mode number and x is the sensor location.

There are four techniques for determining the array weights: 1) Mode Shape; 2) Matrix Inverse; 3) 2-Norm Cost Function; and 4) Infinity-Norm Cost Function. As explained in Section 3.2, the Mode Shape technique sets the weights to the targeted mode shape; the Matrix Inverse technique inverts the transfer function matrix; the 2-Norm Cost Function technique minimizes the average response of the unwanted modes; and the Infinity-Norm Cost Function technique minimizes the peak response of the unwanted modes. The weights for the 2-Norm Cost Function are evaluated with equation (3.14) and the weights for the Infinity-Norm Cost Function are found by minimizing equation (3.5).

The Matrix Inverse and the cost function weighting techniques require the user to specify how many modes are to be minimized. When the number of minimized modes is equal to or less than the number of sensors, then perfect performance can be obtained. When the number of modes to be minimized is greater than the number of sensors, then the unwanted modes are partially observable.

Figure 3.7 illustrates the modal residues if mode number 1 is targeted and modes number 2 through 6 are to be minimized. The modal residues are normalized so that the residue of the targeted mode, mode number 1, has a magnitude of one. Modal residue is a measure of a mode's observability. On this setup, the Matrix Inversion and the 2-Norm Cost Function yield identical results. Over the first 6 modes, the lowest average modal residues are obtained with the Matrix Inversion and with the 2-Norm Cost Function. The lowest peak modal residue is obtained with the Infinity-Norm Cost Function. The modal residue of the 7^{th} mode is much larger than the residue of the lower modes when the weights are calculated with matrix inversion or a cost function. The larger modal residue at the 7^{th} mode arises because the optimization technique seeks to minimize only up to mode number 6.

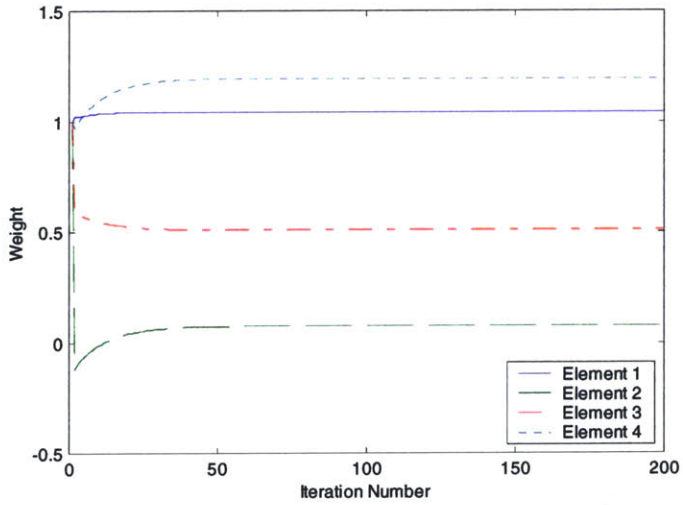

Figure 3.8: Convergence of the weights computed with a 2-Norm Cost Function.

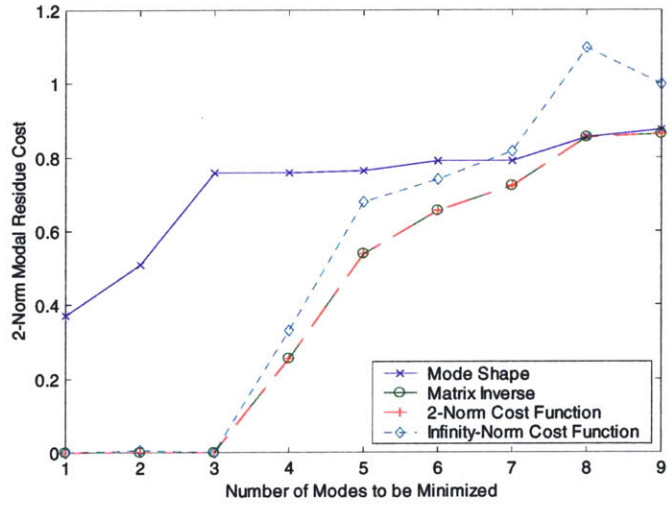

Figure 3.9: 2-Norm performance of the different weighting techniques as a function of the number of modes that are minimized. The 2-norm performance is the sum of the squared modal residues and reflects the average modal residue. The 2-Norm Cost Function and the Matrix Inverse yield the best performance from this performance metric.

The weights based upon the 2-Norm Cost Function are calculated with equation (3.14), which requires iteration for the weights to settle to the optimal value. The convergence of the weights is illustrated in Figure 3.8. In this example, the weights converged to their optimal value within 200 iterations.

The performance of the different weighting techniques as a function of the number of modes to be minimized can also be evaluated. Two methods of evaluating the performance are presented: 2-norm performance and infinity-norm performance. These performances are defined by the cost functions in equation (3.5). The 2-norm performance is a measure of the average unwanted modal residue and the infinity-norm performance is a measure of the peak unwanted modal residue.

The behavior of the 2-norm performance metric is illustrated in Figure 3.9. When less than 4 modes are minimized, then the matrix inverse and the cost function yield perfect performance. When more modes are minimized, then the 2-Norm Cost Function and the Matrix Inverse yield the best 2-norm performance. These two weighting techniques tend to converge to the weights of the Mode Shape when the number of modes to be minimized is much larger than the number of array elements.

The behavior of the infinity-norm performance metric is illustrated in Figure 3.10. As with the 2-norm performance metric, perfect performance is obtained up until 4 modes are minimized. As more modes are minimized, the Infinity-Norm Cost Function provides substantially better performance than the other minimization techniques. The Matrix Inverse and the 2-Norm Cost Function converge to the Mode Shape when the number of modes to be minimized is much larger than the number of array elements.

In summary, the 2-Norm Cost Function and the Matrix Inverse provide the best minimization of the average modal residue. The Infinity-Norm Cost Function provides the best minimization of the peak modal residue. This is expected based upon the definition of the cost functions. Although the 2-Norm Cost Function and the Matrix Inverse techniques yield identical answers for this example, a cost function is more general because it can be applied when actuator and sensor arrays are used and a cost function can provide modal-based weighting to achieve better closed-loop performance. Additionally, matrix inversion will generally yield complex weights, which cannot be implemented causally.

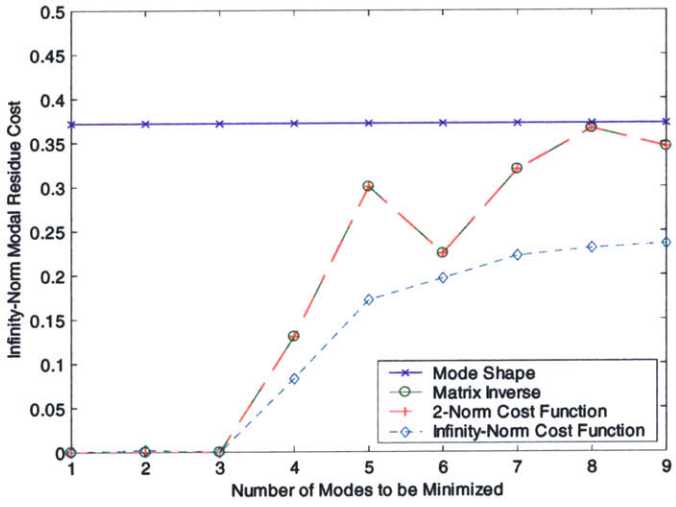

Figure 3.10: Infinity-norm performance of the different weighting techniques as a function of the number of modes that are minimized. The infinity-norm performance is the maximum modal residue, which is an important measure of control performance. The Infinity-Norm Cost Function yields the best performance from this performance metric.

3.6 Summary of Weighted Array Theory

Weighted arrays are arrays of discrete transducers that are weighted in order to isolate individual modes. This chapter presented several methods for calculating the weights, including setting the weights equal to the targeted mode shape, setting the weights from matrix inversion, and setting the weights from the minimization of a cost function. A 2-norm cost function, which seeks to minimize the average response of the unwanted modes, was proven to have a single and global minimum if the weights and mode shapes are real valued. A perturbation analysis showed that the 2-norm cost function is relatively insensitive to variations in the array weights or to variations in the measured mode shapes.

Spatial aliasing is one of the limitations of using discrete transducers because it sets an upper limit to the extent of modal isolation performance. Distributed transducers can be used to low-pass filter the signals, and, thus, reduce the magnitude of the spatial aliasing. Simple numerical examples were presented that illustrated the modal isolation and the spatial aliasing.

CHAPTER 4

Modal Isolation Experiments

The brightest flashes in the world of thought are incomplete
until they have been proved to have their counterparts in the world of fact.
- John Tyndall, 1863

Don't ask what it means, but rather how it is used.
- Ludwig Wittgenstein

A central postulate of this thesis is that weighted arrays of sensors and actuators can be used to isolate individual modes of vibration. This chapter examines the ability of weighted arrays to isolate individual modes by looking at the modal isolation performance of a 30-element array mounted on a cylinder section. This cylinder section is designed to behave similarly to a single panel of the fuselage test-bed. Experimental sensitivity analyses are performed to evaluate the modal isolation performance as a function of the number of transducer elements, of perturbations to the system, and of transducer failure. The importance of collocation for modal isolation is also addressed.

4.1 Experimental Setup

The panel test-bed used in this paper was designed to represent a single panel of the larger aircraft fuselage test-bed. The panel is a 0.762 mm aluminum plate screwed to a curved wooden frame. The frame is located at one end of a wooden impedance tube whose length equals the diameter of the scaled fuselage test-bed. The curved panel covers a 30° arc. The geometry is shown in Figure 4.1.

Although the weighted array methodology can be applied with any actuator and sensor combination, piezoceramic actuators and piezopolymer sensors were chosen for this application. Piezoelectric materials possess high energy densities, deliver broad bandwidth, and couple efficiently with structural vibrations. Additionally, most piezoelectrics are distributed transducers and perform spatial filtering, a fact used to size the elements. The array elements were sized to minimize their coupling with high frequency modes that would be aliased due to the discrete nature of the array. Wafers of PZT-5A measuring 3.18cm x 3.18cm x 0.0254cm (1.25" x 1.25" x 10 mil) from Morgan Matroc Electro Ceramics were chosen as the actuator material. Sheets of unelectroded 52μm PVDF from Measurement Specialties, Inc. were chosen as the sensor material.

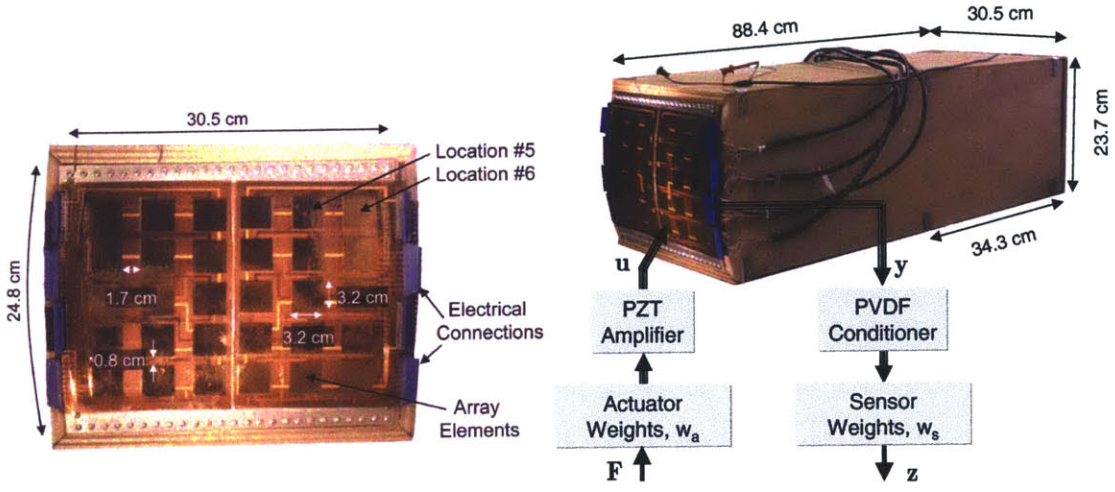

Figure 4.1: Layout and placement of the transducer array on the cylinder section. The cylinder section is located at one end of an impedance tube.

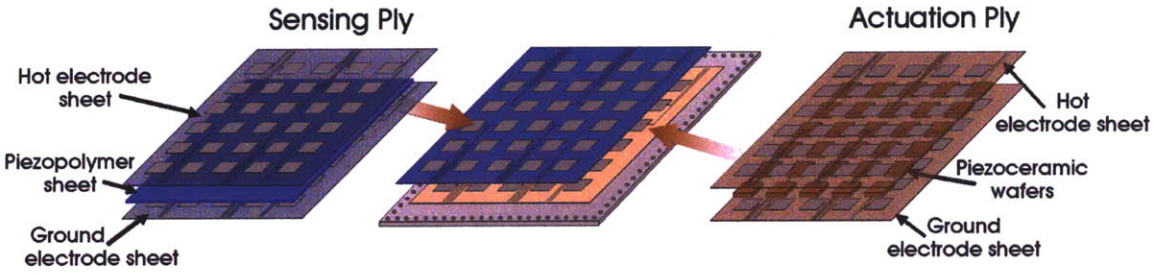

Figure 4.2: The sensor and actuator plies are formed by encapsulating a piezoelectric between layers of etched copper-coated Kapton. The Kapton sheets provide the electrical connections to the transducers, hold the transducers, and provide enhanced robustness.

Each array of transducer material was encapsulated between two layers of flexible electrode. The flexible electrodes are composed of a 0.05 mm thick Kapton polyamide film that is coated with 0.025 mm of copper. The film was used to align and to connect the arrays of transducer materials. The copper-coated Kapton was etched to create electrode patches at the transducer locations and surface wire paths to the edge of the active ply. The mask for the etching was deposited with a Tektronix Phaser 840 printer, ferric chloride was used as the etchant, and the mask was removed with heat and acetone. Spacing of the transducers and the wiring are depicted in Figure 4.1. Crimp connectors allowed external wires to attach to the surface wires on the flexible electrode. Signals from the PVDF sensor elements were conditioned with a unity-gain op-amp amplifier circuit. The active plies were bonded to the flat aluminum plate and then the entire

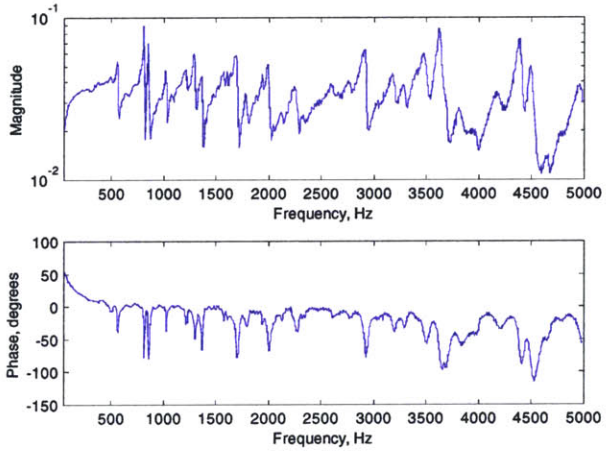

Figure 4.3: The transfer function from an actuator to its collocated sensor displays bounded phase, which means that collocated behavior has been obtained for each transducer pair.

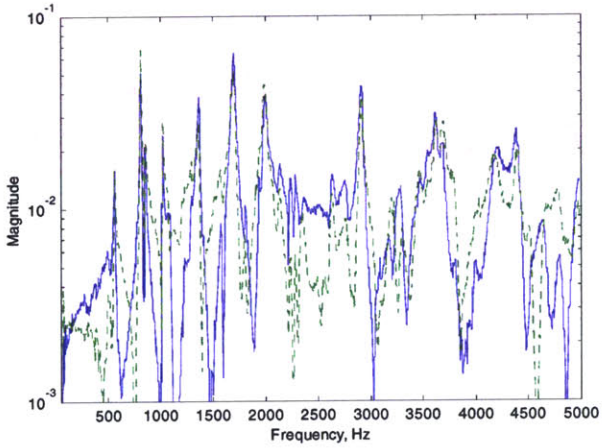

Figure 4.4: The transfer function from the actuator at location #5 to the sensor at location #6 (solid line) is not the same as the transfer function from the actuator at location #6 to the sensor at location #5 (dotted line), which means that the transfer function matrix is not symmetric.

structure was bent as it was attached to the curved frame. The 100 micro strain induced in the actuator layer is far below the fracture strain of piezoceramics.

Each actuator and sensor pair is designed to be collocated in order to simplify the control design [Mac Martin, 1995]. Collocated actuators and sensors have a transfer function that features alternating poles and zeros and, hence, a phase that remains within an 180°-phase band. As a result, a simple control algorithm can be phase stabilized in this region. A collocated transfer function from the actuator-sensor pair at location #5 is shown in Figure 4.3. While each transducer pair exhibits collocated behavior, the transfer function matrix turned out to be asymmetric, as illustrated in Figure 4.4. The transfer function from the actuator at one location to the sensor at another location is not the same as the transfer function from the actuator at the second location to the sensor at the first location. Thus, the transfer function matrix is not strictly a real positive definite transfer function matrix. This is an unexpected feature of this test-bed, and is attributed to the almost-collocated behavior of each element, since the PVDF is bonded to the top surface of the PZT, and to manufacturing variability in the bonding layer between PZT and PVDF.

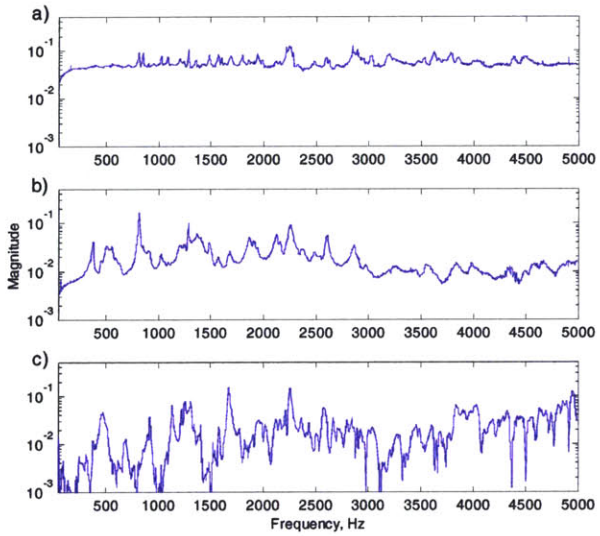

Figure 4.5: a) Maximum power spectral density of the transfer function from actuators to sensors; b) maximum power spectral density of the transfer function from disturbance to sensors; and c) the transfer function from disturbance to performance sensor.

The lack of symmetry in the transfer function matrix has strong implications on the use of weighted arrays. If the transfer function matrix were symmetric, then using the same weights on the actuators and on the sensors would guarantee that the weighted transfer function would exhibit collocated behavior. Since, the experimental transfer function matrix is not symmetric, the weighted transfer function has the potential for having unbounded phase. A phase penalty is used to enforce bounded phase.

The maximum power spectral density of all the actuator to sensor transfer functions is shown in Figure 4.5. Note that this transfer function is almost flat with frequency. Figure 4.5 also shows the maximum power spectral density of the transfer function from the disturbance piezoceramic to all sensors and the transfer function from the disturbance piezoceramic to the microphone performance sensors. The disturbance piezoceramic excites modes that are unobservable and uncontrollable by the actuators and sensors, which limits the array's ability to target these modes individually.

Table 4.1: TECHNIQUES FOR DETERMINING THE WEIGHTS ON THE TRANSDUCER ARRAYS.

Abbreviation	Weighting Metric
M.S.	Mode shape. Weights equal to measured complex mode shape
M.Inv.	Matrix inversion. Weights equal to inverted transfer function matrix. Uses equation (4.1).
I.S.	Infinity-norm cost function with the same weights on the sensor array and on the actuator array. Uses equation (4.2) with β=0.
I.A.	Infinity-norm cost function with different weights on the sensor array and on the actuator array. Uses equation (4.2) with β=0.
I.A.P.	Infinity-norm cost function with different weights on the arrays and a term in the cost function that penalizes phase. Uses equation (4.2).
1A	Infinity-norm cost function with all of the actuators grouped together to form a multiple-input but single-output system
1A.P.	Infinity-norm cost function with all of the actuators grouped together to form a multiple-input but single-output system. Includes term in cost function that penalizes phase.
2.S.	2-norm cost function with the same weights on the sensor array and on the actuator array. Uses equation (4.2) with β=0.
2.A.	2-norm cost function with different weights on the sensor array and on the actuator array. Uses equation (4.2) with β=0.
2.A.P.	2-norm cost function with different weights on the arrays and a term in the cost function that penalizes phase. Uses 2-norm cost from equation (4.2).

4.2 Modal Isolation

The weightings on the actuator and sensor arrays were computed in order to isolate individual modes in the actuator to sensor transfer function. The weights can be determined by several methods. As described in the Chapter 2, weights on the array elements can be determined from the measured mode shape, from matrix inversion, from an infinity-norm cost function, or from a 2-norm cost function. Matrix inversion takes the pseudo-inverse of the experimentally measured system transfer functions, $\mathbf{G}(\omega)$,

$$\mathbf{w}_s = \left(\mathbf{G}_s{}^T\mathbf{G}_s\right)^{-1}\mathbf{G}_s{}^T\mathbf{f} \tag{4.1}$$

where $\mathbf{f}$ is the desired transfer function. The array of weights are calculated column-wise for each sensor, s. The weights must be computed column-wise since the full transfer

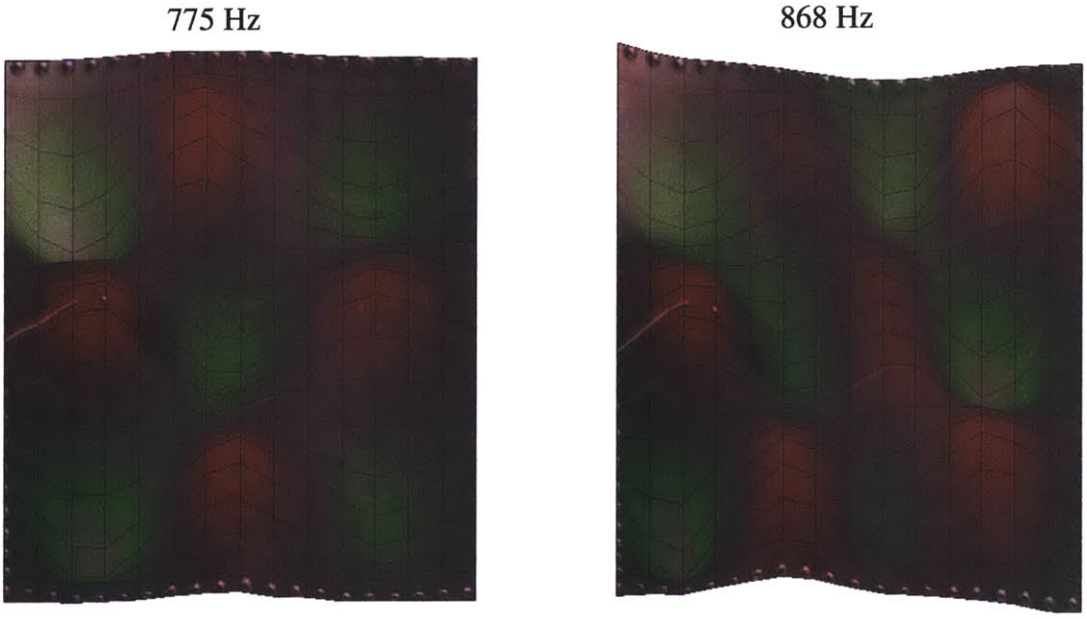

Figure 4.6: Mode shapes of the un-instrumented curved panel. The targeted mode of the instrumented panel lies at 812 Hz andtends to correlate best with the pictured 775 Hz mode.

function matrix is a three-dimensional matrix of dimensions frequency by sensor number by actuator number. The weights calculated through matrix inversion are, in general, complex, which means that the weights cannot be applied in a causal manner. The transfer functions presented in this thesis that use matrix inversion are calculated in a non-causal manner, which greatly limits their applicability.

The infinity-norm cost function, J_∞, and the 2-norm cost function, J_2, are defined as

$$J_\infty = \frac{\max_n \left(\alpha_n \left(\mathbf{w}_s \Psi_n \mathbf{w}_a\right)\left(\mathbf{w}_s \Psi_n \mathbf{w}_a\right)^*\right)}{\left(\mathbf{w}_s \Psi_m \mathbf{w}_a\right)\left(\mathbf{w}_s \Psi_m \mathbf{w}_a\right)^*} + \beta \,\mathrm{int}\left(\frac{\mathrm{abs}\left(\angle \mathbf{w}_s^T \mathbf{G} \mathbf{w}_a\right)}{\pi}\right)$$
$$J_2 = \frac{\sum_n \left(\alpha_n \left(\mathbf{w}_s \Psi_n \mathbf{w}_a\right)\left(\mathbf{w}_s \Psi_n \mathbf{w}_a\right)^*\right)}{\left(\mathbf{w}_s \Psi_m \mathbf{w}_a\right)\left(\mathbf{w}_s \Psi_m \mathbf{w}_a\right)^*} + \beta \,\mathrm{int}\left(\frac{\mathrm{abs}\left(\angle \mathbf{w}_s^T \mathbf{G} \mathbf{w}_a\right)}{\pi}\right) \tag{4.2}$$

where ψ_i is the mode shape evaluated at the transducers, $\mathbf{w_s}$ and $\mathbf{w_a}$ are the sensor and actuator weights, and int takes the integer part of the absolute value of the phase angle of the weighted transfer function, $\angle \mathbf{w}_s^T \mathbf{G} \mathbf{w}_a$. β is a scaling factor to decide the relative weight of the phase penalty. The phase penalty only affects the cost when the weighted transfer

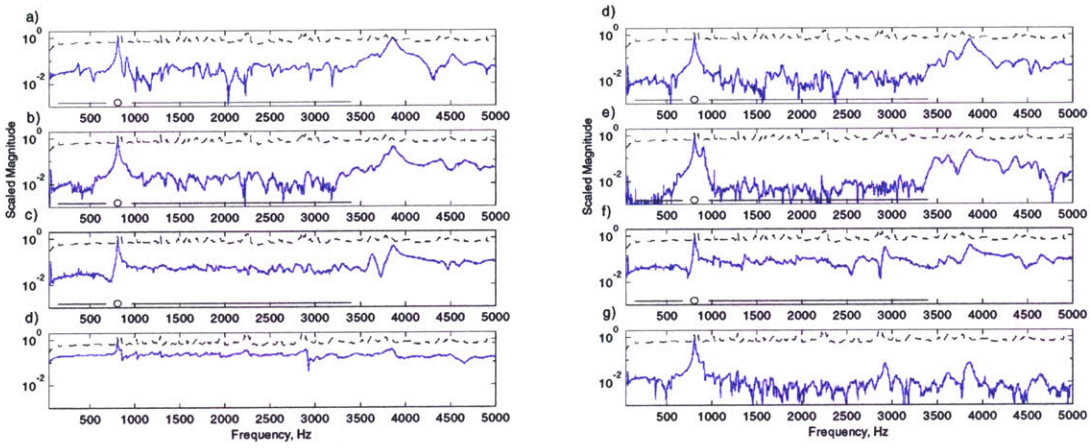

Figure 4.7: Results of seeking to isolate the mode at 812 Hz. The targeted frequency is noted with a circle and the frequency region where the response is minimized is designated with a horizontal line. The maximum singular values of the transfer function are noted with a dotted line. The magnitudes of the curves are scaled so that the response at the targeted frequency has magnitude of one. a) I.S., b) I.A., c) I.A.P., d) M.S., e) 2.S., f) 2.A., g) 2.A.P., h) M.Inv.

function no longer exhibits a phase bounded by $\pm\pi$ radians. The cost function approach allows the use of different weights for the sensors and actuators. The cost functions can also include a term that penalizes unbounded phase. A complete list of the different weighting options investigated in this research and their abbreviations is presented in Table 4.1.

For the purposes of illustration, particular focus is given to the mode at 812 Hz. This mode is readily observable by the sensors and controllable by the actuators and it is prominently featured in the performance transfer functions. The shape of this mode was not directly measured, but the mode shapes of the panel without the sensing and actuation plies were measured with a Polytec scanning laser vibrometer. The nearest mode shapes of the un-instrumented panel are shown in Figure 4.6. The targeted mode at 812 Hz on the instrumented panel with sensing and actuation plies correlates with the 3-3 vibration mode of the plate. A complete list of mode shapes is tabulated in the appendix.

The frequency performances of the weighting techniques are shown in Figure 4.7. In these plots, the mode at 812 Hz is targeted and the modes responses between 150 Hz and 675 Hz and between 975 Hz and 3400 Hz are minimized. Using different weights on

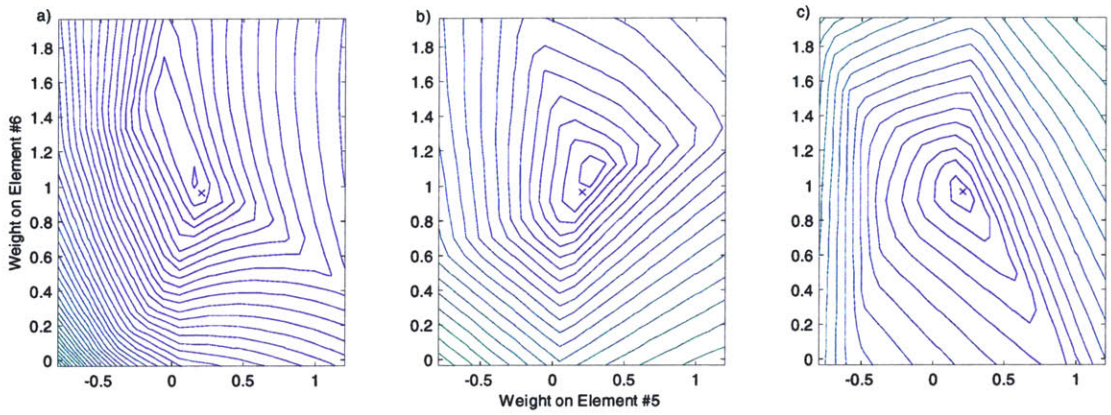

Figure 4.8: Variation of the weighting vectors indicates that there is a single optimum to the infinity-norm cost functions but that the simplex search stops near but not necessary at the optimum. The *logarithmic* cost is plotted as a function of perturbations of the weights about their calculated optimum, which is marked with an x. a) I.S.; b) 1A.; c) I.A.

the sensor and actuator array allows for significantly better performance than requiring the same weights on the two arrays. Including a phase penalty, which requires the weighted transfer function to have bounded phase, decreases the magnitude performance. The decrease in magnitude performance is most noted in the 2-norm cost function. Weights based upon the targeted mode shape yield dismal performance and are very difficult to implement due to their complex nature.

Weights based upon matrix inversion yield excellent performance, but not as good performance as the cost functions with different weights on the sensors and actuators. Additionally, the complex values in the weights from the matrix inversion necessitate a non-causal implementation. Causal implementations of the weights calculated through matrix inversion were attempted by using just the real value of the weights, by using just the complex value of the weights, by using the magnitude of the weights, by using a differentiator to create imaginary weights, and by using an integrator to create the imaginary weights. None of these *ad hoc* methods to provide a causal implementation of the matrix inversion weights yielded decent performance.

Many of the array weights are based upon the minimization of a cost function. A simplex search was performed to minimize the cost function. Chapter 2 demonstrated a proof that the 2-norm cost function has a single global minimum for the case of

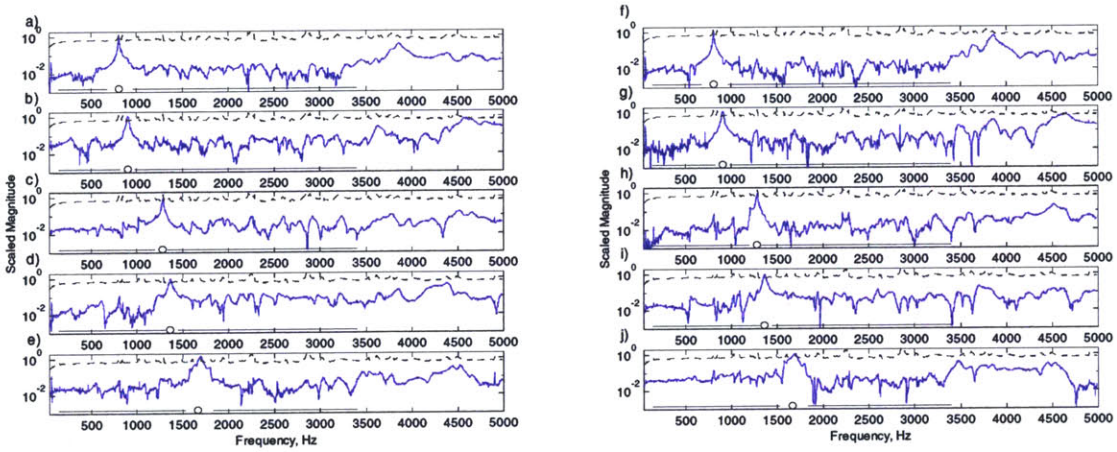

Figure 4.9: Modal isolation performance for different target frequencies. The targeted frequency is noted with a circle and the frequency region where the response is minimized is designated with a horizontal line. The maximum singular values of the transfer function are noted with a dotted line. The magnitudes of the curves are scaled so that the response at the targeted frequency has magnitude of one. a)-e) Weights determined with an infinity-norm cost function with different sensor and actuator weights, I.A. f)-j) Weights determined from a 2-norm cost function with the same weights on sensors and actuators, 2.S. Target frequencies are: a) and f) 812 Hz; b) and g) 915 Hz; c) and h) 1289 Hz; d) and i) 1365 Hz; e) and j) 1670 Hz.

noncomplex weights optimizing a system that is targeting a single mode of a plant that has noncomplex mode shapes. This very desirable behavior could not be proven for the infinity-norm cost function. Experimental evidence indicates that there is a single optimum to the infinity-norm cost function. Starting the optimizations with different initial conditions leads to the same weightings. Variation of the weights about the calculated optimum shows a single minimum, as illustrated in Figure 4.8. Figure 4.8 also shows that the simplex search stops near, but not necessarily at the optimum value. Setting tighter tolerances on the minimization routine would allow the final weights to be closer to the optimal array weights. Note that this figure is plotting the logarithmic cost as a function of variations in the weights and that the steps between the contours are the same in each of the plots.

For modes that were observable to the elements in the array, good modal isolation was obtained. Five targeted frequencies are shown in Figure 4.9. In this case, the separate sensor and actuator weights were calculated based upon the infinity-norm cost function,

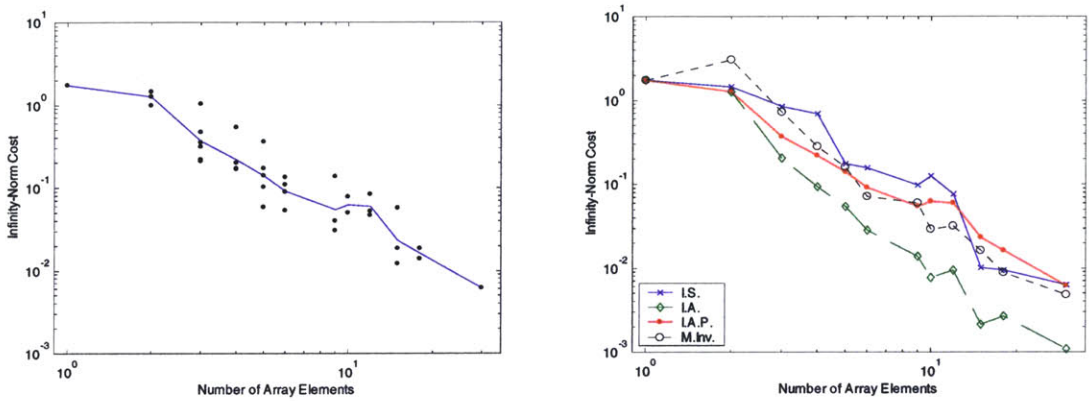

Figure 4.10: Variation of cost with the number of locations in the array for targeting the mode at 812 Hz. a) Infinity-norm cost for a asymmetric phase-penalized infinity-norm cost function, I.A.P., under different groupings and the geometric mean of the groupings b) Geometric mean of the infinity-norm cost for different optimization techniques.

I.A, and upon the 2-norm cost function, 2.S. For all of the targeted modes, the region of minimization was between 150 Hz and 3400 Hz except for a small region around the targeted frequency. The other weighting techniques showed performance similar to those in Figure 4.7. Modes that were not observable to the sensors and actuators were difficult to isolate. Unfortunately, many of the modes that are important to the performance were not observable in the actuator to sensor transfer function, as shown in Figure 4.5.

4.3 Sensitivity Analysis

The preceding section described the successful implementation of weighted arrays on a physical structure that possessed complicated boundary conditions. A successful implementation implies that this process of modal isolation is sufficiently insensitive to perturbations to allow experimental implementation. This section takes a more detailed investigation into the robustness of weighted arrays for modal isolation.

4.3.1 Sensitivity to Array size

The isolation performance is a strong function of the number of array elements. The thirty-transducer locations were grouped to create larger transducer elements. The optimal weights were computed for the smaller number of transducer elements and the

infinity-norm cost was evaluated on the reduced-size array. There are many permutations for grouping the array elements to form a reduced-size array. As a result, for each

Table 4.2: GROUPING SHAPE AND AVERAGE INFINITY-NORM PERFORMANCE.

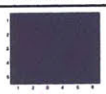 Array Size: 1 Cost: 1.73	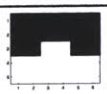 Array Size: 2 Cost: 1.43	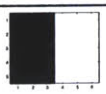 Array Size: 2 Cost: 1.51	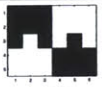 Array Size: 2 Cost: 1.65
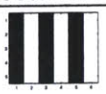 Array Size: 2 Cost: 1.17	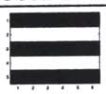 Array Size: 2 Cost: 1.48	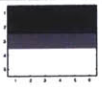 Array Size: 3 Cost: 0.39	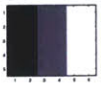 Array Size: 3 Cost: 0.49
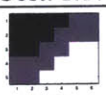 Array Size: 9 Cost: 0.37	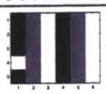 Array Size: 3 Cost: 0.69	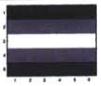 Array Size: 3 Cost: 0.49	 Array Size: 3 Cost: 1.17
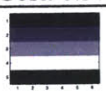 Array Size: 4 Cost: 0.30	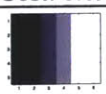 Array Size: 4 Cost: 0.53	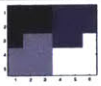 Array Size: 4 Cost: 0.91	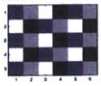 Array Size: 4 Cost: 0.51
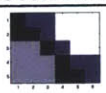 Array Size: 4 Cost: 0.47	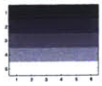 Array Size: 5 Cost: 0.182	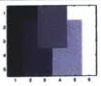 Array size: 5 Cost: 0.196	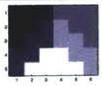 Array size: 5 Cost: 0.63
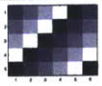 Array Size: 5 Cost: 0.129	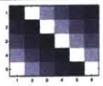 Array Size: 5 Cost: 0.096	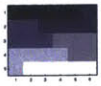 Array size: 6 Cost: 0.187	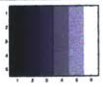 Array size: 6 Cost: 0.181
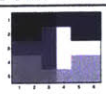 Array size: 6 Cost: 0.173	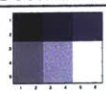 Array size: 6 Cost: 0.055	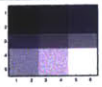 Array size: 9 Cost: 0.042	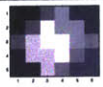 Array size: 9 Cost: 0.062
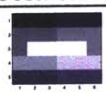 Array Size: 9 Cost: 0.27	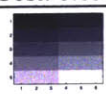 Array size: 10 Cost: 0.082	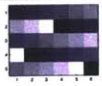 Array size: 10 Cost: 0.091	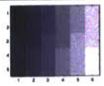 Array size: 12 Cost: 0.077
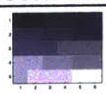 Array size: 12 Cost: 0.049	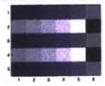 Array size: 12 Cost: 0.191	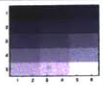 Array size: 15 Cost: 0.0195	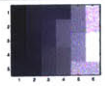 Array size: 15 Cost: 0.038
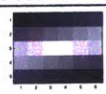 Array size: 15 Cost: 0.029	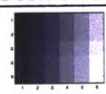 Array size: 18 Cost: 0.037	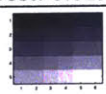 Array size: 18 Cost: 0.027	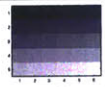 Array size: 30 Cost: 0.023

reduced-size array, multiple arrangements were considered. The subgroups were chosen to be simple geometric shapes. Each reduced-size array features the same area of sensor and actuator material. The groupings for the case of three transducer locations are shown in Table 4.2.

Increasing the number of array elements increases the modal isolation performance and decreases the infinity-norm cost. The cost decreases exponentially as the array size increases. Figure 4.10a shows the variation in the cost for the asymmetric phase-penalized infinity-norm cost function, I.A.P., as a function of the number of array elements. The cost for each grouping is shown as well as the geometric mean of the cost for each reduced-size array.

The spread in the cost due to different transducer locations is small when compared with the variation in the cost due to the increase in the number of array elements. Figure 4.10b shows the change in the cost as a function of the number of array elements for different methods of calculating the array weights. The cost seems to decrease exponentially with the number of array elements for each of the weighting techniques.

4.3.2 Sensitivity to Weighting and Modal Errors

The modal isolation process uses the experimentally measured mode shapes to calculate the array weights. This subsection seeks to elucidate the sensitivity of the modal isolation performance to variations in the array weights or to variations in the mode shapes. In Chapter 2, a perturbation analysis showed that the modal isolation performance is roughly equally dependent on variations in the mode shape as it is to variations in the array weights. This sensitivity analysis will add random perturbations to the array weights, which is much easier than experimentally adding perturbations to the mode shapes.

The modal isolation using discrete weighted arrays is relatively insensitive to weighting errors. Figure 4.11 illustrates the change in the infinity-norm cost based upon an error in the optimal weights. The weights were calculated with an asymmetric infinity-norm cost function, I.A.P., to isolate the mode at 812 Hz. In this sensitivity analysis, a

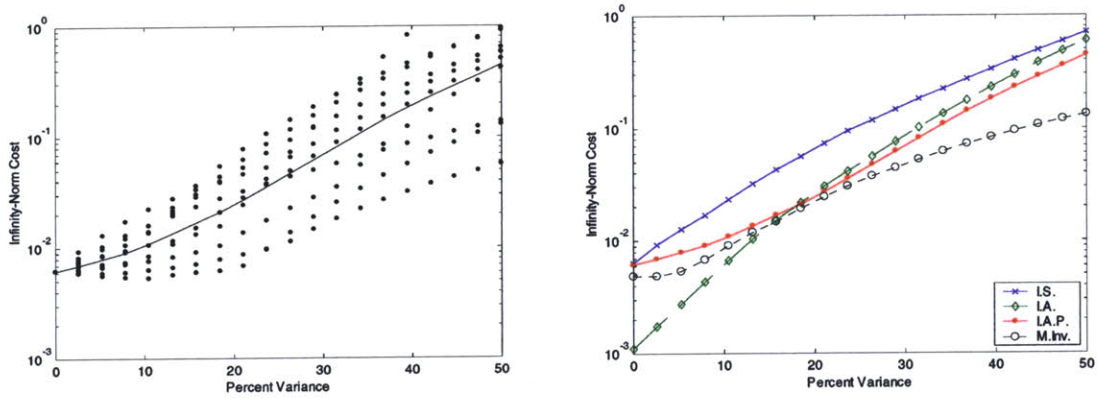

Figure 4.11: Sensitivity of the modal weighting to changes in the modal weight. Determine array weights to target mode at 812 Hz. Look a change in the infinity-norm cost as a function of a random additive error in the weights. a) Asymmetric infinity-norm phase-penalized weights, I.A.P., for each random number and its geometric mean; b) Geometric means of different weighting techniques.

normally distributed random number was added to each weight. Ten different random number seeds were run and the geometric mean was computed. The cost increases (and the performance decreases) as the variance of the random numbers increases. A 10% variance additive error in the weights means that 60% of the weights are off by 10% of the maximum weight. A 10% variance doubles the cost, but the targeted mode is still very effectively isolated. Figure 4.11 also illustrates the sensitivity of other isolation techniques. The symmetric and asymmetric infinity-norm cost functions, I.S. and I.A., exhibit slightly higher sensitivity to perturbations in the weights than the phase-weighted infinity-norm cost function or the matrix inversion, I.A.P. and M.Inv. The differing sensitivities between the weighting techniques is partially the result of differing degrees of optimization. As see in Figure 4.8, the I.A. technique is closer to its true optimum and, thus, it is not surprising that the performance degrades more quickly than the other weighting techniques.

Equally important is that a 10%-20% variation in the weights, or a 10%-20% variation in the mode shapes is the limit of the modal errors or weighting errors in order to obtain good modal isolation. Larger perturbations dramatically degrade the modal isolation performance. Most numerical modeling techniques do not estimate the mode

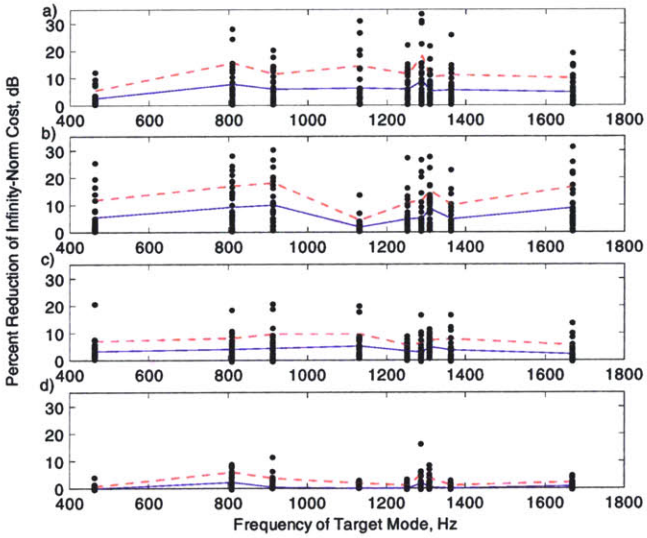

Figure 4.12: Sensitivity of the modal weighting to actuator and sensor failure. A single actuator and sensor location was given zero weight and the modal isolation performance was evaluated. Dots are evaluation at each of the 30 transducer location, solid line is geometric mean, and dashed line is the standard deviation. a) I.S., b) I.A., c) I.A.P., d) M.Inv.

shapes to this accuracy. Thus, determining the array weights based upon a predicted mode shape will lead to very poor modal isolation performance.

4.3.3 Sensitivity to Transducer Failure

The effect of sensor and actuator failure was also evaluated. In this experiment, the modal isolation performance was evaluated when the weights on an actuator and its collocated sensor were set to zero. As expected, the modal isolation performance suffers for sensor and actuator failure. In Figure 4.12, the infinity-norm performance reduction is evaluated for a single location failure for several target frequencies. The infinity-norm cost for failure at each of the 30 transducer locations is noted with a dot and the geometric means are connected. Transducer failure at most locations does not dramatically degrade the performance. However, transducer failure along the edges of the panel can result in substantial performance degradation by up to 30dB. Arrays with weights determined from matrix inversion are much less sensitive to transducer failure than arrays with weights determined from the infinity-norm cost function. The cost function with the

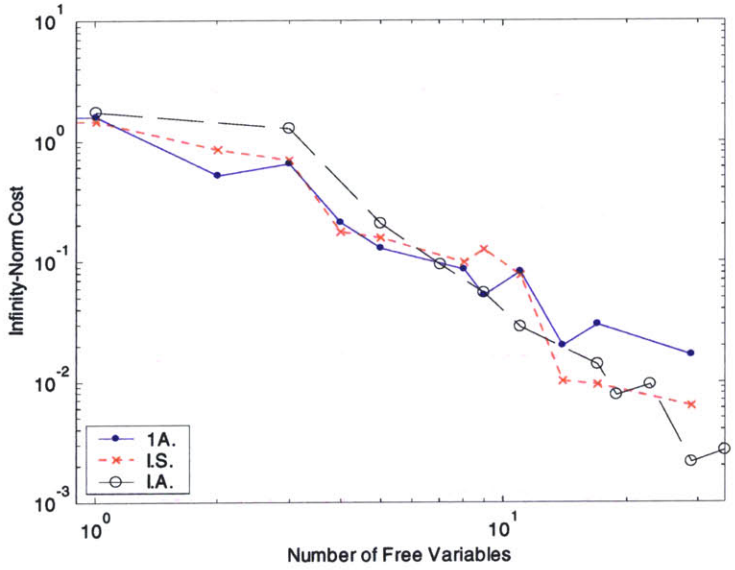

Figure 4.13: The ability to isolate an individual mode, such as the 812 Hz mode shown here, is most directly a function of the number of free variables in the optimization.

phase penalty showed less sensitivity to sensor failure than the arrays with weights determined by the other forms of the infinity-norm cost function.

4.4 Importance of Collocation

The preceding discussion focused upon the use of collocated arrays of sensors and actuators. A collocated array was designed under the assumption that physical collocation of the transducers would result in a symmetric positive-real transfer function matrix, which would ensure that the weighted transfer function would preserve phase. As shown in Figure 4.4, the resulting transfer function matrix is not symmetric and a phase penalty must be included in the cost function in order to preserve phase. Thus, the postulate about the advantage of using collocated transducers becomes circumspect.

The effect of collocation can be noted by grouping the 30 actuators to form a single actuator and transforming the MIMO system to a MISO system. Figure 4.13 illustrates the modal isolation performance as a function of the number of free variables in the optimization. For the cases of a single actuator, 1A., and symmetric weights on multiple actuators and sensors, I.S., the number of free variables is one less than the

number of array elements. For the case of asymmetric weights, I.A., the number of free variables is one less than twice the number of array elements. The number of free variables was varied by grouping the elements of the 30-element array in order to create super-elements, as described in section 4.3 and shown in Table 4.2.

The modal isolation performance is closely correlated with the number of free variables in the optimization. There is very little performance difference between optimizing 30 weights on 30 sensors, 1A., and optimizing 30 weights on 30 transducers, I.S.. Both 1A and I.S. feature the same number of unknowns in the optimization. Doubling the number of free variables by optimizing 60 weights on 30 sensors and 30 actuators, I.A., increases the performance but in an amount that is roughly equal to that which obtained by doubling the number of sensors and having a single actuator. In other words, the performance scales with the number of unknowns in the optimization process. The electronics needed to condition sensors is simpler, cheaper, and smaller than the electronics needed to power actuators, thus, implementation with large arrays of sensors may be easier than and offer the same performance as implementation with arrays of sensors and arrays of actuators. At some level, a single actuator would be unable to control higher modes, but that behavior was not observed on this test-bed.

4.5 Summary of Modal Isolation Experiments

A single panel test-bed was constructed to test the modal isolation performance of the different methods for determining of the weights of weighted arrays. The array weights were determined with 2-norm cost functions, infinity-norm cost functions, matrix inversion, and the targeted mode shape. The cost functions and matrix inversion offered good modal isolation while setting the weights to the targeted mode shape provided poor modal isolation. Matrix inversion yields complex weights, which cannot be implemented causally.

An experimental sensitivity analysis demonstrated that the modal isolation performance increases exponentially as the number of transducer elements increases. Another sensitivity analysis demonstrated that the modal isolation performance is

preserved to variations in the array weights, and, through a perturbation analysis, to moderate variations in the system's mode shapes. In general, transducer does not dramatically degrade the modal isolation performance, but the failure of particular transducers offers the potential to wreck the modal isolation performance.

CHAPTER 5

Vibration Control

In theory, there is no difference between theory and practice.
But, in practice, there is.
- Jan van de Snepscheut

The purpose of weighted arrays is to ease the control design. This chapter describes the active closed-loop broadband feedback control using weighted arrays. The arrays are used to isolate individual modes of vibration and a digital controller is used to minimize the vibrations. Control is performed on a curved panel test-bed and on the representative aircraft fuselage test-bed.

5.1 Numerical Control of a Fuselage Panel

A numerical model of the dynamics of a cylinder section was constructed in order to evaluate the vibration control performance for different control architectures and different sensor types. The three-dimensional Rayleigh-Ritz code for the fuselage was reduced to model a single panel on the fuselage. A reduced-order controller and a Linear-Quadratic-Gaussian (LQG) optimal controller were designed to minimize the vibration of the panel. Control with weighted arrays is compared to control with un-weighted arrays. Control is

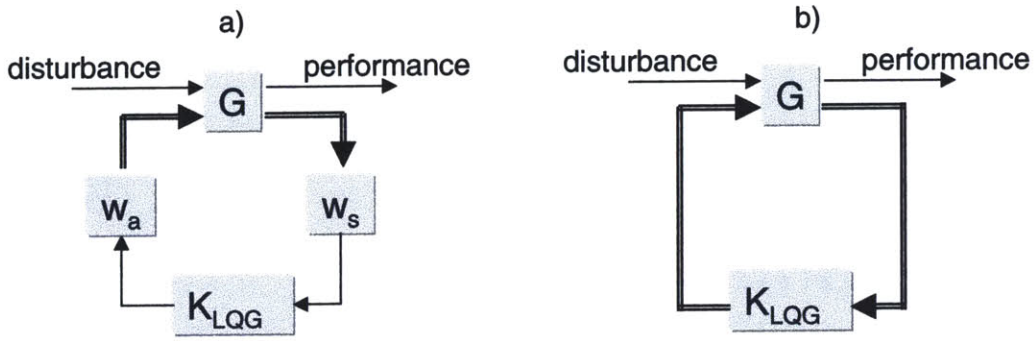

Figure 5.1: Signal path diagrams for numerical control simulations. A) Weighted control; b) Un-weighted control.

implemented for three different types of array weights (2-norm weights, infinity-norm weights, and no weights), for two types of placements (x placement and + placement), and for two types of sensors (distributed piezoelectric sensors and point velocity sensors). The nominal configuration features piezoelectric sensors in an x placement.

The signal path diagrams for the weighted and the un-weighted control are shown in Figure 5.1. In this figure, the disturbance reflects the contribution from a small off-centered piezoelectric patch and the performance is the off-centered velocity signal. The actuator and sensor weights, w_a and w_s, isolate individual modes of vibration. The plant, G, is configured with transducers in x and + placements and with piezoelectric and velocity sensors. The controller, K_{LQG}, is optimized for each configuration.

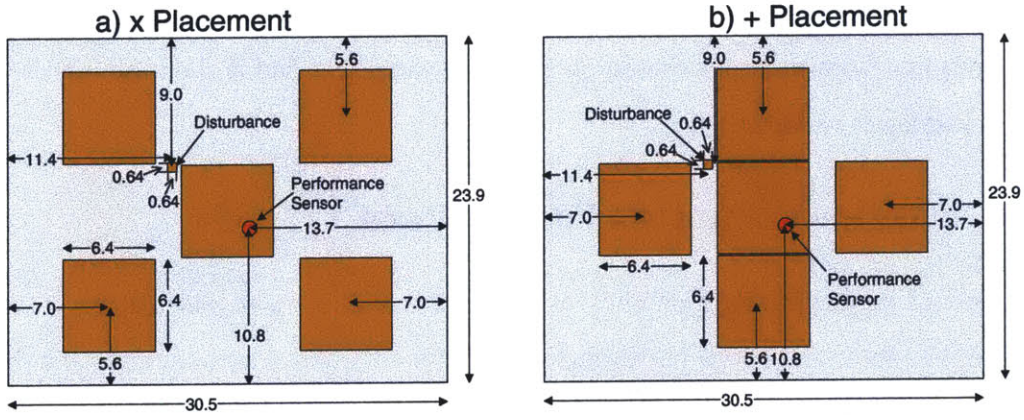

Figure 5.2: Geometry for the numerical simulations on the curved panels. All dimensions are in centimeters and are rounded to the nearest millimeter. The vertical direction is the circumferential direction and has a radius of curvature of 45.7 cm.

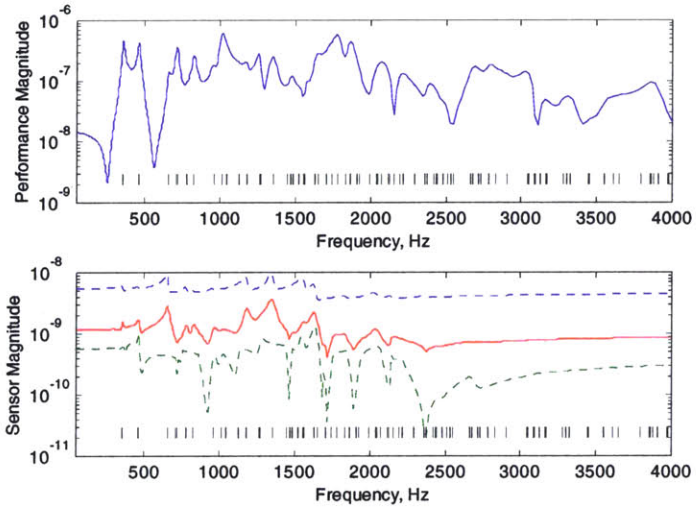

Figure 5.3: Panel transfer functions. The performance transfer function, top plot, features far modes than the actuator to sensor transfer function, bottom plot. The maximum, minimum, and geometric mean of the actuator to sensor transfer functions are plotted. The hashes denote the location of modal resonances.

5.1.1 Panel Model

The three-dimensional dynamics of a single panel of the fuselage test-bed was numerically modeled with a 600 state Rayleigh-Ritz model. The Rayleigh-Ritz model is a geometrically reduced version of the fuselage model that was presented in section Chapter 2. The 600 states in the model allows for 10 longitudinal modes and 10 circumferential modes in each of the three-directions of vibration. In other words, there

Table 5.1: SELECTED MODE SHAPES OF THE PANEL VIBRATIONS

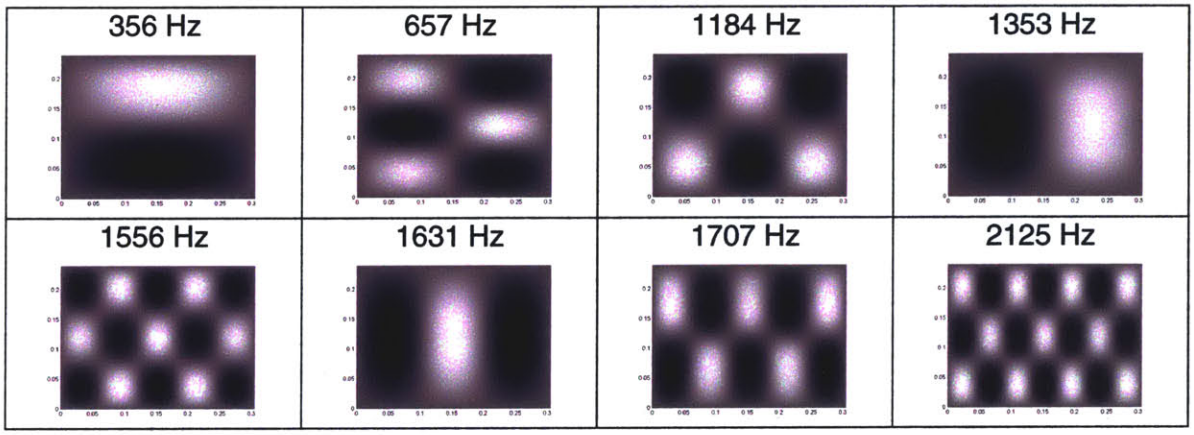

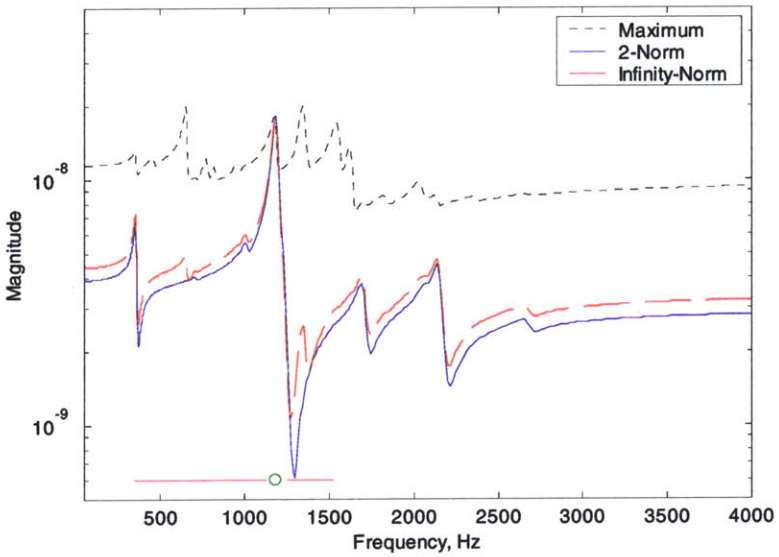

Figure 5.4: Modal isolation performance from an infinity-norm and a 2-norm cost functions. Dashed line is the maximum singular values of the transducer transfer functions. Horizontal line denotes modes that are minimized and the circle denotes the targeted mode. Symmetric weights.

are 100 mode shapes in each of the three directions of motion. Torsional springs along the edges were used to approximate the intermediate boundary conditions presented by the frame structure. The derivations of the equations of motion are presented in Appendix B and the MATLAB code has been included in Appendix C.

Two transducer patterns were considered: an "x" placement and a "+" placement. The geometry of both placements is shown in Figure 5.2. The x placement provides better controllability to more panel modes and, thus, is the proper placement for minimizing the structural vibration. The + placement provides peak observability of the modes with high structural-acoustic coupling, and, thus, is the proper placement to minimize the acoustic radiation. The location of a disturbance piezoelectric and the location of a performance velocity sensor are also shown in Figure 5.2. Piezoelectric strain actuators were modeled as inducing stretching forces and bending moments on the curved panel. Two sensor types were examined: piezoelectric strain sensors and velocity sensors. The piezoelectric sensors were exactly collocated with the piezoelectric actuators. The velocity sensors

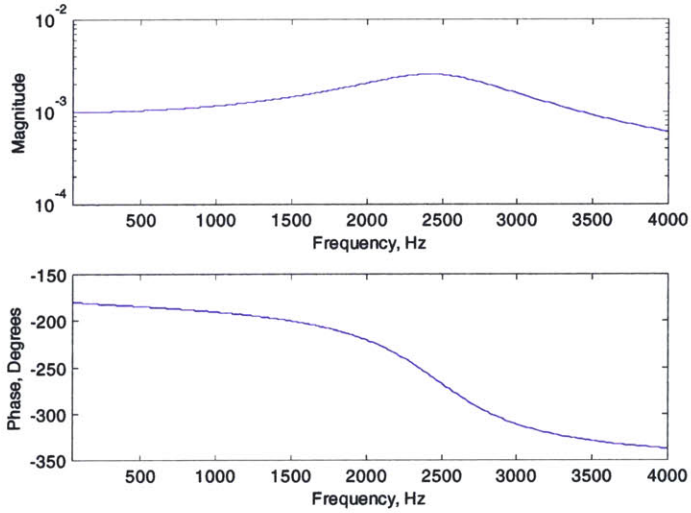

Figure 5.5: Transfer function of the reduced-order controller

were placed in the center of the piezoelectric actuators. The added mass and stiffness of the transducers were not included in the analysis.

The frequency response of the x placement is shown in Figure 5.3. The performance transfer function, from disturbance to performance, is modally dense through the bandwidth of interest. The actuator to sensor transfer function features a nearly flat transfer function beyond 2500 Hz and features coupling to far fewer modes than the performance transfer function. The locations of the structural modes is noted in the figure and shows that there are many modes that do not prominently feature in either the performance transfer function nor in the actuator to sensor transfer function. The mode shapes of some of the dominant modes are shown in Table 5.1.

Modal isolation was performed with a 2-norm cost function and with an infinity-norm cost function. The results for targeting the 3-2 mode at 1184 Hz for a piezoelectric-piezoelectric transducer array with an x placement is shown in Figure 5.4. The targeted mode is strongly isolated and the unwanted modes are reduced by roughly 10 dB. More importantly, the modal filtering reduces the number of modes that are expressed in the system transfer function. The weighted transfer function from the 2-norm cost function features fewer modes than the weighted transfer function from the infinity-norm cost function.

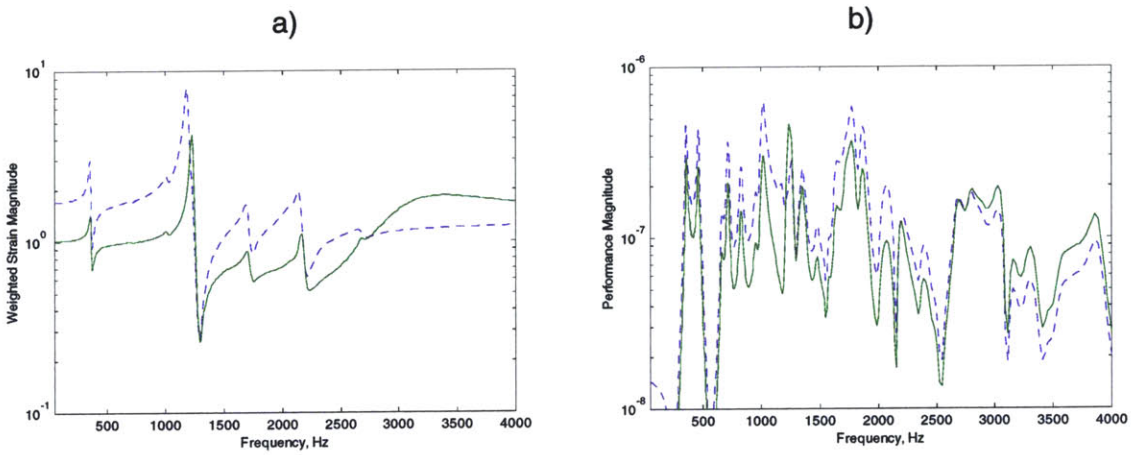

Figure 5.6: Open-loop (dotted line) and closed-loop (solid line) transfer function for reduced-order SISO control of a weighted array of piezoelectric sensors in an x placement. A) 5.0 dB reduction in the weighted sensor strain. B) 4.2 dB reduction in the performance transfer function.

5.1.2 Reduced-Order Control

This simulation compares the vibration performance for weighted and un-weighted reduced-order controllers. The performance transfer function is defined as the transfer function from the off-centered piezoelectric disturbance to an off-centered velocity sensor. A single mode control algorithm was used to minimize the RMS response of the performance transfer function. A SISO controller using a weighted transducer array is compared to MIMO control using the same control algorithm with different gains on an un-weighted transducer array.

A proportional controller is the simplest idealized controller for a collocated transfer function. Dynamics need to be added to the proportional controller in order to achieve roll-off. Thus, one of the simplest stable controllers is a single mode controller of the form

$$K(s) = \frac{g\omega_n^2}{s^2 + 2\zeta w_n s + \omega_n^2} \tag{5.1}$$

where g sets the control gain, ω_n sets the roll-off frequency, and ζ determines the damping at the controller mode. The roll-off frequency should be set beyond the bandwidth of interest but before the advent of instrumentation dynamics. The damping ratio should be

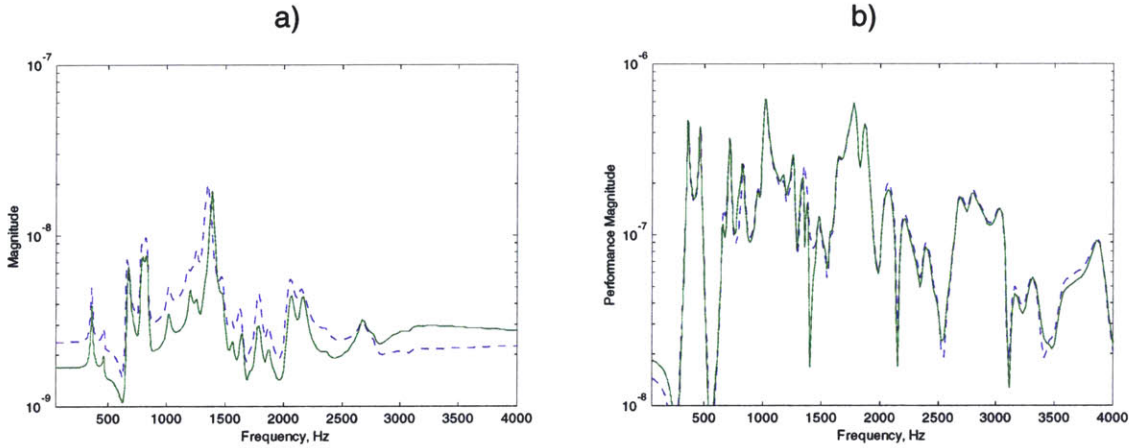

Figure 5.7: Open-loop (dotted line) and closed-loop (solid line) transfer function for the reduced-order control of an un-weighted array of piezoelectric sensors arranged in an x. A) 3.1 dB reduction in the RMS sensor strain. B) 0.1 dB reduction in the performance transfer function.

small enough to allow for a quick transition to roll-off yet large enough to minimize excitation at the roll-off frequency. For these numerical simulations, the roll-off frequency was set to 2500 Hz and the damping ratio to 0.2. A transfer function of the controller is shown in Figure 5.5.

The open-loop and closed-loop frequency response for the weighted array system is shown in Figure 5.6. Weighted transfer function features bounded phase, high gains can be implemented. The weighting in the transfer function minimizes the higher frequency modes, which allows for gain stabilization during the region of roll-off where the system is not phase stabilized. Figure 5.6 depicts a 4.2 dB reduction in the RMS performance transfer function evaluated between 50 Hz and 2500 Hz. Higher gains can stably lead to higher performance in the targeted frequency range. Reductions in the RMS performance of up to 25 dB can be obtained in the targeted frequency range at the expense of much larger vibrations at higher frequencies. The closed-loop design presented in Figure 5.6 presents a balance between performance in the targeted frequency range and performance across all frequencies. Equivalent closed-loop performance was obtain by using array weights determined with a 2-norm cost function as was obtain by using array weights determined with an infinity-norm cost function.

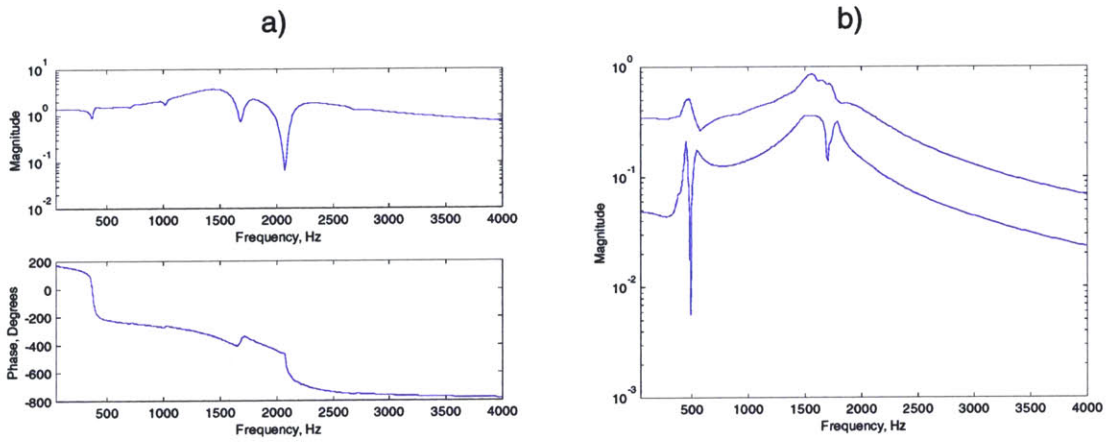

Figure 5.8: Controller for the weighted array. A) Weighted array, weights from 2-norm cost function; b) Maximum and minimum singular values from un-weighted arrays.

The reduced-order controller was unable to obtain as much performance with un-weighted arrays as it was able to obtain with the weighted array. As shown in Figure 5.7, local control with the reduced-order controller presented in equation (5.1) yields limited improvement in the performance transfer function. The sensor response is improved, but the performance transfer function is not. The control performance was limited by the interactions between the local loops closed on each actuator-sensor pair. These interactions limited the control gains and, thus, limited the performance.

5.1.3 LQG Optimal Control

This simulation compares the vibration performance for weighted and un-weighted LQG controllers using piezoelectric and velocity sensors. The performance transfer function is defined as the transfer function from the off-centered piezoelectric disturbance to an off-centered velocity sensor. LQG optimal control was used to minimize the performance transfer function. SISO control using the weighted transducer array is compared to MIMO control using the un-weighted transducer array.

5.1.3.1 LQG Control Algorithm

The controller is based upon a numerical representation of the actuator to sensor transfer functions. This control model is a reduced version of the structural model that was

described in Chapter 2 and elaborated upon in Appendix B. The control model was formed by performing an experimental identification of the transfer function calculated by the structural model. The experimental identification of the control model allows for these numerical results to more closely approximate experimental results.

Experimental identification was performed with a Frequency domain Observability Range Space Extraction (FORSE) routine [Liu, Jacques, and Miller, 1996]. The FORSE routine uses frequency domain transfer function data to estimate the Markov parameters and form the numerical model for designing the controller. The FORSE algorithm is part of the DynaMod software package from Midé Technology Corporation [Midé Technology Corporation, 1999]. The transfer functions were fit with 20 states. The models were tuned with a log-least squares weighting on the additive error. The resulting state-space model formed the basis of the Kalman estimator. The same size control model was used in each of the closed-loop configurations.

The process of forming a Kalman estimator and combining the estimator with a Linear Quadratic Regulator has been elucidated in enumerable locations (see, for example, Preumont, 1997) and shall not be explained here. Control energy is focused at the targeted mode by loop shaping. The process of implanting loop shaping through the noise model is taken directly from Preumont, 1997. Loop shaping was implemented by assuming that the plant noise, $\mathbf{n}$, has a dip at the targeted frequency, instead of being white noise. Thus, we assume that $\mathbf{n}$ is the output of a filter excited by a white noise at the input. If the control model is

$$\begin{Bmatrix} \dot{\mathbf{x}} \\ \mathbf{y} \end{Bmatrix} = \begin{bmatrix} \mathbf{A} & \mathbf{B} \\ \mathbf{C} & \mathbf{D} \end{bmatrix} \begin{Bmatrix} \mathbf{x} \\ \mathbf{u} \end{Bmatrix} + \begin{bmatrix} \mathbf{En} \\ \mathbf{v} \end{bmatrix} \tag{5.2}$$

and the plant noise can be described as

$$\begin{Bmatrix} \dot{\mathbf{z}} \\ \mathbf{n} \end{Bmatrix} = \begin{bmatrix} \mathbf{A}_n & \mathbf{B}_n \\ \mathbf{C}_n & \mathbf{0} \end{bmatrix} \begin{Bmatrix} \mathbf{z} \\ \mathbf{n}^* \end{Bmatrix} \tag{5.3}$$

where $\mathbf{A}_n$ is stable and $\mathbf{n}^*$ is a white noise. The two sets of equations can be coupled together to form the augmented system

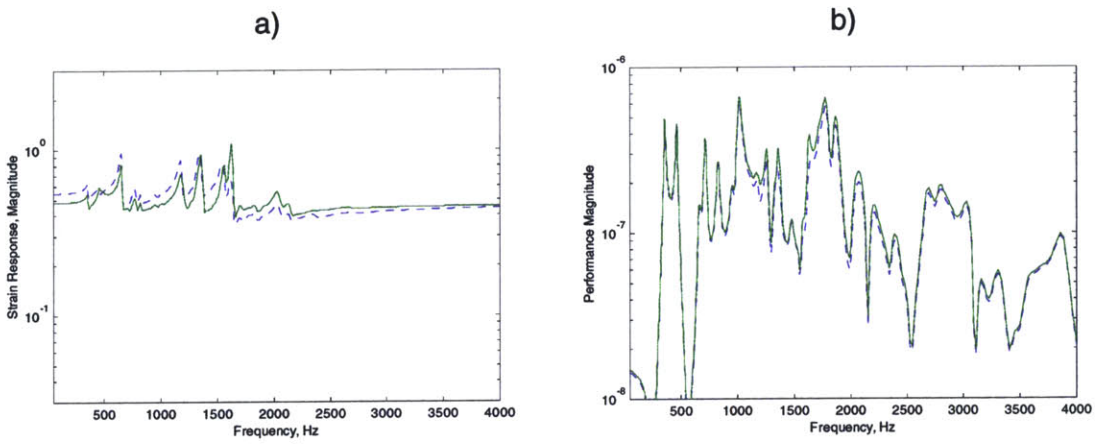

Figure 5.9: Open-loop (dotted line) and closed-loop (solid line) transfer function for un-weighted LQG control of piezoelectric sensors in an x placement. A) 0.3 dB reduction in the RMS sensor strain. B) 0.1 dB *increase* in the performance transfer function.

$$\begin{Bmatrix} \dot{\mathbf{x}} \\ \dot{\mathbf{z}} \end{Bmatrix} = \begin{bmatrix} \mathbf{A} & \mathbf{EC}_n \\ \mathbf{0} & \mathbf{A}_n \end{bmatrix} \begin{Bmatrix} \mathbf{x} \\ \mathbf{z} \end{Bmatrix} + \begin{bmatrix} \mathbf{B} \\ \mathbf{0} \end{bmatrix} \mathbf{u} + \begin{bmatrix} \mathbf{0} \\ \mathbf{B}_n \end{bmatrix} \mathbf{n}^* \qquad (5.4)$$
$$\mathbf{y} = \begin{bmatrix} \mathbf{C} & \mathbf{0} \end{bmatrix} \begin{Bmatrix} \mathbf{x} \\ \mathbf{z} \end{Bmatrix} + \mathbf{Du} + \mathbf{v}$$

Since $\mathbf{n}^*$ and $\mathbf{v}$ are white noise processes, the augmented system fits into the standard LQG framework. The LQG controller is designed for the augmented system described in equation (5.4). In contrast to frequency-shaped cost functionals, the poles of the plant noise model can be changed by the compensator. In the experiments, the plant noise model featured a zero at the target frequency with a damping of 10%.

Examples of the transfer function of the LQG controller are shown in Figure 5.8. The magnitude and phase of the SISO controller for the weighted array of piezoelectric sensors and actuators in an x placement are shown. The maximum and minimum singular values for the MIMO controller for same the un-weighted array are also shown. The excitation of the controller was increased by adjusting the noise estimates until either peak performance was obtained for the sensor signals or until instability was reached, as estimated by a MIMO Nyquist analysis.

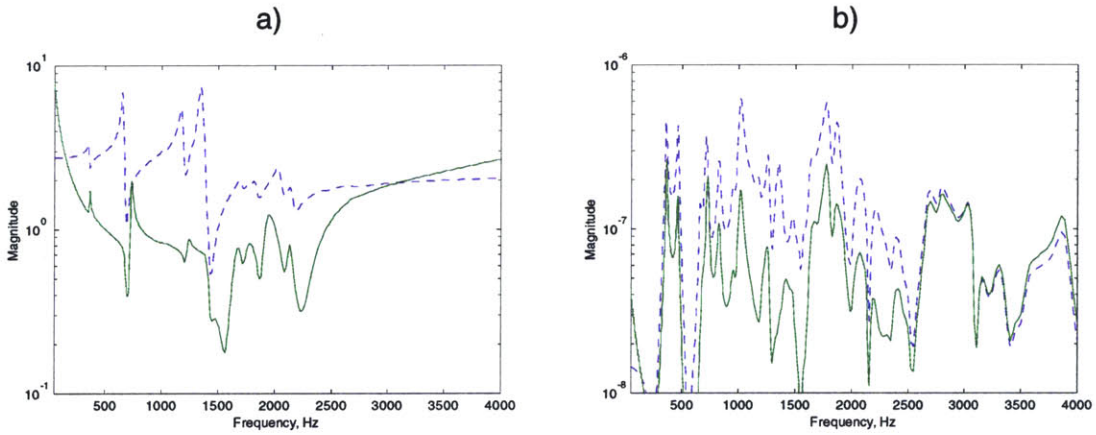

Figure 5.10: Open-loop (dotted line) and closed-loop (solid line) transfer function for SISO weighted LQG control of piezoelectric sensors in an x placement. Array weights calculated with a 2-norm cost function to target mode at 1184 Hz. A) 7.8 dB reduction in the RMS sensor strain. B) 9.0 dB reduction in the performance transfer function.

5.1.3.2 LQG Control Results

The frequency-weighted LQG feedback control was designed and implemented for three types of array weights (2-norm weights, infinity-norm weights, and no weights), for two types of placements (placement in an x and placement in a +), and for two types of sensors (piezoelectric sensors and velocity sensors). The nominal configuration features piezoelectric sensors in an x placement.

The closed-loop performance of the un-weighted array is shown in Figure 5.9. The 20 states in the control model proved insufficient to describe the 5x5 transfer function matrix. Instabilities limited the control gains and the closed-loop performances. Although a small decrease in the sensor response was achieved, the performance transfer function saw an increase in its RMS amplitude. Figure 5.9 illustrates the performance for an array of piezoelectric sensors in an x placement, but the closed-loop transfer function looks similar for the other configurations of sensors and of transducer placements. The closed-loop performance of the other configurations are tabulated in Table 5.3.

Weighting the arrays to isolate individual modes of vibration reduces the number of modes that are featured in the actuator to sensor transfer function. As a result, the weighted actuator to weighted sensor transfer function can be more accurately described

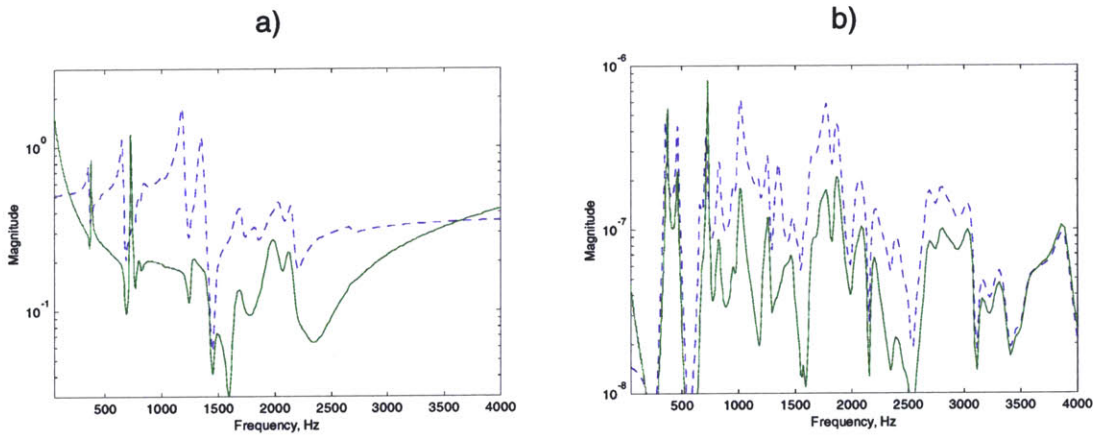

Figure 5.11: Open-loop (dotted line) and closed-loop (solid line) transfer function for SISO weighted LQG control of piezoelectric sensors in an x placement. Array weights determined with an infinity-norm cost function. A) 6.6 dB reduction in the RMS sensor strain. B) 7.6 dB reduction in the performance transfer function.

with the 20 state control model. The transfer functions for piezoelectric sensors arranged in an x and weighted with a 2-norm cost function are shown in Figure 5.10. Substantial reductions in the weighted sensor signal and in the performance are obtained. The broad region of excellent performance is correlated with the accuracy of the control model, which allows high gains in the controller. Performance is limited by a low-frequency instability. The effect of loop shaping is visible in the excellent closed-loop performance at the targeted frequency but limited performance at much higher and much lower frequencies.

Array weights determined with an infinity-norm cost function feature more modes than those determined with a 2-norm cost function. As a result, control with an infinity-norm weighted transfer function tends to be more substantially limited by the unmodeled dynamics. The open-loop and closed-loop transfer functions for piezoelectric sensors placed in an x and weighted with an infinity-norm cost function are presented in Figure 5.11. While substantial performance is obtained, the closed-loop performance is not as good as the performance obtained with a 2-norm weighting on the transducers. Performance is limited by instability in a mode at 707 Hz. As shown in Table 5.3, control with weights determined from a 2-norm cost function consistently outperforms control with weights determined from an infinity-norm cost function.

Table 5.2: Peak RMS REDUCTION IN THE PERFORMANCE TRANSFER FUNCTION EVALUATED USING LQG CONTROL OVER THE REGION FROM 50 HZ TO 2500 HZ.

	Weighted Array 2-Norm	Weighted Array Infinity-norm	Un-weighted Array
Piezoelectric sensors x placement	9.0 dB	7.6 dB	-0.1 dB
Piezoelectric sensors + placement	12.7 dB	4.4 dB	-0.1 dB
Velocity sensors x placement	2.6 dB	1.6 dB	-0.1 dB
Velocity sensors + placement	3.3 dB	3.3 dB	-0.0 dB

The peak reduction in the performance transfer function is obtained with piezoelectric sensors arranged in a + and weighted with a 2-norm cost function. The open-loop and closed-loop transfer functions are illustrated in Figure 5.12. The exceptional performance for this configuration arises from the nearly perfect control model. The high correlation between the control model and the physical model allows for very high gains on the controller. The somewhat lower closed-loop performance exhibited by the infinity-norm weighting is more typical of the performance that is

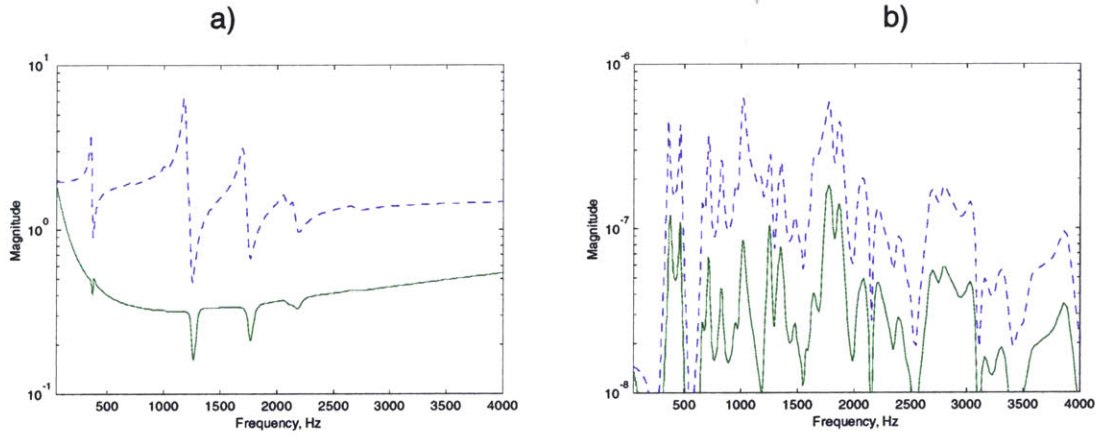

Figure 5.12: Open-loop (dotted line) and closed-loop (solid line) transfer function for SISO weighted LQG control of piezoelectric sensors in an + placement. Array weights determined with a 2-norm cost function. A) 12.6 dB reduction in the RMS sensor strain. B) 12.7 dB reduction in the performance transfer function.

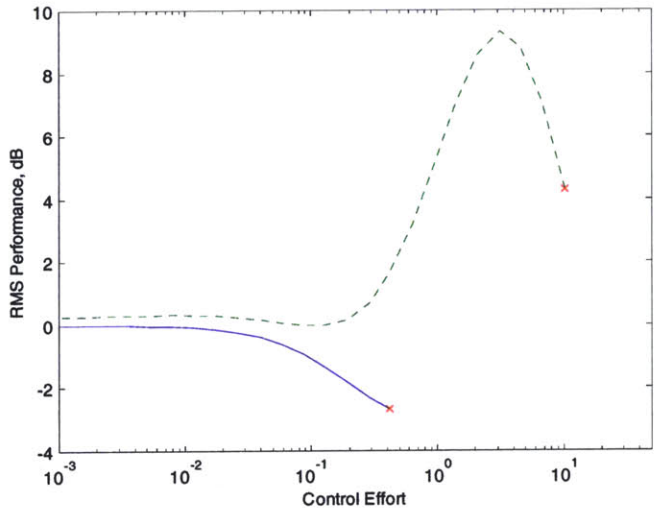

Figure 5.13: RMS reduction in the performance transfer function as a function of the control effort. The control with weighted transducers, dotted line, allows the stable application of greater control effort than the control with un-weighted transducers, solid line. The x denotes where the system went unstable.

obtained for the + placements.

Control with velocity sensors was also considered. Piezoelectric sensors perform area averaging, as described in Chapter 1, and can miss many of the dynamics of the performance transfer function, as shown in Figure 5.3. Velocity sensors were expected to provide better control performance than piezoelectric sensors because the performance transfer function uses velocity sensors. As shown in Table 5.3, control with velocity sensors yielded significantly worse closed-loop performance than control with piezoelectric sensors. The increased number of modes in the velocity transfer function could not be successfully captured with the 20 state control model, which limited the control gains and the closed-loop performance.

The closed-loop performance was calculated as a function of the control effort. While this thesis is most interested in the peak possible performance, the performance versus control effort provides a more complete means to compare the performance of the different controllers. Figure 5.13 illustrates the RMS reduction in the performance transfer function as a function of the control effort. This plot shows the performance of a 2-norm weighted array of piezoelectric sensors in an x placement and the performance of

an un-weighted array of piezoelectric sensors in an x placement. The weighted array consistently provides better performance than the un-weighted array. More importantly, the weighted array allows for the stable application of greater control effort, which allows for much larger performance.

There is a slight dip in the weighted performance around a control effort of 0.1. This dip corresponds to a controller-induced modal restructuring. The weighted controller is seeking to minimize the weighted signal response. At this level of control effort, the controller is shifting the modal structure to minimize the weighted signal instead of minimizing the structural vibration. As a result, while the weighted signal is reduced, the performance transfer function is not reduced. This facet illuminates one of the problems presented by the use of weighted arrays for control. By using weighted arrays to minimize the vibrations, the controller has the potential to restructure the modes so that the summation of the weighted sensors is reduced while the magnitude of each sensor may not be reduced.

5.2 Experimental Curved Panels Control

Prior to implementation on the full fuselage test-bed, experimental active broadband feedback control was performed on a smaller cylinder section. The cylinder section was designed to represent a three-panel section of the fuselage test-bed. The surrounding panels sought to create the cross-panel coupling that was expected to be found on the fuselage test-bed. Sensors and actuators were placed on the central panel in an effort to control the dynamics of the central panel. The goal of this experiment was to minimize the acoustic emission from the panel, as measured with a microphone, due to a piezoceramic disturbance.

The wooden test-bed is illustrated and the transducer locations are sketched in Figure 5.14. In this setup, there is an array of 8 PVDF sensors arranged in a plus-shape and a single PZT actuator located near the center. A PZT disturbance source was located near the control actuator. The transducers were glued to the 0.762 mm (30 mil) aluminum panel with EpoTek 301 2-part epoxy. The aluminum panel was attached to wooden frame

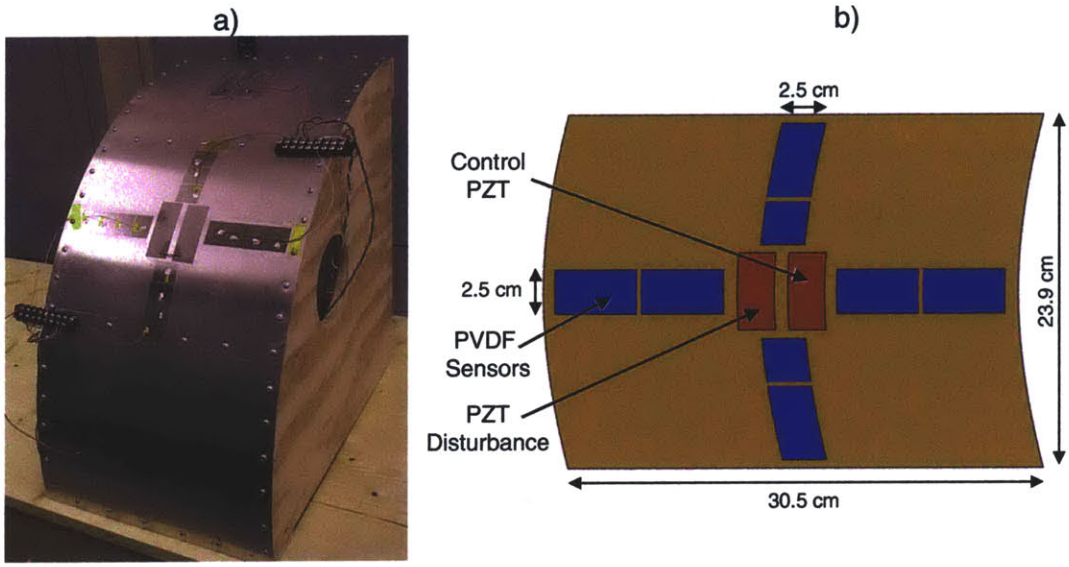

Figure 5.14: a) Picture of the three-panel experimental setup. Control is performed on the central panel section. b) Dimensions of the central panel.

with wood screws. Electrical connections were made by gluing wires to the piezoelectric transducers with a conductive epoxy. The PVDF sensor signals were passed through a unity-gain voltage follower in order to buffer the low charge producing transducer. The PZT actuator signals were passed through Audiopro amplifiers. Array weights and feedback control algorithms were implemented with a dSpace digital controller.

The original purpose of this cylinder section was to test methods for bonding the piezoceramics to the curved fuselage. Applying bond pressure through vacuum bagging proved successful and the relative stiffness of the piezoceramic did not significantly alter the curvature of the panel. The curvature of the panels induced a 100 micro strain net tension along the top surface of the piezoceramic, which is well below the 1000 micro strain tensile load that a piezoceramic can experience.

The first four modes of vibration were isolated with the 8-element sensor array and with a grouped 4-element sensor array. In both cases, an infinity-norm cost function. No extra phase penalties were used. The infinity-norm cost function seeks to maximize the response at the targeted mode and to minimize the weighted transfer function response between 150 Hz and 1500 Hz. As evident in Figure 5.16 the modal isolation on the lower modes was very effective. A consistent 20 dB reduction was obtained. Modal

isolation was also performed for a 4-element sensor array. The 4-element array was formed by adding the strain signal of each pair of elements that radiate from the central actuation and disturbance piezoceramics.

Sequential loop closure with a series of reduced-order controllers was performed on the curved panels test-bed in order to minimize the vibration and noise radiation of the first four modes of vibration. The sensor signals were digitized in the dSpace digital control computer and the previously calculated weights were applied to form four input channels that represent the first four modes of vibration. A separate reduced-order controller was designed for each modal channel.

A reduced-order feedback control algorithm was chosen as the control algorithm because it requires limited *a priori* knowledge of the system; the numerical model that is used to design the controller contains a single mode. The control loop is of the form

$$K(s) = \frac{gs^2}{s^2 + 2\zeta_c\omega_c s + \omega_c{}^2} \frac{\omega_n{}^2}{s^2 + 2\zeta_n\omega_n s + \omega_n{}^2} \tag{5.5}$$

where ω_c is the low frequency corner, ζ_c is the damping ratio at the low frequency corner, ω_n is the target frequency, ζ_n is the damping ratio at the target frequency, g is the gain, and $s = \omega\sqrt{-1}$. The low frequency corner is set at 75 Hz with a damping ratio of 0.5, which creates a high-pass filter and helps to minimize possible low frequency

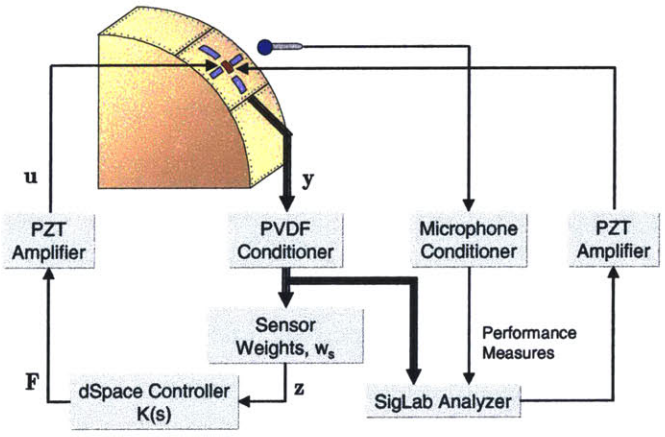

Figure 5.15: Wiring diagram for the curved panels feedback control experiments. Digital control is performed through a dSpace controller operating at 6.7 kHz. Performance is measured with a SigLab analyzer.

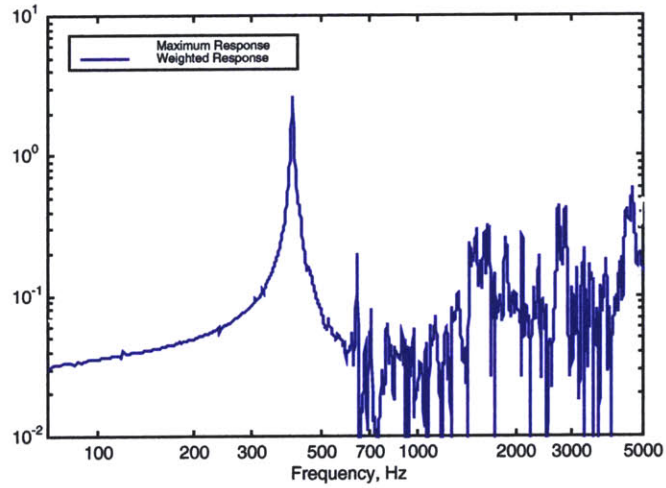

Figure 5.16: Modal isolation of the curved panels test-bed. The first mode of vibration is targeted for isolation with the 8-element sensor array.

instabilities. The target frequency is 10 Hz higher than the mode that was targeted and has a damping ratio of 0.05. The low damping ratio at the target frequency helps to focus the controller energy at the targeted mode. The controller in equation (5.5) is similar in form to a positive position feedback controller. The controller was converted to the digital time domain using the Tustin transform and the control loop was closed at 6.7 kHz with a sampling frequency also of 6.7 kHz.

The open-loop and closed-loop transfer functions are shown in Figure 5.17. Figure 5.17a shows the change in the panel strain measured by the sensors while Figure 5.17b shows the change in the acoustic emission measured by a microphone. Better control performance is obtained at the lower modes where better modal isolation is obtained. The slight increase in disturbance at low frequency reflects a system softening that is typical of a positive position feedback controller. The controller is unable to diminish the acoustic radiation from the mode near 700 Hz. This mode is not observable by the sensor array and is probably located on one of the neighboring panels. Thus, control of the central panel does not diminish the acoustic radiation from this mode.

The performance difference between the plot in Figure 5.17a and the plot in Figure 5.17b illustrates one of the problems of using weighted arrays of strain-based transducers for feedback control. Using strain-based transducers, such as PZT and PVDF,

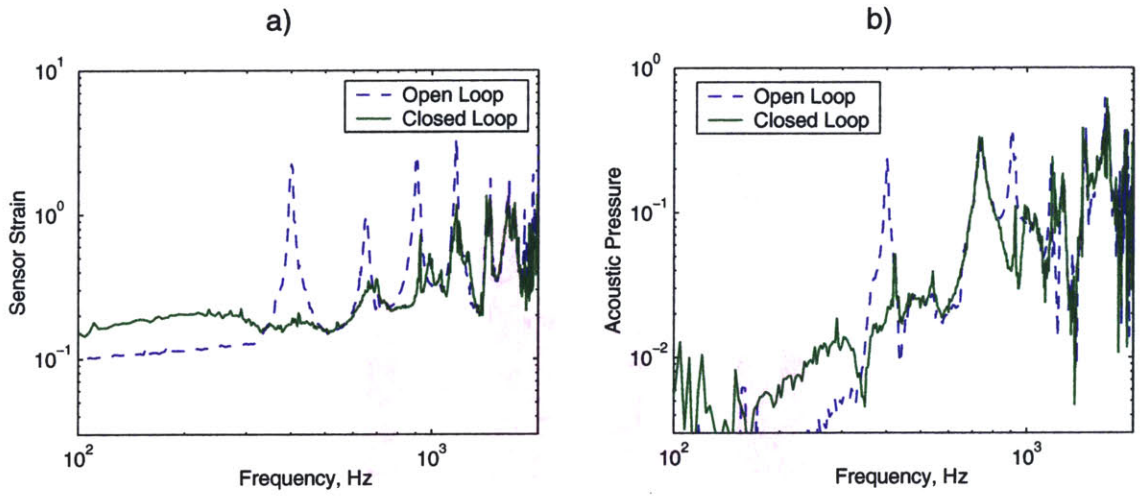

Figure 5.17: Open-loop and closed-loop performance for the 8-element array on the central panel of the curved panels test-bed. a) Magnitude measured by the PVDF sensors; b) Magnitude measured by a microphone.

means that the controller is working to reduce the strain of the structure. When the goal of the controller is vibration control, then strain reduction is a good performance metric. However, when the goal of the controller is acoustic control, then strain reduction often does not directly match the goal. Instead, arrays of accelerometers or microphones might serve as a better sensor.

The difference in control performance of performance sensors, such as microphone, versus the control performance of convenient sensors, such as PVDF, has long been an important issue for control design. All controllers seek to minimize the measured sensor inputs, regardless of whether this is the variable that the designer wishes to be minimized. However, this distinction becomes more important in the case of weighted arrays. In the case of weighted arrays, the controller is seeking to minimize the response of a weighted summation of sensors. The controller will tend to rearrange the mode shapes so that the weighted sensor sum is minimized rather than minimizing the modal amplitudes. As a result, it is very important to chose sensors that closely approximate the performance metric.

The closed-loop performance is a function of the number of elements in the sensor array. Reducing the size of the sensor array reduces the modal isolation

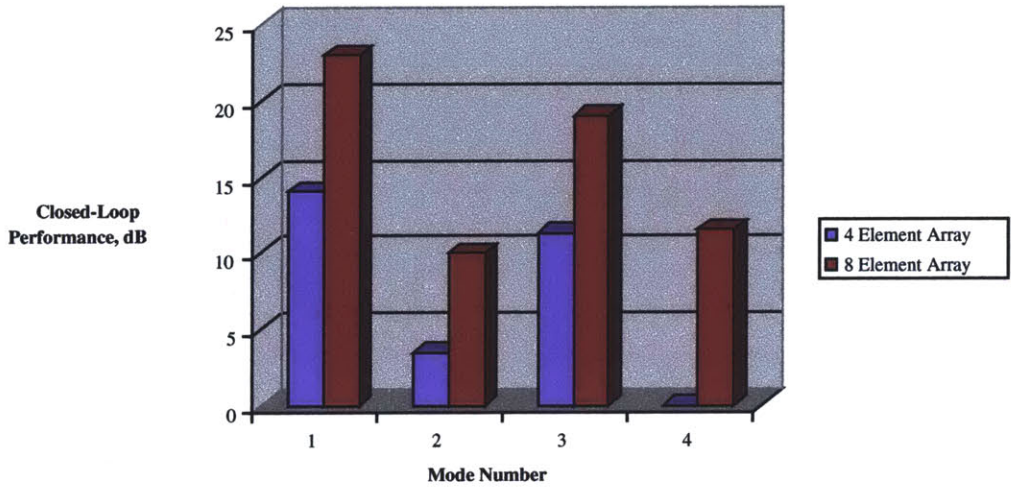

Figure 5.18: Sensor closed-loop performance decreases as the number of array elements decreases.

performance of the sensors. In Chapter 4, the modal isolation performance was shown to change exponentially with the size of the arrays. Figure 5.18 shows that the closed-loop performance also decreases substantially as the number of elements in the sensor array decreases. In fact, no performance was obtained at the 4^{th} structural mode.

5.3 Fuselage Experimental Setup

Weighted arrays are motivated by the need to control the vibration of aircraft. As a result, validation of the arrays for modal isolation and control is conducted on a hybrid-scaled model of an aircraft fuselage. As shown in Figure 5.20, the fuselage is composed of a 0.762 mm (30 mil) aluminum skin riveted over a frame of six C-section ribs and twelve T-section stringers. The cylindrical fuselage has a diameter of 91.44 cm (36 in) and a length of 152.4 cm (60 in). The frame outlines sixty panels of dimension 23.94 cm by 30.48 cm on the skin. End-caps are 30° spherical sections, which were designed to minimize the structural and acoustical coupling to the cylinder section. Details of the fuselage test-bed and its design process have been elaborated in Chapter 2.

Piezoceramic actuators and piezopolymer sensors were chosen due to their high energy densities, broad frequency bandwidth, and efficient coupling with structural vibrations. Additionally, most piezoelectrics are distributed transducers and perform spatial filtering, which tends to minimize their coupling with high frequency modes. As a result, piezoelectrics are a natural choice for transducer material for vibration control on aircraft. Wafers of PZT-5A measuring 6.35cm x 6.35cm x 0.0254cm (2.5"x2.5"x10 mil) from Morgan Matroc Electro Ceramics were chosen as the actuator material. Sheets of unelectroded 52μm PVDF from Measurement Specialties, Inc. were chosen as the sensor material. Each panel-sized array of transducers is encapsulated between two layers of flexible electrode, which served to align and to connect the arrays of transducer materials. A sketch of the assembly is shown in Figure 5.19.

The size of the transducers was chosen to ease the control design, since the size of the transducers influences the amount of spatial filtering that will occur. Spatial filtering initiates when the transducer spans multiple structural wavelengths. Thus, larger sized transducers will tend to have reduced coupling to higher frequency modes. The size of the transducers on the fuselage test-bed was chosen so that there would be good modal observability up to 2 kHz.

Three active panels were instrumented on the fuselage test-bed with the help of Cagri Savran, Daniel Kwon, and Christian Garcia. The wiring diagram is noted in Figure

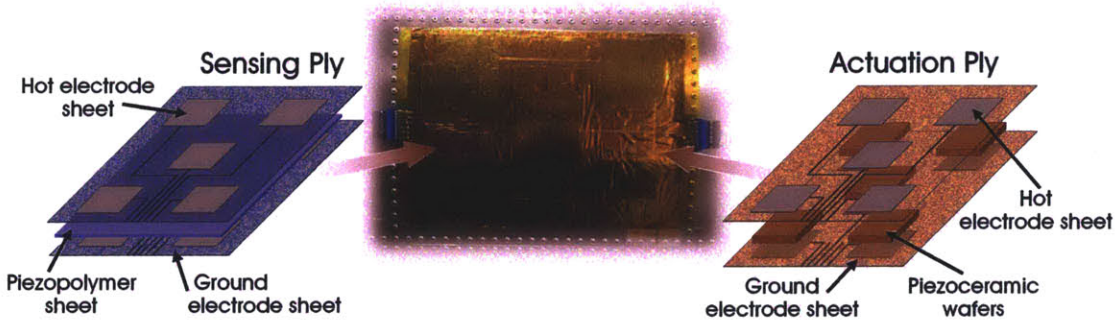

Figure 5.19: Lay-up of the active ply that is composed of collocated piezoceramics actuators and piezopolymer sensors. Electrodes for actuators and sensors are etched into copper-covered Kapton polyimide sheets. The actuation ply and sensing ply are attached to three panels of the fuselage test-bed.

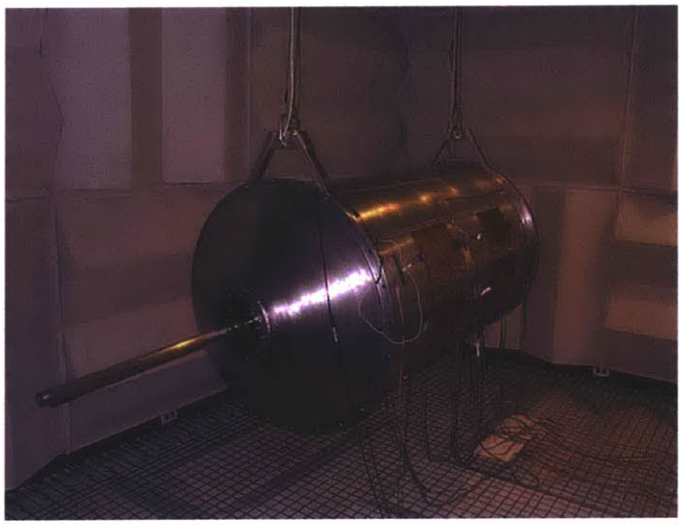

Figure 5.20: The fuselage test-bed is constructed from a thin aluminum skin over a frame of ribs and stringers and represents the dynamics encountered in aircraft.

5.21 and the transducer placement is sketched in Figure 5.22. Signals from the PVDF sensor elements were conditioned with a unity-gain op-amp amplifier circuit that was built by Steve Tistaert. The individual elements were weighted to create a modal sensor. In the case of feedback control, the weighted signals were processed in a digital controller and the weighted signal was amplified and set to the PZT actuators. The control signal used the same weights as the sensor signals. Open loop and closed loop performance were measured with a SigLab analyzer by comparing the transfer functions between piezoceramic disturbance and the performance measures.

5.4 Modal Isolation on the Fuselage Test-Bed

The weighting on the actuators and sensors was calculated in order to isolate individual modes on the fuselage test-bed. An infinity-norm cost function was defined where the targeted mode, m, was maximized and the modes between 350 Hz and 2050 Hz, n, were minimized. The infinity-norm cost function is given by

$$J_\infty = \frac{\max_n \left[\alpha_n \left(\mathbf{w}_s \Psi_n \mathbf{w}_a^T \right) \left(\mathbf{w}_s \Psi_n \mathbf{w}_a^T \right)^* \right]}{\left(\mathbf{w}_s \Psi_m \mathbf{w}_a^T \right) \left(\mathbf{w}_s \Psi_m \mathbf{w}_a^T \right)^*} \tag{5.6}$$

where ψ_i is the mode shape evaluated at the transducers, $\mathbf{w}_s$ and $\mathbf{w}_a$ are the sensor and actuator weights. An infinity-norm cost function was used for the modal isolation because the infinity-norm closely creates the desired modal transfer function from a controls point of view. As mentioned in Chapter 3, an analytical proof of the global minimization is not available for an infinity-norm cost function, but heuristic experimentation indicates that that there is not a problem implementing an infinity-norm cost function.

For the modes that were observable to the elements in the array, good modal isolation was obtained. The optimal weights calculated through the minimization of the infinity-norm cost function were applied to the sensor inputs and to the actuator outputs. Modal isolation on two of the modes, 925 Hz and 975 Hz, is shown Figure 5.23. The peak amplitudes of the unwanted modes are reduced by 15 dB from the response envelope. Since the individual transfer functions of the weighted array exhibit collocated behavior, the transfer function of the weighted summation is also collocated. The collocated behavior is apparent from the alternating pole-zero pattern in Figure 5.23. The good separation between the poles and zeros is encouraging for closed-loop control.

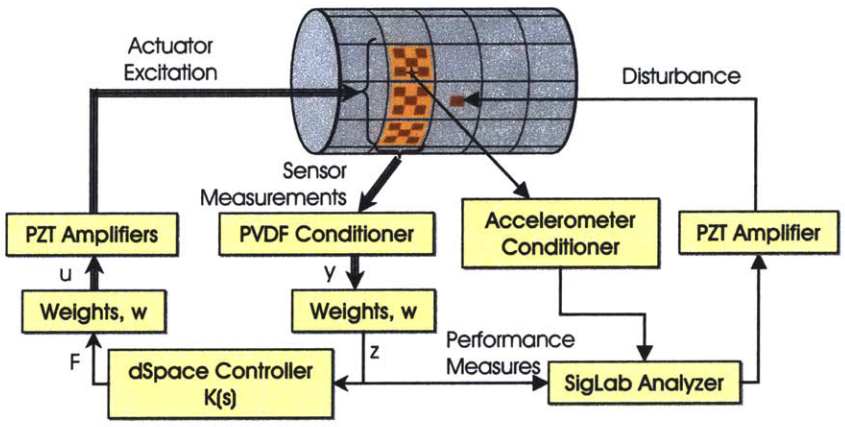

Figure 5.21: Wiring diagram for the feedback control experiments. Digital control is performed through a dSpace controller operating at 6.7 kHz. Performance is measured with a SigLab analyzer.

5.5 Broadband Feedback Control on the Fuselage Test-Bed

Feedback control was implemented to minimize the broadband vibration of the fuselage panels. Performance is measured by the transfer function from a piezoceramic disturbance to an accelerometer. The goal of the experimental control is to obtain the minimum RMS response in the performance transfer function. The results presented in this section represent the peak performance that was obtained.

Control is based upon the weighted sensors and actuators. The weights were optimized to isolate individual modes of vibration. The isolated modes were used in a digital computer equipped with dSpace software and hardware. A reduced-order controller that is similar in form to a positive-position feedback control was chosen as the control algorithm because it requires limited *a priori* knowledge of the system; no numerical model is needed in order to design the control loop. The control loop is of the form as that used in section 5.1,

$$K(s) = \frac{gs^2}{s^2 + 2\zeta_c\omega_c s + \omega_c{}^2} \frac{\omega_n{}^2}{s^2 + 2\zeta_n\omega_n s + \omega_n{}^2} \tag{5.7}$$

where ω_c is the low frequency corner, ζ_c is the damping ratio at the low frequency corner, ω_n is the target frequency, ζ_n is the damping ratio at the target frequency, g is the gain,

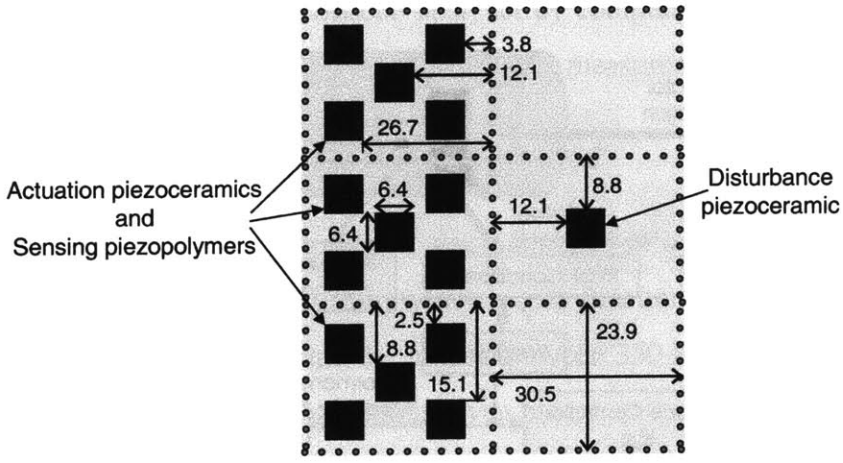

Figure 5.22: Placement of the collocated piezoceramic actuators and piezopolymer sensors as well as location of the disturbance piezoceramic. All actuators and sensors are the same size. All dimensions are in centimeters.

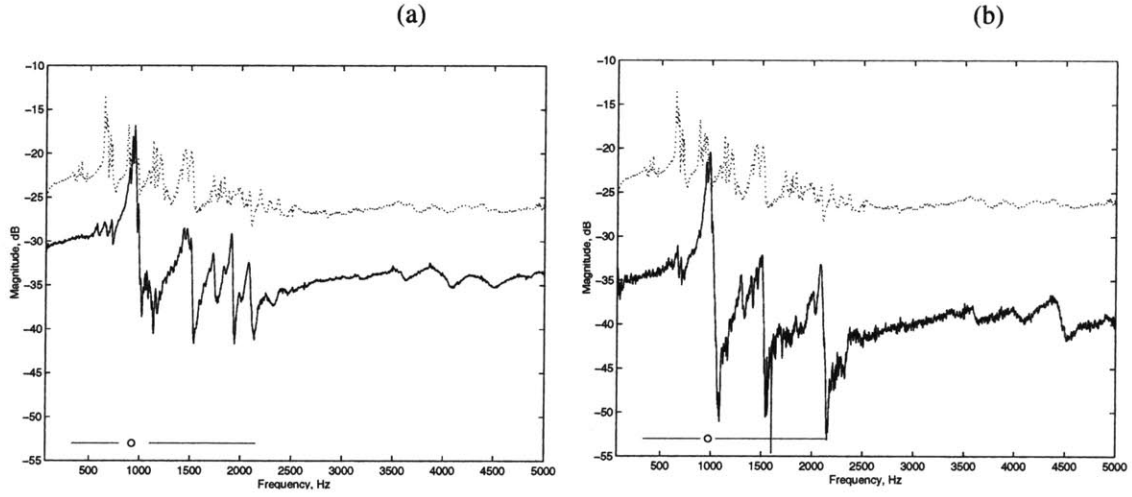

Figure 5.23: Modal isolation on the fuselage test-bed. Figure (a) features the mode at 925 Hz and the figure (b) features the mode at 975 Hz. The dotted line reflects the envelope of all of the modal responses. Circles indicate featured modes and horizontal lines indicate region where the modal response is minimized.

and $s = \omega\sqrt{-1}$. The low frequency corner is set at 150 Hz with a damping ratio of 0.5, which creates a high-pass filter and helps to minimize possible low frequency instabilities. The target frequency is 25 Hz higher than the mode that was targeted and has a damping ratio of 0.05. The low damping ratio at the target frequency helps to focus the controller energy at the targeted mode. The controller was converted to the digital time domain using the Tustin transform and the control loop was closed at 6.7 kHz with a sampling frequency also of 6.7 kHz.

The performance of the closed-loop system was evaluated in two manners. One manner for evaluating the system is the transfer function from the disturbance to the weighted sensor amplitude. The other manner of evaluation is the transfer function from the disturbance to the acceleration of a center-mounted accelerometer. The performance of the accelerometer is used to indicate the vibration reduction of the controller while the weighted sensor reduction is used to evaluate the controller. The key metric is the peak performance that can be obtained from the performance measures. A broadband white noise disturbance with a bandwidth of 70 Hz to 2 kHz was provided by a piezoceramic

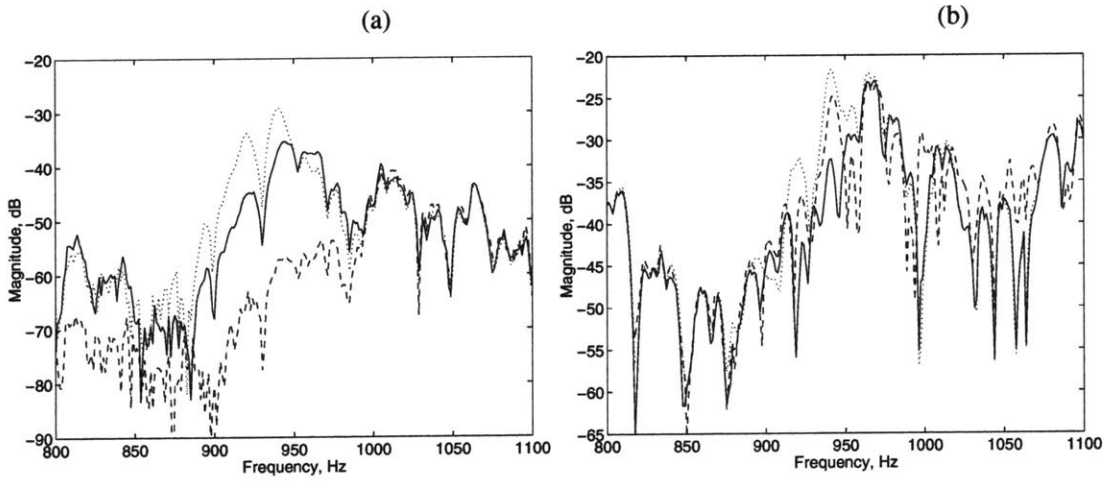

actuator located on an adjacent panel. The disturbance and closed loop performance were measured using a SigLab analyzer. The experimental setup is illustrated in Figure 5.21.

5.5.1 Single Mode Control

The closed-loop performance from targeting the mode at 925 Hz is illustrated in Figure 5.24. The optimal gain for the controller depends on the performance metric. The peak reduction in the weighted sensor response occurs for a controller gain of 1.5 while the peak reduction in the acceleration response occurs for a controller gain of 0.5. Additionally, a better reduction in the response is obtained for the weighted sensor response, 30 dB, than for the acceleration, 12 dB. Although not shown, there is a 5 dB increase in the vibration between 300 Hz and 700 Hz, which arises because a positive position feedback controller softens the system at lower frequencies. Otherwise, the closed-loop response is very similar to the open-loop response at all other frequencies. The RMS performance is tabulated in Table 5.3.

The different behavior between the two performance measures arises because the controller minimizes the weighted strain response. Increasing the gain of the controller increases the control effort and further reduces the weighted strain response. At low

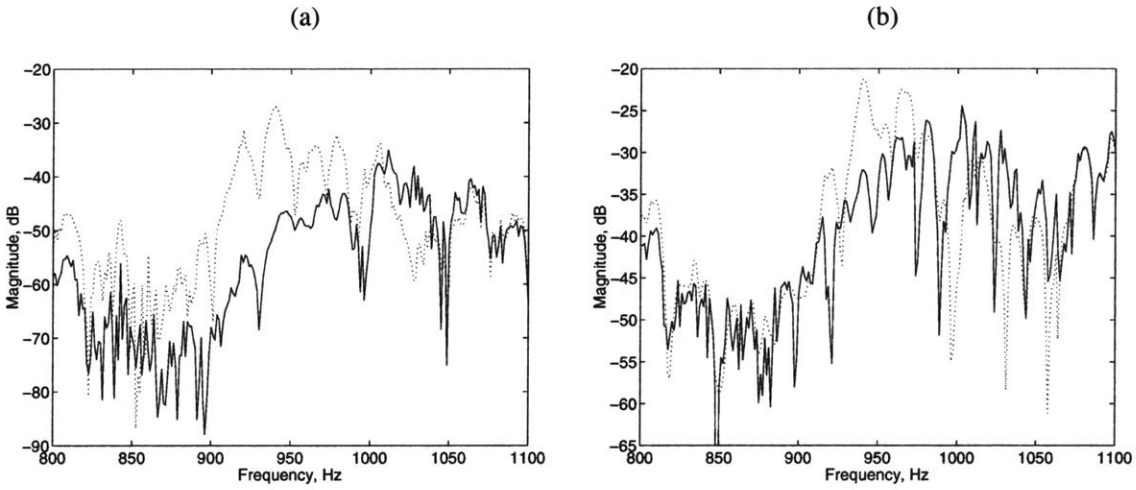

Figure 5.25: Open loop and closed loop performance from targeting modes at 925 Hz and at 975 Hz. Figure (a) is the weighted sensor response and figure (b) is the acceleration. Dotted line is open loop response; solid line is closed loop response with a controller gain of 0.5.

gains, the controller adds damping to the system, which helps to minimize the structural response. At higher gains, the controller adds stiffness to the system, which moves the vibration to other locations on the fuselage. As a result, the high-gain controller yields less acceleration attenuation of the panel than the low-gain controller does.

5.5.2 Multiple Mode Control

Multiple modes can be simultaneously minimized. Using sequential loop closure, the modes at 925 Hz and at 975 Hz were targeted by the controller. Array weights were calculated for each frequency using an infinity-norm cost function. The parameters in the control algorithm were chosen for each mode separately. The controller for the mode at 925 Hz had a gain of g=0.5, a target frequency of ω_n = 950 Hz, and a damping ratio of ζ_n =0.05. The controller for the mode at 975 Hz had a gain of g = 0.4, a target frequency of ω_n = 1000 Hz, and a damping ratio of ζ_n =0.05. Both controllers had the same low frequency corner of ω_c = 150 Hz and a damping ratio of ζ_c = 0.5. Simultaneously closing both loops reduces the weighted sensor strain and the acceleration from just closing each loop alone. The peak closed loop response is illustrated in Figure 5.25.

Table 5.3: MAXIMUM RMS PERFORMANCE EVALUATED OVER INTERVAL FROM 850 HZ TO 1000 HZ.

	Gain	RMS Acceleration Reduction	RMS Weighted Strain Reduction
925 Hz Mode	0.5	3.5 dB	3.8 dB
925 Hz Mode	1.5	2.5 dB	21.1 dB
975 Hz Mode	0.4	1.2 dB	11.3 dB
975 Hz Mode	1.5	1.3 dB	20.3 dB
925 Hz Mode and 975 Hz Mode	0.5	5.1 dB	15.4 dB

The dual-mode controller reduced the weighted sensor response by 28 dB and the central panel acceleration was reduced by 15 dB. Better performance is obtained for the weighted sensor response because the controller directly measures and minimizes this metric. The performance of the dual-mode controller is similar to the performance that was obtained when only the 925 Hz mode was targeted. When compared with the control of similar gain, the solid line in Figure 5.24, then the dual mode controller greatly broadens the region of good performance but does not significantly change the magnitude of the peak performance. The RMS performance is tabulated in Table 5.3.

5.6 Weighted Control versus Un-weighted Control

Control with weighted transducer arrays has been offered in this thesis as a more implementable alternative to un-weighted control implementations. Let us compare control using weighted arrays of transducers with control using individual elements by comparing the implementation costs associated with the two techniques. Open-loop performance is different because the data was taken on subsequent days, and the plant changes with time.

5.6.1 Off-Line Calculations

There are three principle costs associated with implementing weighted and un-weighted control: off-line computations, on-line computations, and hardware infrastructure. In

weighted control, the off-line computations are needed to calculate the array weights and to fit a numerical model to the weighted transfer functions. The number of computations required to calculate the array weights scales as the product of the number of sensors, the number of actuators, and the number of frequency points. The number of computations also varies with the accuracy of the initial guess, the tolerances, and the routine used to minimize the cost function.

In un-weighted control, most of the off-line computations are spent fitting a numerical model to the experimentally measured transfer functions. The number of calculations needed to perform a basic modal model synthesis scales with the product of the cube of the number of states times the number of sensors times the number of actuators times the number of frequency points [Strang, 1993]. Numerical stability of the model synthesis dramatically decreases as the number of input/outputs increases [Kollar, 1995; Uebelhart, 2000]. The 30-in, 30-out experimental data was fed into a synthesis algorithm designed by Midé Technology Corporation [Midé Technology Corporation, 1999]. However, the solution could not be successfully calculated on a 500 MHz Pentium III computer with 128 MB of RAM. While the speed of the off-line calculations is not critical, being able to successfully complete the calculations is critical. In summary, the off-line computations could only be implemented for the case of weighted control and the calculations were too intense to be calculated for the case of un-weighted control.

5.6.2 On-Line Calculations

The on-line computations are dominated by the controller's calculation of the actuator signals based upon the sensor signals. Any linear controller can be put in an **A**, **B**, **C**, **D** form for implementation:

$$\begin{aligned} \mathbf{x}_{k+1} &= \mathbf{A}\mathbf{x}_k + \mathbf{B}\mathbf{y}_k \\ \mathbf{u}_k &= \mathbf{C}\mathbf{x}_k + \mathbf{D}\mathbf{y}_k \end{aligned} \tag{5.8}$$

where **y** is the sensor input, **u** is the actuator output, and **x** is an internal state variable. In general, the **A** matrix can be block diagonalized with 2x2 blocks [Grocott, 1997]. The **B**, **C**, and **D** matrices are in general fully populated.

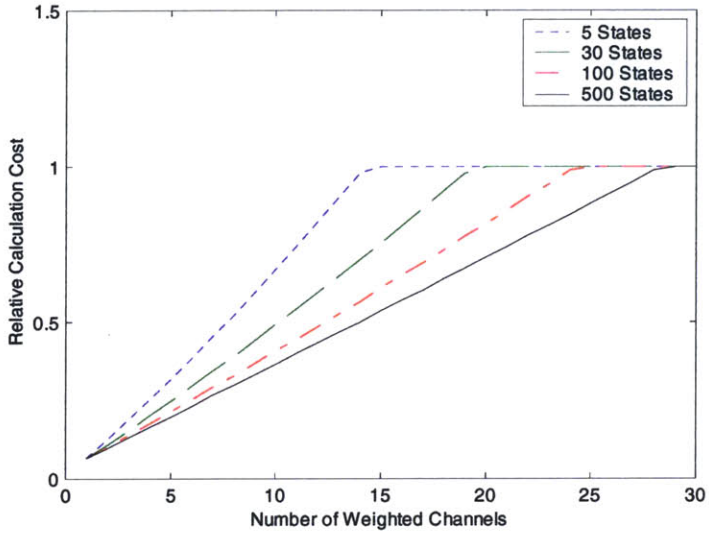

Figure 5.26: The relative number of calculations needed for the weighted and for the un-weighted control is a function of the number of channels in the weighted controller and of the number of states in each controller. The relative calculation cost is defined as the number of on-line calculations required for the weighted controller divided by the number of on-line calculations required for the un-weighted controller.

In weighted control, the number of calculations needed for each time step, c, is

$$c = m(\tilde{s} + \tilde{a} + 2) + \tilde{a} \cdot \tilde{s} + \tilde{a} \cdot a + \tilde{s} \cdot s \tag{5.9}$$

where m is the number of states in $\mathbf{A}$, s is the number of sensor elements, a is the number of actuator elements, $\tilde{s}$ is the number of weighted sensor channels, and $\tilde{a}$ is the number of weighted actuator channels. The last two terms in equation (5.9) reflect the implementation of the array weights. This calculation could be performed using digitally programmable analog circuits, and, hence, might not need to be included in the implementation cost. A 30-element transducer array that is condensed to 3 weighted channels that are fed into a 100 state controller requires 989 calculations per time step.

In un-weighted control, the number of calculations needed for each time step is

$$c = m(s + a + 2) + a \cdot s \tag{5.10}$$

For the case of a 30-element array that uses a 100 state controller, 7100 calculations are required for each time step, over 7 times more calculations than the control with weighted arrays. As shown in Figure 5.26, even if the control with weighted arrays used 24

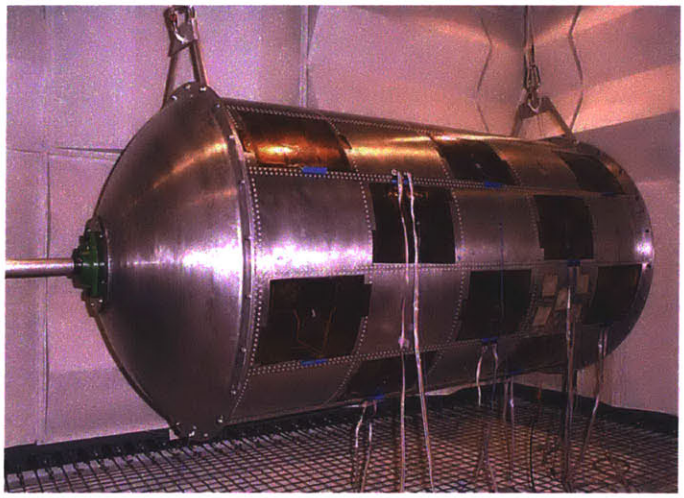

Figure 5.27: The fuselage test-bed for the secondary fuselage control experiments is instrumented with transducer plies constructed from thicker copper-coated Kapton.

weighted input channels, it would still be faster than the control without arrays. This comparison is conservative because it ignores the fact that the weighted controller should be able to use a much lower order control model than the un-weighted controller, which would further boost the relative performance of the weighted controller. In most situations, the calculation of the weighted response requires less time than calculating the full B and C matrix response. In those cases where the extra calculations take very long, the sensor and actuator weights can be rolled into the B and C matrices. In which case, the weighted control can never take more time than the un-weighted control.

5.6.3 Hardware Requirements

If the array weighting of the weighted control is performed digitally, then the hardware requirements are identical between the weighted and un-weighted control. However, if the array weighting can be performed using digitally programmable analog circuits, then fewer A/D conversions and D/A conversions are required. The A/D conversions can often take much longer than the control calculations in large MIMO applications. A/D conversion hardware is often very financially expensive as well as computationally expensive.

Implementing the array weights in analog offers faster control speed and reduced A/D and D/A converters while requiring the extra analog hardware that is necessary to implement the array weights. This trade-off needs to be evaluated by the design engineer on the specifics for each project.

5.7 Secondary Fuselage Control

Seeking improved reliability, new sensor and actuator plies were bonded to the fuselage test-bed. Seeking performance over a wider area, alternating panels of the fuselage test-bed were instrumented. The transfer functions and the closed-loop performance, however, proved to be very similar to those described in section 5.5. This section describes the use of these new panels and their application for modal identification and control.

5.7.1 Experimental Setup

The active transducer plies that were described in section 5.3 were difficult to construct and their performance was limited due to poor connections through the crimp connectors. It was believed that thicker layers of Kapton with a thicker copper coating would solve these problems. As a result, a new set of transducers were constructed and bonded to the fuselage by undergraduates working for the author, Daniel Kwon and Christian Garcia. These transducers feature 2 mil thick Kapton holding a 1 mil thick layer of copper. This

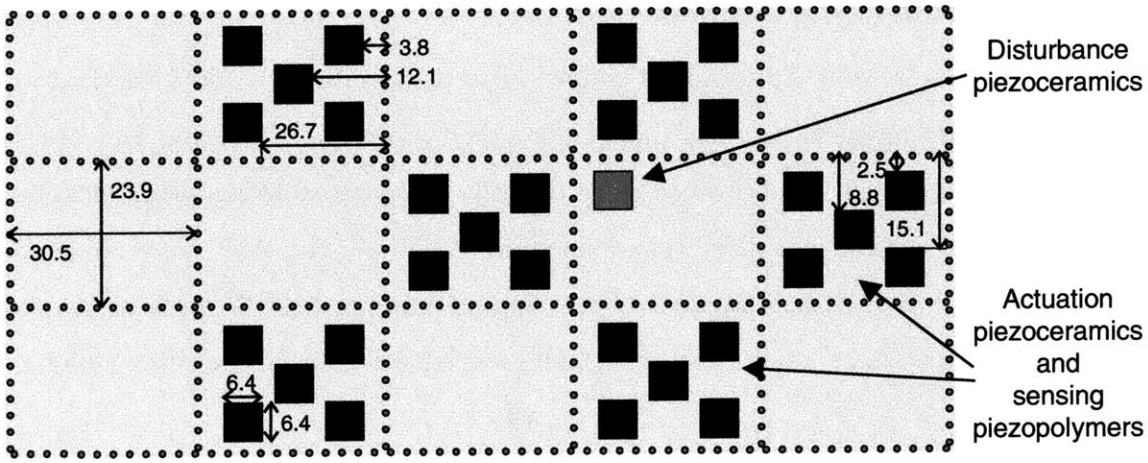

Figure 5.28: Transducer layout for the secondary fuselage control experiments.

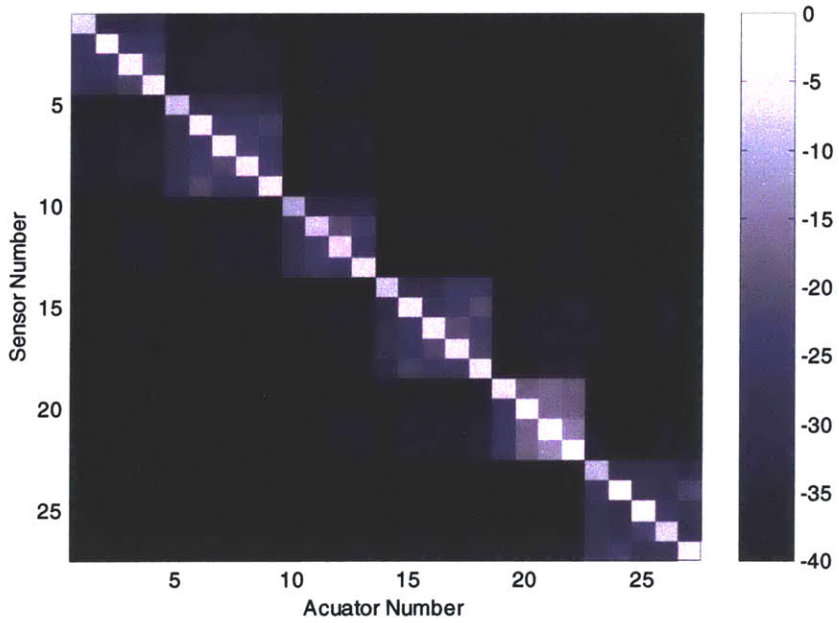

Figure 5.29: The geometric mean of the coupling between the sensor and actuator elements shows that there is little coupling between panels. Color axis is in dB scale where 0 dB is the maximum mean coupling.

thicker layer of copper-coated Kapton is the same as that which was used in Chapter 5. The newly instrumented fuselage is pictured in Figure 5.27 and the layout of the transducers is sketched in Figure 5.28. Unfortunately, the same number of connection problems was experienced in the redesigned transducer plies.

A different layout for the active plies was implemented for the secondary fuselage control experiment. The plies were arranged in a checkerboard pattern. The panel of separation between the plies greatly minimized the coupling between plies on different panels. The average coupling between all of the actuators and all of the sensors on the test-bed is plotted in Figure 5.29. The coupling is clustered into block diagonal groups that represent the transducers located on a panel. In this figure, there are different numbers of transducers on each panel due to transducer failures at the crimp connectors. The strong block-diagonal structure of the coupling indicates that there is very strong coupling between the transducers that are located on the same panel, but that there is very little coupling between transducers located on different panels. Since the transducer

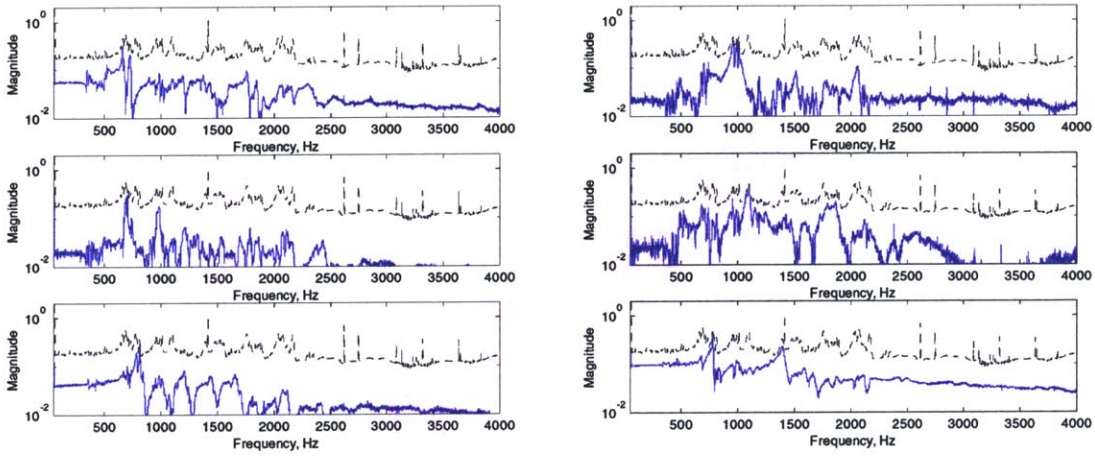

Figure 5.30: Modal isolation performance on the fuselage test-bed

dynamics are strongly confined to each panel, the coupling between panels was ignored. In other words, the off block diagonal terms were assumed zero.

5.7.2 Modal Isolation

The block diagonal nature of the actuator to sensor coupling, Figure 5.29, has strong implications for the modal isolation. The number of calculations required in the optimization of the cost function is greatly reduced since the off diagonal terms can be assumed zero. Each iteration in the minimization process of the cost function requires an evaluation of the weighted transfer function, $\mathbf{w}_s \Psi \mathbf{w}_a{}^T$. Reducing the size of the transfer function matrix, Ψ, reduces the number of computations and greatly speeds the calculation of the array weights. Additionally, the block diagonal nature allows for easier implementation of digitally programmable analog weights that could be located on each panel. The analog implementation is easier because the block diagonality limits the amount of information that would need to be shared between panels.

The block diagonal nature of the actuator to sensor coupling also limits the ability to effectively isolate the modes. The lack of effective coupling between the panels limits the modal isolation ability to that which can be achieved by a single panel. Since the different panels have slightly different natural frequencies, a single frequency peak cannot be effectively isolated. Low frequency modes are difficult to isolate.

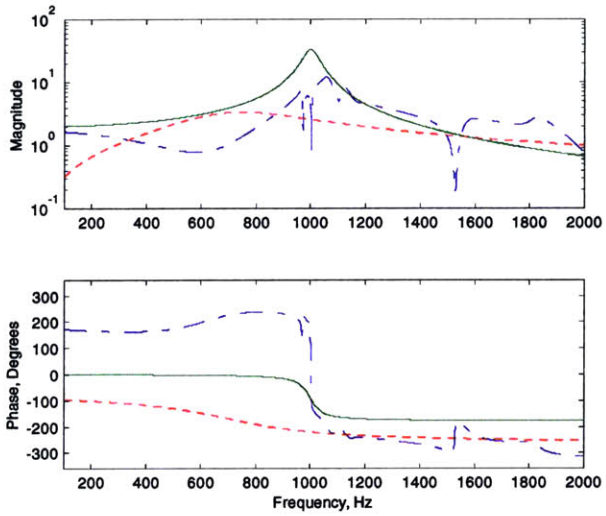

Figure 5.31: Transfer function of the analog control algorithms. Solid line is weighted reduced-order controller, dashed-dot line is weighted LQG controller, and dotted line is un-weighted reducer-order controller.

Several of the modes of vibration were isolated using the infinity-norm cost function described in equation (5.6). The isolated modes are shown in Figure 5.30. The modes are much more poorly extracted with the secondary transducer layout than they were with the initial transducer layout. The weighted transfer functions in Figure 5.23 are much cleaner than the weighted transfer functions in Figure 5.30.

5.7.3 Experimental Control Comparison

The closed-loop performance of weighted arrays is compared with the closed-loop performance of un-weighted arrays. The performance is defined as the transfer function from the disturbance piezoceramic to the RMS strain of all of the sensors. The RMS strain serves to approximate the vibration performance of the fuselage's structural dynamics.

Weighted and un-weighted control are compared. The ultimate control algorithm is independent of the array weighting matrix. The weighted arrays serve as a pre- and post-filter to the control algorithm. A 3-state weighted reduced-order controller and a 25-state LQG controller were used with the weighted arrays. A different un-weighted

reduced-order controller was used on the un-weighted transducer array. The term "weighted" and "un-weighted" is used to differentiate the reduced-order controller that is used on the weighted array from the reduced-order controller that is used on the un-weighted array.

5.7.3.1 Control Algorithms

The control law for the weighted reduced-order controller is the same as that which was presented in equation (5.7). The control law for the un-weighted reduced-order controller is

$$K(s) = \frac{g\omega_n s}{s^2 + 2\zeta\omega_n s + \omega_n^2} \tag{5.11}$$

for each collocated transducer pair. The natural frequency of the controller, ω_n, is set to 750 Hz and the damping ratio, ζ, is 0.35. The natural frequency and damping ratio were set to provide peak performance. The form of the un-weighted reduced-order controller is similar to rate feedback and is of the form used to obtain good broadband performance on the fuselage test-bed by Savran et al. [Savran, Atalla, and Hall, 2000].

An un-weighted reduced-order controller was closed for each of the transducer pairs. The transfer function of the controller is shown in Figure 5.31. Control with this controller was closed at 4.5 kHz. The un-weighted controller was able to reduce the RMS strain by 1.2 dB. Its performance was limited by the phase delay of the digital control. The open-loop and closed-loop transfer functions are shown in Figure 5.32b with the figure legend "Rate."

The weighted reduced-order controller, equation (5.7), was designed to direct the control energy at the targeted modal frequency. The transfer function of the weighted reduced-order controller is shown in Figure 5.31 and its digital representation was closed at 6.7 kHz. This control loop could be closed at a higher rate of speed than either the un-weighted reduced-order controller or the LQG controller because the weighted reduced-order control algorithm features far fewer states than the other control algorithms. Due to the higher rate of loop closure, the weighted reduced-order control was able to achieve a

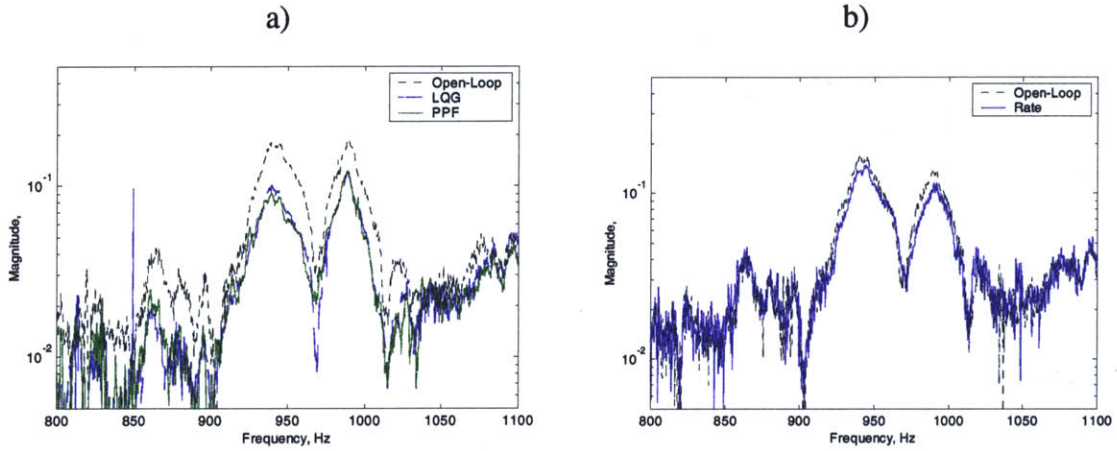

Figure 5.32: Open-loop and closed-loop RMS strain performance. Figure a) uses weighted arrays while figure b) closes a series of single-input, single-output loops.

4.7 dB reduction in the RMS strain. The open-loop and closed-loop performances are shown in Figure 5.32a with the figure legend "PPF."

The weighted and un-weighted reduced-order controllers are of different forms because the weighted and un-weighted actuator to sensor transfer functions featured different phases at the targeted frequencies. The weighted and un-weighted transfer functions are 90 degrees apart from each other in the region near 1 kHz. For peak performance, the weighted and un-weighted control algorithms need to be 90 degrees apart at the targeted region. The presented weighted and un-weighted control algorithms achieve the peak closed-loop performance for a reduced-order controller for their respective systems.

The LQG controller was formed by fitting a 25 state numerical model to the measured weighted transfer function. The experimental identification software [Midé Technology Corporation, 1999] used a Frequency domain Observability Range Space Extraction routine to estimate the numerical model. The model was tuned with a log-least squares weighting on the additive error. The resulting state-space model formed the basis of the Kalman estimator. Loop shaping of the LQR controller was accomplished with a dip in the noise model at the targeted frequency [Preumont, 1997]. The transfer function of the LQG controller is shown in Figure 5.31. The digital representation of the LQG

Table 5.4: RMS PERFORMANCE EVALUATED OVER INTERVAL FROM 800 HZ TO 1100 HZ.

	RMS Strain	Point Acceleration
Un-weighted Reduced-Order Control	1.2 dB	0.7 dB
Weighted LQG Control	4.4 dB	-4.0 dB
Weighted Reduced-Order Control	4.7 dB	-4.5 dB

control algorithm was implemented on an alpha digital signal processor operating at 4.5 kHz. The LQG controller reduced the RMS strain on the 27 transducers by 4.4 dB, as shown in Figure 5.32. The speed of the LQG controller matched the speed of the un-weighted reduced-order controller because both controllers had the same number of states in the control model.

5.7.3.2 Comparison of Control Algorithms

Digital control with weighted arrays produced better closed-loop reduction in the RMS strain on the fuselage test-bed than digital control with un-weighted arrays, as shown in Table 5.4. The phase added from the time delay of the digital control algorithm limited the closed-loop performance of these controllers. The weighted reduced-order controller was able to achieve better performance than the weighted reduced LQG control because the reduced-order controller was able to operate at a faster cycle time and, thus, featured less added phase. The author would have liked to have compared these controllers to an un-weighted LQG controller, but, as described in section 5.6, an un-weighted LQG controller could not be designed for the large number of transducers on the fuselage test-bed.

The effect of the added phase from digital control is noticeable in the un-weighted reduced-order control implementation. The un-weighted reduced order control algorithm is intended to be used on collocated systems where there is very little added phase from the control implementation. Using the un-weighted reduced-order controller to minimize modes at a high fraction of the sampling frequency limits the possible closed-loop performance. The added phase requires the gain crossover in the loop transfer function to

occur at lower frequencies than would be desired if there were no added phase. The lower gain crossover leads to lower overall gains in the controller, and, thus, lower performance in the closed-loop system.

Significantly better performance using a similar un-weighted reduced-order controller on the fuselage test-bed with the initial instrumentation, section 5.3, has been reported by Savran et al. [Savran, Atalla, and Hall, 2000]. As seen in Figure 5.33b, a more substantial 6.7 dB of performance was obtained with an *analog* un-weighted reduced-order controller. The difference in performance between the digital and analog un-weighted reduced-order control approaches lies in the improved closed-loop performance that can be obtained using analog control versus using digital control. According to Cagri Savran [Savran, 2000], he initially implemented his un-weighted reduced-order control on the fuselage using a digital implementation, closing the loop at 4.1 kHz. As seen in Figure 5.33a, a closed-loop reduction in the transfer function of 2.3 dB was obtained. Switching to an analog implementation effectively removed the phase delay over the bandwidth of interest and significantly increased the performance. Note that the analog un-weighted reduced-order controller was able to achieve good performance across a wide frequency bandwidth.

In general, analog control of complex structures is only practical if the transducers

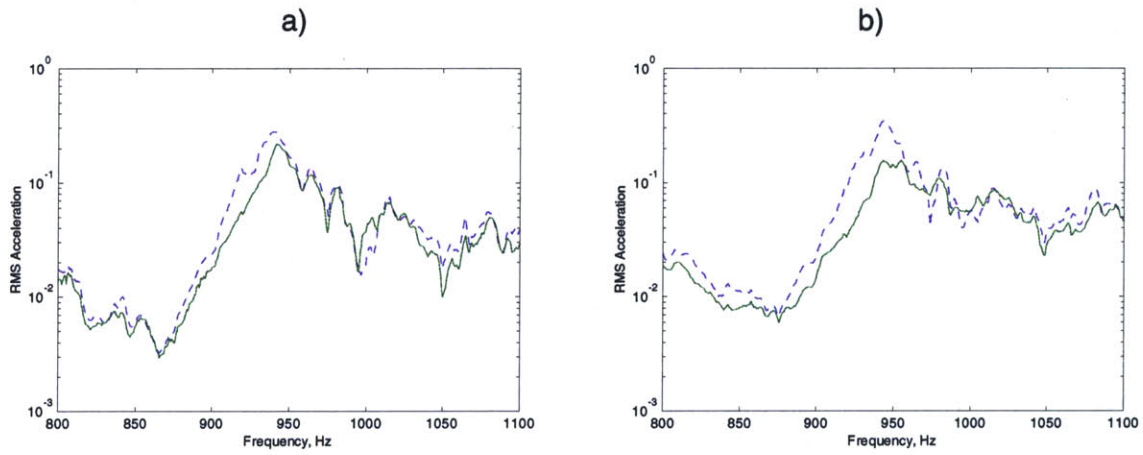

Figure 5.33: Open-loop (dotted line) and closed-loop (solid line) transfer functions of the acceleration on the fuselage test-bed. A) Digital control [Savran, 2000]. B) Analog control [Savran, Atalla, and Hall, 2000].

are collocated and exhibit bounded phase. Thus, analog control could easily be implemented on the fuselage test-bed because the individual transducers exhibit collocated behavior. One of the advantages of weighted arrays is that they allow for analog implementation and analog control on complex structures by simplifying the system dynamics to a series of modal responses. As demonstrated in section 5.2, weighted arrays do not require the use of collocated transducers in order to successfully implement reduced-order control.

It is believed that an analog implementation of weighted reduced-order control would yield significantly better performance than the digital implementation reported here. Weighted arrays can be implemented in analog through the use of digitally programmable analog circuits such as Analog Devices SSM2160 and SSM2163.

5.8 Summary of Control

This chapter demonstrated the use of weighted arrays for vibration control on complex structures. A tabular summary of the control approaches is presented in Table 5.5. Numerical simulations demonstrated that the implementation of weighted arrays simplifies the plant transfer function and can lead to improved closed-loop performance. An experiment on a cylinder section demonstrated that weighted arrays allow the use of reduced-order control algorithms on complex structures that do not have collocated transducers. The structural vibrations and the acoustic emissions were reduced by as much as 20 dB.

Experiments were also conducted on the fuselage test-bed. The fuselage test-bed was instrumented in two different configurations. The first instrumentation configuration demonstrated excellent modal isolation performance. A pair of modal weights was simultaneously implemented to isolate two modes and a reduced-order controller achieved a 15.4 dB reduction in the weighted RMS strain and a 5.1 dB reduction in the RMS acceleration.

The second instrumentation configuration featured a checkerboard of instrumented panels that exhibited little structural coupling between the panels. As a

Table 5.5: SUMMARY OF CONTROL APPROACHES PRESENTED IN CHAPTER 5.

	Numerical	Curved Panels	Fuselage Test-bed	Secondary Fuselage Test-bed
Section	5.1	5.2	5.5	5.7
Style	Numerical	Experimental	Experimental	Experimental
Structure	Curved panel	Curved panel	Fuselage	Fuselage
Type of Sensor	Piezoelectric and velocity	Piezopolymer	Piezopolymer	Piezopolymer
Number of Sensors	5	4 and 8	15	27
Type of Actuator	Piezoelectric	Piezoceramic	Piezoceramic	Piezoceramic
Number of Actuators	5	1	15	27
Disturbance	Piezoelectric	Piezoceramic	Piezoceramic	Piezoceramic
Primary Performance	RMS velocity	RMS noise	RMS acceleration	RMS sensor strain
Secondary Performance	Weighted sensor and RMS sensor	Weighted sensor	Weighted sensor	-
Control Algorithms	LQG and reduced-order	Reduced-order	Reduced-order	LQG and reduced-order
Arrays	Weighted and Un-Weighted	Weighted	Weighted	Weighted and Un-Weighted

The second instrumentation configuration featured a checkerboard of instrumented panels that exhibited little structural coupling between the panels. As a result, the modal isolation performance and the closed-loop performance of the second instrumentation configuration was not as good as the performances of the first instrumentation configuration. An un-weighted reduced-order controller yielded a small reduction in the RMS strain that was comparable to that obtained by Cagri Savran on the first instrumentation configuration [Savran, 2000]. Controllers using weighted arrays obtained significantly larger reductions in the RMS strain. Un-weighted controllers were shown to have higher implementation costs than weighted controllers.

CHAPTER 6

Conclusions

One never notices what has been done;
one can only see what remains to be done.
- Marie Curie
In a letter to her brother, March 18, 1894

Data without generalization is just gossip.
- Robert Pirsig

This chapter summarizes the development of the theory of weighted arrays and their implementation for modal isolation and for vibration and acoustic control. The limitations of using weighted arrays and the avenues for future work are also illuminated. Finally, the critical contributions offered by this thesis are detailed.

6.1 Summary

This thesis is motivated by the need to minimize the fuselage vibrations and interior noise of aircraft. Performance requirements and weight limitations necessitate the use of broadband feedback control. An aircraft fuselage test-bed was designed to represent the important dynamics, structural-acoustic couplings, and geometry of fixed-wing aircraft

and helicopters while simplifying the design to facilitate control implementation. Hybrid scaling was used to retain some of the full-size aircraft's global and panel structural dynamics, interior acoustic dynamics, and structural-acoustic coupling.

Computer models were created to help understand the dynamics of the representative fuselage test-bed and to help refine its design. Two models of the test-bed were constructed: a finite element model and a Rayleigh-Ritz model. The finite element model was used to predict the coupled dynamics of the test-bed and to design the end-caps. The Rayleigh-Ritz model also was used to predict the structural-acoustic dynamics and to provide further insight into the coupled dynamics. It was expected that one of the numerical models would form the basis of the control algorithm. After extensive modeling, the models yielded insufficient resolution in order to design a control algorithm.

Complex structures, such as an aircraft fuselage, tend to exhibit high modal densities and time-varying dynamics, which make them very difficult to numerically model. Active control of these structures necessitates a good numerical model of the system. Modal sensors and actuators have been offered as a method to simplify the apparent complexity of these systems by reducing the cacophony of modes into a series of single mode responses. Traditional implementations of modal transducers feature elements that are shaped to the desired mode. Shaped modal transducers are limited to implementation on simple structures because of errors in placement, errors in construction, and errors in modeling, among others.

Weighted arrays of discrete transducer elements have been presented as a means to robustly implement modal transducers on complex structures. Weighted arrays feature arrays of sensors and actuators that are weighted to isolate a targeted mode. By isolating individual modes of vibration, all of the control effort can be directed towards the targeted mode. The reduced amplitudes of the unwanted modes provide gain stabilization throughout the region of controller roll-off.

Determining the optimal array weights is the key to successful implementation of weighted arrays. There are several methods for calculating the array weights. The

simplest method sets the weights to the targeted mode shape. Weights based on the mode shape will be complex and offer dismal modal isolation performance on real structures. Another intuitive method for setting the weights involves taking the pseudo-inverse of the transfer function matrix. Weights based on matrix inversion offer excellent modal isolation performance and excellent robustness to transducer failure. However, the matrix inversion yields complex weights, which cannot be implemented causally, and yields a weighting matrix that cannot be decomposed into an array of sensor weights and an array of actuator weights.

This thesis has developed a cost function, which is used to determine the array weights. The cost function is formed from the ratio of the amplitudes of the weighted transfer function at the unwanted modes divided by the amplitude of the weighted transfer function at the targeted mode. The optimal weights are determined by minimizing the cost function. The infinity-norm cost function seeks to minimize the *peak* response of all the unwanted modes. The infinity-norm cost function is the metric that is most applicable to control stability. The 2-norm cost function seeks to minimize the *average* response of the unwanted modes. If mode shapes are real valued, which is almost never true in real systems, then it can be proven that there is only one minimum in the cost function and that there is an implicit equation for the optimal weights. Numerical and experimental investigations indicate that there is a single minimum to both the infinity-norm and the 2-norm cost functions. The cost functions can be modified to specifically weigh troublesome unwanted modes and can be modified to include a phase penalty that forces the weighted transfer function to have bounded phase. Both of the cost functions offer excellent modal isolation performance and are easy to implement.

The sensitivity of the modal isolation techniques was evaluated on a single panel fuselage section. The ability to isolate an individual mode, the modal isolation performance, varies exponentially with the number of array elements. Experiments showed that a 10% variance in the array weights still allows good modal isolation performance. An analytical perturbation analysis indicates that the mode shapes measured at the transducers can handle the same 10% variance before the modal isolation

performance suffers. Transducer failure has the potential to dramatically reduce the modal isolation performance although a single transducer failure at most locations is not critical.

Vibration control and modal isolation were conducted on increasingly complex test-beds. Modal isolation, vibration control, and acoustic emission control were conducted on a 3-panel cylinder section with a single actuator and an 8-element sensor array. An infinity-norm cost function was used to isolate the first four modes of vibration that were also featured in the performance transfer function. Vibration control performance as a function of the number of array elements is measured. Modal isolation and vibration control also was performed on the fuselage test-bed. A 15-element collocated sensor and actuator array was used to isolate several modes that were important to the performance by using an infinity-norm cost function. A detailed comparison is made of the implementation costs associated with control using weighted arrays and with control using un-weighted arrays. A 27-element collocated sensor and actuator array was used to compare the vibration reduction of control using weighted arrays to control using un-weighted arrays.

6.2 Limitations and Future Work

The control experiments presented in this thesis used strain-based piezoelectric transducers, which means that the controller is working to reduce the strain of the structure. When the goal of the controller is vibration control, then strain reduction is a good performance metric. However, when the goal of the controller is acoustic control, then strain reduction often does not directly match the goal. Instead, arrays of accelerometers or microphones might serve as a better sensor.

The difference in control performance of sensors that directly measure the performance, such as microphones, versus the control performance of sensors that are easy to use, such as PVDF, has long been an important issue for control design. All controllers seek to minimize the measured sensor inputs, regardless of whether this is the variable that the designer wishes to be minimized. However, this distinction becomes

more important in the case of weighted arrays. In the case of weighted arrays, the controller is seeking to minimize the response of a weighted summation of sensors. Thus, the controller will tend to rearrange the mode shapes so that the weighted sensor sum is minimized rather than minimizing the modal amplitudes. As a result, it is very important to chose sensors that closely approximate the performance metric.

Weighted arrays have proven to be successful at modal isolation on complex structures. Weights based upon the minimization of a cost function are clearly the best method for assigning the weights. However, collecting the transfer function data needed for calculating the weights necessitates measuring the complete transfer function matrix. In the case of a 30-input, 30-output system, this means that 900 separate transfer functions need to be evaluated, which is a time consuming process. The off-line optimization of the weights is numerically expensive and the gradient descent simplex search could take hours for the 30-input, 30-output system. Improved optimization techniques, such as an interior-reflective Newton method [Coleman and Li, 1994], could greatly speed convergence to the optimal weights. Although the off-line calculations may be more tractable than the off-line calculations used in other control techniques, the off-line computations are an impediment to implementation.

Weighted arrays are an effective tool for isolating individual modes of vibration and for targeted the control effort at those targeted modes. As a result, these weighted arrays are most applicable to modally dense structures whose performance is dominated by a few modes. If all modes contribute equally to the performance, then other techniques may be more appropriate.

Much of the work in this thesis focused upon the use of collocated arrays of sensors and actuators. Collocated arrays with equal sensor and actuator weights were used under the assumption that physical collocation of the transducers would result in a symmetric positive-real transfer function matrix, which would ensure that the weighted transfer function would preserve phase. When isolating higher modes, the asymmetry in the transfer function matrix would not allow the weighted transfer function to preserve phase. Including a phase penalty in the cost function allowed the phase to remain

bounded. Preliminary evidence presented in this thesis indicates that equivalent modal isolation performance can be obtained from non-collocated transducers and from a single actuator and a larger sensor array. Sensor arrays are much easier to implement than actuator arrays, thus subsequent research should focus upon using reduced actuator arrays and a larger sensor array.

6.3 Contributions

The principle contributions from this doctoral dissertation have been in the development of weighted arrays for modal isolation and for control. This thesis also contributed towards the implementation of weighted arrays for vibration and structural-acoustic control of a representative aircraft fuselage.

- This thesis was the first work to suggest a cost function in order to optimize the array weights in the context of modal sensing and actuation. The cost function can be phrased as a 2-norm optimization or as an infinity-norm optimization. The cost function can include phase penalties to ensure bounded phase or modal weights to preferentially minimize unwanted modes.
- The 2-norm cost function was analytically proven to have a global minimum and that there is an implicit equation for calculating the optimal weights. This proof had substantial assumptions. The effects of violating the assumptions were shown.
- An analytical perturbation analysis illustrated the sensitivity of the modal isolation performance to variations in the array weights, to variations in the target mode shaped, and to variations in the unwanted mode shapes. Perturbations in the weights are of the same order as perturbations in the mode shapes, which allows for easier experimental investigations.
- The sensitivity of the modal isolation performance to variations in the number of array elements, to perturbations on the array weights, and to transducer failure was experimentally investigated.
- A comprehensive comparison of modal transducers and of the different array weighting techniques was conducted. The implementation costs of the different

techniques as well as the modal isolation performance are compared both numerically and experimentally.

- The performance limitations and implications of spatial aliasing to modal sensing and actuation were illuminated. The ability to use spatial filtering to limit the effects of spatial aliasing also was shown.
- The use of weighted arrays for modal isolation was validated on a complex structure. Effective modal isolation was limited to those modes that were observable and controllable to the transducers. Multiple modes were simultaneously isolated on the representative fuselage test-bed using the same transducer array. Control with weighted arrays was shown to outperform control using un-weighted arrays.
- A high-order 3-dimensional structural-acoustic numerical model of the fuselage test-bed was developed. Off-center frame elements were modeled as well as an exterior speaker disturbance. The lack of correlation between the model and the experiments led to an understanding of the limits of numerical models.
- A 3-dimensional numerical model of a panel of the fuselage test-bed was used to compare the performance of closed-loop control using weighted arrays to control using an un-weighted array. The simulation indicated that the peak performance was obtained from using weighted arrays of piezoelectric sensors.
- A simple process for manufacturing embedded sensor and actuator plies was developed.

Bibliography

To the devil with those who published before us.
- Aelius Donatus, 300 C.E.

ANDERSSON, M. S. and E. F. CRAWLEY. 1995. "Structural Shape Estimation Using Shaped Sensors," *AIAA/ ASME/ ASCE/ AHS Structures, Structural Dynamics & Materials Conference - Collection of Technical Papers*, AIAA: New York, NY, **5**:3368-3378.

BANKS, H. T., R. C. SMITH, D. E. BROWN, R. J. SILCOX, and V. L. METCALF. 1995. "Experimental Confirmation of a PDE-Based Approach to Design of Feedback Controls," NASA Contractor Report 198167 and also ICASE Report 95-42, Institute for Computer Applications in Science and Engineering, Hampton, VA.

BARUH, H. and L. SILVERBERG. 1985. "Robust Natural Control of Distributed Systems," *Journal of Guidance Control & Dynamics*, v 8, p 717-724.

BAUMANN W.T., FU-SHENG HO, and H.H. ROBERTSHAW, "Active Structural Acoustic Control of Broadband Disturbances," *Journal of the Acoustical Society of America*, 1992, pp. 1998-2005.

BAZ, A. and S. POH. 1990. "Experimental Implementation of the Modified Independent Modal Space Control Method," *Journal of Sound and Vibration*, **139**(1), 133-149.

BAZ, A., S. POH, and J. GILHEANY. 1993. "A Multi-Mode Distributed Sensor for Vibrating Beams," *Journal of Sound and Vibration*, **165**(3), p. 481-495.

BERNSTEIN D.S., D.C. HYLAND. 1988. "Optimal Projection for Uncertain Systems (OPUS): A Unified Theory of Reduced-Order, Robust Control Design", *Large Space Structures: Dynamics and Control*, pp. 263-302.

BLEVINS R.D. 1995. *Formulas for Natural Frequency and Mode Shapes*, Krieger Publishing Company: Malabar, FL.

BOFILIOS, D. and LYRINTZIS, C. 1991. "Structure-Borne Noise Transmission into Cylindrical Enclosures of Finite Extent", *AIAA Journal*, **29**(8): 1193-1201.

BURKE, S. E. and J. E. HUBBARD. 1988. "Distributed Actuator Control Design for Flexible Beams," *Automatica*, **24**(5): 619-627.

BURKE, S. E. and J. E. HUBBARD. 1990A. "Distributed Transducer Control Design for Thin Plates," *Electro-Optical Materials for Switches, Coatings, Sensor Optics and Detectors*, SPIE Proc. 1307: 222-231.

BURKE, S. E. and J. E. HUBBARD. 1990B. "Distributed Transducers, Collocation, and Smart Structural Control," *Electro-Optical Materials for Switches, Coating, Sensor Optics, and Detectors*, SPIE Proc. 1307: 211-221.

BURKE, S. E. and J. E. HUBBARD. 1991. "Distributed Transducer Vibration Control of Thin Plates," *Journal of the Acoustical Society of America*, **90**(2): 937-944.

BURKE, S. E. and J. M. SULLIVAN. 1995A. "Distributed Transducer Shading via Spatial Gradient Electrodes," *Smart Structures and Materials 1995: Smart Structures and Integrated Systems*, SPIE, ed. I. Chopra, San Diego, CA, **2443**: 715-726.

BURKE, S. E. and J. M. SULLIVAN. 1995B. "Limitations of Large Area Piezoelectric Sensors Used for Structural Control," *Smart Structures and Materials 1995: Smart Structures and Integrated Systems*, SPIE, ed. I. Chopra, San Diego, CA, **2443**: 590-596.

BURKE, S. E. and R. L. CLARK. 1995C. "Transducer Tolerance Theory for Structural Control," *Smart Structures and Materials 1995: Smart Structures and Integrated Systems*, SPIE Proc. 2443: 410-421.

BURKE, S. E., and J. E. HUBBARD. 1987. "Active Vibration Control of a Simply Supported Beam Using a Spatially Distributed Actuator," *IEEE Control System Magazine*, **109**:25-30.

CALLAHAN, J. and H. BARUH. 1999. "Modal Sensing of Circular Cylindrical Shells Using Segmented Piezoelectric Elements," *Smart Materials and Structures*, **8**: 125-135.

CALLAHAN, J. and H. BARUH. 1995. "Modal Analysis Using Segmented Piezoelectric Sensors," *AIAA Journal*, **33**: 2371-2378.

CABELL R.H., H.C. LESTER, G.P. MATHUR, B.N. TRAN. 1993. "Optimization of Actuator Arrays for Aircraft Interior Noise Control," *1993 AIAA Aeroacoustics Conference*, AIAA Paper No. 93-4447.

CAZEAU, P. A. 1994. *The Implementation of Optimal Full State Feedback Using Area Averaging Sensors*, Masters of Science Thesis, Massachusetts Institute of Technology, Department of Aeronautical and Astronautical Engineering.

CHARETTE, F., A. BERRY, and C. GUIGOU. 1998. "Active Control of Sound Radiation from a Plate Using a Polyvinylidene Fluoride Volume Displacement Sensor," *Journal of the Acoustical Society of America*, **103**(3): 1493-1503.

CHEN, C.-K. and Y.-P. SHEN. 1997. "Optimal Control of Active Structures with Piezoelectric Modal Sensors and Actuators," *Smart Materials and Structures*, **6**: 403-409.

CHIANG, W.-W. and C.-K. LEE. 1989. "Critical Active Damping Control of a Flexible Slender Plate Using a Distributed Modal Actuator and Sensor," *Proceedings of the 1989 American Control Conference*, Pittsburgh, PA, **1**: 700-705.

CLARK R.L., M.R. FLEMMING, C.R. FULLER.1993. "Piezoelectric Actuators for Distributed Vibration Actuation of thin Plates: A Comparison Between Theory and Experiment," *Journal of Vibration and Acoustics*, July 1993, Vol. 115, pp. 332-339.

CLARK, R. L. 1995. "Adaptive Feedforward Modal Space Control," *Journal of the Acoustical Society of America*, **98**(5): 2639-2650.

CLARK, R. L. and C. R. FULLER. 1992A. "Modal Sensing of Efficient Acoustic Radiators with Polyvinylidene Fluoride Distributed Sensors in Active Structural Acoustic Control Approaches," *Journal of the Acoustical Society of America*, **91**(6): 3321-3329.

CLARK, R. L. and C. R. FULLER. 1992B. "Optimal Placement of Piezoelectric Actuators and Polyvinylidene Fluoride Error Sensors in Active Structural Acoustic Control Approaches," *Journal of the Acoustical Society of America*, **92**(3): 1521-1533.

CLARK, R. L. and C. R. FULLER. 1992C. "A Model Reference Approach for Implementing Active Structural Acoustic Control," *Journal of the Acoustical Society of America*, **92**(3): 1534-1544.

CLARK, R. L. and C. R. FULLER. 1994. "Active Control of Structurally Radiated Sound from an Enclosed Finite Cylinder," *Journal of Intelligent Material Systems and Structures*, **5**(3): 379-391.

CLARK, R. L. and S. E. BURKE. 1996. "Practical Limitations in Achieving Shaped Modal Sensors with Induced Strain Materials," *Journal of Vibration and Acoustics, Transactions of the ASME*, **118**: 668-675.

CLARK, R. L., C. R. FULLER, B. R. FOGG, W. V. MILLER, A. M. VENGSARKAR, AND R. O. CLAUS. 1991A. "Structural Acoustic Control Using Optical Fiber Sensors and Piezoelectric Actuators," *Proceedings of the International Symposium and Exhibition on Active Materials and Adaptive Structures*, Alexandria, VA.

CLARK, R. L., R. A. BURDISSO, and C. R. FULLER. 1993. "Design Approaches for Shaping Polyvinylidene Fluoride Sensors in Active Structural Acoustic Control (ASAC)," *Journal of Intelligent Material Systems and Structures*, **4**(3): 354-365.

CLARK, R. L., W. R. SAUNDERS, and G. P. GIBBS. 1998. *Adaptive Structures: Dynamics and Control*, John Wiley and Sons, Inc.: New York.

CLARK, R. W. and C. R. FULLER. 1991B. "Control of Sound Radiation with Adaptive Structures," *Journal of Intelligent Materials, Systems and Structures*, **2**(3): 431-452.

COLEMAN, T. F. and Y. LI. 1994. "On the Convergence of Reflective Newton Methods for Large-Scale Nonlinear Minimization Subject to Bounds," *Mathematical Programming*, **67**(2): 189-224.

COLLINS, S. A., C. E. PADILLA, R. J. NOTESTINE, and A. H. VON FLOTOW. 1992. "Design, Manufacture, and Application to Space Robotics of Distributed Piezoelectric Film Sensors," *Journal of Guidance, Control, and Dynamics*, **15**(2): 396-403.

COLLINS, S. A., D. W. MILLER, and A. H. VON FLOTOW. 1994. "Distributed Sensors as Spatial Filters in Active Structural Control," *Journal of Sound and Vibration*, **173**(4): 471-501.

COX, D. E., G. P. GIBBS, R. L. CLARK, and J. S. VIPPERMAN. 1999. "Experimental Robust Control of Structural Acoustic Radiation," *Journal of Vibration and Acoustics*, **121**: 433-439.

DICKEY J., G. MAIDANIK. 1991. "Active Control of Response of Ribbed Panels," *Recent Advances in Active Control of Sound and Vibration*, pp.525-533.

DOWELL, E. H. and Y. KUBOTA. 1985. "Asymptotic Modal Analysis and Statistical Energy Analysis," *Journal of Applied Mechanics*, **110**(3): 371-376.

FAHY, F. 1985. *Sound and Structural Vibration Radiation, Transmission and Response*, Academic Press: New York.

FLEMING, F. and E. CRAWLEY. 1991. "The Zeroes of Controlled Structures: Sensor/Actuator Attributes and Structural Modeling," *AIAA/ ASME/ ASCE/ AHS/ ASC Structures, Structural Dynamics, and Materials Conference*, 32nd, Baltimore, MD, Apr. 8-10, 1991, Technical Papers. Pt. 3 (A91-31826 12-39). Washington, DC, American Institute of Aeronautics and Astronautics, p. 1806-1816.

FLÜGGE, W. 1973. *Stresses in Shells*, Springer-Verlag: New York.

FOGG, B. R., W. V. MILLER, A. M. VENGSARKAR, R. O. CLAUS, R. L. CLARK, and C. R. FULLER. 1992. "Optical Fiber Sensors for Active Structural Acoustic Control," *Optical Engineering*, **31**(1): 28-33.

FRIPP, J. B., M.L. FRIPP, and D. M. FRIPP. 2000. *Speaking of Science: Notable Quotes on Science, Engineering, and the Environment*, LLH Technology Press: Eagle Rock, VA.

FRIPP, M. L., D. Q. O'SULLIVAN, S. R. HALL, N. W. HAGOOD, and K. LILIENKAMP. 1997. "Test-bed Design and Modeling for Aircraft Interior Acoustic Control," *Proceedings of SPIE, Smart Structures and Materials 1997: Smart Structures and Integrated Systems*, **3041**:88-99.

FRIPP, M. L., M. J. ATALLA, and N. W. HAGOOD. 2000. "Reconfigurable Arrays of Collocated Sensors and Actuators for Modal Isolation," To be published in the *Proceedings of SPIE, Smart Structures and Materials* 2000 and submitted to the *ASME Journal of Vibration and Acoustics*.

FRIPP, M.L., M.J. ATALLA, N.W. HAGOOD, C. SAVRAN, and S. TISTAERT. 1999. "Reconfigurable Arrays for Broadband Feedback Control of Aircraft Fuselage Vibrations," *10th International Conference on Adaptive Structures and Technologies*, Paris, France: 447-457.

FULLER C.R., S.D. SNYDER, C.H. HANSEN, R.J. SILCOX. 1992. "Active Control of Interior Noise in Model Aircraft Fuselages Using Piezoceramic Actuators," *AIAA Journal*, **30**(11): 2613-2617

FULLER, C. R., S. J. ELLIOTT, and P. A. NELSON. 1996. *Active Control of Vibration*, Academic Press: Boston.

GROCOTT, S. C. O. 1997. *Dynamic Reconstruction and Multivariable Control for Foce-Actuated, Thin Facesheet Adaptive Optics*, Doctoral of Philosophy, Massachusetts Institute of Technology, Department of Aeronautics and Astronautics.

GU. Y., R. L. CLARK, C. R. FULLER, and A. C. ZANDER. 1994. "Experiments on Active Control of Plate Vibration Using Piezoelectric Actuators and Polyvinylidene Fluoride (PVDF) Modal Sensors," *Journal of Vibration and Acoustics*, **116**(3): 303-308.

HAGOOD N.W., W.H. CHUNG, and A. VON FLOTOW. 1990. "Modelling of Piezoelectric Actuator Dynamics for Active Structural Control," *Journal of Intelligent Material Systems and Structures*, **1**: 327-354.

HANSEN C.H. and S.D. SNYDER. 1991. "Effect of Geometric and Structural/Acoustic Variables on the Active Control of Sound Radiation from a Vibrating Surface", *Recent Advances in Active Control of Sound and Vibration*, pp.487-505.

HENRY, J.K. and R.L. CLARK. 1999a. "Smart Aircraft Panels: The Effects of Internal Pressure Loading on Panel Dynamics," Proceedings of *SPIE's 6th Annual International Symposium on Smart Structures and Materials*, Newport Beach, CA. Paper 3668-09.

HENRY, J.K. and R.L. CLARK. 1999b. "Structural Acoustic Control of a Cylindrical Enclosure: Analysis of Structural Acoustic Coupling," Proceedings of *Active99*, Fort Lauderdale, FL., December 2-4.

HOVD M. and S. SKOGESTAD. 1994. "Sequential Design of Decentralized Controllers", *Automatica*, **30**(10): 1601-1607.

HOW J.P. 1990. *Local Control Design Methodologies for a Hierarchic Control Architecture*, Masters of Science Thesis, Massachusetts Institute of Technology, Department of Aeronautics and Astronautics, (Space Systems Laboratory Report #5-90).

JACKSON A.C., F.J. BALENA, W.L. LABARGE, G. PEI, W.A. PITMAN, and G. WITTLIN. 1986. *Transport Composite Fuselage Technology - Impact Dynamics and Acoustic Transmission*, NASA Contractor Report 4035.

JOHNSON, M. E. and S. J. ELLIOTT. 1993. "Volume Velocity Sensors for Active Control," *Proceedings of the Institute for Acoustics*, **15**(3): 411-420.

JOHNSON, M. E. and S. J. ELLIOTT. 1995. "Experiments on the Active Control of Sound Radiation Using a Volume Velocity Sensor," *Proceedings of SPIE 1995: Smart Structures and Integrated Systems*, 2443: 658-669.

JUNGER, M. C. and D. FEIT. 1993. *Sound, Structures, and Their Interaction*, Acoustical Society of America and the American Institute of Physics: Melville, NY.

KOHNKE P. 1992. "ANSYS User's Manual, Theory," Swanson Analysis Systems, Inc.: Houston, PA.

KOLLAR, I. 1995. *Frequency Domain System Identification Toolbox User's Guide*, The Math Works, Inc: Natick, MA.

LAMAIRE, R. O., L. VALAVANIS, M. ATHANS, and G. STEIN. 1991. "A Frequency-domain Estimator for Use in Adaptive Control Systems," *Automatica*, **27**(1): 23-28.

LEE, C.-K. and F. C. MOON. 1990. "Modal Sensors/Actuators," *Journal of Applied Mechanics*, **57**: 434-441.

LEE, C.-K., W.-W. CHIANG, and T. C. O'SULLIVAN. 1989. "Piezoelectric Modal Sensors and Actuators Achieving Critical Active Damping on a Cantilever Plate," *AIAA, ASME, ASCE, AHS, and ASC, Structures, Structural Dynamics and Materials Conference*, 30th, Mobile, AL, Apr. 3-5, 1989, Technical Papers. Part 4 (A89-30651 12-39). Washington, DC, American Institute of Aeronautics and Astronautics, 1989, p. 2018-2026.

LEE, C.-K., W.-W. CHIANG, and T. C. O'SULLIVAN. 1991. "Piezoelectric Modal Sensor/Actuator Pairs for Critical Active Damping Vibration Control," *Journal of the Acoustical Society of America*, **90**(1): 374-384.

LEISSA, A. W. 1973. *Vibration of Shells*, National Aeronautics and Space Administration: Washington, D.C., NASA SP-288.

LEO, D. J. and J. P. HOW. 1997. "Reconfigurable Actuator-Sensor Arrays for the Active Control of Sound," *Smart Structures and Materials 1997 – Smart Structures and Integrated Systems*, SPIE Proceedings, **3041**: 100-111.

LIVELY, P. S. 2000. *Dynamic Structural Shape Estimation Using Integral Sensor Arrays*, Masters of Science Dissertation, Massachusetts Institute of Technology, Department of Aeronautical and Astronautical Engineering.

LIU, K., R. N. JACQUES, and D. W. MILLER. 1996. "Frequency Domain Structural System Identification by Observability Range Space Extraction," *ASME Journal of Dynamic Systems, Measurement, and Control*, **118**(2): 211-220.

LYON, R. H. 1975. *Statistical Energy Analysis of Dynamical Systems: Theory and Application*, MIT Press: Cambridge, MA.

MAC MARTIN, D. G. 1995. "Collocated Structural Control: Motivation and Methodology," *Proceedings of the 4th IEEE Conference on Control Applications*, Albany, NY: 1092-1097.

MACMARTIN D.G., G.L. Basso, B. Leigh. 1994. "Noise Transmission and Reduction in Turboprop Aircraft," *78th AGARD Meeting*, pp. 21-29.

MACMARTIN D.G. 1996. United Technologies Research Center, Personal correspondance, June.

MAILLARD, J. 1997. *Advanced Time Domain Sensing for Active Structural Acoustic Control*, Doctor of Philosophy Dissertation, Virginia Polytechnic Institute and State University, Department of Mechanical Engineering. Available at http://etd.vt.edu/.

MAILLARD, J. P. and C. R. FULLER. 1994A. "Advanced Time Domain Wave-Number Sensing for Structural Acoustic Systems. I. Theory and Design," *Journal of the Acoustical Society of America*, **95**(6): 3252-3261.

MAILLARD, J. P. and C. R. FULLER. 1994B. "Advanced Time Domain Wave-Number Sensing for Structural Acoustic Systems. II. Active Radiation Control of a Simply Supported Beam," *Journal of the Acoustical Society of America*, **95**(6): 3262-3272.

MAILLARD, J. P. and C. R. FULLER. 1995. "Advanced Time Domain Wave-Number Sensing for Structural Acoustic Systems. Part III. Experiments on Active Broadband Radiation Control of a Simply Supported Plate," *Journal of the Acoustical Society of America*, **98**(5): 2613-2621.

MAILLARD, J. P. and C. R. FULLER. 1998. "Comparison of Two Structural Sensing Approaches for Active Structural Acoustic Control," *Journal of the Acoustical Society of America*, **103**(1): 396-400.

MAINS, M. and H. VOLD. 1995. "Investigation of the Effects of Transducer Cross-Sensitivity and Misalignment Error on Modal Vector Correlation," *Proceedings of the 13th International Modal Analysis Conference*, Nashville, TN, **2**: 1048-1056.

MATHUR G.P., B.N. TRAN. 1993. "Aircraft Cabin Noise Reduction Tests Using Active Structural Acoustic Control," *1993 AIAA Aeroacoustics Conference*, AIAA Paper No. 93-4437.

MEASUREMENT SPECIALTIES, INC. 1999. Valley Forge, PA. http://www.msiusa.com.

MEIROVITCH, L. 1967. *Analytical Methods in Vibrations*, The Macmillan Company: New York.

MEIROVITCH, L. 1986. *Elements of Vibration Analysis*, McGraw-Hill: New York.

MEIROVITCH, L. and H. BARUH. 1981. "On the Problem of Observation Spillover in Distributed-Parameter Systems," Journal of Optimization Theory and Applications, v 39 n2; 1981, p 611-620.

MEIROVITCH, L. and H. BARUH. 1982. "Control of Self-Adjoint Distributed-Parameter Systems," *Journal of Guidance Control & Dynamics*. **5**(1): 60-66.

MEIROVITCH, L. and H. BARUH. 1983B. "Robustness of the Independent Modal-Space Control Method," *Journal of Guidance Control & Dynamics*, v6, p 20-25.

MEIROVITCH, L. and H. BARUH. 1985. "The Implementation of Modal Filters for Control of Structures," *Journal of Guidance Control & Dynamics*. v 8 n 6; Nov-Dec 1985, p 707-716 .

MEIROVITCH, L., H. BARUH, and H. OZ. 1983A. "A Comparison of Control Techniques for Large Flexible Systems," Journal of Guidance Control & Dynamics. v6, p 302-310.

MIDÉ TECHNOLOGY CORPORATION. 1999. Cambridge, MA. http://www.mide.com/

MILLER, D. W., S. A. COLLINS, and S. P. PELTZMAN. 1990. "Development of Spatially Convolving Sensors for Structural Control Applications," *AIAA/ ASME/ ASCE/ AHS/ ASC Structures, Structural Dynamics and Materials Conference*, 31st, Long Beach, CA, Apr. 2-4, 1990, Technical Papers. Part 4 (A90-29409 11-39). Washington, DC, American Institute of Aeronautics and Astronautics, 1990, p. 2283-2297.

MILLER, S. E., H. ABRAMOVICH, and Y. OSHMAN. 1997. "Experimental Validation of a Modal Transducer for an Orthotropic Rectangular Plate," *AIAA/ ASME/ ASCE/ AHS/ ASC Structures, Structural Dynamics, and Materials Conference – Adaptive Structures Forum*, **1**: 471-481.

MORGAN, D. R. 1990. "An Adaptive Modal-Based Active Control System," *Journal of the Acoustical Society of America*, 89(1): January 1991, p 248-256.

NIESEL G., E. LAUDIEN. 1994. "Helicopter Internal Noise," *78th AGARD Meeting*, pp. 2-11.

O'SULLIVAN, D. Q. 1998. *Aircraft Interior Structural-Acoustic Control Design*, Masters of Science Dissertation, Massachusetts Institute of Technology, Department of Mechanical Engineering.

PINES, D. J. and A. H. VON FLOTOW. 1997A. "Spatially Convolving Wave Propagation Sensors for Structural Control – Part I: Analytical Development for One-Dimensional Structures," *Journal of Intelligent Material Systems and Structures*, **8**(11): 929-952.

PINES, D. J. and A. H. VON FLOTOW. 1997B. "Spatially Convolving Wave Propagation Sensors for Structural Control – Part II: Experimental Verification Using PVDF Sensors," *Journal of Intelligent Material Systems and Structures*, **8**(12): 1059-1072.

POH, S. and A. BAZ. 1996. "Distributed Sensor for Rectangular Plates," *Proceedings of SPIE Conference on Smart Sensing, Processing, and Instrumentation* **2718** p. 355-373.

PRAKASH, B. G. 1980. "Free Vibration of Rectangular Plates," Journal of Sound and Vibration, v 70, p 303-305.

PREUMONT, A. 1997. *Vibration Control of Active Structures: An Introduction*, Kluwer Academic Publishers: Boston, MA.

PREUMONT, A. and A. FRANCOIS. 1999. "Piezoelectric Array Sensing for Real-Time, Broad-Band Sound Radiation Measurement," *Proceedings of the 10th International Conference on Adaptive Structures and Technologies – ICAST'99*, Paris, France.

PREUMONT, A., A. FRANÇOIS, and S. DUBRU. 1999. "Piezoelectric Array Sensing for Real-Time, Broad-Band Sound Radiation Measurement," *Transactions of the ASME*, **121**: 446-452.

RAO, S. S.. 1990. *Mechanical Vibrations*, Addison-Wesley Publishing Company, Inc.: New York.

RAYLEIGH, J.W.S. 1896. *The Theory of Sound*, The Macmillan Company: New York.

REX, J. and S. J. ELLIOTT. 1992. "The QWSIS – A New Sensor for Structural Radiation Control," *1st International Conference on Motion and Vibration Control*, Yokohama: 339-343.

ROSARIO, R. del. 1995. *Numerical Approximation of Thin Shell Dynamics*, Masters of Science Dissertation, Iowa State University, Department of Applied Mathematics.

ROSSETTI D.J., M.A. NORRIS. 1994. "A Comparison of Actuation and Sensing Techniques for Aircraft Cabin Noise Control," *1994 AIAA Aeroacoustics Conference*, AIAA Paper No. 94-1738.

SAVRAN, C. 2000. Massachusetts Institute of Technology, Personal communications.

SAVRAN, C. A., M. J. ATALLA, and S. R. HALL. 2000. "Broadband Active Structural-Acoustic Control of a Fuselage Test-Bed Using Collocated Piezoelectric Sensors and Actuators," To be published in the *Proceedings of SPIE, Smart Structures and Materials 2000.*

SCHULTZ, J. F., R. W. ROST, and S. J. SHELLEY. 1997. "Adaptive Modal Space Control of Flexible Structures: Applications," *Proceedings of the 15th International Modal Analysis Conference – IMAC*, 745-751.

SHELLEY, S. J. 1991A. *Investigation of Discrete Modal Filters for Structural Dynamic Applications*, Doctor of Philosophy Dissertation, University of Cincinnati, Department of Mechanical, Industrial, and Nuclear Engineering.

SHELLEY, S. J., K. L. LEE, T. AKSEL, and A. E. AKTAN. 1995. "Active-Control and Forced-Vibration Studies on Highway Bridge," *Journal of Structural Engineering*, **121**(9): 1306-1312.

SHELLEY, S. J., L. C. FREUDINGER, and R. J. ALLEMANG. 1992. "Development of an On-Line Parameter Estimation System Using the Discrete Modal Filter," *Proceedings of the 10th International Modal Analysis Conference - IMAC*, **1**: 173-183.

SHELLEY, S. J., L. C. FREUDINGER, and R. J. ALLEMANG. 1993B. "Development of an On-Line Modal State Monitor," *Proceedings of the 11th International Modal Analysis Conference – IMAC*, **1**: 606-612.

SHELLEY, S. J., R. J. ALLEMANG, G. L. SLATER, and J. F. SCHULTZE. 1993A. "Active Vibration Control Utilizing an Adaptive Modal Filter Based Modal Control Method," *Proceedings of the 11th International Modal Analysis Conference – IMAC*, **1**: 751-758.

SHELLEY, S., H. VOLD, M. MAINS, and T. SHARP. 1997. "Structural Control and Monitoring Using Adaptive Spatio-Temporal Filtering," *Proceedings of the 15th International Modal Analysis Conference – IMAC*, 732-738.

SHELLEY, S., L. FREUDINGER, R. J. ALLEMANG, and Q. ZHANG. 1991B. "Implementation of a Modal Filter on a Five Meter Truss Structure," *Proceedings of the 9th International Modal Analysis Conference*, **2**: 1036-1044.

SIMPSON M., B. TRAN. 1993. "Aircraft Cabin Active Noise Control Performance Sensitivity Tests," *1993 AIAA Aeroacoustics Conference*, AIAA Paper No. 93-4436.

SIMPSON M.A., G.P. MATHUR, M.R. CANNON, B.N. TRAN, P.L. BURGE. 1991. "Fuselage Shell and Cavity Response Measurements on a DC-9 Test Section," NASA Contractor Report 187557.

SIMPSON M.A., P.M. DRUEZ, A.J. KIMBROUGH, M.P. BROCK, P.L. BURGÉ, G.P. MATHUR, M.R. CANNON, and B.N. TRAN. 1989. "UHB Demonstrator Interior Noise Control Flight Tests and Analysis," NASA Contractor Report 181897.

SLATER, G. L. and S. SHELLEY. 1993C. "Health Monitoring of Flexible Structures Using Modal Filter Concepts," *Smart Structures and Intelligent Systems*, SPIE vol. 1917: 997-1008.

SNYDER, S. D., C. H. HANSEN, and N. TANAKA. 1993. "Shaped Vibration Sensors for Feedforward Control of Structural Radiation," *Proceedings of the Second Conference on Recent Advances in Active Control of Sound and Vibration*, Blacksburg, VA: 177-188.

SNYDER, S. D., N. TANAKA, and Y. KIKUSHIMA. 1995. "The Use of Optimally Shaped Piezoelectric Film Sensors in the Active Control of Free Field Structural Radiation, Part 1: Feedforward Control," *Transactions of the ASME Journal of Vibration and Acoustics*, **117**: 311-322.

SNYDER, S. D., N. TANAKA, and Y. KIKUSHIMA. 1996. "The Use of Optimally Shaped Piezoelectric Film Sensors in the Active Control of Free Field Structural Radiation, Part 2: Feedback Control," *Transactions of the ASME Journal of Vibration and Acoustics*, **118**:112-121.

STÖBENER, U. and L. GAUL. 1998. "Active Control of Plate Vibration by Discrete PVDF Actuator and Sensor Segments," *International Conference on Adaptive Structures and Technologies – ICAST*, Boston, MA, Oct 14-16, Technomic Publishing Co.: Lancaster, PA, p 349-358.

STRANG, G. 1986. *Introduction to Applied Mathematics*, Wellesley-Cambridge Press: Wellesley, MA.

STRANG, G. 1993. *Introduction to Linear Algebra*, Wellesley-Cambridge Press: Wellesley, MA.

SULLIVAN, J. M., J. E. HUBBARD, and S. E. BURKE. 1994. "Distributed Transducer Design for Plates: Spatial Shape and Shading as Design Parameters," *Smart Structures and Materials 1994: Mathematics and Control in Smart Structures*, SPIE, ed. H. Banks, Orlando, FL, **2192**: 132-144.

SULLIVAN, J. M., J. E. HUBBARD, and S. E. BURKE. 1996. "Modeling Approach for Two-Dimensional Distributed Transducers of Arbitrary Spatial Distribution," *Journal of the Acoustical Society of America*, **99**: 2965-2974.

SULLIVAN, J. M., J. E. HUBBARD, and S. E. BURKE. 1997. "Distributed Sensor/Actuator Design for Plates: Spatial Shape and Shading as Design parameters," *Journal of Sound and Vibration*, **203**(3): 473-493.

SULLIVAN, J. M., S. E. BURKE, and J. E. HUBBARD. 1995. "Experimental Demonstration of Active Broadband Vibration Suppression of a Rectangular Plate Using Gain-Weighted, Shaped Distributed Transducers," *AIAA/ ASME/ ASCE/ AHS Structures, Structural Dynamics & Materials Conference – Collection of Technical Papers*, **5**: 668-674.

SUMALI, H. 1998. "Measuring Deflection Rate with an Array of Strain Sensors," *Proceedings of the ASME Dynamics Systems and Control Division – 1998*, ed. R. Furness, ASME: New York, **64**: 623-628.

SUMALI, H. and H. CUDNEY. 1993. "Segmented Two-Dimensional Modal-Filtering Sensors," *Vibration and Control of Mechanical System*, ed. C. A. Tan and L. A. Bergman, ASME: New York, **61**: 59-66.

SUMALI, H. and H. H. CUDNEY. 1991. "Experimental Investigation of Piezoelectric Film Used as Modal Sensors," Proceedings of the International Modal Analysis Conference – IMAC: Schenectady, NY, v 2; p 1174-1180.

SUMALI, H., H. H. CUDNEY, K. MEISSNER. 1997. "Numerical and Experimental Analyses of Segmented Modal Sensors," *Adaptive Structures and Materials Systems*, ed. D. Brei and J. Sirkis, ASME: New York, **54**: 91-98.

SUNG, C. K., T. F. CHEN, and S. G. CHEN. 1996. "Piezoelectric Modal Sensor/Actuator Design for Monitoring Generating Flexural and Torsional Vibrations of Cylindrical Shells," *Journal of Vibration and Acoustics, Transactions of the ASME*, **118**: 48-55.

TANG, Y. 1993. "Adaptive Frequency Response Identification Using the Lagrange Filter," *Automatica*, **29**(2): 451-455.

TANG, Y. and R. ORTEGA. 1993. "Adaptive Tuning to Frequency Response Specification," *Automatica*, **29**(6): 1557-1563.

TANAKA, N., S. D. SNYDER, and C. H. HANSEN. 1996. "Distributed Parameter Modal Filtering Using Smart Sensors," *Journal of Vibration and Acoustics – Transactions of the ASME*, **118**: 630-640.

TZOU, H. S. and C. I. TSENG. 1990. "Distributed Piezoelectric Sensor/Actuator Design for Dynamic Measurement/Control of Distributed Parameter Systems: A Piezoelectric Finite Element Approach," *Journal of Sound and Vibration*, **138**(1): 17-34.

UEBELHART, S. 2000. *Model Quality Management in Flexible Space Telescopes*, Masters of Science Dissertation, Massachusetts Institute of Technology, Department of Aeronautical and Astronautical Engineering.

VAN SCHOOR, M. and C. BLAUROCK. 1999. *Area Averaging Sensors: Phase II Final Report*, Midé Technology Corporation: Cambridge, MA.

VANDEPITTE, D. and P. SAS. 1990. "Sensitivity of Spatial Strain Distribution to Modal Parameters," *International Modal Analysis Conference*, 8th, Kissimmee, FL, Jan. 29-Feb. 1, 1990, Vol. 2, p. 774-779.

VON FLOTOW, A. H. 1988. "The Acoustic Limit of Control of Structural Dynamics," in *Large Space Structures: Dynamics and Control*, S. N. Atluri and A. K. Amos, eds. New York: Springer-Verlag: 213-237.

WEEMS D. 1996. Boeing Helicopter, Personal communications.

WILSON, D., J. ANDERSON, R. REMPT, and R. IKEGAMI. 1990. "Shape Memory Alloys and Fiber Optics for Flexible Structure Control," *Proceedings of SPIE Conference on Fiber Optic Smart Structures and Skins III* **1370**: 286-295.

YOUNG K.D. 1990. "A Hierarchical Approach to Large Space Structure Control", *Dynamics of Flexible Structures in Space - 1st International Conference*, pp. 183-196.

YUNG, J. H. and E. F. CRAWLEY. 1999. "Compensation Methodologies for Local Control using Strain Actuators and Sensors," *Smart Structures and Integrated Systems; Proceedings of the Meeting*, Newport Beach, CA, March 1-4, 1999. Pt 2, Society of the Photo-Optical Instrumentation Engineers: Bellingham, WA, (SPIE Proceedings Vol. 3668): p 913-924.

ZHANG, Q., C. Y. SHIH, and R. J. ALLEMANG. 1989. "Orthogonality Criterion for Experimental Modal Vectors," *Vibration Analysis – Techniques and Applications*, ASME Publication DE, 18(4): p 251-258.

ZHANG, Q., R. J. ALLEMANG, and D. L. BROWN. 1990. "Modal Filter: Concept and Applications," *Proceedings of the International Modal Analysis Conference – IMAC*: 487-496.

ZHOU, N., H. SUMALI, and H. CUDNEY. 1991. "Experimental Development of Piezofilm Modal Sensors and Characterization of Piezofilm Strain Rate Gages," *AIAA/ ASME/ ASCE/ AHS/ ASC Structures, Structural Dynamics, and Materials Conference*, Baltimore, MD, **1**: 735-743.

APPENDIX A

Deflection Shapes

Although this may seem a paradox,
all exact science is dominated by the idea of approximation.
- Bertrand Russell

Some of the deflection shapes of the representative test-bed were experimentally measured with a scanning laser vibrometer. A scanning laser vibrometer uses a laser to measure of the out-of-plane displacements at discrete points on a structure. An array of point measurements from a known disturbance source is combined to create a picture of the modal deflection. Deflection shapes from a speaker disturbance and from a surface mounted piezoceramic disturbance were measured.

This chapter presents deflection shapes instead of true mode shapes. Mode shapes are the eigen-vectors of the system and are independent of the excitation; they are the homogenous solution to the eigen-problem. Deflection shapes are composed of mode shapes and are weighted by the nature of the excitation. At resonances, the deflection shape will be close approximation of the mode shape corresponding to that resonance.

A.1 Speaker Excitation Deflection Shapes

Deflection shapes of the fuselage test-bed are presented below. The excitation was a speaker approximately 2 meters from the test-bed. A broadband excitation ranging from 40 Hz to 2 kHz was used to excite the structural vibrations. A high-resolution scan was conducted in the central region and a low-resolution scan was conducted over the rest of the fuselage. The different scan densities allows for efficient representation of both the global modes and the local panel modes.

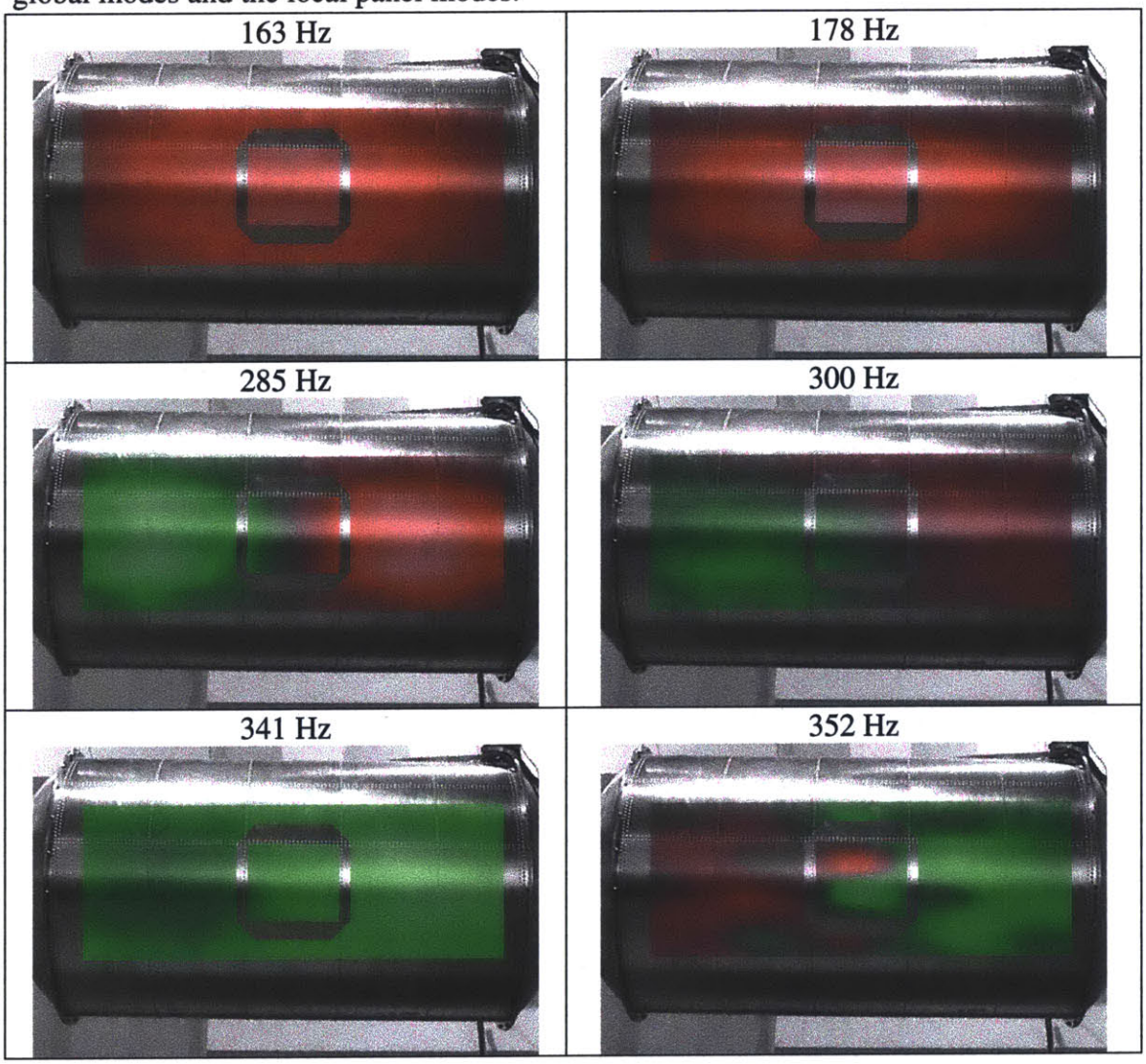

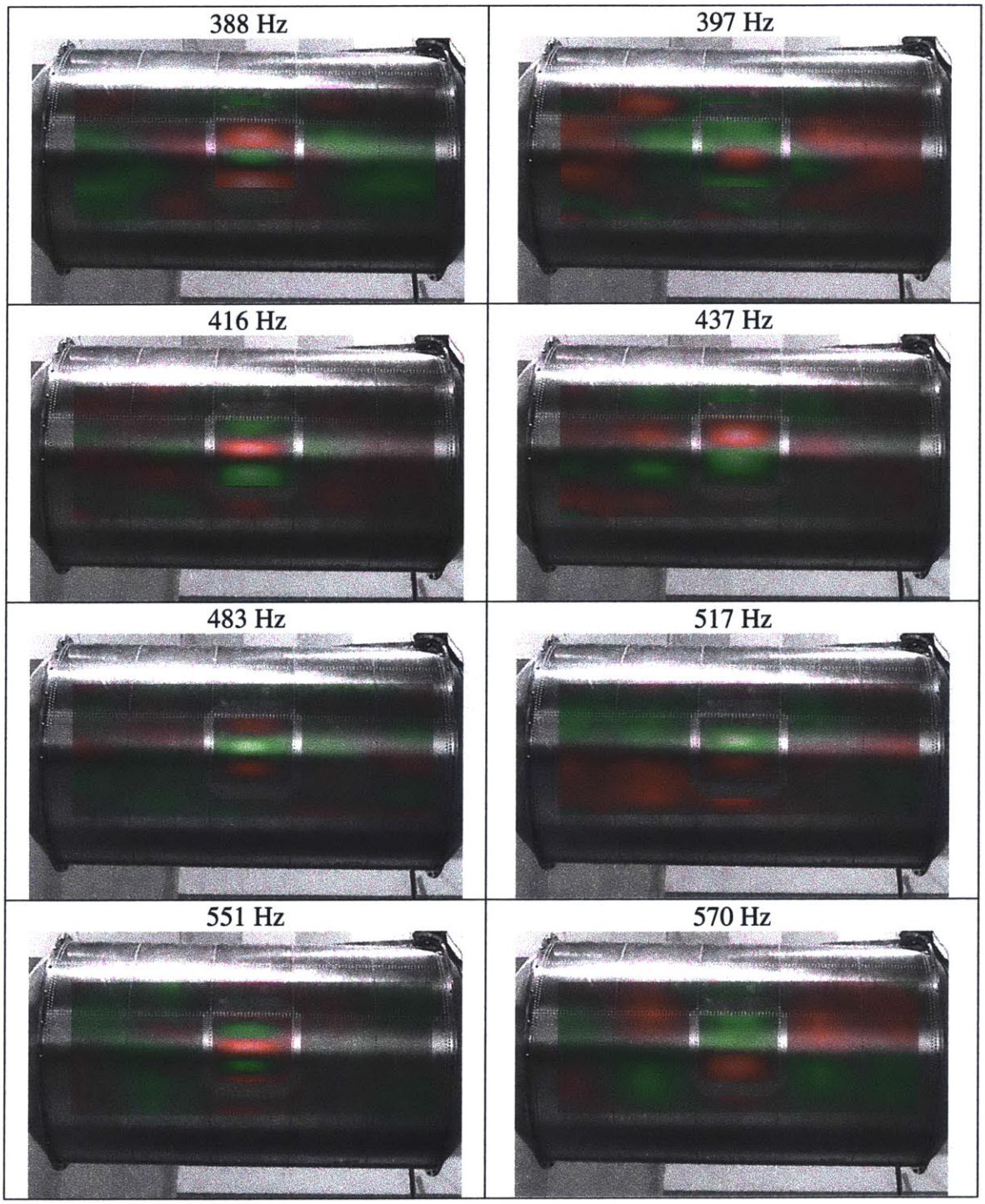
388 Hz
397 Hz
416 Hz
437 Hz
483 Hz
517 Hz
551 Hz
570 Hz

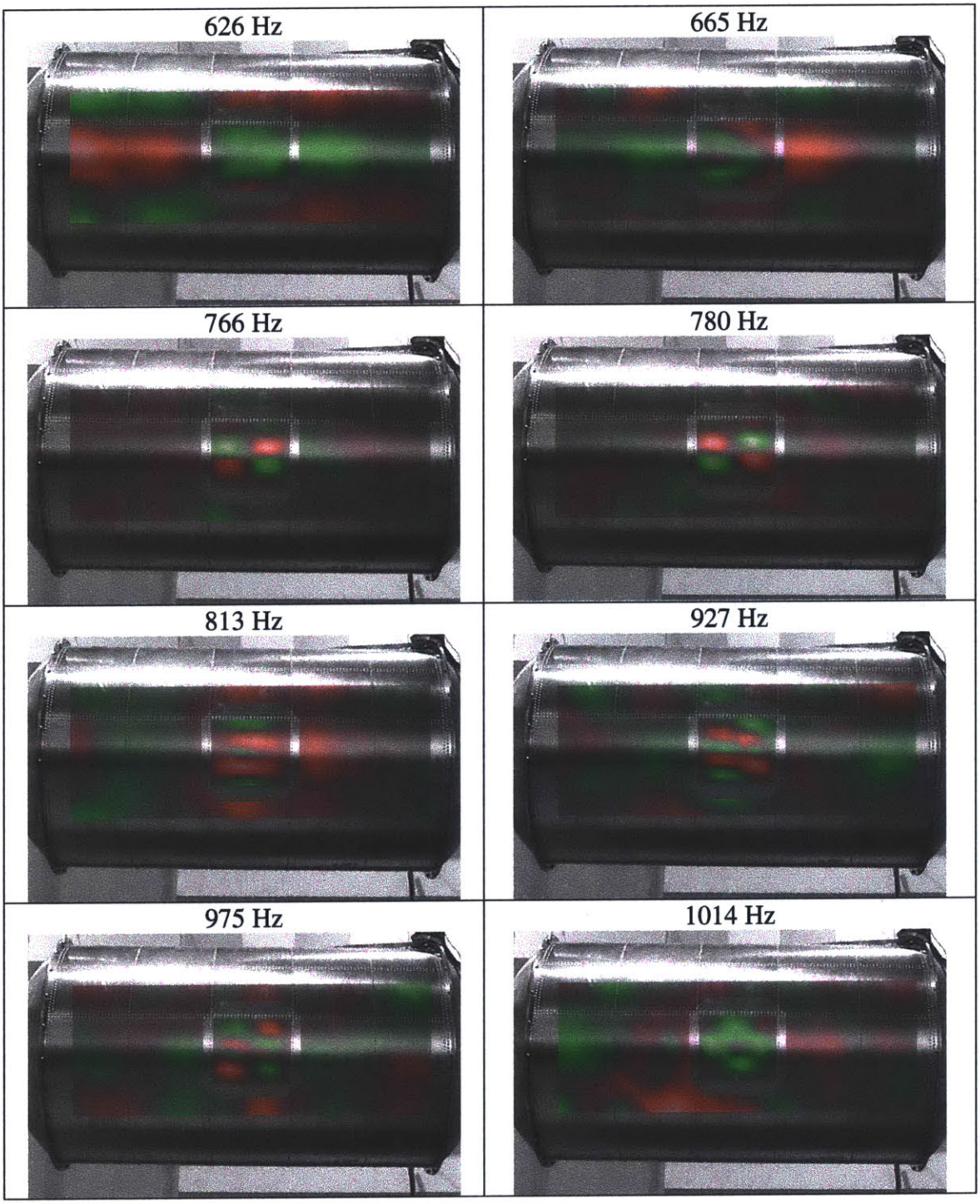
626 Hz
665 Hz
766 Hz
780 Hz
813 Hz
927 Hz
975 Hz
1014 Hz

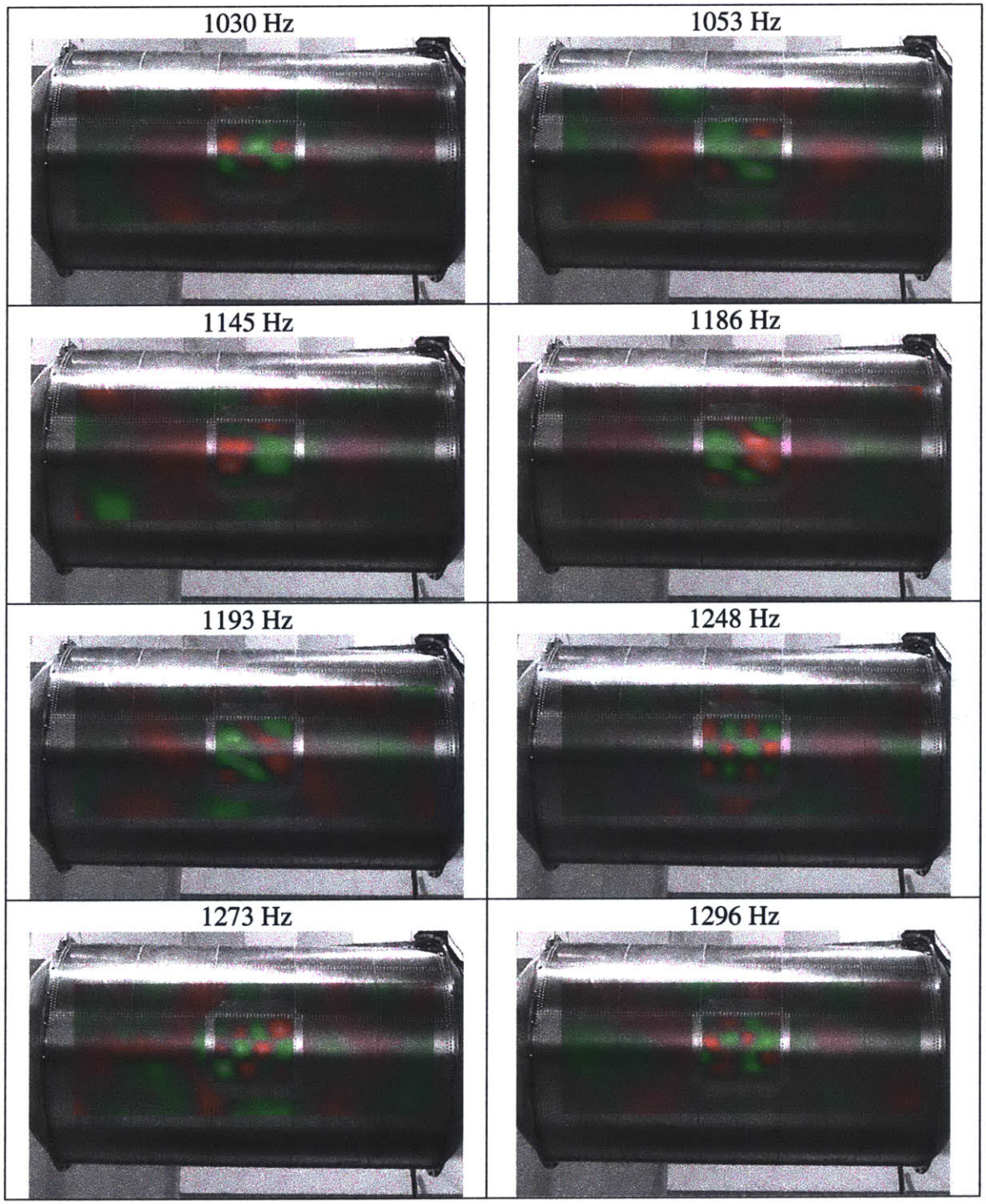
1030 Hz
1053 Hz
1145 Hz
1186 Hz
1193 Hz
1248 Hz
1273 Hz
1296 Hz

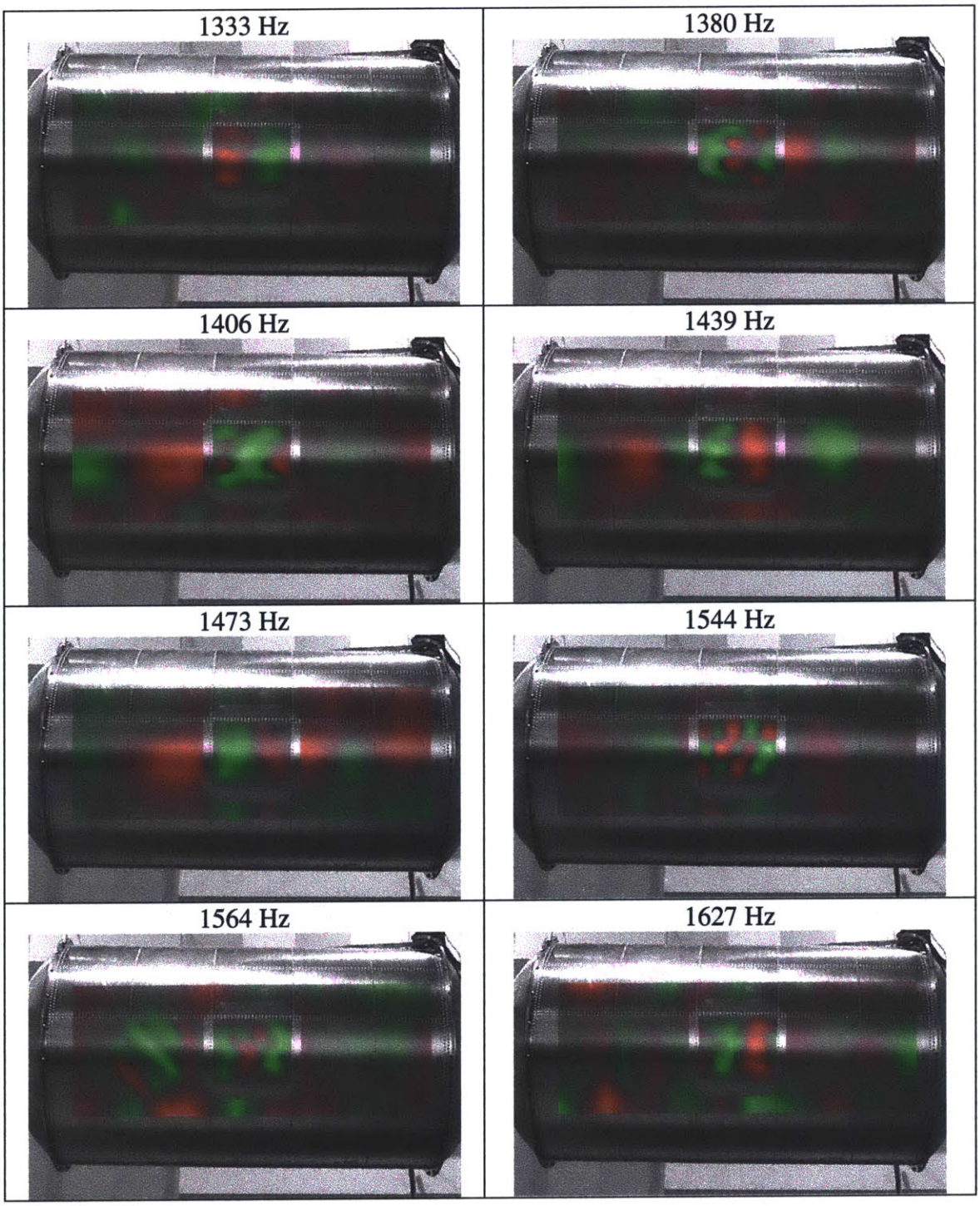
1333 Hz
1380 Hz
1406 Hz
1439 Hz
1473 Hz
1544 Hz
1564 Hz
1627 Hz

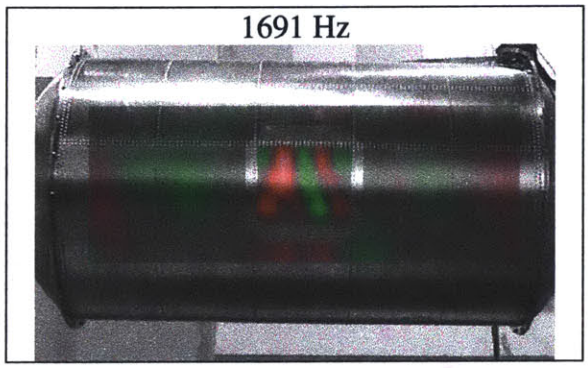

A.2 Piezoceramic Excitation Deflection Shapes

Deflection shapes of the fuselage test-bed are presented below. The excitation was two piezoceramic wafers mounted on the panel. These images illuminate the modal coupling between the panels. A broadband excitation ranging from 40 Hz to 2 kHz was used to excite the structural vibrations. A high-resolution scan was conducted over the entire fuselage test-bed. Low coherence was obtained for points at the top and bottom of the scanned region; hence, the mode shapes along the top and bottom should be viewed with discretion.

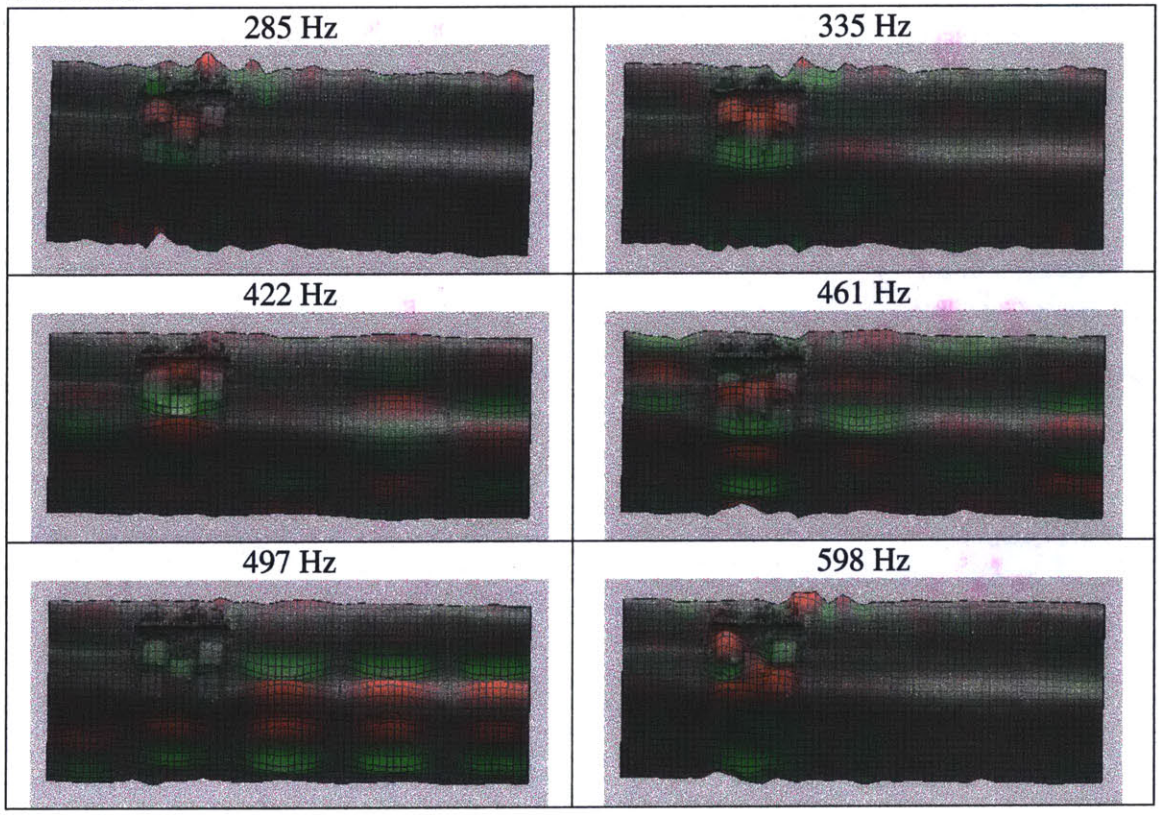

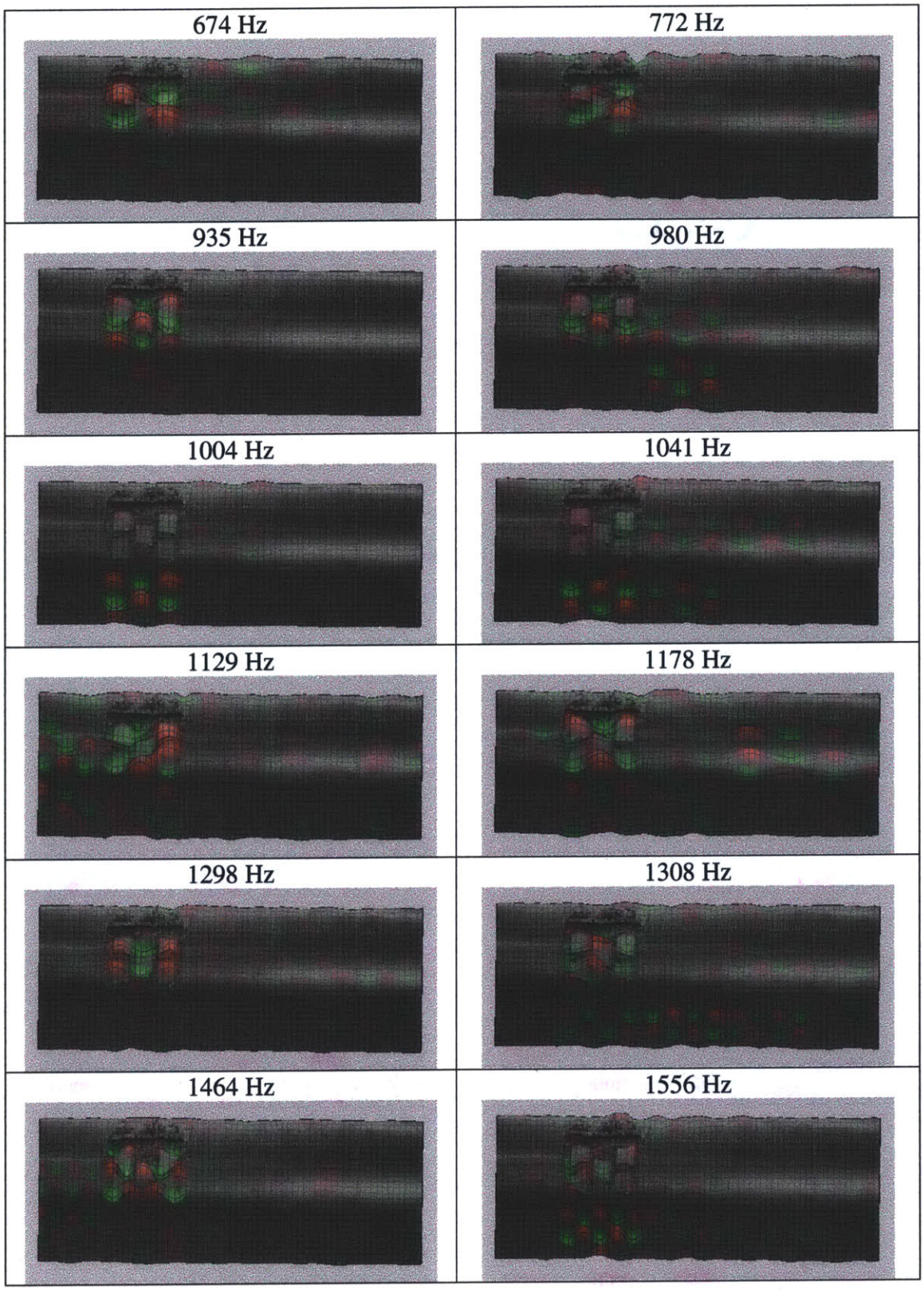
674 Hz
772 Hz
935 Hz
980 Hz
1004 Hz
1041 Hz
1129 Hz
1178 Hz
1298 Hz
1308 Hz
1464 Hz
1556 Hz

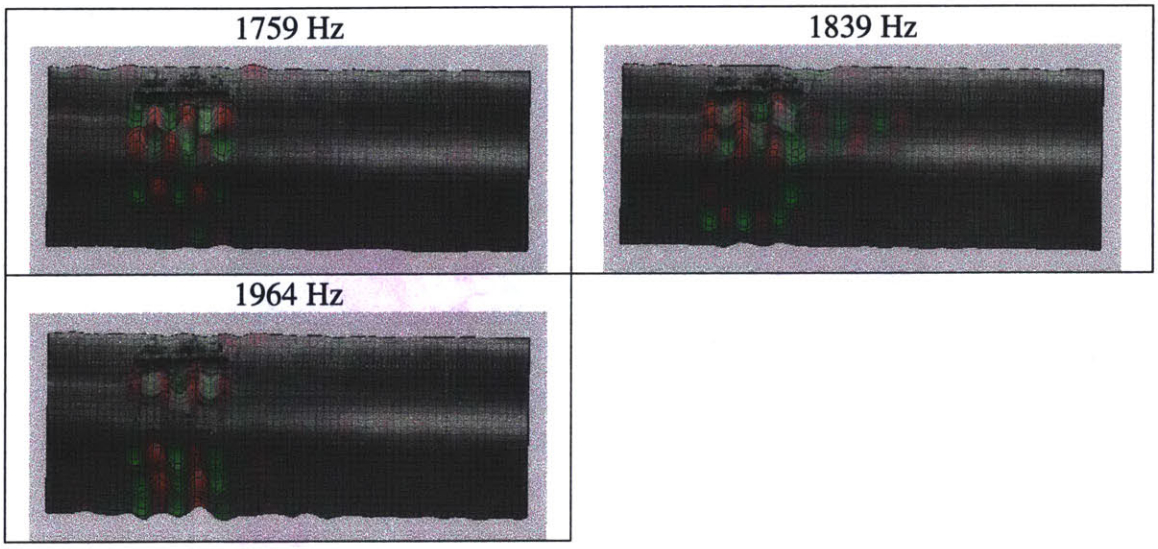

A.3 Deflection Shapes of the Curved Panel

The deflection shapes of the single panel test-bed are presented below. The excitation was a piezoceramic wafer mounted on the left of the picture. These mode shapes illuminate the modes of vibration of the curved panel. A broadband excitation ranging from 40 Hz to 2.5 kHz was used to excite the structural vibrations. Deflections along the edges of the plate indicate the presence of complicated boundary conditions. Note that these images do not include the sensing and actuation layers on the plate. These layers will add extra stiffness, extra compliance, and extra damping to the structure and may significantly alter the dynamics.

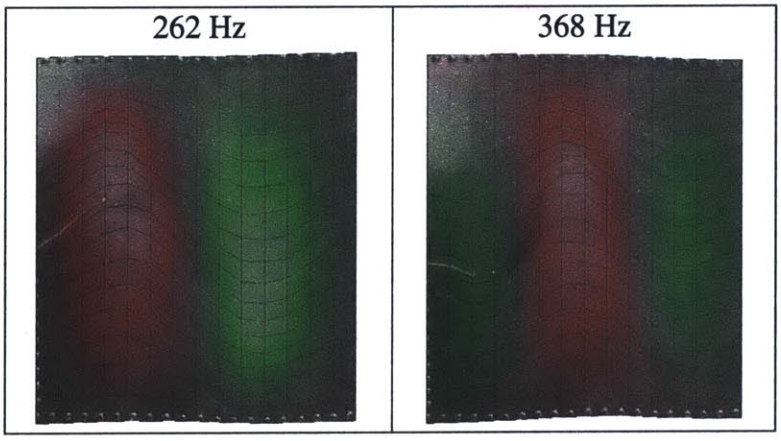

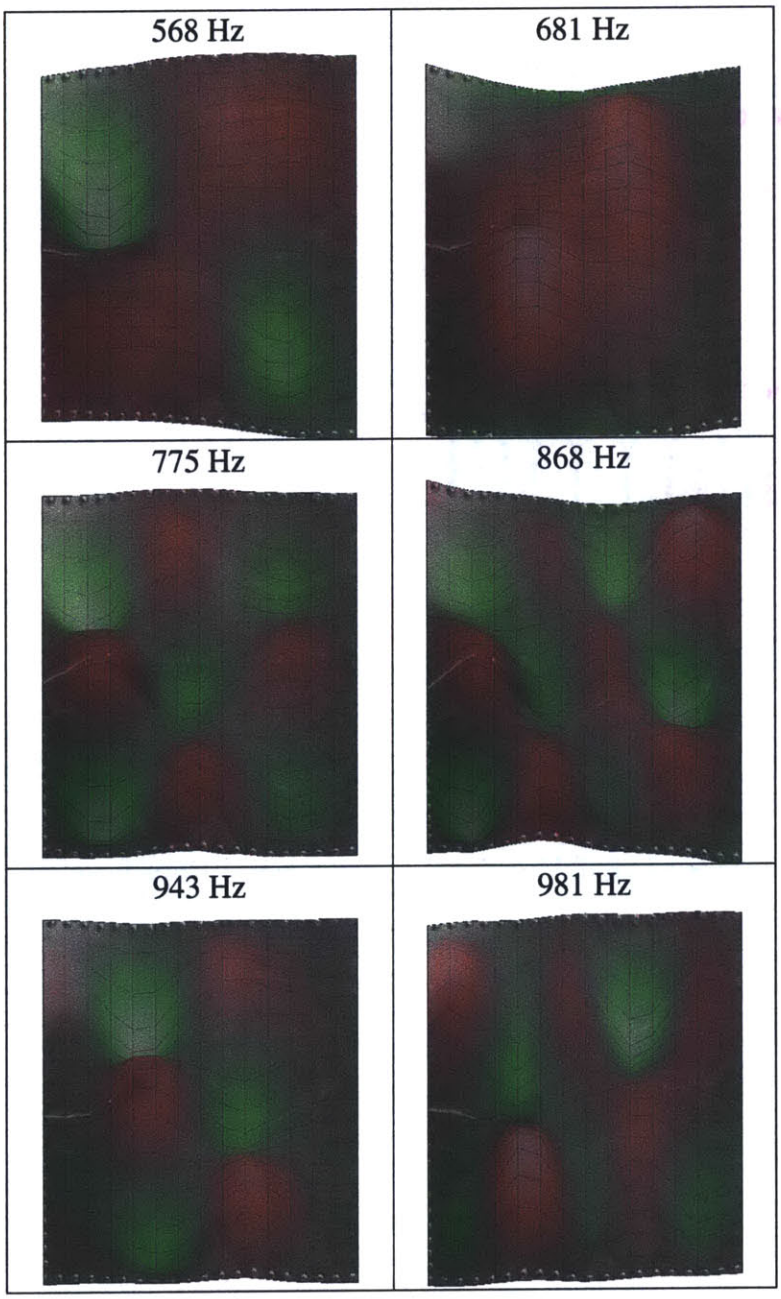
568 Hz
681 Hz
775 Hz
868 Hz
943 Hz
981 Hz

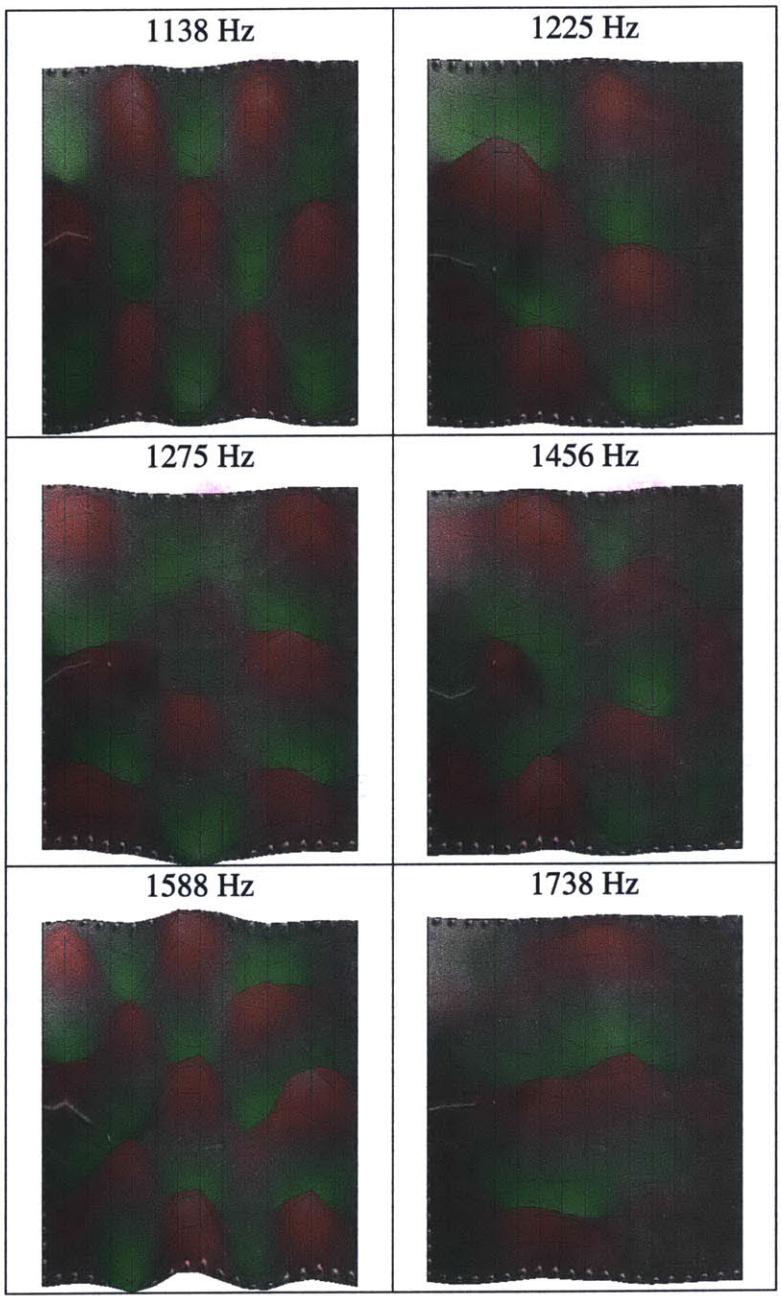
1138 Hz
1225 Hz
1275 Hz
1456 Hz
1588 Hz
1738 Hz

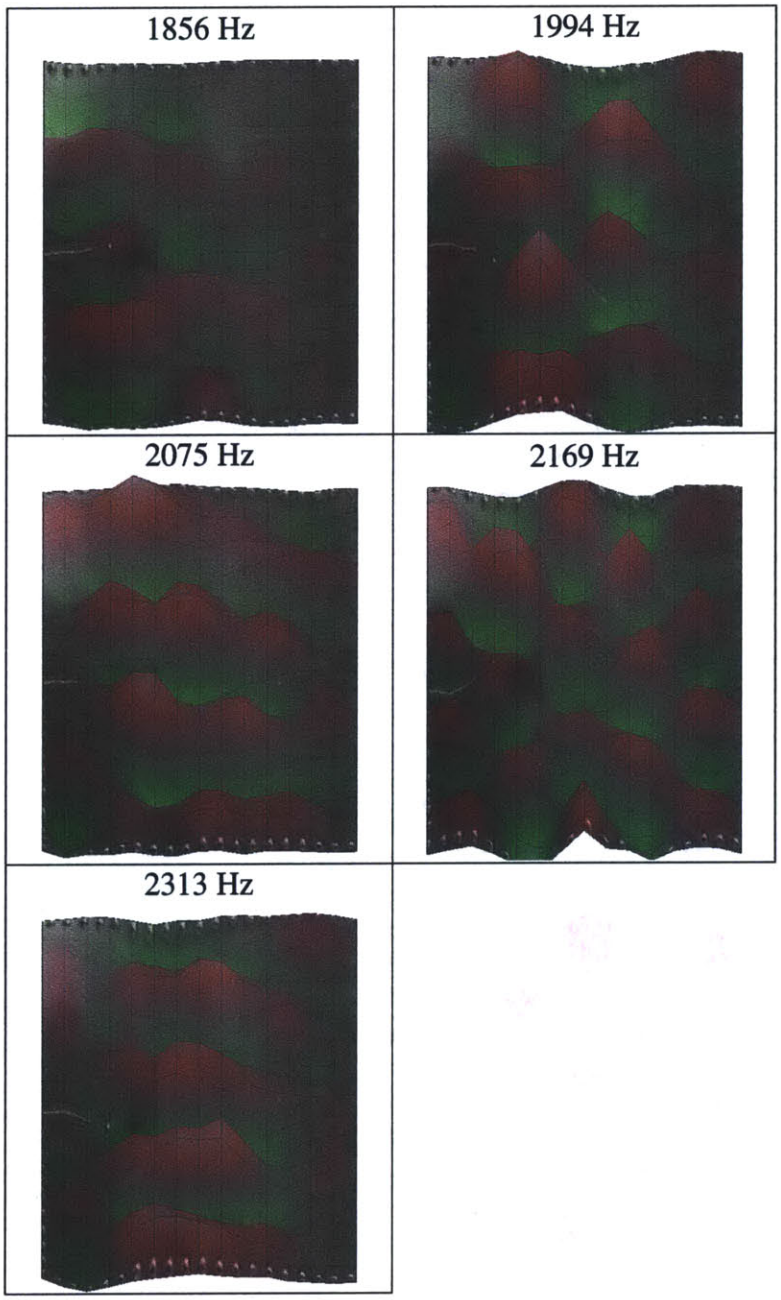
1856 Hz
1994 Hz
2075 Hz
2169 Hz
2313 Hz

CHAPTER B

Structural-Acoustic Equations-of-Motion

[The universe] cannot be read until we have learnt the language
and become familiar with the characters in which it is written.
It is written in mathematical language, and the letters are triangles, circles
and other geometrical figures, without which means
it is humanly impossible to comprehend a single word.
- Galileo Galilei in Opere II Saggiatore, *1623*

If you see a formula... that extends over a quarter of a page, forget it. It's wrong.
Nature isn't that complicated.
- Bernd T. Matthias

This appendix describes the process of transforming the differential equations-of-motion into the state space form that can be solved with an assumed modes analysis. This transformation from the weak form of the equations to the strong form of the equations is simplistic for single degree-of-freedom systems, but can become very complicated for multiple degree-of-freedom systems.

B.1 Acoustic Equations-of-Motion

The acoustic equations-of-motion can be found by considering a volume V surrounded by a surface S which contains an inviscid, compressible fluid. The pressure within the surface must satisfy the acoustic wave equations

$$\begin{aligned} \tfrac{1}{c^2}\frac{\partial^2 p}{\partial t^2} - \nabla^2 p &= 0 \\ \tfrac{1}{c^2}\frac{\partial^2 p}{\partial t^2} - \nabla \cdot \nabla p &= 0 \\ \tfrac{1}{c^2}\frac{\partial^2 p}{\partial t^2} - \mathbf{L}^t(\mathbf{L}p) &= 0 \end{aligned} \tag{7.1}$$

where c is speed of sound, p is pressure, and $\mathbf{L}$ is defined as

$$\begin{aligned} \nabla \cdot (\,) = \mathbf{L}^t &= \left[\tfrac{\partial}{\partial x} \quad \tfrac{\partial}{\partial y} \quad \tfrac{\partial}{\partial z}\right] \\ \nabla(\,) &= \mathbf{L} \end{aligned} \tag{7.2}$$

Multiplying equation (7.1) by a virtual pressure change and integrating over the volume yields

$$\int_V \tfrac{1}{c^2}\delta p \frac{\partial^2 p}{\partial t^2} dV + \int_V (\mathbf{L}^t \delta p)(\mathbf{L}p)\, dV = \int_S \mathbf{n}^t \delta p (\mathbf{L}p)\, dS \tag{7.3}$$

where $\mathbf{n}$ is the unit normal vector to the surface S. The last term incorporates the boundary conditions. The normal pressure gradient of the fluid is related to the normal acceleration of the structure by

$$\begin{aligned} \mathbf{n} \cdot \nabla p &= -\rho \mathbf{n} \cdot \frac{\partial^2 \mathbf{U}}{\partial t^2} \\ \mathbf{n}^t(\mathbf{L}p) &= -\rho \mathbf{n}^t \frac{\partial^2 \mathbf{U}}{\partial t^2} \end{aligned} \tag{7.4}$$

where $\mathbf{U}$ is the displacement of the surface. Substituting equation (7.4) into equation (7.3) yields the general form of equations of motion for an acoustic fluid

$$\int_V \tfrac{1}{c^2}\delta p \frac{\partial^2 p}{\partial t^2} dV + \int_V \mathbf{L}^t \delta p (\mathbf{L}p)\, dV + \int_S \rho \delta p \mathbf{n}^t \frac{\partial^2 \mathbf{U}}{\partial t^2}\, dS = 0 \tag{7.5}$$

B.1.1 Assumed Modes Analysis

For the Rayleigh-Ritz assumed mode solution, the pressure is assumed to be

$$p(x,t) = \begin{bmatrix} \psi_{p_1}(x) & \psi_{p_2}(x) & \cdots \end{bmatrix} \begin{Bmatrix} p_{m1}(t) \\ p_{m1}(t) \\ \vdots \end{Bmatrix} = \Psi_p(x)\mathbf{p}_m(t) \tag{7.6}$$

where p_m is the modal amplitude and Ψ_p is the mode shape. For a circular cylinder, the pressure mode shapes are assumed to be of the form [Bofilios and Lyrintzis, 1991]

$$\psi_{p_i} = \psi_{p_{m,n}} = \mathrm{J}_n\left(\alpha_{m,n} r\right)\cos(n\theta)\cos(m\pi x / l) \tag{7.7}$$

and the corresponding orthogonal mode

$$\psi_{p_i} = \psi_{p_{m,n}} = \mathrm{J}_n\left(\alpha_{m,n} r\right)\sin(n\theta)\cos(m\pi x / l) \tag{7.8}$$

Similarly, the structural displacements can be represented as

$$\mathbf{U}(x,t) = \begin{bmatrix} \psi_{s1}(x) & \psi_{s2}(x) & \cdots \end{bmatrix} \begin{Bmatrix} \mathbf{U}_{m1}(t) \\ \mathbf{U}_{m1}(t) \\ \vdots \end{Bmatrix} = \Psi_s(x)\mathbf{U}_m(t) \tag{7.9}$$

where $\mathbf{U}_m$ is the modal amplitude and Ψ_s is the mode shape. For a circular cylinder with simply supported end conditions, the displacement mode shapes are assumed to be of the form

$$\Psi_{s_i} = \Psi_{sm,n} = \sin\left(m\pi x / l\right)\sin(n\theta) \tag{7.10}$$

and the corresponding orthogonal mode is

$$\Psi_{s_i} = \psi_{sm,n} = \sin\left(m\pi x / l\right)\cos(n\theta) \tag{7.11}$$

The assumed pressure is substituted into the general equation, equation (7.5). Looking at each term:

$$\begin{aligned} \int_V \tfrac{1}{c^2}\delta p \frac{\partial^2 p}{\partial t^2} dV &= \int_V \tfrac{1}{c^2}\delta \mathbf{p}_m{}^t \Psi_p \Psi_p{}^t dV \ddot{\mathbf{p}}_m \\ &= \delta \mathbf{p}_m{}^t \left(\tfrac{1}{c^2} \int_V \Psi_p \Psi_p{}^t dV \right) \ddot{\mathbf{p}}_m \\ &= \delta \mathbf{p}_m{}^t \mathbf{M}_p \ddot{\mathbf{p}}_m \end{aligned} \tag{7.12}$$

$$\begin{aligned}\int_V \mathbf{L}^t \delta p(\mathbf{L}p)\, dV &= \int_V \delta \mathbf{p}_m{}^t \mathbf{B}^t \mathbf{B}\, dV \mathbf{p}_m \\ &= \delta \mathbf{p}_m{}^t \left(\int_V \mathbf{B}^t \mathbf{B}\, dV \right) \mathbf{p}_m \\ &= \delta \mathbf{p}_m{}^t \mathbf{K}_p \mathbf{p}_m \end{aligned} \tag{7.13}$$

$$\begin{aligned}\int_S \rho \delta p \mathbf{n}^t \frac{\partial^2 \mathbf{U}}{\partial t^2}\, dS &= \int_S \rho \delta \mathbf{p}_m{}^t \boldsymbol{\psi}_p \mathbf{n}^t \boldsymbol{\psi}_s{}^t dS \ddot{\mathbf{U}}_m \\ &= \delta \mathbf{p}_m{}^t \rho \left(\int_S \boldsymbol{\psi}_p \mathbf{n}^t \boldsymbol{\psi}_s{}^t dS \right) \ddot{\mathbf{U}}_m \\ &= \delta \mathbf{p}_m{}^t \rho_a \mathbf{R} \ddot{\mathbf{U}}_m \end{aligned} \tag{7.14}$$

where

$$\mathbf{B} = \mathbf{L} \boldsymbol{\psi}_p{}^t \tag{7.15}$$

Stating that the variations in the modal pressures must be zero, the variation drops out of equations (7.12) to (7.14). The equation of acoustics now becomes

$$\mathbf{M}_p \ddot{\mathbf{p}}_m + \mathbf{K}_p \mathbf{p}_m + \rho_a \mathbf{R} \ddot{\mathbf{U}}_m = 0 \tag{7.16}$$

Dissipation due to reflections can be introduced through an integral over the surface. The additional term can be expressed as

$$\begin{aligned}\int_S \delta p \left(\tfrac{r}{\rho c}\right) \tfrac{1}{c} \frac{\partial p}{\partial t}\, dS &= \int_S \delta \mathbf{p}_m{}^t \boldsymbol{\psi}_p \left(\tfrac{r}{\rho c}\right) \tfrac{1}{c} \boldsymbol{\psi}_p{}^t dS \frac{\partial \mathbf{p}_m}{\partial t} \\ &= \delta \mathbf{p}_m{}^t \left(\tfrac{\beta}{c} \int_S \boldsymbol{\psi}_p \boldsymbol{\psi}_p{}^t dS \right) \dot{\mathbf{p}}_m \\ &= \delta \mathbf{p}_m{}^t \mathbf{C}_p \dot{\mathbf{p}}_m \end{aligned} \tag{7.17}$$

Combining all of the terms and declaring that the integral of the variations must go to zero, the discretized wave equation for acoustics is given by

$$\mathbf{M}_p \ddot{\mathbf{p}}_m + \mathbf{C}_p \dot{\mathbf{p}}_m + \mathbf{K}_p \mathbf{p}_m + \rho_a \mathbf{R} \ddot{\mathbf{U}}_m = 0 \tag{7.18}$$

B.1.2 Nondimensionalization of Acoustic Equations

We shall not be performing full-scale model tests, thus it seems advisable to nondimensionalize the equations of motion. This analysis will be performed especially for the case of a circular cylinder. There are several natural nondimensionalizing

parameters. The most notable are the radius, R, a characteristic time, $1/\omega_o$, and the density of air, ρ_a.

A natural choice for the reference frequency is the first mode of the cylinder. In acoustic literature, this is referred to as the cutoff frequency [Fahy, 1985]. The first mode corresponds to the "ring frequency" or the breathing mode in the radial direction. This frequency is given by

$$\omega_o = \frac{c}{R} \tag{7.19}$$

As a result, the system variables can be nondimensionalized as

$$\begin{aligned}
r^* &= \frac{r}{R} & z^* &= \frac{z}{R} \\
L^* &= \nabla^* = R\nabla & \mathbf{B}^* &= R\mathbf{B} \\
\mathbf{U}_m^* &= \frac{1}{R}\mathbf{U}_m & \mathbf{p}_m^* &= \frac{1}{c^2\rho_a}\mathbf{p}_m \\
dV^* &= \frac{1}{R^3}dV & dS^* &= \frac{1}{R^2}dS \\
t^* &= \omega_o t = \frac{c}{R}t & \omega^* &= \frac{1}{\omega_o}\omega = \frac{R}{c}\omega
\end{aligned} \tag{7.20}$$

Substituting the nondimensionalized variables into the system variables yields

$$\begin{aligned}
\mathbf{M}_p &= \tfrac{1}{c^2}\int_V \Psi_p \Psi_p{}^t dV \\
&= \tfrac{1}{c^2}\left(\int_{V^*} \Psi_p \Psi_p{}^t dV^*\right) R^3 \\
&= \tfrac{R^3}{c^2}\mathbf{M}_p^*
\end{aligned} \tag{7.21}$$

$$\begin{aligned}
\mathbf{C}_p &= \tfrac{\beta}{c}\int_S \Psi_p \Psi_p{}^t dS \\
&= \tfrac{\beta}{c}\int_{S^*} \Psi_p \Psi_p{}^t dS^* R^2 \\
&= \frac{\beta R^2}{c}\mathbf{C}_p^*
\end{aligned} \tag{7.22}$$

$$\begin{aligned}
\mathbf{K}_p &= \int_V \mathbf{B}^t \mathbf{B} dV = \int_V \psi_p \mathbf{L}^t \mathbf{L} \psi_p{}^t dV \\
&= \left(\int_{V^*} \frac{1}{R}\psi_p \mathbf{L}^{*t} \frac{1}{R}\mathbf{L}^* \psi_p{}^t dV^*\right) R^3 \\
&= R\,\mathbf{K}_p^*
\end{aligned} \tag{7.23}$$

$$\begin{aligned}\mathbf{R} &= \int_S \psi_p \mathbf{n}^t \psi_s{}^t dS \\ &= \left(\int_{S^*} \psi_p \mathbf{n}^t \psi_s{}^t dS^* \right) R^2 \\ &= R^2 \, \mathbf{R}^*\end{aligned} \tag{7.24}$$

$$\ddot{\mathbf{p}}_m = \rho_a \frac{c^4}{R^2} \ddot{\mathbf{p}}^*_m \tag{7.25}$$

$$\ddot{\mathbf{U}}_m = \frac{c^2}{R} \ddot{\mathbf{U}}^*_m \tag{7.26}$$

Substitution into equation (18) yields the nondimensionalized assumed mode relation for the acoustic dynamics.

$$\frac{R^3}{c^2} \rho_a \frac{c^4}{R^2} \mathbf{M}^*_p \ddot{\mathbf{p}}^*_m + \frac{\beta R^2}{c} \rho_a \frac{c^3}{R} \mathbf{C}^*_p \dot{\mathbf{p}}^*_m + R c^2 \rho_a \mathbf{K}^*_p \mathbf{p}^*_m + \rho_a R^2 \frac{c^2}{R} \mathbf{R}^* \ddot{\mathbf{U}}^*_m = 0 \tag{7.27}$$

Rearranging terms serves to cancel all of the dimensional scaling variables and equation (28) becomes

$$\mathbf{M}^*_p \ddot{\mathbf{p}}^*_m + \beta \mathbf{C}^*_p \dot{\mathbf{p}}^*_m + \mathbf{K}^*_p \mathbf{p}^*_m + \mathbf{R}^* \ddot{\mathbf{U}}^*_m = 0 \tag{7.28}$$

B.2 Cylinder Dynamics

This section describes the general equations of motion for a reinforced cylinder structure. The differential equations are setup to be solved with an assumed modes or Rayleigh-Ritz analysis. The cylinder and the coordinate system are sketched in Figure B.1.

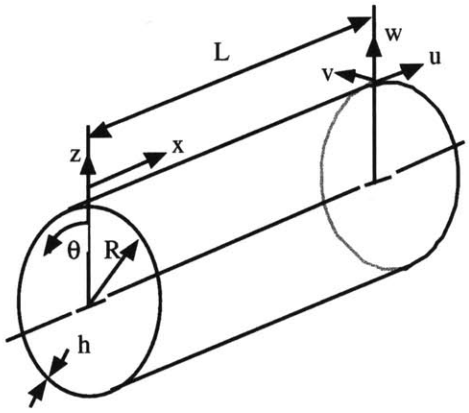

Figure B.1: Rayleigh-Ritz cylinder geometry

B.2.1 Cylinder differential equations

The equations of the cylinder are found by combining the strain-displacement, the stress-strain, and the stress-moment resultant equations in the equilibrium equations of motion. By changing the limits of integration over the thickness, the same general process can be used for either a smooth cylinder or a cylinder with a reinforcing frame.

The strain-displacement relationship for a thin cylinder can be expressed as

$$S_x = \frac{1}{R}u' - z\frac{1}{R^2}w'' \tag{7.29}$$

$$S_\theta = \frac{1}{R}v^{\cdot} - \frac{1}{R^2}zw^{\cdot\cdot} + \frac{1}{R}w \tag{7.30}$$

$$S_{x\theta} = \frac{1}{R}u^{\cdot} + \frac{1}{R}v' - \frac{2}{R^2}zw'^{\cdot} \tag{7.31}$$

where R is the radius, z is the shell thickness, S is the strain, u is the longitudinal coordinate, v is the transverse coordinate, and w is the radial coordinate, as indicated in figure 3. The derivatives are

$$R\frac{\partial(\,)}{\partial x} = (\,)' \qquad \frac{\partial(\,)}{\partial\theta} = (\,)^{\cdot} \tag{7.32}$$

The linear stress-strain relationships are

$$T_x = \frac{E}{1-\nu^2}\left(S_x + \nu S_\theta\right) \tag{7.33}$$

$$T_\theta = \frac{E}{1-\nu^2}\left(S_\theta + \nu S_x\right) \tag{7.34}$$

$$T_{x\theta} = \frac{E}{2(1-\nu)}S_{x\theta} \tag{7.35}$$

The stress displacement relationships can be expressed in terms of the stress resultants N and M. Substituting the strain-displacement relationship into the stress-strain relationship and integrating the stress resultants over the area of the cylinder and assuming a thin cylinder (thickness<<radius), the resultants can be expressed as

$$
\begin{aligned}
N_x &= \int_a^b T_x dz = \frac{E}{1-\nu^2}\left[\frac{A}{R}\left(u' + \nu v^{\cdot} + \nu w\right) - \frac{I_1}{R^2}\left(w'' + \nu w^{\cdot\cdot}\right)\right] \\
N_\theta &= \int_a^b T_\theta dz = \frac{E}{1-\nu^2}\left[\frac{A}{R}\left(v^{\cdot} + w + \nu u'\right) - \frac{I_1}{R}\left(w^{\cdot\cdot} + \nu w''\right)\right] \\
N_{x\theta} &= N_{\theta x} = \int_a^b T_{x\theta} dz = \frac{E}{2(1+\nu)}\left[\frac{A}{R}\left(u^{\cdot} + v'\right) - \frac{I_1}{R^2}\left(2w'^{\cdot}\right)\right] \\
M_x &= -\int_a^b T_x z dz = \frac{-E}{1-\nu^2}\left[\frac{I_1}{R}\left(u' + \nu v^{\cdot} + \nu w\right) - \frac{I_2}{R^2}\left(w'' + \nu w^{\cdot\cdot}\right)\right] \\
M_\theta &= -\int_a^b T_\theta z dz = \frac{-E}{1-\nu^2}\left[\frac{I_1}{R}\left(v^{\cdot} + w + \nu u'\right) - \frac{I_2}{R^2}\left(w^{\cdot\cdot} + \nu w''\right)\right] \\
M_{x\theta} &= M_{\theta x} = -\int_a^b T_{x\theta} z dz = \frac{-E}{2(1+\nu)}\left[\frac{I_1}{R}\left(u^{\cdot} + v'\right) - \frac{I_2}{R^2}\left(2w'^{\cdot}\right)\right]
\end{aligned}
\tag{7.36}
$$

where A, I_1, and I_2 are

$$
\begin{aligned}
A &= \int_a^b dz \\
I_1 &= \int_a^b z\, dz \\
I_2 &= \int_a^b z^2\, dz
\end{aligned}
\tag{7.37}
$$

The thickness integrals need to include the ribs and stringers for a rib-stringer reinforced cylinder.

The cylinder equations of motion are found by substituting the stress resultants into the general equations of motion, which are [Flügge, 1973, Chapter 5]

$$
\begin{aligned}
RN_x{}' + RN_{\theta x}{}^{\cdot} + p_x R^2 &= 0 \\
RN_\theta{}^{\cdot} + RN_{x\theta}{}' - M_\theta{}^{\cdot} - M_{x\theta}{}' + p_\theta R^2 &= 0 \\
-M_\theta{}^{\cdot\cdot} - M_{\theta x}{}'^{\cdot} - M_{x\theta}{}'^{\cdot} - M_x{}'' - RN_\theta + p_r R^2 &= 0
\end{aligned}
\tag{7.38}
$$

Substituting for the stress resultants into the equations of motion yields:

$$
\begin{aligned}
f_1(u,v,w) &= A\left(u'' + \frac{1-\nu}{2}u^{\cdot\cdot} + \frac{1+\nu}{2}v'^{\cdot} + \nu w'\right) - \frac{I_1}{R}\left(w''' + w'^{\cdot\cdot}\right) + \frac{R^2}{D}p_x = 0 \\
f_2(u,v,w) &= A\left(\frac{1+\nu}{2}u'^{\cdot} + \frac{1-\nu}{2}v'' + v^{\cdot\cdot} + w^{\cdot}\right) - \frac{I_1}{R}\left(\frac{1+\nu}{2}u'^{\cdot} + \frac{1-\nu}{2}v'' + v^{\cdot\cdot} + w^{\cdot} - w^{\cdot\cdot} - w''^{\cdot}\right) \\
&\quad + \frac{I_2}{R^2}\left(w''^{\cdot} + w^{\cdot\cdot}\right) + \frac{R^2}{D}p_\theta = 0 \\
f_3(u,v,w) &= A\left(-\nu u' - v^{\cdot} - w\right) + \frac{I_1}{R}\left(u'^{\cdot\cdot} + u''' + v^{\cdot\cdot} + v''^{\cdot} + 2w^{\cdot\cdot} + 2\nu w''\right) \\
&\quad + \frac{I_2}{R^2}\left(-w^{\cdot\cdot} - 2w''^{\cdot\cdot} - w''''\right) + \frac{R^2}{D}p_r = 0
\end{aligned}
\tag{7.39}
$$

The three coupled equations of motion for the cylinder are a three-dimensional representation of the cylinder dynamics. The cylinder is assumed to be thin and circular but is not necessarily smooth. A frame of ribs and stringer is included in the equations through the evaluation of A, I_1, and I_2 during the integration over the surface of the cylinder.

B.2.2 Assumed modes analysis for cylinder

The general equations of motion for the cylinder are transformed into the assumed modes analysis by first transforming the three coupled equations of motion into the equations of virtual work or the weak form of the equation. The three differential equations, f_1, f_2, f_3, are multiplied by test functions and integrated over the surface to form the virtual work of the cylinder:

$$V = \int_S \begin{bmatrix} f_1(u_n, v_n, w_n) & f_2(u_n, v_n, w_n) & f_3(u_n, v_n, w_n) \end{bmatrix} \begin{bmatrix} u_n \\ v_n \\ w_n \end{bmatrix} dS = 0 \tag{7.40}$$

Integration by parts is needed to achieve symmetry between the coordinates. Additionally the test functions are chosen to be the same as the trial functions. This process is also the basis for Galerkin's method [Strang, 1986, pg. 428-433.].

Ignoring the boundary condition terms, the strain energy in the system is

$$\begin{aligned} V = A\Bigg(& u_m' u_n' - \frac{1-\nu}{2} \dot{u}_m \dot{u}_n - \frac{1+\nu}{4} u_m' v_n - \frac{1+\nu}{4} \dot{u}_m v_n' - \nu u_m' w_n - \frac{1+\nu}{4} v_m' \dot{u}_n - \frac{1+\nu}{4} v_m u_n' - \frac{1+\nu}{2} v_m' v_n' \\ & - \dot{v}_m w_n - \dot{v}_m \dot{v}_n - \nu w_m u_n' - w_m \dot{v}_n - w_m w_n \Bigg) + \frac{I_1}{R}\Bigg(u_m' w_n'' + \dot{u}_m w_n' - \frac{1+\nu}{4} v_m' \dot{u}_n - \frac{1+\nu}{4} \dot{v}_m u_n' \\ & - \frac{1-\nu}{2} v_m' v_n' - \dot{v}_m \dot{v}_n - \dot{v}_m w_n + \frac{1}{2} v_m' w_n' + \frac{1}{2} \dot{v}_m w_n'' + \dot{v}_m \dot{w}_n + \frac{1}{2} w_m' \dot{u}_n + \frac{1}{2} \dot{w}_m u_n' + w_m'' u_n' + \dot{w}_m \dot{v}_n \\ & + \frac{1}{2} w_m' v_n' + \frac{1}{2} w_m'' \dot{v}_n + \frac{1}{2} \dot{w}_m w_n + \frac{1}{2} w_m \dot{w}_n + \nu w_m'' w_n + \nu w_m w_n'' \Bigg) + \frac{I_2}{R^2}\Bigg(-\frac{1}{2} v_m' w_n' - \frac{1}{2} \dot{v}_m w_n'' \\ & - \dot{v}_m \dot{w}_n - w_m'' w_n'' - \frac{1}{2} w_m'' \dot{w}_n - \frac{1}{2} \dot{w}_m w_n'' - w_m' w_n' - \dot{w}_m \dot{w}_n \Bigg) \end{aligned} \tag{7.41}$$

The deflections of the cylinder, [u v w] can be expressed in terms of assumed deflection shape, [U V W], and a vector of time varying modal amplitudes, [α β γ]:

$$\begin{bmatrix} u(x,\theta,t) \\ v(x,\theta,t) \\ w(x,\theta,t) \end{bmatrix} = \begin{bmatrix} U_1(x,\theta) & 0 & 0 & U_2(x,\theta) & 0 & 0 & \cdots \\ 0 & V_1(x,\theta) & 0 & 0 & V_2(x,\theta) & 0 & \cdots \\ 0 & 0 & W_1(x,\theta) & 0 & 0 & W_2(x,\theta) & \cdots \end{bmatrix} \begin{bmatrix} \alpha_1(t) \\ \beta_1(t) \\ \gamma_1(t) \\ \alpha_2(t) \\ \beta_2(t) \\ \gamma_2(t) \\ \vdots \end{bmatrix} = \begin{bmatrix} \mathbf{U} \\ \mathbf{V} \\ \mathbf{W} \end{bmatrix} \mathbf{q} \quad (7.42)$$

Taking the variations of the variation of the strain energy and allowing the coefficients of the variations to go to zero yields the cylinder stiffness matrix becomes

$$\mathbf{K}_s = \begin{bmatrix} 2K_{11} & K_{12}+K_{21} & K_{13}+K_{31} & K_{11} & K_{12} & K_{13} \\ K_{12}+K_{21} & 2K_{22} & K_{23}+K_{32} & K_{21} & K_{22} & K_{23} \\ K_{13}+K_{31} & K_{23}+K_{32} & 2K_{33} & K_{31} & K_{32} & K_{33} \\ K_{11} & K_{21} & K_{31} & 2K_{11} & K_{12}+K_{21} & K_{13}+K_{31} \\ K_{12} & K_{22} & K_{32} & K_{12}+K_{21} & 2K_{22} & K_{23}+K_{32} \\ K_{13} & K_{23} & K_{33} & K_{13}+K_{31} & K_{23}+K_{32} & 2K_{33} \end{bmatrix} \quad (7.43)$$

where

$$\begin{aligned}
K_{11} &= -\int_S A\left(U_m'U_n' + \frac{1-\nu}{2}U_m^{\cdot}U_n^{\cdot}\right)dS \\
K_{12} &= -\int_S A\left(\frac{1+\nu}{4}U_m'V_n^{\cdot} + \frac{1+\nu}{4}U_m^{\cdot}V_n'\right)dS \\
K_{13} &= \int_S \left(-A\nu U_m'W_n + \frac{I_1}{R}\left(U_m'W_n'' + U_m^{\cdot}W_n^{\prime\cdot}\right)\right)dS \\
K_{21} &= -\int_S \frac{1+\nu}{4}\left(A + \frac{I_1}{R}\right)\left(V_m'U_n^{\cdot} - V_m^{\cdot}U_n'\right)dS \\
K_{22} &= -\int_S \frac{1-\nu}{2}\left(A + \frac{I_1}{R}\right)\left(\frac{1-\nu}{2}V_m'V_n' - V_m^{\cdot}V_n^{\cdot}\right)dS \\
K_{23} &= \int_S \left(-\left(A + \frac{I_1}{R}\right)V_m^{\cdot}W_n + \frac{1}{2}\left(\frac{I_1}{R} + \frac{I_2}{R^2}\right)V_m'W_n^{\prime\cdot} + \left(\frac{I_1}{R} - \frac{I_2}{R^2}\right)\left(\frac{1}{2}V_m^{\cdot}W_n'' + V_m^{\cdot}W_n^{\cdot\cdot}\right)\right)dS \\
K_{31} &= \int_S \left(-A\nu W_m U_n' + \frac{I_1}{R}\left(\frac{1}{2}W_m'U_n^{\cdot} + \frac{1}{2}W_m^{\cdot\cdot}U_n' + W_m''U_n'\right)\right)dS \\
K_{32} &= \int_S \left(-A\,W_m V_n^{\cdot} + \frac{I_1}{R}\left(W_m^{\cdot\cdot}V_n^{\cdot} + \frac{1}{2}W_m^{\prime\cdot}V_n' + \frac{1}{2}W_m''V_n^{\cdot}\right)\right)dS \\
K_{33} &= \int_S \left(-A\,W_m W_n + \frac{I_1}{R}\left(\frac{1}{2}W_m^{\cdot\cdot}W_n + \frac{1}{2}W_m W_n^{\cdot\cdot} + \nu W_m''W_n + \nu W_m W_n''\right)\right. \\
&\quad \left. + \frac{I_2}{R^2}\left(-W_m''W_n'' - \frac{1}{2}W_m''W_n^{\cdot\cdot} - \frac{1}{2}W_m^{\cdot\cdot}W_n'' - W_m^{\prime\cdot}W_n^{\prime\cdot} - W_m^{\cdot\cdot}W_n^{\cdot\cdot}\right)\right)dS
\end{aligned} \quad (7.44)$$

The inertia terms can be found in the virtual work through D'Alembert's principle:

$$R^2\begin{bmatrix} p_x \\ p_\theta \\ p_r \end{bmatrix} = R^2\rho\begin{bmatrix} \ddot{u} \\ \ddot{v} \\ \ddot{w} \end{bmatrix} \tag{7.45}$$

where the dots over the variable indicates a second derivative with respect to time.

Repeating the process performed for the strain energy expression, multiplying by a test function, integrating by parts, assuming a mode shape and a time varying modal amplitude yields the mass matrix for the cylinder.

$$\mathbf{M}_s = R^2\rho\int_{\blacklozenge} A\begin{bmatrix} 2u^m u^n & 0 & 0 & u^m u^n & 0 & 0 \\ 0 & 2v^m v^n & 0 & 0 & v^m v^n & 0 \\ 0 & 0 & 2w^m w^n & 0 & 0 & w^m w^n \\ u^m u^n & 0 & 0 & 2u^m u^n & 0 & 0 \\ 0 & v^m v^n & 0 & 0 & 2v^m v^n & 0 \\ 0 & 0 & w^m w^n & 0 & 0 & 2w^m w^n \end{bmatrix} dS \tag{7.46}$$

B.2.3 Forced Structure Equations-of-Motion

The electro-mechanical behavior of the cylinder will be represented as a mass-spring-damper system that is driven by acoustic forcing and by piezoelectric forcing. The basic form of the equation is [Hagood, Chung, and von Flotow, 1990]

$$\mathbf{M}_s\ddot{\mathbf{U}}_m + \mathbf{C}_s\dot{\mathbf{U}}_m + \mathbf{K}_s\mathbf{U}_m = \mathbf{B}_f\mathbf{f}_m + \mathbf{F}_p + \Theta_s\mathbf{v}_m \tag{7.47}$$

where the structural parameters are defined by

$$\Theta_s = \int_V \mathbf{N}_s{}'\mathbf{d}\,\mathbf{C}^E\mathbf{N}_v\,dV, \tag{7.48}$$

$$\mathbf{B}_f = \int_A \psi_s\,dA \tag{7.49}$$

and where $\mathbf{d}$ is the piezoelectric electro-mechanical coupling. The acoustic pressure loading is the integral of the pressure over the surface:

$$\begin{aligned} F_p &= \int_S \psi_s p \, \mathbf{n} \, dS \\ &= \int_S \psi_s \psi_p{}' \, \mathbf{n} \, dS \, \mathbf{p}_m \\ &= \mathbf{R} \, \mathbf{p}_m \end{aligned} \tag{7.50}$$

B.2.4 Nondimensionalization of Structural Equations

Using the same nondimensionalization for the structural dynamics as was applied to the acoustic dynamics. With the introduction of the piezoceramic elements, a new nondimensionalization is needed for the voltage or charge. This analysis uses the coercive field of the piezoceramic, v_c. The variables become

$$\begin{aligned} \rho_s^* &= \frac{1}{\rho_a}\rho_s & \mathbf{v}_m^* &= \frac{1}{v_c}\mathbf{v}_m \\ \mathbf{N}_s^* &= R\,\mathbf{N}_s & \mathbf{N}_v^* &= R\,\mathbf{N}_v \\ \mathbf{d}^* &= \frac{v_c}{R}\mathbf{d} & \mathbf{C}^{E*} &= \frac{1}{c^2\rho_a}\mathbf{C}^E \end{aligned} \tag{7.51}$$

and the system matrix variables become

$$\begin{aligned} \mathbf{M}_s &= \int_V \psi_s{}^t \rho_s \psi_s \, dV \\ &= \int_{V^*} \psi_s{}^t \rho_s{}^* \psi_s \, dV^* \rho_a R^3 \\ &= \rho_a R^3 \, \mathbf{M}_s^* \end{aligned} \tag{7.52}$$

$$\begin{aligned} \mathbf{K}_s &= \int_V \mathbf{N}_s{}^t \mathbf{C}^E \mathbf{N}_s \, \mathrm{dV} \\ &= \int_{V^*} \mathbf{N}_s^{*t} \mathbf{C}^E \mathbf{N}_s^* \, \mathrm{dV}^* \frac{1}{R}\rho_a c^2 \frac{1}{R} R^3 \\ &= R\,\rho_a c^2 \mathbf{K}_s^* \end{aligned} \tag{7.53}$$

$$\begin{aligned} \Theta_s &= \int_V \mathbf{N}_s{}^t \mathbf{d}\, \mathbf{C}^E \mathbf{N}_v \, \mathrm{dV} \\ &= \int_{V^*} \mathbf{N}_s^{*t} \mathbf{d}^* \, \mathbf{C}^{*E} \mathbf{N}_v^* \, \mathrm{dV}^* \frac{1}{R}\frac{R}{v_c} c^2 \rho_a \frac{1}{R} R^3 \\ &= \frac{c^2 R^s}{v_c} \rho_a \Theta_s^* \end{aligned} \tag{7.54}$$

$$\begin{aligned}\mathbf{B}_f &= \int_A \psi^U \, dA \\ &= \int_{A^*} \psi^U \, dA^* \, R^2 \\ &= R^2 \mathbf{B}_f^*\end{aligned} \tag{7.55}$$

The nondimensionalized structural dynamics equation is

$$R^3 \rho_a \frac{c^2}{R} \mathbf{M}_s^* \ddot{\mathbf{U}}_m^* + \mathbf{C}_s^* \dot{\mathbf{U}}_m^* + R \rho_a c^2 R \mathbf{K}_s^* \mathbf{U}_m^* - R^2 c^2 \rho_a \mathbf{R}^* \mathbf{p}_m^* - \rho_a \frac{c^2 R^2}{v_c} v_c \theta_s^* \mathbf{v}_m^* = R^2 c^2 \rho_a \mathbf{B}_f^* \mathbf{f}_m^* \tag{7.56}$$

or

$$\mathbf{M}_s^* \ddot{\mathbf{U}}_m^* + \mathbf{K}_s^* \mathbf{U}_m^* - \mathbf{R}^* \mathbf{p}_m^* - \theta_s^* \mathbf{v}_m^* = \mathbf{B}_f^* \mathbf{f}_m^* \tag{7.57}$$

B.3 Coupled Nondimensional Structural Acoustic

Combining equations (18,31), the coupled equations of motion for structural-acoustic system can be expressed as

$$\begin{bmatrix} \mathbf{M}_s & \mathbf{0} \\ \rho \mathbf{R}^t & \mathbf{M}^p \end{bmatrix} \begin{Bmatrix} \ddot{\mathbf{U}}_m \\ \ddot{\mathbf{p}}_m \end{Bmatrix} + \begin{bmatrix} \mathbf{C}_s & \mathbf{0} \\ \mathbf{0} & \mathbf{C}_p \end{bmatrix} \begin{Bmatrix} \dot{\mathbf{U}}_m \\ \dot{\mathbf{p}}_m \end{Bmatrix} + \begin{bmatrix} \mathbf{K}_s & -\mathbf{R} \\ \mathbf{0} & \mathbf{K}_p \end{bmatrix} \begin{Bmatrix} \mathbf{U}_m \\ \mathbf{p}_m \end{Bmatrix} = \begin{bmatrix} \mathbf{B}_f & \theta_s \\ \mathbf{0} & \mathbf{0} \end{bmatrix} \begin{Bmatrix} \mathbf{f}_m \\ \mathbf{v}_m \end{Bmatrix} \tag{7.58}$$

The nondimensionalized coupled structural-acoustic equations can be expressed as

$$\begin{bmatrix} \mathbf{M}_s^* & \mathbf{0} \\ \mathbf{R}^{*t} & \mathbf{M}_p^* \end{bmatrix} \begin{Bmatrix} \ddot{\mathbf{U}}_m^* \\ \ddot{\mathbf{p}}_m^* \end{Bmatrix} + \begin{bmatrix} \mathbf{C}_s^* & \mathbf{0} \\ \mathbf{0} & \beta \mathbf{C}_p^* \end{bmatrix} \begin{Bmatrix} \dot{\mathbf{U}}_m^* \\ \dot{\mathbf{p}}_m^* \end{Bmatrix} + \begin{bmatrix} \mathbf{K}_s^* & -\mathbf{R}^* \\ \mathbf{0} & \mathbf{K}_p^* \end{bmatrix} \begin{Bmatrix} \mathbf{U}_m^* \\ \mathbf{p}_m^* \end{Bmatrix} = \begin{bmatrix} \mathbf{B}_f^* & \theta_s^* \\ \mathbf{0} & \mathbf{0} \end{bmatrix} \begin{Bmatrix} \mathbf{f}_m^* \\ \mathbf{v}_m^* \end{Bmatrix} \tag{7.59}$$

CHAPTER C

Computer Codes

The Computer is incredible fast, accurate and stupid.
Man is unbelievably slow, inaccurate and brilliant.
The marriage of the two is a challenge and an opportunity beyond imagination.
- Walesh, 1989

The purpose of computing is insight, not numbers!
- R. W. Hamming

This appendix presents some of the MATLAB code that was used in this thesis. Far more pages of code were written than deserve to be published in this thesis. In an effort to pair the volume of code while still presenting a complete story with the code, the code for the numerical modeling, isolation, and control of a single panel is presented. The results from this code were presented in Chapter 4.

There are two principle files, panel.m, which creates the structural model, and LQGcontrolMIMO.m, which closes the control loop. The file panel.m is a master program and calls other programs. The file panel_evec.m solves the structural equations-of-motion. The files panel_strain.m and panel_disp.m determine the modal coupling to the transducers. The files killmodeHi.m and killmodeH2.m are cost functions, which are

used to isolate the targeted mode. The mode shapes are defined in the files pumodes.m, pvmodes.m, and pwmodes.m.

C.1 File: panel.m

```
%  MASTER PROGRAM FOR PANEL DYNAMICS
%  This is the code that calls the other programs to create the
dynamics and
%  model the behavior of a curved panel


clear Coupling target ortho sig_in
global Coupling target ortho sig_in

% Calculate Mass and Stiffness of Panel
figure(1)
[Geom,MandK,Modes] = panel_evec;


% Plot Select Mode Shape
l_mode    = 1;      % Longitudinal panel mode number to plot
t_mode    = 2;      % Circumferential panel mode number to plot
modeshapeplot(Geom,Modes,l_mode,t_mode);
drawnow

% Calculate coupling to individual strain sensor
dlsens = 2.5/12;      % Proportional size of long sensor elements
dtsens = 2.5/9.42;    % Proportional size of circum sensor elements
% Transducers in X
%lcenters = [.5 .23 .77 .23 .77];
%tcenters = [.5 .234 .234 .765 .765];
% Transducers in +
lcenters = [.5 .5 .23 .77 .5];
tcenters = [.5 .234 .5 .5 .765];
nsensor  = length(lcenters);

% Define range of each element
lmins = lcenters - dlsens/2;
lmaxs = lcenters + dlsens/2;
tmins = tcenters - dtsens/2;
tmaxs = tcenters + dtsens/2;

% Loop over elements and calculate coupling
clear strain
figure(1);clf
for ii = 1:nsensor,
   lmin=lmins(ii); lmax=lmaxs(ii);
   tmin=tmins(ii); tmax=tmaxs(ii);
   PiezDimAct  =
struct('lmin',lmin,'lmax',lmax,'tmin',tmin,'tmax',tmax);
   strainAct(:,ii) = panel_strain(Geom,Modes,PiezDimAct)';
```

```
   %PiezDimSen  =
struct('lcenter',lcenters(ii),'tcenter',tcenters(ii));
   %strainSen(:,ii) = panel_disp(Geom,Modes,PiezDimSen)';
   strainSen(:,ii) = panel_strain(Geom,Modes,PiezDimAct)';
end

% Define Disturbance
lcenterd = 0.375;
tcenterd = 0.375;
DistDim = struct('lmin',lcenterd-dlsens/10,'lmax',lcenterd+dlsens/10,
...
   'tmin',tcenterd-dtsens/10,'tmax',tcenterd+dtsens/10);
dist     = 30*panel_strain(Geom,Modes,DistDim)';

% Define Performance
lcenter = 0.55;
tcenter = 0.55;
PerfDim  = struct('lcenter',lcenter,'tcenter',tcenter);
perf     = panel_disp(Geom,Modes,PerfDim);


% Reshape strain to linear vector
sig_in = zeros(nsensor,nsensor,Geom.nsmodes);
for ii = 1:Geom.nsmodes
   sig_in(:,:,ii) = strainSen(ii*3-1,:)' * strainAct(ii*3-1,:);
end

Coupling = struct('strainAct',strainAct,'lmins',lmins,'lmaxs',lmaxs,...
   'tmins',tmins,'tmaxs',tmaxs,'dlsens',dlsens,'dtsens',dtsens,...
   'nsmodes',Geom.nsmodes,'sig_in',sig_in,'perf',perf,'dist',dist,...
   'strainSen',strainSen);


%%% Optimize weighting %%%
% Define target modes
target = Modes.findx(12);              % Mode number to target
ortho  = Modes.findx([1:11 13:20]);    % Modes to minimize


% Search for Weights
x0    = ones(nsensor*2,1);
% Infinity Norm
xHi   = fmins('killmodeHi',x0);
xHi   = fmins('killmodeHi',xHi);
xHi   = fmins('killmodeHi',xHi);
xHi   = xHi / norm(xHi);
nmatHi= xHi;
costHi   = killmodeHi(xHi);
% 2 Norm
xH2   = fmins('killmodeH2',xHi);
xH2   = fmins('killmodeH2',xH2);
xH2   = fmins('killmodeH2',xH2);
xH2   = xH2 / norm(xH2);
nmatH2= xH2;
costH2   = killmodeH2(xH2);
```

```
% Scale Results
sig_max  = squeeze(max(max(abs(sig_in),[],1),[],2))' / ...
   squeeze(max(max(abs(sig_in(:,:,target)),[],1),[],2));
for ii = 1:length(sig_in),
   respHi(ii) = squeeze(abs(xHi(nsensor+1:2*nsensor)'*...
      sig_in(:,:,ii)*xHi(1:nsensor)));
   respH2(ii) = squeeze(abs(xH2(nsensor+1:2*nsensor)'*...
      sig_in(:,:,ii)*xH2(1:nsensor)));
end
respHi   = respHi / respHi(target);
respH2   = respH2 / respH2(target);

% Plot Results
figure(2)
subplot 211
semilogy(Modes.fsort,respHi(Modes.findx),'x')
hold on
semilogy(Modes.mf,sig_max,'co')
semilogy([Modes.mf; Modes.mf],[sig_max; 1e-
30*ones(1,Geom.nsmodes)],'c:')
semilogy([Modes.fsort; Modes.fsort],[respHi(Modes.findx); ...
      1e-30*ones(1,Geom.nsmodes)],'b-')
semilogy(Modes.mf(target)*[1 1],[respHi(target); 1e-30],'r-')
semilogy([Modes.mf(ortho); Modes.mf(ortho)],[respHi(ortho); ...
      1e-30*ones(size(ortho))],'k-')
hold off
xlabel('Frequency, Hz');ylabel('Modal Amplitude')
axs = axis;
axis([axs(1) 1500 1e-15 max([axs(4) 10])])

subplot 212
semilogy(Modes.fsort,respH2(Modes.findx),'x')
hold on
semilogy(Modes.mf,sig_max',,'co')
semilogy([Modes.mf; Modes.mf],[sig_max; 1e-
30*ones(1,Geom.nsmodes)],'c:')
semilogy([Modes.fsort; Modes.fsort],[respH2(Modes.findx); ...
      1e-30*ones(1,Geom.nsmodes)],'b-')
semilogy(Modes.mf(target)*[1 1],[respH2(target); 1e-30],'r-')
semilogy([Modes.mf(ortho); Modes.mf(ortho)],[respH2(ortho); ...
      1e-30*ones(size(ortho))],'k-')
hold off
xlabel('Frequency, Hz');ylabel('Modal Amplitude')
axs = axis;
axis([axs(1) 1500 1e-15 max([axs(4) 10])])
drawnow

Weights = struct('target',target,'ortho',ortho,'nmatHi',nmatHi,...
   'nmatH2',nmatH2,'respHi',respHi,'respH2',respH2,'sig_in',sig_in);


% Form ABCD Matrices
Cs = .01*diag(Modes.f/2/pi);
A = [zeros(Geom.nsmodes*3) eye(Geom.nsmodes*3); ...
```

```
      -1*inv(MandK.Ms)*MandK.Ks -1*inv(MandK.Ms)*Cs];
Fact = strainAct;
Fsen = strainSen;
B = [zeros(Geom.nsmodes*3,nsensor+1); inv(MandK.Ms)*[Fact dist]];
C = [Fsen' zeros(nsensor,Geom.nsmodes*3); perf
zeros(1,Geom.nsmodes*3)];
D = zeros(nsensor+1,nsensor+1);

w = logspace(2,5,1000);
P = ss(A,B,C,D);
freq = w/2/pi;
nchnl = min(size(B)) - 1;

% Calculate Frequency Response
[m,p] = bode(P,w);
c = m .* exp(p*pi/180 * i);
filtH2 = squeeze(sum(sum(c(1:nchnl,1:nchnl,:) .* ...
   repmat(nmatH2(nsensor+1:2*nsensor)*nmatH2(1:nsensor)',...
   [1 1 length(freq)]), 1), 2));
filtHi = squeeze(sum(sum(c(1:nchnl,1:nchnl,:) .* ...
   repmat(nmatHi(nsensor+1:2*nsensor)*nmatHi(1:nsensor)',...
   [1 1 length(freq)]), 1), 2));

TF = struct('P',P,'freq',freq,'nchnl',nchnl,'mag',m,'phs',p,...
   'filtH2',filtH2,'filtHi',filtHi);
save data TF Weights Coupling Geom MandK Modes


% Plot Frequency Response
mmax = squeeze(max(max(TF.mag(1:nchnl,1:nchnl,:),[],1),[],2));
mmin = squeeze(min(min(abs(TF.mag(1:nchnl,1:nchnl,:)),[],1),[],2));
mmean =
10.^squeeze(mean(mean(log10(abs(TF.mag(1:nchnl,1:nchnl,:))),1),2));
Perf = squeeze(abs(TF.mag(nchnl+1,nchnl+1,:)));

figure(2);clf
semilogy(TF.freq,.236*mmax,'k:',TF.freq,.256*abs(TF.filtH2),'b-',...
   TF.freq,abs(TF.filtHi),'r--')
xlabel('Frequency, Hz'); ylabel('Magnitude')
legend('Maximum','2-Norm','Infinity-Norm')
set(gca,'xlim',[50 4000])

figure(3); clf
subplot 211
semilogy(TF.freq,Perf)
hold on
semilogy([Modes.f; Modes.f],2e-9+1e-9*[zeros(size(Modes.f)); ...
      ones(size(Modes.f))],'k-')
hold off
set(gca,'xlim',[50 4000])
xlabel('Frequency, Hz'); ylabel('Performance Magnitude')

subplot 212
semilogy(TF.freq,mmax,':',TF.freq,mmin,':',TF.freq,mmean)
hold on
```

```
semilogy([Modes.f; Modes.f],2e-11+1e-11*[zeros(size(Modes.f)); ...
      ones(size(Modes.f))],'k-')
hold off
set(gca,'xlim',[50 4000])
xlabel('Frequency, Hz'); ylabel('Sensor Magnitude')
```

C.2 File: panel_evec.m

```
function [Geom,MandK,Modes] = panel_evec
%  FINDS THE STRUCTURAL RESPONSE OF A CURVED PANEL

%  Note that the ith column of shapes contains the weights to be
%  applied to the assumed shapes to make up the ith actual mode
%
%
%  Coordinates: w is out of plane
%           v is tangential
%           u is longitudinal

global ntmodes Length nzmodes swtch nrib nstring trib tstring Radius
global nwtmodes nwlmodes nutmodes nulmodes nvtmodes nvlmodes
clear  shapes index evec Ts

%  DEFINE STRUCTURAL MODAL RESOLUTION
ntmodes = 10;      % No. modes in theta direction      >=0
nlmodes = 10;      % No. modes in long direction       >=0
offsett = 1;       % Starting Mode No. for theta modes
offsetl = 0;       % Starting Mode No. for long modes
nrpoint  = (ntmodes+1)*5;      % No. integration points along radius
nzpoint  = nlmodes*5;          % No. longitudinal integration points
swtch    = 'c';    % Designate cosine only modes 'c'
% or sin&cos acoustic modes 'sc' for theta
SaveIt   = 'n';       % To save the results in junks.m? y/n

%  DEFINE STRUCTURE
Radius = 18*.0254;       % Radius of Cylinder [m]
Length = 60*.0254;       % Length of Cylinder [m]
h        = 0.032*.0254;     % Shell Thickness     [m]
BCstiff= 0.8;            % Relative stiffness of edge spring for BC

%  PANEL OR CYLINDER
nribs = 5;         % Set = 5 for panels, = 1 for cylinder dynamics
nstring  = 12;        % Set =12 for panels, = 1 for cylinder dynamics

E     = 1.2*66e9;        % Modulus of Cyliner [N/m^2]
nu     = 0.3;         % Poisson of Structure  [ ]
rho    = 2700;        % Density of Cylinder   [(kg/m^3)]

%  DECIDE ORDER OF MODES
nsmodes = nlmodes*(ntmodes+1);          % No. structural modes
if nlmodes == 0,
   nsmodes = ntmodes;
   offsetl = offsetl-1;                 % Otherwise off by one
```

```
end
mn    = (1:nsmodes)';                    % mode number vector

%       ORDER MODES
jnk   = (1:nsmodes/2)';                  % Counter for modes
l   = ceil(.999*mn/((ntmodes+1)));       % Longitudinal mode number
t   = rem( mn-1,ntmodes+1);              % Circumferential mode number

wl = (l + offsetl)*nribs;
wt = (t + offsett)*nstring/2;

%  CREATE STRUCTURED ARRAYS
Geom   = struct('Radius',Radius,'Length',Length,'nsmodes',nsmodes, ...
   'wt',wt,'wl',wl,'nlmodes',nlmodes,'ntmodes',ntmodes,'nstring', ...
   nstring,'nribs',nribs,'thick',h);

%%%%%%%%%%%%%%%%%%%%%%%%%%%%%%%%%%%%%%%%%%%%%%%%%%%%%%%%%%%%%%%%%%%%%%%%%%%%
%   SYSTEM MATRIX
%
disp('Compute Structural Mass and Stiffness Matrices')

Ms = zeros(nsmodes,nsmodes);
Ks = zeros(nsmodes,nsmodes);
Kst= zeros(nsmodes,nsmodes);
Identity = eye(nsmodes,nsmodes);
termK22t=0; termK23t=0; termK32t=0;

%  FORM MESH FOR LENGTH AND THETA ON THE SHELL
[pz,pt] = meshgrid(0.5/(1+nzpoint):...
   1/(1+nzpoint):(.5+nzpoint)/(1+nzpoint),...
   1*pi/nrpoint:2*pi/nrpoint:(2*pi-pi/nrpoint));
pz = pz / nribs;          % Reduce dimension to individual panel
pt = pt / nstring;          %   "        "        "       "        "

%  COORDINATES OF THE EDGES OF THE PANEL FOR SPRING B.C.
pz_edgez = repmat([0 1],nrpoint,1) / nribs;
pt_edget = repmat([0 2*pi],nzpoint+1,1)' / nstring;
%  SET SIGN ON SPRING TO BE POSITIVE ON ONE SIDE AND NEG ON OTHER
bc_signz = repmat([1 -1],nrpoint,1);
bc_signt = repmat([1 -1],nzpoint+1,1)';

delta = 2*pi/nrpoint*Radius/nstring * Length/nribs/(1+nzpoint);
disp('Integrate over the Shell');

k = (h/Radius)^2*1/12;  % Shell Equation Term    [ ]

for ii = 1:nsmodes,

   %    EVALUATE MODES ON THE MESH
   %    CALCULATE THE ii MODE SHAPES AND DERIVATIVES
   modeui   = pumodes(wt(ii),wl(ii),1,0,pt,pz,Geom);
   modevi   = pvmodes(wt(ii),wl(ii),1,0,pt,pz,Geom);
   modewi   = pwmodes(wt(ii),wl(ii),1,'no',pt,pz,Geom);
   modeusi  = pumodes(wt(ii),wl(ii),1,'s',pt,pz,Geom);
   modeuti  = pumodes(wt(ii),wl(ii),1,'t',pt,pz,Geom);
```

```
   modevsi = pvmodes(wt(ii),wl(ii),1,'s',pt,pz,Geom);
   modevti = pvmodes(wt(ii),wl(ii),1,'t',pt,pz,Geom);
   modewti = pwmodes(wt(ii),wl(ii),1,'to',pt,pz,Geom);
   modewssi= pwmodes(wt(ii),wl(ii),1,'ss',pt,pz,Geom);
   modewtti= pwmodes(wt(ii),wl(ii),1,'tt',pt,pz,Geom);
   modewsti= pwmodes(wt(ii),wl(ii),1,'st',pt,pz,Geom);
   modewtedgei = pwmodes(wt(ii),wl(ii),1,'to',pt_edget,pz(1:2,:),Geom);
   modewsedgei = pwmodes(wt(ii),wl(ii),1,'so',pt(:,1:2),pz_edgez,Geom);

   for jj = ii:nsmodes,
      %         CALCULATE jj MODE SHAPES AND DERIVATIVES
      modeuj  = pumodes(wt(jj),wl(jj),1,0,pt,pz,Geom);
      modevj  = pvmodes(wt(jj),wl(jj),1,0,pt,pz,Geom);
      modewj  = pwmodes(wt(jj),wl(jj),1,'no',pt,pz,Geom);
      modeusj = pumodes(wt(jj),wl(jj),1,'s',pt,pz,Geom);
      modeutj = pumodes(wt(jj),wl(jj),1,'t',pt,pz,Geom);
      modevsj = pvmodes(wt(jj),wl(jj),1,'s',pt,pz,Geom);
      modevtj = pvmodes(wt(jj),wl(jj),1,'t',pt,pz,Geom);
      modewtj = pwmodes(wt(jj),wl(jj),1,'to',pt,pz,Geom);
      modewssj= pwmodes(wt(jj),wl(jj),1,'ss',pt,pz,Geom);
      modewttj= pwmodes(wt(jj),wl(jj),1,'tt',pt,pz,Geom);
      modewstj= pwmodes(wt(jj),wl(jj),1,'st',pt,pz,Geom);
      modewtedgej =
pwmodes(wt(jj),wl(jj),1,'to',pt_edget,pz(1:2,:),Geom);
      modewsedgej =
pwmodes(wt(jj),wl(jj),1,'so',pt(:,1:2),pz_edgez,Geom);

      %         ASSEMBLE TERMS IN INTEGRAND
      fct = 1+Identity(ii,jj);    % Diagonal blocks are twice as big
      termM11 = fct*modeui.*modeuj;
      termM22 = fct*modevi.*modevj;
      termM33 = fct*modewi.*modewj;

      termK11 = fct*(modeusi.*modeusj + (1-nu)/2*modeuti.*modeutj);
      termK12 = fct*(-1*(1-nu)/2*modeuti.*modevsj+modeusi.*modevtj);
      termK13 = fct*nu*modeusi.*modewj;

      termK21 = fct*(-1*(1-nu)/2*modevsi.*modeutj+modevti.*modeusj);
      termK22 = fct*((1-nu)/2*modevsi.*modevsj+ modevti.*modevtj);
      termK23 = fct*modevti.*modewj;

      termK31 = fct*nu*modewi.*modeusj;
      termK32 = fct*modewi.*modevtj;
      termK33 = fct*(modewi.*modewj + k*(modewssi.*modewssj+...
         modewtti.*modewttj + nu*modewtti.*modewssj + ...
         nu*modewssi.*modewttj + 2*(1-nu)*modewsti.*modewstj));

      termBC_t= fct*(modewtedgei.*modewtedgej);
      termBC_z= fct*(modewsedgei.*modewsedgej);

      i_indx = 3*(ii-1) + 1;
      j_indx = 3*(jj-1) + 1;

      %         INTEGRATE FOR THIS CONSTANT RADIUS SLICE
      Ms(i_indx,j_indx)     =h/2*delta*rho*Radius^2*sum(sum(termM11)) ;
```

```
      Ms(i_indx+1,j_indx+1) =h/2*delta*rho*Radius^2*sum(sum(termM22));
      Ms(i_indx+2,j_indx+2) =h/2*delta*rho*Radius^2*sum(sum(termM33));

      KBC(ii,jj)      = BCstiff*(sum(sum(termBC_t))+sum(sum(termBC_z)));
      Ks(i_indx,j_indx)     = h/2*delta * E/(1-nu^2)*sum(sum(termK11));
      Ks(i_indx+1,j_indx)   = h/2*delta * E/(1-nu^2)*sum(sum(termK12));
      Ks(i_indx+2,j_indx)   = h/2*delta * E/(1-nu^2)*sum(sum(termK13));
      Ks(i_indx,j_indx+1)   = h/2*delta * E/(1-nu^2)*sum(sum(termK21));
      Ks(i_indx+1,j_indx+1) = h/2*delta * E/(1-nu^2)*sum(sum(termK22));
      Ks(i_indx+2,j_indx+1) = h/2*delta * E/(1-nu^2)*sum(sum(termK23));
      Ks(i_indx,j_indx+2)   = h/2*delta * E/(1-nu^2)*sum(sum(termK31));
      Ks(i_indx+1,j_indx+2) = h/2*delta * E/(1-nu^2)*sum(sum(termK32));
      Ks(i_indx+2,j_indx+2) = h/2*delta * E/(1-nu^2)*sum(sum(termK33))
+ KBC(ii,jj);

      %      FILL IN SYMMETRY OF M AND K MATRICES
      Ms(j_indx,i_indx)     = Ms(i_indx,j_indx);
      Ms(j_indx+1,i_indx)   = Ms(i_indx,j_indx+1);
      Ms(j_indx+2,i_indx)   = Ms(i_indx,j_indx+2);
      Ms(j_indx,i_indx+1)   = Ms(j_indx,i_indx+1);
      Ms(j_indx+1,i_indx+1) = Ms(i_indx+1,j_indx+1);
      Ms(j_indx+2,i_indx+1) = Ms(i_indx+1,j_indx+2);
      Ms(j_indx,i_indx+2)   = Ms(i_indx+2,j_indx);
      Ms(j_indx+1,i_indx+2) = Ms(i_indx+2,j_indx+1);
      Ms(j_indx+2,i_indx+2) = Ms(i_indx+2,j_indx+2);
      Ks(j_indx,i_indx)     = Ks(i_indx,j_indx);
      Ks(j_indx+1,i_indx)   = Ks(i_indx,j_indx+1);
      Ks(j_indx+2,i_indx)   = Ks(i_indx,j_indx+2);
      Ks(j_indx,i_indx+1)   = Ks(i_indx+1,j_indx);
      Ks(j_indx+1,i_indx+1) = Ks(i_indx+1,j_indx+1);
      Ks(j_indx+2,i_indx+1) = Ks(i_indx+1,j_indx+2);
      Ks(j_indx,i_indx+2)   = Ks(i_indx+2,j_indx);
      Ks(j_indx+1,i_indx+2) = Ks(i_indx+2,j_indx+1);
      Ks(j_indx+2,i_indx+2) = Ks(i_indx+2,j_indx+2);

   end
end

%%%%%%%%%%%%%%%%%%%%%%%%%%%%%%%%%%%%%%%%%%%%%%%%%%%%%%%%%%%%%%%%%%%%%%%%%%%%
%   Frequencies and Mode Shapes
%  Eigenvectors are columns in evec and shapes.
%  Modes are sorted to have increasing frequency

[evec,eval]=eig(inv(Ms)*Ks);
[omega,index]=sort(sqrt(diag(eval)));
freqss=(1/(2*pi))*omega;
disp('Structural Natural Frequencies')
disp(freqss)

%  SORT MODES SO THAT FREQ CORRESPONDS TO MODAL NUMBER
clear shapes f y i
prev = zeros(nsmodes*3,1);
for ii=1:nsmodes*3,
   [y,i]=sort(-1*abs(evec(ii,:)));
   if prev(i(1)) == 0,
```

```
      indx = i(1);
      prev(i(1)) = 1;
   else
      indx = i(2);
      disp('Unusual Modal ordering with Mode Number')
      disp([i(1) i(2)])
   end
   shapes(:,ii)=evec(:,indx);
   f(ii) = sqrt(eval(indx,indx))/2/pi;
end

%  FIND WHICH OF THE 3 FREQ AT A MODAL NUMBER HAS LOWEST FREQUENCY
jj = 0;
clear f1 f2 f3 ff mf
for ii=1:3:(nsmodes)*3,
   jj = jj+1;
   f1(jj) = f(ii);
   f2(jj) = f(ii+1);
   f3(jj) = f(ii+2);
end
ff = [f1' f2' f3'];
mf = min(ff');

% Sort Modes and Label Indexes
[fsort,findx] = sort(mf);

%  CREATE STRUCTURED ARRAYS
Geom  = struct('Radius',Radius,'Length',Length,'nsmodes',nsmodes, ...
   'wt',wt,'wl',wl,'nlmodes',nlmodes,'ntmodes',ntmodes,'nstring', ...
   nstring,'nribs',nribs,'thick',h);
MandK = struct('Ms',Ms,'Ks',Ks);
Modes =
struct('shapes',shapes,'f',f,'mf',mf,'fsort',fsort,'findx',findx);


%  PLOT NATURAL FREQUENCIES
xax = 0+offsett:Geom.ntmodes+offsett;
plot(xax,Modes.mf(1:Geom.ntmodes+1),'-x');hold on
for ii = 2:Geom.nlmodes,
plot(xax,Modes.mf((Geom.ntmodes+1)*(ii-1)+1:(Geom.ntmodes+1)*ii),'-x');
end
xlabel('Circumferential Mode')
ylabel('Natural Frequency, Hz')
grid;
hold off;
drawnow

if SaveIt=='y'
   save junks Ms Ks Radius Length swtch nlmodes ntmodes...
   shapes nsmodes mf wt wl
end
```

C.3 File: modeshapeplot.m

```
function modeshape(Geom,Modes,l_mode,t_mode)
%  PLOT MODE SHAPES

%  DEFINE VARIABLES AND EXTRACT THEM FROM STRUCTURED ARRAYS
nribs = Geom.nribs;
nstring  = Geom.nstring;
nsmodes  = Geom.nsmodes;
wt     = Geom.wt;
wl     = Geom.wl;
shapes   = Modes.shapes;

nzpoint  = l_mode*10;
nrpoint  = t_mode*10;

%  Desired mode number is intersection.  x3 for 3 DOF
mdnum = 3*find( (wl==l_mode*nribs) & (wt==t_mode*nstring/2) );

%  Define evaluation space
[x,y] = meshgrid(0:.25/nzpoint:1, 0:.25/nrpoint:1);
x      = x/nribs;
y      = y*2*pi/nstring;
z      = zeros(size(x));

%  Calculate mode shape
for ii = 1:nsmodes,
   z  = z + shapes(mdnum,3*ii) *
pwmodes(wt(ii),wl(ii),1,'no',y,x,Geom);
end

surf(x*Geom.Length,y*Geom.Radius,z);
view([0 0 1])
shading interp
```

C.4 File: panel_strain.m

```
function strain = panel_strain(Geom,Modes,PiezDim)
% Calculate modal coupling to strain

% Define edges of the piezo PROPORTIONAL TO LENGTH
ldelta   = PiezDim.lmax - PiezDim.lmin;
tdelta   = PiezDim.tmax - PiezDim.tmin;

% Number of integration points
lpoint   = ceil(Geom.nlmodes*5*ldelta) + 2;
tpoint   = ceil(Geom.ntmodes*5*tdelta) + 2;

% Define integration mesh
[pz,pt]  = meshgrid(
PiezDim.lmin+.5*ldelta/lpoint:ldelta/lpoint:PiezDim.lmax-
.5*ldelta/lpoint, ...
```

```
   PiezDim.tmin+.5*tdelta/tpoint:tdelta/tpoint:PiezDim.tmax-
.5*tdelta/tpoint );
pz     = pz/Geom.nribs;
pt     = pt*2*pi/Geom.nstring;

% Loop over mode shapes
for ii = 1:Geom.nsmodes,
   modewss   = pwmodes(Geom.wt(ii),Geom.wl(ii),1,'ss',pt,pz,Geom);
   modewtt   = pwmodes(Geom.wt(ii),Geom.wl(ii),1,'tt',pt,pz,Geom);
   modeus    = 5*pumodes(Geom.wt(ii),Geom.wl(ii),1,'s',pt,pz,Geom);
   modevt    = .2*pvmodes(Geom.wt(ii),Geom.wl(ii),1,'t',pt,pz,Geom);
   modew     = pwmodes(Geom.wt(ii),Geom.wl(ii),1,'no',pt,pz,Geom);

   for jj = 0:2,
      indx = (ii-1)*3 + 1;
      strainx = 1./Geom.Radius*Modes.shapes(indx,indx+jj)*modeus - ...
         1/Geom.Radius^2*Modes.shapes(indx+2)*Geom.thick*modewss;
      straint = 1/Geom.Radius*Modes.shapes(indx+1)*modevt - ...
         1/Geom.Radius^2*Modes.shapes(indx+2)*Geom.thick*modewtt + ...
         1/Geom.Radius*Modes.shapes(indx+2)*modew;
      dA = (ldelta*Geom.Length/Geom.nribs/lpoint) * ...
         (tdelta*2*pi*Geom.Radius/Geom.nstring/tpoint);
      strain(indx+jj)    = dA*sum(sum(strainx+straint));
   end
end

linecolor = ['r';'b';'g';'m';'k';'c'];numcolor = 6;
% Plot Strain Coupling
for ii = 1:Geom.nlmodes,
   colormod= mod(ii-1,numcolor) + 1;
   indx   = (ii-1)*(Geom.ntmodes+1);
   xax       = 1:Geom.ntmodes;
   eval([' semilogy(xax,abs(strain(indx+1:indx+Geom.ntmodes)),'' '
linecolor(colormod) '-o '')'])
   hold on
end
hold off
xlabel('Circumferential Mode Number')
ylabel('Magnitude of Modal Coupling')
if Geom.ntmodes > 1,
   axis([ 1 Geom.ntmodes 1e-10 1])
else
   axis([ 0 2 1e-10 1])
end
drawnow
```

C.5 File: panel_disp.m

```
function disp = panel_disp(Geom,Modes,PerfDim)
% Calculate modal coupling to strain

pz = PerfDim.lcenter / Geom.nribs;
pt = PerfDim.tcenter * 2*pi / Geom.nstring;
```

```
% Loop over mode shapes
for ii = 1:Geom.nsmodes,
   modew    = pwmodes(Geom.wt(ii),Geom.wl(ii),1,'no',pt,pz,Geom);

   for jj = 0:2,
      indx = (ii-1)*3 + 1;
      disp(indx+jj) = Modes.shapes(indx+jj,indx+2) * modew;
   end
end

linecolor = ['r';'b';'g';'m';'k';'c'];numcolor = 6;
% Plot Strain Coupling
for ii = 1:Geom.nlmodes,
   colormod= mod(ii-1,numcolor) + 1;
   indx  = (ii-1)*(Geom.ntmodes+1);
   xax      = 1:Geom.ntmodes;
   eval([' semilogy(xax,abs(disp(indx+1:indx+Geom.ntmodes)),'' '
linecolor(colormod) '-o '')'])
   hold on
end
hold off
xlabel('Circumferential Mode Number')
ylabel('Magnitude of Modal Coupling')
if Geom.ntmodes > 1,
   axis([ 1 Geom.ntmodes 1e-10 1])
else
   axis([ 0 2 1e-10 1])
end
drawnow
```

C.6 File: killmodeHi.m

```
function [cost] = killmode(x)
% Cost function for the killmode routine
%  x - weights for each sensor element

global Coupling target ortho sig_in
clear resp

xa = x(1:length(x)/2);
xs = x(length(x)/2+1:length(x));

for ii = 1:length(sig_in),
   resp(ii) = squeeze(abs(xs'*sig_in(:,:,ii)*xa));
end

cost  = max(resp(ortho)) / resp(target);
```

C.7 File: killmodeH2.m

```
function [cost] = killmodeH2(x)
% Cost function for the killmode routine
%  x - weights for each sensor element

global Coupling target ortho sig_in

xa = x(1:length(x)/2);
xs = x(length(x)/2+1:length(x));

for ii = 1:length(sig_in),
   resp(ii) = squeeze(abs(xs'*sig_in(:,:,ii)*xa));
end

cost  = sum(resp(ortho)) / resp(target);
```

C.8 File: pumodes.m

```
function [value] = pumodes(ut,ul,ss,deriv,theta,pz,Geom)
%  SUMODES(modenumber in theta,modenumber in
length,ss,deriv,theta,fractlength)
%
%       Returns the structural mode shapes of the system.
%
   Length    = Geom.Length;
   Radius    = Geom.Radius;

% VARIABLE DEFINITIONS
%       deriv - derivative of mode
%       theta - angle of evaluation, in radians
%       pz    - fractional longitudinal distance
%       Length- length of the cylinder
%       Radius- radius of the cylinder
%       ss    - dictates whether cosine mode or sine mode shape
%       ut    -                u         theta
%       ul    -                u         long

% CALCULATE SHAPE FUNCTION

if deriv == 0,
   value = cos(ul*pz*pi) .* cos(ut*theta + ss*pi/2+ 0*pi/4);

elseif deriv == 's',            % Derivative with respect to pz
   value = -Radius/Length*ul*pi* sin(ul*pz*pi).* ...
               cos(ut*theta + ss*pi/2+ 0*pi/4);

elseif deriv == 't',            % Derivative with respect to theta
   value = -1*ut* cos(ul*pz*pi) .* sin(ut*theta + ss*pi/2+ 0*pi/4);

else
   disp('An unreasonable derivative was desired in SUMODES');
```

```
end
```

C.9 File: pvmodes.m

```
function [value] = pvmodes(vt,vl,ss,deriv,theta,pz,Geom);
%  SVMODES(modenumber in theta,modenumber in
length,ss,deriv,theta,fractlength)
%
%  Returns the structural mode shapes of the system.
%
   Length    = Geom.Length;
   Radius    = Geom.Radius;

% VARIABLE DEFINITIONS
%  deriv - derivative of mode
%  theta - angle of evaluation, in radians
%  pz    - fractional longitudinal distance
%  Length- length of the cylinder
%  Radius- radius of the cylinder
%  ss    - dictates whether cosine mode or sine mode shape
%  vt    -                v          theta
%  vl    -                v          long


% CALCULATE SHAPE FUNCTION

if deriv == 0,
   value = sin(vl*pz*pi) .* sin(vt*theta + ss*pi/2 +  0*pi/4);

elseif deriv == 's',     % Derivative with respect to pz
   value = Radius/Length*vl*pi* cos(vl*pz*pi).* ...
      sin(vt*theta + ss*pi/2+ 0*pi/4);

elseif deriv == 't',     % Derivative with respect to theta
   value = vt* sin(vl*pz*pi) .* cos(vt*theta + ss*pi/2+ 0*pi/4);

else
   disp('An unreasonable derivative was desired in SVMODES');
end
```

C.10 File: pwmodes.m

```
function [value] = pwmodes(wt,wl,ss,deriv,theta,pz,Geom);
%  SWMODES(modenumber in theta,modenumber in
length,ss,deriv,theta,fractlength)
%
%  Returns the structural mode shapes of the system.
%
   Length    = Geom.Length;
   Radius    = Geom.Radius;
```

```
% VARIABLE DEFINITIONS
%  deriv - derivative of mode
%  theta - angle of evaluation, in radians
%  pz    - fractional longitudinal distance
%  Length- length of the cylinder
%  Radius- radius of the cylinder
%  ss    - dictates whether cosine mode or sine mode shape
%  wt    - mode number of w mode in theta direction
%  wl    -                 w         long


% CALCULATE SHAPE FUNCTION
if deriv == 'no', % No Derivative
  value = sin(wl*pz*pi) .* cos(wt*theta + ss*pi/2);

elseif deriv == 'to',   % Derivative wrt THETA
  value = -1*wt* sin(wl*pz*pi) .* sin(wt*theta + ss*pi/2);

elseif deriv == 'so',   % Derivative wrt S
  value = Radius/Length*wl*pi*cos(wl*pz*pi) .* cos(wt*theta + ss*pi/2);

elseif deriv == 'ss',   % Second Derivative wrt S
   value = -1*(Radius/Length*wl*pi)^2*sin(wl*pz*pi).*...
   cos(wt*theta + ss*pi/2);

elseif deriv == 'tt',   % Second Derivative wrt THETA
  value = -1*wt^2*sin(wl*pz*pi) .* cos(wt*theta + ss*pi/2);

elseif deriv == 'st',   % Second Derivative wrt S & THETA
  value = Radius/Length*wl*pi*wt*cos(wl*pz*pi) .* ...
   sin(wt*theta + ss*pi/2);

else
  disp('An unreasonable derivative was desired in SWMODES');
  disp(deriv)
end
```

C.11 File: LQGcontrolMIMO.m

```
% Modal ID and Control

if exist('P','var') ~= 1,

   load data      %Written by Panel.m

   % Reduce size of modal id data
   indx  = 1:2:900;
   freqR = TF.freq(indx);

   weighting = 'y';
   if weighting == 'n',
      nchnl = TF.nchnl;
      filtP = 1e8*TF.mag .* exp(TF.phs * i *pi/180);
```

```
      filtR = shiftdim(filtP(1:nchnl,1:nchnl,indx),2);
      filtD = TF.mag(nchnl+1,nchnl+1,:) .* ...
              exp(i*pi/180*TF.phs(nchnl+1,nchnl+1,:));
      sgn   = 1;
   else
      nchnl = 1;
      filtP = 1e8 * TF.filtH2;
      filtR = filtP(indx);
      sgn   = 1;
      filtD = squeeze(TF.mag(TF.nchnl+1,TF.nchnl+1,:) .* ...
              exp(i*pi/180*TF.phs(TF.nchnl+1,TF.nchnl+1,:)));
   end

   % Designate Transfer Function
   data  = reshape(filtR,[length(indx) nchnl^2]);
   fmatch = 1100;


   % Identify Best-Fit Model
   % Call DynaMod
   xfer = fpck(data,freqR,[nchnl nchnl]);
   sys = transferid(xfer);
   [A B C D] = funpck(sys);

   P  = canon(ss(A,B,C,D));
   Psize = length(A);

   [mP,pP] = bode(P,TF.freq*2*pi);
   cP = mP .* exp(i*pP*pi/180);
   figure(1)
   if weighting == 'n',
      semilogy(TF.freq,squeeze(max(max(mP,[],1),[],2)),':',
TF.freq,squeeze(max(max(abs(filtP),[],1),[],2)));
   else
      semilogy(TF.freq,squeeze(mP),':',TF.freq,abs(filtP))
   end
   axis([50 4000 5e-2 5])
   xlabel('Frequency, Hz'); ylabel('Magnitude')
   legend([num2str(sys.n) ' State Model'],'Experiment')
   drawnow
end

%-----------------DESIGN CONTROLLER-------------------%
% KALMAN FILTER DESIGN
Rkf   = 2e-2*eye(nchnl);          % Sensor noise = Vyy = Dyw*Dyw'
Qkf   = B*B';                  % Actuator noise
Pkf   = are( A',C'*inv(Rkf)*C,Qkf);
KF    = Pkf*C'*inv(Rkf);

% LQR DEISGN
rho   = 2e-2*eye(nchnl);          % Control penalty = Ruu = Dzw'*Dzw
Qlqr  = C'*C;                  % State penalty
KG    = lqr(A,B,Qlqr,rho);
klqg0 = ss(A - B*KG - KF*C, KF, KG, 0);
```

```
P_cl0 = feedback(P,klqg0,1:nchnl,1:nchnl,-1*sgn);
loop0 = klqg0*P;

% Evaluate Magnitudes
[mklqg0,pklqg0] = bode(klqg0,TF.freq*2*pi);
cklqg0 = mklqg0 .* exp(i*pklqg0*pi/180);
[mPcl0,pPcl0] = bode(P_cl0,TF.freq*2*pi);
cPcl0 = mPcl0 .* exp(i*pPcl0*pi/180);
[mloop0,ploop0] = bode(loop0,TF.freq*2*pi);
cloop0 = mloop0 .* exp(i*ploop0*pi/180);


figure(1)
if weighting == 'n',
   % Use Measured Plant Data
   cTloop0 = sgn*cklqg0 .* filtP(1:nchnl,1:nchnl,:);
   cTcl0   = filtP(1:nchnl,1:nchnl,:) ./ (1 + cTloop0);
   cTclp0     = repmat(filtD,[nchnl nchnl 1]) ./ (1 + cTloop0);
   subplot 211

semilogy(TF.freq,squeeze(max(max(abs(filtP(1:nchnl,1:nchnl,:)),[],1),[]
,2)),':',TF.freq,squeeze(max(max(abs(cTcl0),[],1),[],2)))
   set(gca,'xlim',[50 4000])
   subplot 212

semilogy(TF.freq,squeeze(abs(filtD)),':',TF.freq,squeeze(max(max(abs(cT
clp0),[],1),[],2)))
   set(gca,'xlim',[50 4000])
else
   % Use Measured Plant Data
   cTloop0   = sgn*squeeze(cklqg0) .* filtP;
   cTcl0     = filtP ./ (1 + cTloop0);
   cTclp0    = filtD ./ (1 + cTloop0);
   subplot 211
   semilogy(TF.freq,abs(filtP),':',TF.freq,abs(cTcl0))
   set(gca,'xlim',[50 4000])
   subplot 212
   semilogy(TF.freq,abs(filtD),':',TF.freq,abs(cTclp0))
   set(gca,'xlim',[50 4000])
end
xlabel('Frequency, Hz'); ylabel('Magnitude')
drawnow

%%%%%%%%%%%%%%%%%%%%%%%%%%%%%%%%%%%%%%%%%%%%%%%%%%%%%%%%%%%%%%%%%%%%%%%
% Frequency Weights based upon Noise Model                              %
% Follows formulation in Preumont's book. Section 8.16.2 and 8.10 %
% Weights on R, input filter, s, w2
zR = .1;
Rw = mean(fmatch)*2*pi;
Rw1    = Rw/1.5;
Rw2    = Rw*1.5;
Rnum   = 1*[1 2*zR*Rw Rw^2];
Rden   = [1 Rw1+Rw2 Rw1*Rw2];
[Ra,Rb,Rc,Rd] = tf2ss(Rnum,Rden);
Rb = repmat(Rb,[1 nchnl]);
```

```
Rc = repmat(Rc,[nchnl 1]);
Rd = repmat(Rd,[nchnl nchnl]);
Rsize = length(Ra);
[Rm,Rp] = bode(Rnum,Rden,TF.freq*2*pi);

E = B;      % Kalman noise
Aaug = [A E*Rc; zeros(Rsize,Psize) Ra];
Baug = [B; zeros(Rsize,nchnl)];
Caug = [C zeros(nchnl,Rsize)];
Daug = D;
Eaug = [zeros(Psize,nchnl); Rb];

% KALMAN FILTER DESIGN
Rkf= 2e-2*eye(nchnl);   % Sensor noise = Vyy = Dyw*Dyw'
Qkf= Eaug*Eaug';     % Actuator noise
Pkf= are( Aaug',Caug'*inv(Rkf)*Caug,Qkf);
KF = Pkf*Caug'*inv(Rkf);

% LQR DEISGN
rho   = 2e-2*eye(nchnl);   % Control penalty = Ruu = Dzw'*Dzw
Qlqr  = Caug'*Caug;     % State penalty
KG    = lqr(Aaug,Baug,Qlqr,rho);
klqg  = ss(Aaug - Baug*KG - KF*Caug, KF, KG, 0);

P_cl  = feedback(P,klqg,1:nchnl,1:nchnl,-1*sgn);
loop  = klqg*P;


% Evaluate Magnitudes
[mklqg,pklqg] = bode(klqg,TF.freq*2*pi);
cklqg       = mklqg .* exp(i*pklqg*pi/180);
[mP,pP]     = bode(P,TF.freq*2*pi);
cP          = mP .* exp(i*pP*pi/180);
[mPcl,pPcl] = bode(P_cl,TF.freq*2*pi);
cPcl        = mPcl .* exp(i*pPcl*pi/180);
[mloop,ploop] = bode(loop,TF.freq*2*pi);
cloop       = mloop .* exp(i*ploop*pi/180);

figure(4);  % Open-Loop and Closed-Loop Performance
if weighting == 'n',
   % Use Measured Plant Data
   cTloop = sgn * cklqg .* filtP(1:nchnl,1:nchnl,:);
   cTcl   = filtP(1:nchnl,1:nchnl,:) ./ (1 + cTloop);
   cTclp  = repmat(filtD,[nchnl nchnl 1]) ./ (1 + cTloop);
   subplot 211

semilogy(TF.freq,squeeze(max(max(abs(filtP(1:nchnl,1:nchnl,:)),[],1),[]
,2)),':',TF.freq,squeeze(max(max(abs(cTcl),[],1),[],2)))
   set(gca,'xlim',[50 4000]);hold on
   subplot 212

semilogy(TF.freq,squeeze(abs(filtD)),':',TF.freq,squeeze(max(max(abs(cT
clp),[],1),[],2)))
   set(gca,'xlim',[50 4000])
else
```

```
   % Use Measured Plant Data
   cTloop = sgn * squeeze(cklqg) .* filtP;
   cTcl   = filtP ./ (1 + cTloop);
   cTclp  = filtD ./ (1 + cTloop);
   subplot 211
   semilogy(TF.freq,abs(filtP),':',TF.freq,abs(cTcl),'-'); hold on
   subplot 212
   semilogy(TF.freq,abs(filtD),':',TF.freq,abs(cTclp),'-')
   set(gca,'xlim',[50 4000])
end
subplot 211
semilogy(TF.freq,squeeze(max(max(abs(mPcl),[],1),[],2)),'b:');
semilogy(TF.freq,squeeze(max(max(abs(mP),[],1),[],2)),'r:'); hold off
xlabel('Frequency, Hz'); ylabel('Magnitude')
set(gca,'xlim',[50 4000])
legend('Open-Loop','Closed-Loop')

figure(2);  clf% MIMO Nyquist
for ii = 1:length(TF.freq),
   if weighting == 'n',
      ny(ii) = det(eye(nchnl) + cTloop(:,:,ii));
      ny0(ii) = det(eye(nchnl) + cTloop0(:,:,ii));
   else
      ny(ii) = det(eye(nchnl) + cTloop(ii));
      ny0(ii) = det(eye(nchnl) + cTloop0(ii));
   end
end
plot(real(ny),imag(ny),real(ny0),imag(ny0),'r:',0,0,'rx')
xlabel('Real Part'); ylabel('Imaginary Part')
legend('Frequency Weighted','Un-Weighted',3)

figure(3)
subplot 211
if weighting == 'n',

semilogy(TF.freq,squeeze(max(max(abs(filtP(1:nchnl,1:nchnl,:)),[],1),[]
,2)),'r-'); hold on
   semilogy(TF.freq,squeeze(max(max(abs(cTcl0),[],1),[],2)),'k--')
   semilogy(TF.freq,squeeze(max(max(abs(cTcl),[],1),[],2)),'b-');
else
   semilogy(TF.freq,abs(filtP),'r-'); hold on
   semilogy(TF.freq,abs(cTcl0),'k--',TF.freq,abs(cTcl),'b-')
end

semilogy(TF.freq,squeeze(max(max(abs(mPcl),[],1),[],2)),'b:');
semilogy(TF.freq,squeeze(max(max(abs(mP),[],1),[],2)),'r:'); hold off
xlabel('Frequency, Hz'); ylabel('Magnitude of Sys')
set(gca,'xlim',[50 2500])
subplot 212
semilogy(TF.freq,squeeze(max(max(mklqg,[],1),[],2)),'b'); hold on
semilogy(TF.freq,squeeze(max(max(mklqg0,[],1),[],2)),'k');
semilogy(TF.freq,Rm,'r'); hold off
xlabel('Frequency, Hz'); ylabel('Magnitude of K')
set(gca,'xlim',[50 2500])
legend('Frequency Weighted','No Weights','Frequency Penalty',4)
```

```
% Calculate Performance
fmineval = 500;
fmaxeval = 2500;
indx    = find(TF.freq>fmineval);  % Find frequency index
indxmin= indx(1);
indx    = find(TF.freq>fmaxeval);  % Find frequency index
indxmax= indx(1);

if weighting == 'n',
   costT =
squeeze(sum(sum(trapz(TF.freq(indxmin:indxmax),abs(filtP(1:nchnl,1:nchn
l,indxmin:indxmax)).^2,3),1),2)).^.5;
   costTcl0 =
20*log10(costT/squeeze(sum(sum(trapz(TF.freq(indxmin:indxmax),abs(cTcl0
(:,:,indxmin:indxmax)).^2,3),1),2)).^.5);
   costTcl =
20*log10(costT/squeeze(sum(sum(trapz(TF.freq(indxmin:indxmax),abs(cTcl(
:,:,indxmin:indxmax)).^2,3),1),2)).^.5);
   costTp =
sum(trapz(TF.freq(indxmin:indxmax),squeeze(abs(filtD(:,:,indxmin:indxma
x)).^2))).^.5;
   costTclp0 =
20*log10(costTp/squeeze(max(max(trapz(TF.freq(indxmin:indxmax),abs(cTcl
p0(:,:,indxmin:indxmax)).^2,3),[],1),[],2)).^.5);
   costTclp =
20*log10(costTp/squeeze(max(max(trapz(TF.freq(indxmin:indxmax),abs(cTcl
p(:,:,indxmin:indxmax)).^2,3),[],1),[],2)).^.5);
else
   costT =
sum(trapz(TF.freq(indxmin:indxmax),abs(filtP(indxmin:indxmax)).^2)).^.5
;
   costTcl0 =
20*log10(costT/sum(trapz(TF.freq(indxmin:indxmax),abs(cTcl0(indxmin:ind
xmax)).^2)).^.5);
   costTcl =
20*log10(costT/sum(trapz(TF.freq(indxmin:indxmax),abs(cTcl(indxmin:indx
max)).^2)).^.5);
   costTp =
sum(trapz(TF.freq(indxmin:indxmax),abs(filtD(indxmin:indxmax)).^2)).^.5
;
   costTclp0 =
20*log10(costTp/sum(trapz(TF.freq(indxmin:indxmax),abs(cTclp0(indxmin:i
ndxmax)).^2)).^.5);
   costTclp =
20*log10(costTp/sum(trapz(TF.freq(indxmin:indxmax),abs(cTclp(indxmin:in
dxmax)).^2)).^.5);
end
costP =
squeeze(sum(sum(trapz(TF.freq(indxmin:indxmax),mP(:,:,indxmin:indxmax).
^2,3),1),2)).^.5;
costPcl0 =
20*log10(costP/squeeze(sum(sum(trapz(TF.freq(indxmin:indxmax),mPcl0(:,:
,indxmin:indxmax).^2,3),1),2)).^.5);
```

```
costPcl =
20*log10(costP/squeeze(sum(sum(trapz(TF.freq(indxmin:indxmax),mPcl(:,:,
indxmin:indxmax).^2,3),1),2)).^.5);


disp(['                Evaluate Performance from ' num2str(fmineval) '
Hz to ' num2str(fmaxeval) ' Hz'])
disp(['    Weighted Performance: No Weights: ' num2str(costTcl0) ' dB.
Weighted: ' num2str(costTcl) ' dB.'])
disp(['Displacement Performance: No Weights: ' num2str(costTclp0) ' dB.
Weighted: ' num2str(costTclp) ' dB.'])
disp(['   Predicted Performance: No Weights: ' num2str(costPcl0) ' dB.
Weighted: ' num2str(costPcl) ' dB.'])
```

ברוך אתה יי אלהינו מלך העולם שהחינו וקימנו והגיענו לזמן הזה

Baruch atah adonai, elohaynu melech haolum shekiyanu v'kiamanu v'higianu lazman hazeh

- Traditional Hebrew prayer of Thanksgiving

Literal translation: Blessed are You, Lord our God, Ruler of the universe, Who has kept us in life, sustained us, and enabled us to this reach this joyous occasion.

Loose translation: Thank God we made it!